Doctoral Dissertation
博士論文

Innovative positron spectrometer for $\mu^+ \to e^+\gamma$ search beyond 10^{-13} sensitivity with most intense μ^+ beam

（最大強度 μ^+ ビームを用いた 10^{-13} を超える感度の $\mu^+ \to e^+\gamma$ 探索のための革新的な陽電子スペクトロメータ）

A Dissertation Submitted for the Degree of Doctor of Philosophy
May 2021
令和 3 年 5 月博士（理学）申請

Department of Physics, Graduate School of Science,
The University of Tokyo

東京大学大学院理学系研究科
物理学専攻

Usami Masashi

宇佐見正志

Abstract

The $\mu^+ \rightarrow e^+\gamma$ decay is one of the charged lepton flavor violation (cLFV) phenomena. It is strongly suppressed in the standard model but predicted to occur around the branching ratio of O(10^{-13} – 10^{-15}) in the physics beyond the standard model. The discovery of $\mu^+ \rightarrow e^+\gamma$ will, therefore, be unambiguous evidence of the new physics. Innovative detectors have been developed for the MEG II experiment to achieve the $\mu^+ \rightarrow e^+\gamma$ search in a branching ratio of O(10^{-14}), which is one order better than the current upper limit of 4.2×10^{-13} (90% confidence level) by the MEG experiment. The positron spectrometer is composed of two detectors, the pixelated timing counter (pTC) for timing measurement and the cylindrical drift chamber (CDCH) for track reconstruction, and a spectrometer magnet. The requirement of the positron spectrometer in the MEG II experiment is twice better positron-tracking resolution and positron-reconstruction efficiency than the MEG experiment under twice higher beam intensity. The commissioning of the positron spectrometer was performed to demonstrate the detector performance. The radiation damage of the pTC, which deteriorates the timing resolution significantly, was observed during the commissioning in 2015. The new cooling system was developed to minimize the deterioration, and the stable operation of the pTC was demonstrated. The performance of the full pTC was evaluated in the commissioning in 2017 – 2019, and time resolution of 34.3 ps was achieved with newly developed reconstruction algorithms. As for the CDCH, the noise analysis and the waveform analysis were performed to implement the realistic performances in the simulation. The global tracking algorithms which utilize both the pTC and the CDCH information were newly developed to evaluate the performance of the MEG II positron spectrometer. With realistic simulations and newly developed algorithms, it is demonstrated that new MEG-II positron spectrometer has twice better tracking efficiency and resolution than the MEG experiment under twice higher beam rate. As a results, the projected sensitivity of $\mu^+ \rightarrow e^+\gamma$ search is improved by one order of magnitude better than that of the the MEG experiment, 6.0×10^{-14}, which is powerful probe to discover the new physics.

Contents

Abstract iii

Introduction 1

Chapter 1 Physics Motivation 13
- 1.1 Standard Model 13
- 1.2 Beyond the Standard Model 13
  - 1.2.1 SUper-SYmmetric (SUSY) Model 14
  - 1.2.2 Seesaw Mechanism 15
  - 1.2.3 Grand Unified Theory (GUT) 15
- 1.3 Overview of Charged Lepton Flavor Violation (cLFV) Search 15
- 1.4 Muon Properties 16
  - 1.4.1 Basic Properties of Muon 16
  - 1.4.2 Interactions and Decay Modes 16
- 1.5 Motivation of cLFV Search Experiment 18
  - 1.5.1 Energy Frontier and Intensity Frontier 18
  - 1.5.2 $\mu \to e\gamma$ Decay 19
  - 1.5.3 Prospect of $\mu \to e\gamma$ Search 20

Chapter 2 MEG and MEG II Experiment 23
- 2.1 Experimental Requirements 23
  - 2.1.1 Signal Events 23
  - 2.1.2 Background Events 24
  - 2.1.3 Requirements 26
- 2.2 MEG Experiment 26
  - 2.2.1 Apparatus 27
  - 2.2.2 Result and Limitation 27
  - 2.2.3 Proposal of the MEG II Experiment 29
- 2.3 MEG II Experiment 30
  - 2.3.1 Coordinate systems 31
  - 2.3.2 Muon Beam Line 32
  - 2.3.3 Target 33
  - 2.3.4 Liquid Xenon (LXe) photon Detector 34
  - 2.3.5 Radiative Decay Counter (RDC) 36
  - 2.3.6 Trigger and Data Acquisition (TDAQ) System 37

2.4 Positron Spectrometer . . . 40
2.4.1 Concept of Upgrade from MEG . . . 40
2.4.2 Pixelated Timing Counter (pTC) . . . 41
2.4.3 Cylindrical Drift CHamber (CDCH) . . . 46
2.4.4 COnstant Bending RAdius (COBRA) Magnet . . . 50

Chapter 3 Investigation of Radiation Damage for pTC 53
3.1 Radiation Damage on Series Connected SiPMs . . . 53
3.2 Total Fluence . . . 54
3.3 Irradiation on SiPMs . . . 54
3.3.1 SiPM Irradiation . . . 54
3.4 Effect on pTC Performance by Dark Current Increase . . . 55
3.4.1 IV Curves for Each Damage Level . . . 55
3.4.2 Timing Measurement Setup . . . 55
3.4.3 Deterioration of Time Resolution . . . 55
3.4.4 Cooling System for pTC . . . 57

Chapter 4 Commissioning Runs from 2017 to 2019 63
4.1 Commissioning Overview . . . 63
4.2 Status of Detectors . . . 63
4.3 DAQ for Positron Spectrometer . . . 63
4.3.1 Readout Channels . . . 63
4.3.2 Triggers for Positron Spectrometer . . . 66
4.3.3 Muon Beam Rate . . . 66
4.3.4 Data Size . . . 67

Chapter 5 Overview of Positron Analysis Flow 69
5.1 Data Flow . . . 69
5.2 Event Generation . . . 70
5.2.1 Simulation of Interactions . . . 70
5.2.2 Simulation of Detector Response . . . 70
5.3 Positron Reconstruction Chain . . . 70
5.4 Updates from MEG II Official Previous Studies . . . 71

Chapter 6 Performance of the pTC 73
6.1 Goal of This Chapter . . . 73
6.2 Overview of Timing Reconstruction Algorithm . . . 73
6.3 Algorithms for pTC Analysis . . . 73
6.3.1 Waveform Analysis . . . 73
6.3.2 Hit Reconstruction . . . 74
6.3.3 Clustering . . . 77
6.3.4 Standalone pTC Track Fitting . . . 78
6.3.5 Timing Calibration . . . 80

6.3.6 Refinement of the Timing Reconstruction . . . 84
6.4 Performance of pTC . . . 86
6.4.1 Even-Odd Analysis . . . 86
6.4.2 Overall Timing Resolution . . . 87
6.5 Performance Studies Using MC Simulations . . . 88
6.5.1 Tuning of S/N . . . 89
6.5.2 Hit Rate . . . 89
6.5.3 Tracking Quality . . . 90
6.5.4 Position Dependence of Tracks . . . 91
6.5.5 Evaluation with MC Truth . . . 91
6.5.6 Implementation of Systematics by Hit Position . . . 91
6.6 Performance of pTC . . . 92

Chapter 7 CDCH Analysis 97
7.1 Waveform Analysis of CDCH . . . 97
7.1.1 Signal Search . . . 97
7.1.2 Cross-Fitting . . . 97
7.2 Analysis of Low Rate Data . . . 98
7.2.1 Noise Reduction . . . 98
7.2.2 Observed S/N . . . 100
7.3 Reproduction of Commissioning Data by MC Simulations . . . 101
7.3.1 Update of Simulation . . . 101
7.3.2 Space-Charge Effect for High Rate Environment . . . 102
7.4 Comparison between MC and Commissioning Data at MEG II Beam Rate . . . 102
7.5 CDCH Tracking Algorithms . . . 104
7.5.1 Hit Reconstruction . . . 104
7.5.2 Track Finding . . . 105
7.5.3 CDCH Track Fitting . . . 107

Chapter 8 Performance of Positron Spectrometer 109
8.1 CDCH-pTC Combined Analysis for Global Tracking . . . 109
8.1.1 CDCH-pTC Matching . . . 109
8.1.2 pTC-CDCH Global Track Refinment . . . 111
8.2 Positron Spectrometer Performance . . . 112
8.2.1 Definition of Reconstruction Efficiency . . . 112
8.2.2 Global Track Selection . . . 112
8.2.3 Truth Check . . . 115
8.2.4 Tail Cut . . . 115
8.2.5 Angle Correlation Correction . . . 116
8.2.6 Resolution and Efficiency . . . 116
8.2.7 Breakdown of Inefficiency . . . 117
8.2.8 Rate Dependence of pTC and CDCH Efficiencies . . . 118

Chapter 9 Projected Sensitivity of MEG II 123
9.1 Maximum Likelihood Fit . . . 123
9.1.1 Maximum Likelihood Function . . . 123
9.1.2 Probability Density Function . . . 123
9.1.3 Discriminant Variables . . . 124
9.1.4 Expected Number of Muon Decays . . . 125
9.1.5 Systematic Uncertainty . . . 125
9.1.6 Confidence Interval and Sensitivity . . . 125
9.2 Comparison with MEG Experiment . . . 126
9.2.1 Extension of MEG Experiment . . . 127
9.2.2 Several Upgrade Cases from MEG Experiment . . . 127
9.3 Comparison with MEG II Design Values . . . 127
9.3.1 Sensitivity with Design Values . . . 127
9.3.2 Impact of Update . . . 128
9.4 Comparison with Previous Works . . . 128
9.5 Possible Other Scenarios . . . 129
9.5.1 Gain Improvement and Software Optimization . . . 129
9.5.2 Additive Gas Impact . . . 130
9.5.3 New Detector Installation: CDCH II/US-RDC . . . 130
9.5.4 Reduced Muon Stopping Rate . . . 130

Chapter 10 Conclusions 133

A Laser components 135

B Radiation damage with differently damaged SiPMs 137
B.1 SiPMs Irradiation . . . 137
B.2 Patterns for SiPMs Connection . . . 137
B.3 IV Curves for Each Pattern . . . 138
B.4 New SiPM test . . . 138

C Online Synchronization in 2018 - 2019 143
C.1 Analysis of Online Synchronization . . . 143
C.1.1 Clock Analysis . . . 143
C.1.2 12.5 ns Jump . . . 143
C.1.3 Out-of-synchronization . . . 144

D Kalman Filter Algorithm 145
D.1 Kalman Filter Formalism . . . 145
D.2 Deterministic Annealing Filter (DAF) . . . 147

E Track Extrapolation from pTC to CDCH 149
E.1 Extrapolation . . . 149

F Noise Spectrum from Commissioning 2020 151
F.1 Noise Spectrum and Noise Level 151
F.2 Expected Performances 152

G Performance Evaluated with Reconstructed Kinematics 153
G.1 Performance Evaluated with Reconstructed Kinematics 153
G.1.1 CDCH Tracking Resolution 153

Reference 159

Introduction

The MEG II experiment is designed to search for $\mu^+ \to e^+\gamma$ which is known as one of the charged lepton flavor violation (cLFV) phenomena. The cLFV phenomena are prohibited in the standard model of particle physics, or even if the tiny neutrino mass is included, the expected rate is too low to be detected in an experiment. However, in new theories called "beyond the standard models (BSM)" the cLFV phenomena are predicted to occur within the experimental reach - this means that to find the cLFV phenomena means to find the new physics.

The current most strict upper limit of $\mathrm{BR}(\mu^+ \to e^+\gamma) < 4.2 \times 10^{-13}$ (90% C.L.) was set by the MEG experiment [1]. The region of $\mathrm{Br}(\mu^+ \to e^+\gamma) \sim O(10^{-14})$, where some of the BSM predict, has not been explored yet. MEG II experiment was proposed in 2013 to improve the sensitivity by one order of magnitude. One of the largest upgrades from the MEG to the MEG II experiment is the positron spectrometer which is fully replaced with the new detectors. The sensitivity to 10^{-14} region is reachable by improving the positron reconstruction efficiency and resolution by a factor of two under twice higher muon beam intensity.

Two innovative positron detectors were constructed to achieve the twice better efficiency and resolution of positron reconstruction; one is the pixelated timing counter (pTC), and the other is the cylindrical drift chamber (CDCH). The pTC is composed of 512 small scintillation counters with series-connected Silicon-PhotoMultipliers (SiPMs) readout. The segmented design of the pTC is tolerant to the event pileup under high muon beam intensity and improves the timing resolution by a factor of two by using the multiple-hit information. As for the CDCH, the high-granularity readout and ultra-low material improve the precision of the positron tracking. Also, the large tracking volume with the cylindrical shape greatly improves the matching efficiency and the path-length estimation between the pTC and CDCH.

Structure of This Thesis

This thesis describes the details of the performance of the positron spectrometer in the MEG II experiment. Chap. 1 summarizes the physics motivation of the cLFV search. The apparatus of the MEG II experiment is described in Chap. 2. In early 2015 commissioning runs, a rapid current increase of the pTC channels by the radiation damage was observed. The author performed the dedicated studies to mitigate the deterioration of the pTC performance and this is described in Chap. 3, and 2017 - 2019 commissioning runs with pTC cooling systems are summarized in Chap. 4. The analysis overview and the simulation framework are introduced in Chap. 5. The performance of the pTC was demonstrated in Chap. 6 with the refined algorithms for the timing reconstruction, which lead twice better resolution than the MEG experiment and 15% improvement from the previous studies, which used the not-optimal timing reconstruction algorithms without any tracking information. The CDCH analysis from commissioning runs in 2017 – 2019 is described in Chap. 7. The realistic simulations, which take into account detector response obtained from analysis, were developed. The signal-noise ratio of the simulated waveforms was tuned to reproduce the observed waveforms. The performance of the positron spectrometer was demonstrated with the simulation in Chap. 8. The global tracking algorithms which utilizes both the pTC information and the CDCH information were developed. Finally, a realistic estimation of the MEG II sensitivity is reported in Chap. 9. Then this thesis is concluded in Chap. 10.

Author’s Contribution

The author played a central role for the construction and the operation of the pTC with the collaboration of the MEG II pTC group; construction of the pTC counters, development of the calibration systems and algorithms, dedicated studies for the radiation damage effect on the timing resolution, preparation of temperature and cooling systems, data taking in the commissioning at site in 2017 – 2019. The author had the large contribution on the development of the reconstruction algorithms and the analysis of the commissioning data taken in 2017 – 2019 with the collaboration of the MEG II positron analysis group; establishment and refinement of the positron reconstruction algorithms, performance evaluation of the pTC, raw data analysis of the positron spectrometer, check of the consistency between the simulation and the commissioning data. The author performed an up-to-date calculation of the achievable sensitivity with the collaboration of the MEG II positron analysis group, the LXe group, and the RDC group.

List of Tables

1.1 Basic parameters of muon from the experiment summarized by the Particle Data Group (PDG)[2] 16
1.2 Decay modes of muons in standard model [2]. 17

2.1 The detector performance of MEG and expected performance of MEG II [3]. 28
2.2 The list of the systematic uncertainties considered in the physics analysis in the MEG experiment [4]. The fractions of “All the other” are also shown in parentheses. 30
2.3 The materials for a pTC counter 43
2.4 The basic properties of BC-422 from the datasheet [5]. 43
2.5 The datasheet values (provided by AdvanSiD [6]) of SiPMs used for the pTC ounter. 44
2.6 The CDCH wires. 48

3.1 Summary of the damage level of the SiPMs. 54

4.1 The number of the maximum readout channels for pTC and CDCH each year. 64

5.1 Data mainly used in the following chapters. 72

6.1 Parameters extracted from the position calibration. 76
6.2 The summary of the uncertainties for the laser-based calibration. 81
6.3 Comparison between two time calibration methods. 83
6.4 The pTC performance evaluation with the commissioning data: comparison of the updated studies and previous studies. 88
6.5 The pTC performance evaluation with the commissioning data and MC. 91
6.6 The pTC performance. 92

7.1 The major updates of the CDCH waveform analysis after 2018 [7]. 101

8.1 The timing resolution (calculated from the pTC performance in Table 6.6 and the path length estimation of the CDCH in Fig. 7.15) at the vertex. 112
8.2 The criteria for the 5σ efficiency cut. 116
8.3 The performance of the positron reconstruction under the several beam rates. The “optimistic” case uses the 3.7 times better S/N condition. 117
8.4 The breakdown of the inefficiency of the positron measurement with pileups of $7{\times}10^7$ Michel positrons. . 118
8.5 The efficiency of CDCH tracking, CDCH-pTC matching, and pTC timing reconstruction under the beam of the MEG II intensity. 119
8.6 The rate dependence of CDCH tracking, CDCH-pTC matching, and pTC timing reconstruction efficiency. 119

9.1 Default values for the sensitivity calculation of MEG II experiment. 125
9.2 The number of background events obtained in the MEG experiment, and that expected in the MEG II experiment. 126
9.3 The input parameters of the positron spectrometer for the likelihood analysis with several possible scenarios. 127
9.4 Summary of the contribution for the results in this thesis. 129

A.1 Optical components used in the laser calibration system [8] 136

B.1 V_{br} values of Pattern A and Pattern D. 140

F.1 The positron reconstruction resolution under the several beam rates. 152

G.1 The extracted and estimated resolutions for the detector. 153
G.2 Comparison of the results from Michel-Fit with MEG II expected and MEG 2013 data. 154

List of Figures

1.1 The particles to describe the fundamental interactions and matters. 13
1.2 The coupling constants of three gauge groups calculated in the standard model framework and in the minimal supersymmetric standard model (MSSM) framework [2]. 15
1.3 The positron energy spectrum from the polarized Michel decay. (a), (b), (c) shows the case of $\cos\theta_{\rm e} = 0$, $\cos\theta_{\rm e} = +1$ and $\cos\theta_{\rm e} = -1$ respectively [9]. 17
1.4 The energy spectrum of RMD gamma ray [9]. 18
1.5 The diagram of $\mu \rightarrow {\rm e}\gamma$ in the standard model with the neutrino oscillation [10]. 19
1.6 An example of the diagram of $\mu \rightarrow {\rm e}\gamma$ with the TeV scale SUSY particles [10]. 19
1.7 The expected branching ratios of $\mu \rightarrow {\rm e}\gamma$ and $\tau \rightarrow \mu\gamma$ in the CMSSM with seesaw mechanism [11]. 19
1.8 Br($\mu \rightarrow {\rm e}\gamma$) as functions of the universal scaler mass m_0 and tanβ for $M_N = 3 \times 10^{15}$ GeV, $M_{1/2} = m_0$, $a_0 = 0$, and sign(μ) > 0 in the mSUGRA. Numbers of the figures correspond to the values of Br($\mu \rightarrow {\rm e}\gamma$). Dark green, light green, and dashed green region for m_h [GeV] correspond to the region of $125 < m_h < 127$, $124 < m_h < 128$, and $120 < m_h < 130$, respectively [12]. 20
1.9 Br($\mu \rightarrow {\rm e}\gamma$) as functions of the universal scaler mass m_0 and tanβ for $M_N = 3 \times 10^{13}$ GeV, $M_{1/2} = m_0$, $a_0 = 0$, and sign(μ) > 0 in the mSUGRA. $r = 2.2$ is one of the CI parameters. With the increase of r value, the Yukawa coupling can become larger. The detail of the other CI parameters can be found in [13]. The black lines are for Higgs mass of 125 GeV, and the dashed/dot lines are ± 1 GeV/2 GeV from the Higgs mass. The current upper limit of electron EDM $d_e < 1.1 \times 10^{-29} e$ cm [14] is shown with the green dashed line, which is almost equivalent to the current upper limit of Br($\mu \rightarrow {\rm e}\gamma$) by the MEG experiment (shown with the brawn dashed line) in this parameter space. 21
1.10 The history of the upper limits of three cLFV phenomena [3]. 22

2.1 The schematics of a signal event and background events (accidental and RMD). 23
2.2 Effective branching ratio of the RMD background as a function of the positron energy (δx) and gamma-ray energy (δy) [9]. 25
2.3 Effective branching ratios of the accidental and RMD background into the kinematic window of MEG experiment defined by $E_{{\rm e}^+,{\rm min}} < E_{{\rm e}^+} < 53.5$ MeV, $E_{\gamma,{\rm min}} < E_\gamma < 53.5$ MeV, $|t_{{\rm e}^+\gamma}| < 0.24$ ns and $\cos\Theta_{{\rm e}^+\gamma} < -0.9996$. (a) Accidental background from the side-band data. (b) RMD background calculated with the theoretical formula folded with the MEG detector response [1]. 25
2.4 The overview of the apparatus used in MEG experiment. The picture of DRS chip and board from [15]. The picture of the LXe from [3]. The other pictures and sketch from [1]. 27
2.5 Event distributions for the 2009 – 2013 full dataset on the ($E_{{\rm e}^+}, E_\gamma$)-plane with the selections of $\cos\Theta_{{\rm e}^+\gamma} < -0.99963$ and $|t_{{\rm e}^+\gamma}| < 0.24$ ns (left), and ($\cos\Theta_{{\rm e}^+\gamma}, t_{{\rm e}^+\gamma}$)-plane (right) with $51.0 < E_\gamma < 55.5$ MeV and $52.4 < E_{{\rm e}^+} < 55.0$ MeV. The contours of the averaged signal PDFs (1σ, 1.64σ and 2σ) are superimposed [1]. 28
2.6 The branching ratio sensitivity as a function of the DAQ days in the MEG experiment [4]. 29

2.7 The overview of the MEG II experiment [3]. 30
2.8 The global coordinate system of MEG II positron spectrometer. 31
2.9 The local coordinate on a CDCH wire. 31
2.10 The local coordinate of a pTC counter. 31
2.11 The dedicated coordinate of the LXe detector (u, v, w) [16]. 31
2.12 The coordinate of the target ellipse. 31
2.13 The Cockcroft-Walton pre-accelerator [17]. 32
2.14 The large proton ring accelerator [17]. 32
2.15 The πE5 beam line [18]. 33
2.16 The MEG II scintillator target [3]. 33
2.17 The distribution of positron reconstructed position at the target with 2011 MEG data [3]. 34
2.18 The perspective corrected and 2D gaussian fitted beam image viewed originally under 15° to the target plane and taken in 2016 commissioning [3]. 34
2.19 The picture of the LXe photon detector [3]. 34
2.20 The sketch of a large area VUV sensitive MPPC used in MEG II LXe photon detector [19]. 35
2.21 A large area MPPC used in MEG II LXe photon detector [19]. 35
2.22 Example of scintillation light distribution detected by PMTs (left) and MPPCs (right) for a same simulated event [3]. 35
2.23 The schematic view of the RDC. The horizontal long plates in front are the plastic scintillator bars and the cubes behind are the LYSO crystals [3]. 36
2.24 The expected (MC) distribution of the timing difference between the RDC and LXe. Red line shows the accidental background events and blue line shows the signal events [3]. 37
2.25 The expected (MC) energy distribution at the RDC for RMD events with E_γ >48 MeV (red) and for Michel events (blue) [3]. 37
2.26 The sketch of the single WaveDAQ crate [20]. The green boards are WDB, magenta DCB and blue TCB. CMB is drawn on the right side. Arrows show connections in the backplane: red arrows for data transmission to backend machines, blue for trigger serial links, orange to distribute back the trigger signal and green for hardware compensated clock distribution, and brown shows low level access for slow control and configuration. 37
2.27 The schematics of the WDB [3]. 38
2.28 The mechanism of the Domino Ring Sampler chip (DRS chip). 38
2.29 The online timing distribution of positrons in MC (black) fitted with multiple gaussian function (red) [7]. . . 39
2.30 The comparison of the online $t_{e^+\gamma}$ trigger selection efficiency of the MEG II expected (blue) timing window and the MEG (red) timing window. The width (FWHM) is reduced from 20 ns (MEG) to 14 ns (MEG II) [3]. 39
2.31 The overview of the MEG (up) and MEG II (down) experiment [21]. The blue line shows the gamma ray and the red positron. The positron tracker volume (green region) was extended to the pTC interface, which increased the number of CDCH hits for one track and improved the trajectory and timing integration (matching efficiency). The timing counter (light blue region) was segmentalized into small pixels. 40
2.32 The design of pTC detector [3]. 41
2.33 The picture of pTC detector. 41
2.34 The backplanes on the pTC support structure [7]. 41

2.35 The signal lines of the backplane [7]. 41

2.36 A simulated signal positron trajectory (blue line) and the pTC counters (yellow). The positron crossed the red counters [3]. 42

2.37 (Left) The picture of single pTC counter. The picture of the two types of PCBs are also shown in right sketch [3]. (Right) The sketch of the counter design pattern. L-shape and mix-shape counters were designed to put counters on inner step of the support structure. 42

2.38 (Left) A mounted flat-type counter on the backplane. (Right) Mounted L-shape counters on the inner step of the support structure [7]. 43

2.39 The pTC counter map [22]. Counter region is ~20 –110 along the beam axis (z-axis) for both downstream and upstream. 44

2.40 The difference of the pulse shape with different connections of 3 SiPMs (3-SiPM parallel, single, and 3-SiPM series) with BC422 with HPK SiPM (S10362-33-050C) [23]. 45

2.41 The counter resolution measured in the lab-test with 4 cm counters (pink-line) and 5 cm counters (blue-line), which include type-I and type-II SiPMs [24]. The histograms filled with pink and blue show the resolution with type-III SiPMs for 4 cm and 5 cm counters, respectively. 45

2.42 The support structure viewed from the bottom side [7]. Cooling pipes and laser optical fibers can be seen. 46

2.43 The schematics of humidity and temperature sensor positions. 46

2.44 (a) Schematic and (b) picture of the laser-based calibration system for the MEG II pTC (from [25]). The individual components are described in the Table A.1. 47

2.45 The mechanical sketch of cylindrical drift chamber [3]. 47

2.46 The picture of CDCH mounted all wires [3]. 48

2.47 The layer structure in the CDCH [26]. 49

2.48 Drift cell configuration of MEG II CDCH. Top: Simplified sketch of a single drift cell (an anode circle and cathode circles are depicted). Bottom: schematic view of the wires in the CDCH [26]. 49

2.49 Isochrones for a single 6×6 mm^2 drift cell [26]. The vertical color is ns. The drift lines are curved and the isochrone map is distorted by the magnetic field. 49

2.50 Front-end electronics for CDCH [3]. 50

2.51 COBRA magnet [27]. 51

2.52 The concept of the COBRA gradient magnetic field [1]. (a) Positrons with the same momentum have the almost same bending radius, even with the different emission angles. (b) Positrons with low longitudinal momentum are quickly swept away. 51

3.1 The pTC current of each channel (16 channels are shown with colored lines) in 2015 commissioning. . . . 53

3.2 The I-V curves of the six electron-irradiated SiPMs. The I-V data of each SiPM were taken at 30°C (a–e), and the breakdown voltages are plotted in (f). The I-V data of six series-connected SiPMs were taken at 30°C (g) and 10°C (h). 56

3.3 The timing resolution measurement setup for the radiation tolerance test. 57

3.4 The schematics of the amplifier [23]. The pole-zero cancellation filter can be applied by tuning the adjustable resistor in the circuit. 57

3.5 The example of the waveform at each damage level. 58

3.6 Timing resolution versus over-voltage at 30°C (left) and 10°C (right). The CFD fraction is 20%. 59

3.7 The timing resolution with the different damage level at the fixed 3 applied voltage (157.5, 160 and 162.5 V). The dashed curves $\sigma_t = \sqrt{\beta I_{\mathrm{dark}} + \sigma_0^2}$ are fitted to the data. 59
3.8 Relation between the dark current and the RMS noise at 30°C for three applied voltages. The dashed curves $N_{\mathrm{RMS}} = \sqrt{\alpha I_{\mathrm{dark}} + N_0^2}$ are fitted to the data. 59
3.9 Relation between the RMS noise and the timing resolution at 30°C for three applied voltages. The dashed curves are $\sigma_t = \sqrt{\gamma N_{\mathrm{RMS}}^2 + \sigma_0^2}$ fitted to the data. 60
3.10 The system for pTC cooling. The pictures for a chiller, water pipes, a heat exchanger, air lines are also shown. 60
3.11 The picture of pTC for the low temperature operation. 61
3.12 The temperature and humidity measured on the pTC sensors. 61

4.1 The pTC counter map with identification number (0-511). In 2017, all of the counters (512) were tested, in 2018 and 2019 128 counters were tested (# 128 - 255 in 2018 and # 304 - 431 in 2019). The colors of the counters show the counter types (inner magenta: 4cm-L, yellow: 4cm-Mix, light blue: 5 cm-Flat, outer magenta: 4cm-Flat). 64
4.2 The CDCH readout in 2018 commissioning [26]. Data acquisition was conducted with the readout in S3 (L1-3) and S4 (L1-3). 65
4.3 The CDCH readout in 2019 commissioning [26]. Data acquisition was conducted mainly with the readout in S4 (L1 - 6). 65

5.1 The overview of the MEG II analysis framework. 69
5.2 The overview of the MEG II positron reconstruction algorithms. 71
5.3 The fixed combinations of counters used in [7] for the evaluation of the pTC resolution. 71

6.1 The sine waveform in the clock channel for the pTC WDB synchronization. 74
6.2 The template noise extracted from the pedestal data taken in 2017 in the experimental area [28]. 74
6.3 The pedestal waveforms of the pTC (left black) and their amplitude of the power spectrum (right red) before / after the noise reduction (up / down) [28]. 75
6.4 The RMS-noise of each pTC channel with pedestal data before / after the noise reduction [28]. 75
6.5 The extracted waveform from a pTC counter [29]. 75
6.6 An example of the x-position histogram of a counter. The green line is the original histogram, black after the moving average, blue-dashed the trapezoid function. The fitting result is shown with red line. The center of the fit result corresponds to the relative offset between the two channels [30]. 76
6.7 The position distributions of counters before/after the calibration [30]. 76
6.8 The position calibration difference in 2017 and 2018, and the outlier examples. 77
6.9 The definition of the geometrical order in pTC (left) and the distribution of the geometrical order from the first hit and timing from the first hit [7]. 77
6.10 A typical tail event of pTC cluster. After crossing a first cluster (orange), that positron loses the momentum by material effects and its turn radius becomes small, and it soon comes back to the pTC region (green). . 78
6.11 The hit addition to the cluster by using the projected hit position. The green counter in the left plot cannot be assigned to the purple cluster only with the timing information, but it can be assigned to the purple cluster with the cross-check of the timing information and the position information. The positron passed through under the counters in the middle of the cluster. 78

6.12 The schematics of the y_{local} estimation algorithm (left) and its result (right). 79

6.13 The sketch of KF algorithm. 80

6.14 The reconstructed positron track by GENFIT. 80

6.15 The time offset history of a counter in a month [8]. The histogram of the RMS of monitored counters is also shown. 82

6.16 The concept of track-based calibration. 82

6.17 The result of track-based calibration compared with the simulation random offset. The standard deviation is estimated to be ~13 ps. 83

6.18 The consistency between two pTC timing calibration methods with 2017 commissioning data [8]. 84

6.19 The hit position dependence of the channel by channel time offset after the correction of the time offset in x direction for 4 cm counters [24]. The left plot shows channel 1, and right plot shows channel 2. 84

6.20 The hit position dependence of the channel timing resolution (right) for 4 cm counters [24]. The left plot shows channel 1, and right plot shows channel 2. 85

6.21 The relation between the energy deposit and the time offset (left) and the timing resolution (right) [24]. . . 85

6.22 The hit position dependence of the counter timing offset (left) and the timing resolution [24]. 86

6.23 The timing resolution from even-odd analysis with 2017 commissioning data with the latest analysis. . . . 87

6.24 The probability distribution of the number of pTC hits for signal positrons. 88

6.25 2017 pTC amplitude. 89

6.26 2017 pTC RMS-noise 89

6.27 pTC amplitude (MC). 89

6.28 pTC RMS-noise (MC). 89

6.29 The timing distribution of the pTC hits in 2018 data with the muon beam. Triggered events can be seen around 410 ns – 430 ns. For the rate calculation, the flat region (pedestal region) is used with the assumption of the Poisson distribution. 90

6.30 Hit rates calculated with 2017 data (magenta) and MC (black) with MEG II nominal beam rate settings [7]. Larger discrepancy between the MC and the data was observed in the large |Z| region (position ~200 - 256/~450 - 512). 93

6.31 Hit rates calculated with 2017, 2018, and 2019 data with MEG II nominal beam rate settings each year. . . 94

6.32 The 2D scatter plot of the difference between the estimated position and the MC truth. The magenta line shows the resolution, white square shows the mean of the distribution at each counter. 94

6.33 Timing resolution from even-odd analysis with 2017 commissioning data at several $|z|$ position of tracks. . 95

6.34 Timing resolution from even-odd analysis with MC at several $|z|$ position of tracks. 95

6.35 The y-dependence of the timing center in a counter at the edge ($x_{\text{hit}} > 5$ cm) with 2017 data [24]. 95

6.36 The y-dependence of the timing center in a counter at the edge ($x_{\text{hit}} > 5$ cm) with MC to reproduce the 2017 data [24]. 95

6.37 Position dependence of the time center in a counter at $x = -4.25$ cm. The applied voltage was fixed to 162.5 V at 30°C [31]. 96

6.38 The y-dependence of the timing center in a counter at $x = -4.25$ cm [24]. 96

6.39 The y-dependence of the timing center in a counter at the edge ($x_{\text{hit}} > 5$ cm) with 1.8 times increased dependence, i.e. 108 (4 cm counters)/135 ps (5 cm counters) time offset between adjacent SiPMs [24]. . . 96

7.1 The example of the simulated CDCH waveforms and the cross-fitting algorithm. The sky-blue horizontal line shows the threshold for the signal finding, and the orange, green, magenta, and blue lines on the waveform shows the fitted results, respectively. . . . 98

7.2 The noise spectrum of the CDCH noise in 2018. . . . 98

7.3 The example of the CDCH waveform with the muon beam rate of 1.34×10^7 taken in 2018 commissioning. 99

7.4 (Black) The observed 50 MHz noise in the 2019 commissioning. (Red) The template noise spectrum extracted from the waveform themselves by the sine fitting. . . . 99

7.5 The signal amplitude histograms from the commissioning data taken in 2018 and 2019. . . . 100

7.6 The RMS-noise histograms from the commissioning data taken in 2018 and 2019. The dashed line shows the RMS-noise calculated from the raw waveform and the solid line shows that after the noise subtraction by the moving average filter. . . . 100

7.7 The distributions of simulated RMS-noise (dashed line: before noise subtraction, solid line: after noise subtraction) and signal amplitude. . . . 101

7.8 The scatter plots of the simulated signal amplitude at ch1 (x-axis) and ch2 (y-axis). Left plot is before the update of the gain parameters, center plot is after the update, and right plot is from the commissioning data in 2018 ($1.34{\times}10^7$ rate at 1460V). Note that the scale of the axis is one-order different between left plot and center/right plot. . . . 102

7.9 The signal height and the RMS-noise under the MEG II nominal beam rate. . . . 103

7.10 S/N distributions from the commissioning data and the simulation. S from the commissioning data and N from the simulated mean (0.8 mV) is also shown. . . . 103

7.11 The difference in z between the MC truth and the reconstruction (left: time difference, center: charge division). The right histogram shows the consistency between the two methods under the MEG II expected muon decay rate (7×10^7). . . . 105

7.12 The difference in z between the MC truth and the measurement (left: time difference, center: charge division). The right histogram shows the consistency between the two methods under the single Michel decay. . . . 105

7.13 The illustration of the CDCH seeding procedure. The blue and green circles show the drift circle, and the dashed lines are the candidate of the track (left-right for each circle). The yellow line shows the constructed track seed. . . . 106

7.14 Event monitor with a simulated signal positron from the x-y projected view (left) and the 3-D monitor from the top view (right). . . . 107

7.15 The estimated flight time precision ($\sigma_{\mathrm{TOF}} \approx 6.9$ ps) in the CDCH region with the simulation. . . . 108

8.1 The difference between the pTC hit position and the CDCH extrapolated position. . . . 109

8.2 The timing difference between the pTC clusters and the CDCH tracks. ±15 ns timing window for the matching is applied. . . . 109

8.3 The number of matched cluters for one CDCH track. . . . 110

8.4 The propagation length from the CDCH region to the pTC counter which is illustrated in the histogram: the length of the pink line is the propagation length, the black circle is the CDCH outer foil, and yellow boxes are pTC counters. The red histogram shows the after 5σ resolution cut. . . . 110

8.5 The distribution of (x, y) matched positions in the counter local coordinate. Up: 4cm counters (the counter region is ±6 cm for x and ±2 cm for y), down: 5 cm counters (±6 cm for x and ±2.5 cm for y). . . . 110

8.6 The matched $|z|$-position. 110

8.7 The impact parameter resolutions with a simulated signal positron. The blue histogram was updated to the red histogram by the pTC-CDCH track re-fitting. The resolution changed from 106 μm to 85 μm (the standard deviation from 123 μm to 112 μm). 111

8.8 The impact parameter resolutions with a simulated signal positron and 7×10^7 Michel positrons. The blue histogram was updated to the red histogram by the pTC-CDCH track re-fitting. The resolution changed from 111 μm to 84 μm (the standard deviation from 130 μm to 114 μm). 111

8.9 The number of positron tracks in each event with no selections (black), those with the track pre-selection (purple), and those with the track quality selection (red). 114

8.10 The distribution of the per-errors of MEG II kinematic parameters. 115

8.11 The distribution of the χ^2 of tracks (black) and selected tracks with good quality (red, within 5σ tail cut). . 116

8.12 The relation between the θ and ϕ. 117

8.13 The difference between the MC truth and the reconstructed kinematics with the pileup of $7 \times 10^7 \mathrm{e}^+$/s. The red region contains the effective events after the tail cut. The tail cut will reduce the efficiency 10% (75.5% → 65.2%) at this rate. The blue line shows the double-gaussian fitting without tail cut, and the light blue shows the single gaussian fitting after the tail cut. The resolution is extracted from the σ of the latter fitting. 118

8.14 The relation between the efficiency of the hit reconstruction by signal positrons and the beam rate. 120

8.15 An example of an inefficiency event by turn merge failure from ± stereo view. The green-dot segment and the blue-dot segment were not merged. 120

8.16 Distribution of the number of hits in one signal track under the MEG II beam intensity before (black) and after (red) the tail cut. One track segment has ~20 hits (first peak), and these segments are merged to improve the quality of the tracks. 121

9.1 The distribution of the upper limits of $N_{\mathrm{sig}}/N_{\mathrm{obs}}$ at 90% C.L. for 3000 pseudo-experiments with null-signal hypothesis. The obtained median is $N_{\mathrm{sig}}^{\mathrm{median}} = 5.6$, and the sensitivity is 6.0×10^{-14}. 126

9.2 The distribution of the upper limits of seudo-experiments in the MEG experiment [4]. Vertical dashed line shows the search sensitivity from the median calculation (5.3×10^{-13}), and two arrows show the upper limits obtained from the timing sidebands. 126

9.3 The generated signal event in the pseudo-experiments. Red histogram is made with the assumption of σ_p = 93 keV and blue histogram σ_p = 130 keV. 128

9.4 The generated background event in the pseudo-experiments. Red histogram is made with the assumption of σ_p = 93 keV and blue histogram σ_p = 130 keV. 128

9.5 The distribution of the upper limits of N_{sig} at 90% C.L. for 3000 pseudo-experiments with null-signal hypothesis at a half rate beam. The obtained median is $N_{\mathrm{sig}}^{\mathrm{median}} = 3.2$. 130

9.6 The example event distribution within 1.64σ angles, positions, and timing resolution at half rate beam. $N_{\mathrm{sig}} = 2.2$ was obtained in this pseudo-experiment. 131

9.7 The example of event distribution within 1.64σ angles, positions, and timing resolution at MEG II nominal beam. $N_{\mathrm{sig}} = 7.4$ was obtained in this pseudo-experiment. 131

9.8 The branching ratio sensitivity as a function of the DAQ years. (Black) With the updated resolutions under $7 \times 10^7 \mu$/s. (Red) With the updated resolutions under $3.5 \times 10^7 \mu$/s. 132

B.1 Schematic of SiPMs' pattern A, pattern B, pattern C in normal order and pattern A in reverse order. The SiPMs with highest dark currents are in black, those with lowest in white. 138

B.2 I-V curves of each SiPM used for pattern A. . . . 139
B.3 I-V curves of each SiPM used for pattern B 139
B.4 I-V curves of each SiPM used for pattern C. . . . 139
B.5 I-V curves of several patterns of series-connected SiPMs measured at 30°C. . . . 139
B.6 I-V curves of several patterns of series-connected SiPMs measured at 10°C. . . . 139
B.7 The explanation of breakdown voltage shift arising from the difference in dark currents. If n SiPMs have the same dark current I at the breakdown voltage V_{br}, the breakdown voltage of the series-connected SiPMs is expected to be $n \times V_{\mathrm{br}}$. In pattern A, the breakdown voltage becomes $6 \times V_{\mathrm{br}} + 4 \times \delta V_{\mathrm{br}}$, and in pattern B, $6 \times V_{\mathrm{br}} + 2 \times \delta V_{\mathrm{br}}$ to accommodate the same current $I + \delta I$ at the breakdown voltage. . . . 139
B.8 The irradiation test setup at BTF. . . . 140
B.9 The IV curves of the SiPMs after irradiation at 10°C and 30°C. The type-II SiPMs shown in ”New”. . . . 141
B.10 The bias scan of the timing resolution of type-II SiPMs (shown as “New”) after irradiation at 10°C and 30°C. . . . 141

C.1 The relation among the clock, PLL and DRS cycle. . . . 143
C.2 The reconstructed hit positions on CDCH wires (left) and the timing difference between both ends (right). Clearly unphysical jump can be seen. . . . 144
C.3 The cell-zero chip-id difference from the reference chip. If the synchronization completely works and no trigger jitter, the difference should be zero. . . . 144
C.4 Drift of the difference of the cell-zero from the reference chip during a run which caused the out-of-synchronization problem. The cell-zero id of the chip drifted to the one direction. . . . 144

D.1 The coordinate system of the wire measurement in GENFIT [32]. . . . 145
D.2 Illustration of the probability assignment with deterministic annealing filter [33]. (a) The algorithm starts with high temperature and all measurements (green circles) in the same layer have the similar weight. (b) At the lower temperature, the measurements far from the estimate obtain the lower assignment probabilities. (c) Finally, the assignments are frozen out. . . . 148

E.1 A positron partial track reconstructed with pTC hits and CDCH hits (MC). Blue rectangular planes show pTC hits, blue cylinders show drift circles of CDCH hits, and gray planes show CDCH hits. . . . 149

F.1 The noise spectrum observed in 2020 with the standard FE card. . . . 151
F.2 The RMS-noise sin 2020 with the standard FE card. The muon rate is MEG II nominal (7×10^7/s) 151
F.3 The waveforms in the 2020 commissioning under the muon beam. (Left) before the noise subtraction, (right) after the noise subtraction. . . . 152

G.1 The distributions of CDCH tracks between the first turn and the second turn. . . . 154
G.2 Michel-Fit with the reconstructed energy spectrum (MC). The grey line shows the theoretical Michel spectrum, the blue dashed line response function, and the red line is the fitting result. . . . 155
G.3 The acceptance function of MEG II (MC, blue) and MEG 2013 data (red) normalized at 52.8 MeV. The relative efficiency (normalized at 52.8 MeV) from the reconstructed tracks in the range of 43 – 53 MeV/2 MeV is also shown with cross marks. . . . 155
G.4 The momentum dependence of the momentum resolution with Michel positrons. . . . 155

Chapter 1

Physics Motivation

In this chapter, the physics motivation for the $\mu^+ \to e^+\gamma$ search is discussed.

1.1 Standard Model

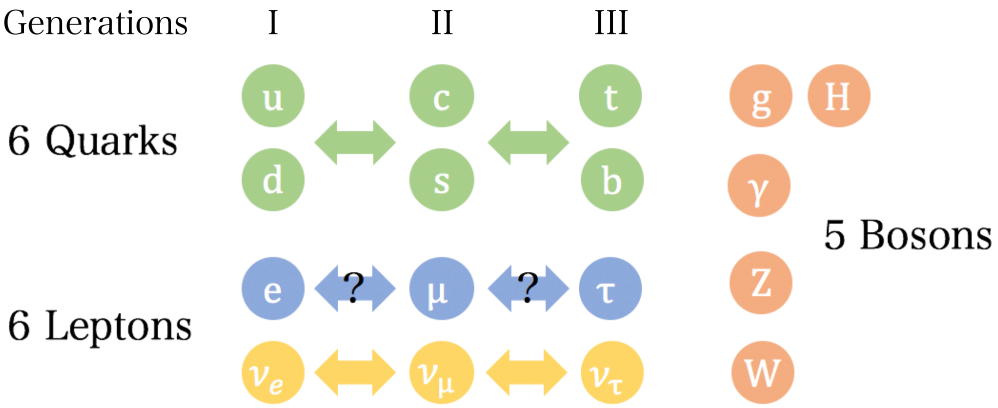

Fig. 1.1: The particles to describe the fundamental interactions and matters.

The standard model in particle physics is one of the most fundamental theories of physics, which well explains the interactions with 17 elementary particles (12 fermions for matters and 5 bosons for interactions). Fig. 1.1 shows the elementary particles in the Standard Model.

Theoretically, the Standard Model Lagrangian has the gauge symmetry of $\mathrm{SU(3)_C} \times \mathrm{SU(2)_L} \times \mathrm{U(1)_Y}$, and this symmetry describes the three fundamental interactions: strong interaction, weak interaction, and electromagnetic interaction. The gauge bosons are derived from the gauge fields, and the Higgs boson is derived from the Higgs mechanism and provides the mass term for gauge bosons (W / Z).

In 2012, the Higgs boson was discovered in ATLAS and CMS experiments [34, 35], and all of the elementary particles predicted in the Standard Model were experimentally observed.

1.2 Beyond the Standard Model

Though the Standard Model explains the fundamental interactions and reproduces most of the experimental observations up to the electroweak energy scale (O(100) GeV), it is not a perfect theory to explain all of the interactions and particles in the Universe.

The major mysteries that the Standard Model does not explain are summarized as follows:

- The Standard Model does not explain the dark matter and the dark energy in the Universe. It does not explain the gravitational force which is also considered as the fundamental interaction in nature.
- The mass of the Higgs particle (125 GeV) suggests the difficulties for the extension of the Standard Model to the GUT scale (Grand-Unified-Theory energy scale where the electromagnetic-weak interaction and the strong interaction are considered to be unified in O(10^{16}) GeV) or Planck scale (gravitational interaction is considered to be unified in O(10^{19}) GeV), and this is known as the hierarchy problem. To be consistent with GUT region, the quantum correction term for the Higgs mass must be fine-tuned precisely.
- In the Standard Model, neutrinos are assumed to be massless. However, the neutrino oscillation [36] indicates that the neutrino has a tiny mass. The inconsistency between the experiments and the theories suggests the necessity for the extension of the model.

Currently, the Standard Model is considered as an approximation of a more general and fundamental model in the low energy region, which is called Beyond Standard Model (BSM). Promising BSMs are shortly summarized in the following sections.

1.2.1 SUper-SYmmetric (SUSY) Model

The supersymmetric (SUSY) model can solve the hierarchy problem. In this model, new supersymmetric fermion (boson) partners are introduced for all the standard model boson (fermion) under the symmetry of the fermion and boson transformation:

$$Q|Fermion\rangle = |Boson\rangle, \ \ Q|Boson\rangle = |Fermion\rangle, \tag{1.1}$$

where Q is the operator that generates the SUSY transformation. The SUSY partner's sign of the radiative correction term for Higgs mass is inverse from the original particle, so the correction terms (quadratically divergent terms) are canceled out [37]. In addition, the lightest SUSY particle, which is stable, electrically neutral, and weakly interacts with the ordinary matter, can be an attractive candidate for the dark matter [38, 39]. For these reasons, the SUSY model is considered as one of the promising BSM theories.

The general SUSY models have too many soft SUSY parameters and reasonable constrains for the models are often introduced. One of the typical constraints are called mSUGRA (minimal SUperGRAvity) for the constraint on minimal SUSY models (MSSM) with five parameters, (m_0, a_0, $M_{1/2}$, tanβ, sign(μ)). The soft SUSY breaking parameters satisfy the mSUGRA boundary conditions; the soft scalar mass-squared parameters at the Planck scale are assumed to be universal (m_0^2, universal scaler mass) and the tri-linear scalar couplings (A-terms) are proportional to the corresponding Yukawa couplings with the coefficient of a_0. $M_{1/2}$ is the universal gaugino mass at the Planck scale, and tanβ is the ratio of the vacuum expectation of up-type and down-type of Higgs bosons, and μ is the supersymmetric Higgs mass parameter. With the universal assumption, the source of flavor violation from SUSY particles is absent at the Planck scale, which solves the so-called SUSY flavor problem. Even in such a case, the flavor violation source in the neutrino Yukawa enters into the slepton mass matrix through the renormalization group equation, and an avoidable flavor violation source is introduced at the low energy.

1.2.2 Seesaw Mechanism

The seesaw mechanism can explain the neutrino tiny mass. In this mechanism, the neutrino is assumed to be a Majorana particle and the heavy right-handed neutrino is introduced. The neutrino mass term can be described as follows:

$$(\overline{N_1}\ \overline{N_2})\begin{pmatrix} 0 & m_\mathrm{D} \\ m_\mathrm{D} & m_\mathrm{R} \end{pmatrix}(N_1\ N_2), \tag{1.2}$$

where N_1 and N_2 are the Majorana fields, m_D is the Dirac mass, m_R is the Majorana mass of the right-handed neutrino, respectively. By calculating the eigenvalues of this mass matrix with the assumption of $m_\mathrm{R} \gg m_\mathrm{D}$, we can obtain two neutrino masses of:

$$\frac{m_\mathrm{D}^2}{m_\mathrm{R}}, m_\mathrm{R}. \tag{1.3}$$

These two masses suggest that $\frac{m_\mathrm{D}^2}{m_\mathrm{R}}$ of left-handed neutrino mass, which is observed in the experiments, becomes tiny when m_R of right-handed neutrino mass, which is not yet observed, is huge.

1.2.3 Grand Unified Theory (GUT)

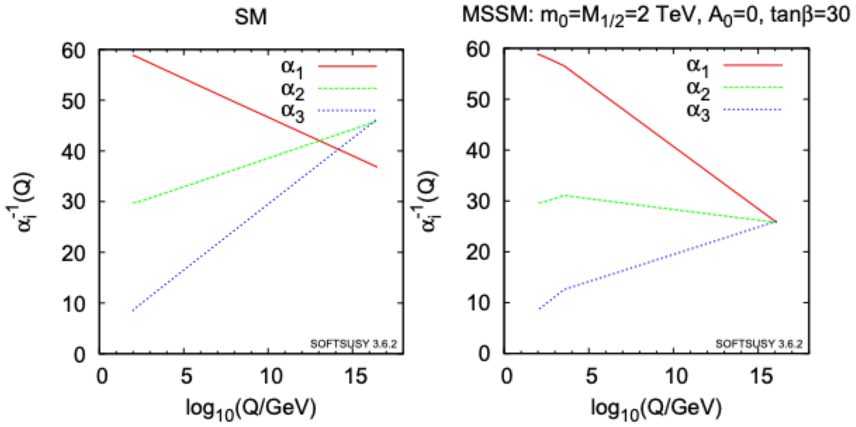

Fig. 1.2: The coupling constants of three gauge groups calculated in the standard model framework and in the minimal supersymmetric standard model (MSSM) framework [2].

In the GUT model, three gauge groups, $\mathrm{SU(3)_C} \times \mathrm{SU(2)_L} \times \mathrm{U(1)_Y}$, are assumed to be unified to a single and larger group at a very high energy scale (GUT scale). Actually, it is known that the running coupling constants of three interactions become close to each other around $\mathrm{O}(10^{16})$ GeV, and if the SUSY particles exist at the TeV scale, they are well unified as shown in Fig. 1.2.

1.3 Overview of Charged Lepton Flavor Violation (cLFV) Search

The Standard Model fermions with the same charge have three generations depending on their masses, which are called flavors. It is already observed that quark and neutrino flavors can mutate to flavors in the different generations (this phenomenon is called flavor mixing), while it is not observed in the charged lepton sector, i.e. among e, μ, and τ.

The flavor mixing in the quark sector is explained in the framework of the Standard Model through the CKM matrix.The observation of the neutrino oscillation, which showed the evidence of the flavor mixing in the neutrino sector, gave a strong impact on the particle physics. Actually, the conservation of the lepton flavor derives from not fundamental symmetries but the assumption of the mass-less neutrino and the non-observation of the flavor mixing in the lepton sector.

Now, the flavor mixing in the charged lepton sector, which is called charged Lepton Flavor Violation (cLFV), is one of probes for the new physics. If the cLFV is observed in an experiment, it is clearly evidence of the new physics beyond the Standard Model. Even if the cLFVs are not observed, the upper limit for the branching ratio gives a strict constraint on the BSM theories.

1.4 Muon Properties

Muon is widely used as a probe of new physics because of its relatively long lifetime and availability of the intense beam as explained in the next chapter. In this section, the important properties of a muon for the search of $\mu \to e\gamma$ are summarized, and the physics motivations of $\mu \to e\gamma$ search are discussed.

1.4.1 Basic Properties of Muon

Table 1.1: Basic parameters of muon from the experiment summarized by the Particle Data Group (PDG)[2]

Parameter	Value
Mean Lifetime	$(2.1969811 \pm 0.0000022) \times 10^{-6}$ s
Mass	$105.6583745 \pm 0.0000024$ MeV
Magnetic Moment Anomaly ($\frac{g_\mu - 2}{2}$)	$(11659208.9 \pm 5.4 \pm 3.3) \times 10^{-10}$
Electric Dipole Moment (EDM)	$(-0.1 \pm 0.9) \times 10^{-19} e$ cm

Table 1.1 summarizes the basic parameters of a muon. The muon mass is ~ 200 times larger than the electron's one. The muon decay is characterized by the weak interaction, and therefore the lifetime of the muon is relatively longer than the particles whose decays are caused by the electromagnetic interaction or the strong interaction. The $g_\mu - 2$ and EDM measurements are also considered as one of the attractive measurements for new physics [40].

1.4.2 Interactions and Decay Modes

In the Standard Model, the muon interaction is given as follows:

$$\begin{aligned} L &= e\bar{\mu}\gamma^\mu \mu A_\mu \\ &- \frac{g}{\sqrt{2}}(\bar{\nu}_{\mu_L}\gamma^\mu \mu_L W_\mu^+ + \bar{\mu}_L \gamma^\mu \nu_{\mu_L} W_\mu^-) \\ &- \sqrt{g^2 + g'^2}(\bar{\mu}_L \gamma^\mu (-\frac{1}{2} + \sin^2\theta_W)\mu_L + \bar{\mu}_R \gamma^\mu \sin^2\theta_W \mu_R) Z_\mu^0 \\ &- \frac{m_\mu}{v}\bar{\mu}\mu H, \end{aligned} \tag{1.4}$$

where g and g' are the coupling constants from SU(2) and U(1) interactions, θ_W is the Weinberg angle ($\sin\theta_W = \frac{g'}{\sqrt{g^2+g'^2}}$), m_μ is the muon mass. Each line corresponds to the interaction with photon (first line), W boson (second line), Z boson (third lines) and Higgs boson (final line).

The decay modes of muon are summarized in Table 1.2. In the MEG II experiment we use a positive muon beam to avoid the formation of the muonic atoms. So in the following sections, we basically discuss not the negative muon decay but the positive muon decay.

Table 1.2: Decay modes of muons in standard model [2].

Mode	Fraction	Note
$\mu^- \to e^-\nu_\mu\overline{\nu_e}$	≈ 1	Michel Decay
$\mu^- \to e^-\nu_\mu\overline{\nu_e}\gamma$	$6.0 \pm 0.5 \times 10^{-8}$	Radiative Muon Decay, E_γ >40 MeV and E_e >45 MeV
$\mu^- \to e^-\nu_\mu\overline{\nu_e}e^+e^-$	$(3.4 \pm 0.4) \times 10^{-5}$	
$\mu \to e\gamma$	$< 4.2 \times 10^{-13}$ (90% C.L.)	[1]

Michel Decay

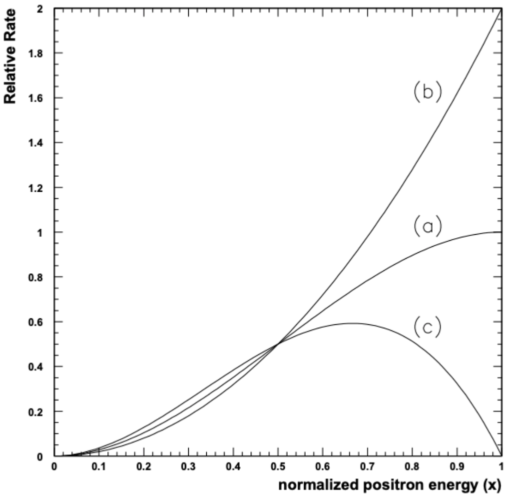

Fig. 1.3: The positron energy spectrum from the polarized Michel decay. (a), (b), (c) shows the case of $\cos\theta_e = 0$, $\cos\theta_e = +1$ and $\cos\theta_e$ = -1 respectively [9].

$\mu^+ \to e^+\nu_e\overline{\nu_\mu}$, called Michel decay, is described by the weak interaction mediated by a W boson. The Michel decay is the dominant source of the background positrons for $\mu^+ \to e^+\gamma$ search. The differential decay rate is described as [9]:

$$\frac{d^2\Gamma(\mu^\pm \to e^\pm\nu\overline{\nu})}{dx\, d\cos\theta_e} = \frac{m_\mu^5 G_F^2}{192\pi^3} x^2[(3-2x) \pm P_\mu \cos\theta_e(2x-1)], \tag{1.5}$$

where G_F is the Fermi constant ($G_F = \frac{g^2}{4\sqrt{2}m_W^2}$), $x = \frac{2m_\mu}{m_\mu^2+m_e^2}E_e$, P_μ is the polarization of μ, θ_e is the angle between the μ polarization and the electron (positron) momentum. Fig. 1.3 shows the energy spectrum of polarized ($P_\mu = 1$) Michel positron[*1]. In the MEG II simulation and analysis software, the radiative correction calculated in Ref.[41] is also used in addition to (1.5).

Radiative Muon Decay (RMD)

Radiative Muon Decay (RMD) can be included as a kind of radiative correction for the Michel decay with the lowest-order. RMD emits a positron and a gamma ray at the same time, and if the neutrinos go out with a tiny momentum, the decay mimics the signal decay $\mu^+ \to e^+\gamma$ and becomes the background event. In addition, when a high energy γ is emitted from a

---

[*1] We count the positron from the all direction in the experiment, so we can effectively assume the distribution of (a), which is equivalent to unpolarized muon case.

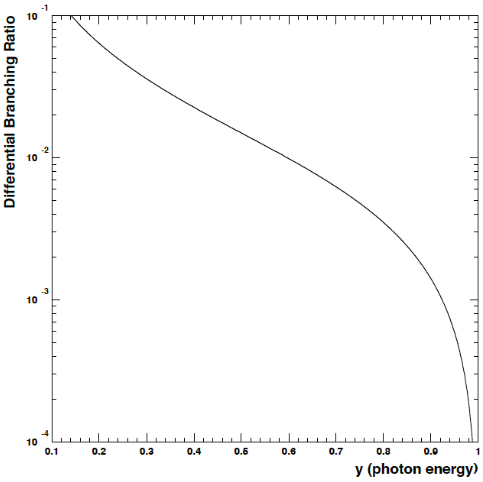

Fig. 1.4: The energy spectrum of RMD gamma ray [9].

RMD and a high energy positron is emitted from a Michel decay at the same timing, they become the accidental background event. The differential branching ratio of the radiative muon decay is expressed by [9]:

$$\frac{\mathrm{d}B(\mu \to e\nu\bar{\nu}\gamma)}{\mathrm{d}y\mathrm{d}\cos\theta_\gamma} = \frac{1}{y}(J_+(y)(1 \pm P_\mu \cos\theta_\gamma) + J_-(y)(1 \mp P_\mu \cos\theta_\gamma)), \tag{1.6}$$

where $y = \frac{2E_\gamma}{m_\mu}$, θ_γ is the angle between muon polarization and γ momentum. $J_+(y)$ and $J_-(y)$ is defined as follows:

$$J_+ = \frac{\alpha}{6\pi}(1-y)\left[\left(3\ln\frac{1-y}{r} - \frac{17}{2}\right) + \left(-3\ln\frac{1-y}{r} + 7\right)(1-y) + \left(2\ln\frac{1-y}{r} + \frac{13}{3}\right)(1-y)^2\right], \tag{1.7}$$

$$J_- = \frac{\alpha}{6\pi}(1-y)^2\left[\left(3\ln\frac{1-y}{r} - \frac{93}{12}\right) + \left(-4\ln\frac{1-y}{r} + \frac{29}{3}\right)(1-y) + \left(2\ln\frac{1-y}{r} - \frac{55}{12}\right)(1-y)^2\right], \tag{1.8}$$

where $r = (\frac{m_e}{m_\mu})^2$. Fig. 1.4 shows the energy spectrum of the RMD gamma ray from unpolarized muons.

1.5 Motivation of cLFV Search Experiment

1.5.1 Energy Frontier and Intensity Frontier

In the search of the BSM candidates, "energy frontier" experiments like ATLAS and CMS at the LHC and "intensity frontier" experiments like the MEG are both important. The LHC experiment directly searches the new particles in BSM through the strong interaction. Its discovery reach is limited by the beam energy and luminosity. On the other hand, the MEG II experiment can indirectly reach for the BSM whose energy scale is much higher than the energy scale of the LHC and it is sensitive to new particles interacting through the weak interaction. Therefore, the two approaches are complementary.

The search for the TeV-scale SUSY particles has been one of the motivations of the LHC experiments. However, the results so far have been negative for masses up to 1 - 2 TeV [42, 43]. Considering that the LHC has not yet observed significant signs of new physics, it is effective to take a different strategy from the energy frontier: indirect search of the new particles in the intensity frontier.

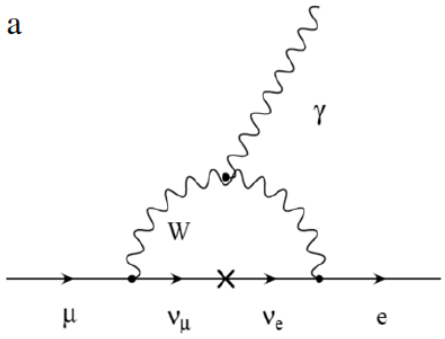

Fig. 1.5: The diagram of $\mu \to e\gamma$ in the standard model with the neutrino oscillation [10].

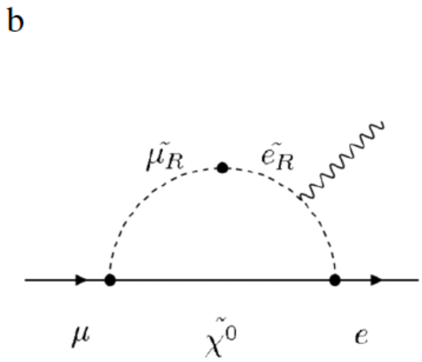

Fig. 1.6: An example of the diagram of $\mu \to e\gamma$ with the TeV scale SUSY particles [10].

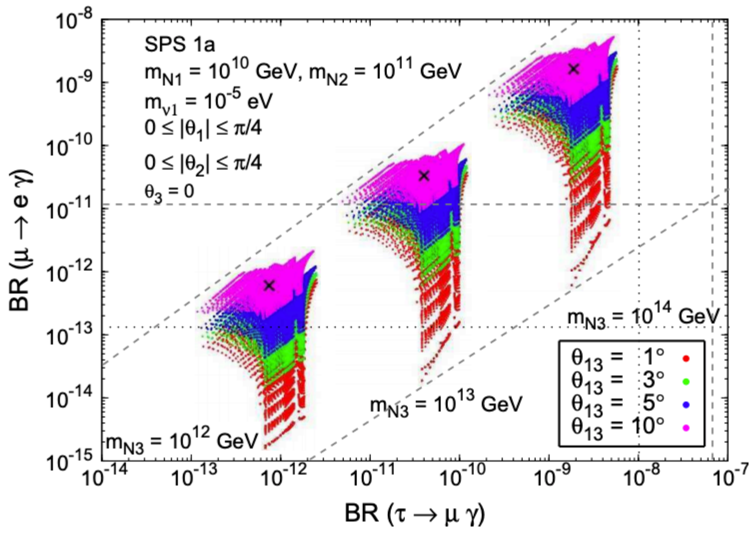

Fig. 1.7: The expected branching ratios of $\mu \to e\gamma$ and $\tau \to \mu\gamma$ in the CMSSM with seesaw mechanism [11].

1.5.2 $\mu \to e\gamma$ Decay

This thesis shows the latest progress of the MEG II experiment which searches for one of the cLFV phenomena, $\mu \to e\gamma$. This decay violates the lepton flavor conservation and is strongly suppressed in the Standard Model. Taking the neutrino mass into account, the $\mu \to e\gamma$ can occur within the Standard Model by the process shown in Fig. 1.5 and the rate is calculated as [10]:

$$Br(\mu \to e\gamma) = \frac{3\alpha}{32\pi}\left|\Sigma_{i=2,3} U^*_{\mu i} U_{ei} \frac{\Delta m^2_{i1}}{M^2_W}\right|^2 \sim 10^{-54}. \tag{1.9}$$

The most strict upper limit is currently set by MEG experiment, Br($\mu \to e\gamma$) $< 4.2 \times 10^{-13}$ (90% C.L.) [1]. In the BSM, the branching ratio of this decay becomes much larger by introducing heavy new particles like SUSY particles or right-handed neutrinos. Fig. 1.6 shows the diagram of the $\mu \to e\gamma$ with SUSY particles.

The limit by the MEG experiment already puts a stringent constraint on some of the BSMs and improving the experimental sensitivity by another order of magnitude will cover the majority of the parameter space. As an example, the expected

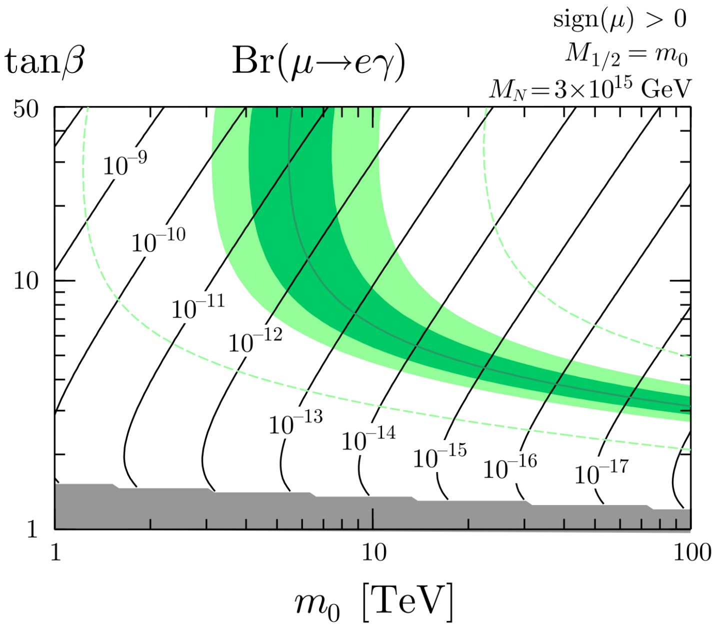

Fig. 1.8: Br($\mu \to e\gamma$) as functions of the universal scaler mass m_0 and tanβ for $M_N = 3 \times 10^{15}$ GeV, $M_{1/2} = m_0$, $a_0 = 0$, and sign(μ) > 0 in the mSUGRA. Numbers of the figures correspond to the values of Br($\mu \to e\gamma$). Dark green, light green, and dashed green region for m_h [GeV] correspond to the region of $125 < m_h < 127$, $124 < m_h < 128$, and $120 < m_h < 130$, respectively [12].

$\mu \to e\gamma$ branching ratio in the constrained-MSSM (CMSSM) with seesaw mechanism is shown in Fig. 1.7. The neutrino mixing angle $\theta_{13} \sim 9^\circ$ [44] suggests a higher branching ratio for $\mu \to e\gamma$, and the search of O(10^{-14}) region approaches the parameter region of the heaviest right-handed neutrino mass around 10^{12} GeV for SPS 1a parameters[*2].

Fig. 1.8 shows the relation between mSUGRA parameters (m_0, a_0, $M_{1/2}$, tanβ, sign(μ)), the branching ratio of $\mu \to e\gamma$ and the Higgs mass [12] with the heavy right-handed neutrino ($M_N = 3 \times 10^{15}$). The limit by the MEG experiment already explored the parameter space of m_0 around 5 TeV at $m_h = 126$ GeV. If the MEG II experiment is completed and the one-order higher sensitivity of O(10^{-14}) is achieved, the access to the parameter space of the new particles up to around O(10 TeV), which is not achievable by the direct search experiments, becomes feasible.

Another example is shown in Fig. 1.9 [13]. In this paper, several parameters pointed out by Casas and Ibarra [46] (CI parameters), which complicate the mixing structure of the neutrino Yukawa matrix and affect the CP and flavor violating observables by enhancing the off-diagonal elements of the mass matrix, are studied carefully. They showed that the proper introduction of the CI parameters has a significant impact on the CP and flavor violating observables, and thus Br($\mu \to e\gamma$) is enhanced. The MEG II experiments has an enough sensitivity to explore the parameter space of the heavy SUSY particles, O(10 TeV).

1.5.3 Prospect of $\mu \to e\gamma$ Search

Fig. 1.10 shows the history of the searches for these three major cLFV phenomena. The sensitivity of $\mu^+ \to e^+\gamma$ searches have reached O($10^{-11} - 10^{-13}$) region in the past ~ 30 years, which is already within the predicted region of some BSM

[*2] The “Snowmass Points and Slopes” (SPS) are a set of benchmark points and parameter lines in the MSSM parameter space corresponding to different scenarios in the search for Supersymmetry at present and future experiments [45].

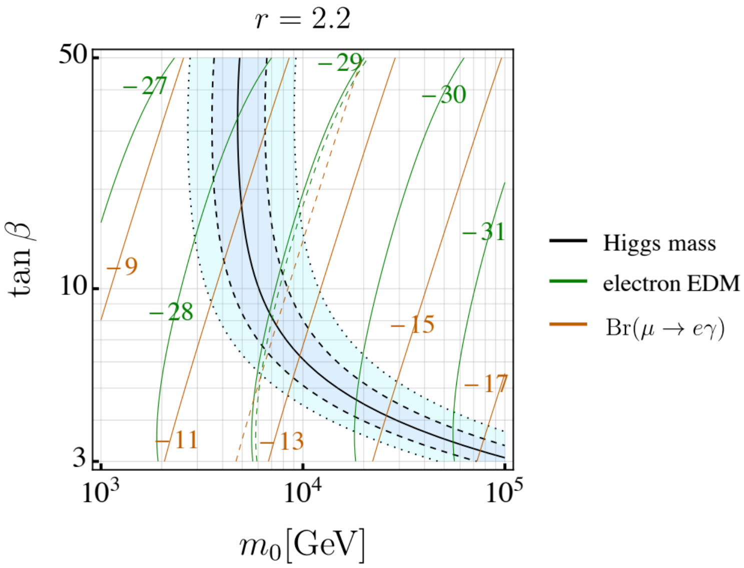

Fig. 1.9: Br($\mu \to e\gamma$) as functions of the universal scaler mass m_0 and tanβ for $M_N = 3 \times 10^{13}$ GeV, $M_{1/2} = m_0$, $a_0 = 0$, and sign(μ) > 0 in the mSUGRA. $r = 2.2$ is one of the CI parameters. With the increase of r value, the Yukawa coupling can become larger. The detail of the other CI parameters can be found in [13]. The black lines are for Higgs mass of 125 GeV, and the dashed/dot lines are ± 1 GeV/2 GeV from the Higgs mass. The current upper limit of electron EDM $d_e < 1.1 \times 10^{-29} e$ cm [14] is shown with the green dashed line, which is almost equivalent to the current upper limit of Br($\mu \to e\gamma$) by the MEG experiment (shown with the brawn dashed line) in this parameter space.

theories. The experimental sensitivity of $\mu \to e\gamma$ continues to be improved toward O(10^{-14}) region. The unprecedented sensitivities are achieved by the improvement of the detectors (new apparatus and sophisticated design like Sec. 2.2: MEG and Sec. 2.3: MEG II) and beam technologies (surface muon beam explained in Sec. 2.3.2).

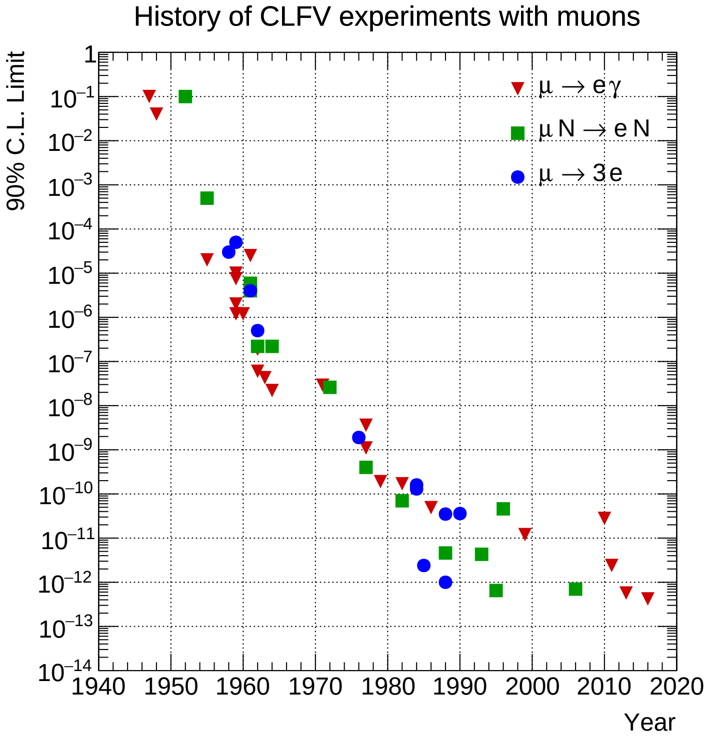

Fig. 1.10: The history of the upper limits of three cLFV phenomena [3].

Chapter 2

MEG and MEG II Experiment

This chapter describes experiential requirements for $\mu^+ \to \mathrm{e}^+\gamma$ detection. An overview of the MEG experiment and its limitation in the past searches are summarized. Then, MEG II upgrade is explained in details.

2.1 Experimental Requirements

The signal event and two main background (accidental background event and RMD event) events in the $\mu^+ \to \mathrm{e}^+\gamma$ search are shown in Fig. 2.1. The signal and RMD events are single physics phenomena while the accidental background event is composed of two physics phenomena close in time.

2.1.1 Signal Events

The signal event, $\mu^+ \to \mathrm{e}^+\gamma$, is a two-body decay and the kinematics of the signal positron and the signal gamma-ray can be characterized as follows:

- $t_{\mathrm{e}^+\gamma} = 0$,
- $\Theta_{\mathrm{e}^+\gamma} = 180°$,
- $E_{\mathrm{e}^+} = E_\gamma = m_\mu/2$,

where $t_{\mathrm{e}^+\gamma}$ is the time difference between the positron and the gamma-ray at the vertex, $\Theta_{\mathrm{e}^+\gamma}$ is the opening angle between the positron and the gamma-ray, E_{e^+} and E_γ are the energies of the positron and the gamma-ray, respectively, and m_μ is the muon mass ($m_\mu/2 \simeq 52.8$ MeV).

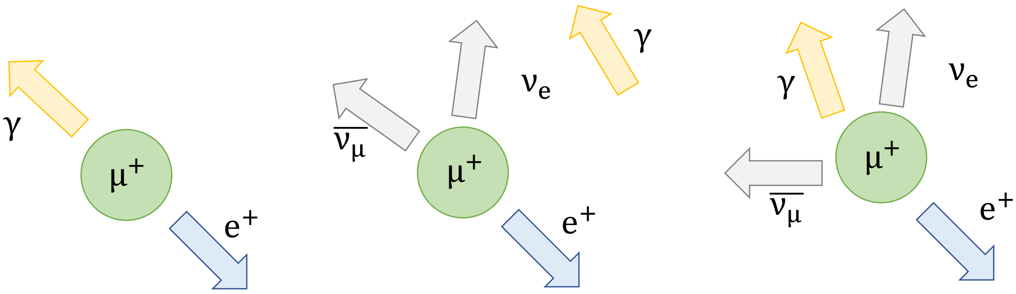

Signal Event

Accidental Background Event
(Michel Positron + Gamma Ray)

RMD Event

Fig. 2.1: The schematics of a signal event and background events (accidental and RMD).

The number of the expected signal events can be written as follows:

$$N_{\mathrm{sig}} = R_\mu \times T \times \Omega \times B \times \epsilon_\gamma \times \epsilon_e \times \epsilon_s, \tag{2.1}$$

where R_μ is the rate of stopped muons, T is the total data acquisition (DAQ) live time, Ω is the solid angle of the detectors, B is the branching ratio of the signal decay, $\epsilon_\gamma, \epsilon_e, \epsilon_s$ are the efficiencies of the gamma-ray, positron, and event selection by the trigger and the offline analysis, respectively.

2.1.2 Background Events

The major background events are the accidental coincidence between gamma-rays and positrons. The main source of the accidental positron is the Michel decay, $\mu^+ \to \mathrm{e}^+\nu\bar{\nu}$. The accidental gamma-rays are from the RMD event $\mu^+ \to \mathrm{e}^+\nu\bar{\nu}\gamma$, bremsstrahlung, and positron annihilation-in-flight (AIF). Another background source is the RMD when the emitted neutrinos carry a low momentum. Fig. 2.1 shows these schematics.

Here these two types of backgrounds are summarized based on [9]. For the discussion, the following 4 parameters, $x = 2E_{\mathrm{e}^+}/m_\mu$, $y = 2E_\gamma/m_\mu$, $z = \theta_{\mathrm{e}^+\gamma} - \pi$, and $t_{\mathrm{e}^+\gamma}$ are used and the signal region is defined as below:

$$\begin{aligned} 1 - \delta x \le & x \le 1 + \delta x, & (2.2a)\\ 1 - \delta y \le & y \le 1 + \delta y, & (2.2b)\\ 0 \le & z \le \delta z, & (2.2c)\\ -\delta t_{\mathrm{e}^+\gamma} \le & t_{\mathrm{e}^+\gamma} \le \delta t_{\mathrm{e}^+\gamma}, & (2.2d) \end{aligned}$$

where δx, δy, δz and $\delta t_{\mathrm{e}^+\gamma}$ is the signal region for each variable. For example, by using the design resolutions obtained in Ref. [1], the signal region in the MEG experiment can be defined to have 90% coverage:

$$\begin{aligned} \delta x \approx & 0.015, & (2.3a)\\ \delta y \approx & 0.019, & (2.3b)\\ \delta z \approx & 20 \text{ mrad}, & (2.3c)\\ \delta t_{\mathrm{e}\gamma} \approx & 200 \text{ ps}. & (2.3d) \end{aligned}$$

RMD Events

One of the backgrounds for the $\mu^+ \to \mathrm{e}^+ + \gamma$ search is the radiative muon decay (RMD), $\mu \to \mathrm{e}^+\nu\bar{\nu}\gamma$, when the positron and gamma ray are emitted back to back with two neutrinos carrying off little energy ($x \approx 1$, $y \approx 1$ and $z \approx 0$). The background fraction from the RMD (dB_{RMD}) can be calculated by integrating the RMD differential branching ratio ($dB(\mu^+ \to e^+\nu\bar{\nu}\gamma)$) over the signal region:

$$dB_{\mathrm{RMD}} = \int_{1-\delta x}^{1+\delta x} dx \int_{1-\delta y}^{1+\delta y} dy \int_0^{\delta z} dz \frac{dB(\mu^+ \to e^+\nu\bar{\nu}\gamma)}{dxdydz}. \tag{2.4}$$

Then the number of the RMD background events can be estimated as follows:

$$N_{\mathrm{RMD}} = R_\mu \times T \times \Omega \times dB_{\mathrm{RMD}} \times \epsilon_\gamma \times \epsilon_e, \tag{2.5}$$

Fig. 2.2 shows the achievable sensitivity for RMD with the given δx and δy values. For example, the effective branching ratio of the RMD background in the MEG experiment was $\sim 1 \times 10^{-14}$, which was almost negligible compared to the single event sensitivity[*1] of $(5.84 \pm 0.21) \times 10^{-14}$. To achieve the sensitivity of $\mathrm{O}(10^{-15})$ level, which will be the target for the MEG II experiment, both δx and δy should be on less than 0.01. In the MEG II experiment, the resolution of the positron momentum will be improved by a factor of three (~90 keV), and the that of the gamma-ray will be by a factor of two. This requirement can be satisfied and the RMD background will not be a dominant source of the background.

[*1] The single event sensitivity (SES) is defined as B in N_{signal}, which is the sensitivity value for the experiment to see one signal event.

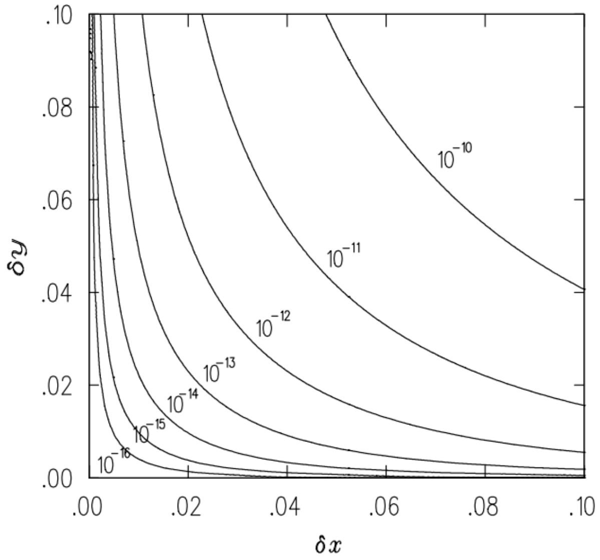

Fig. 2.2: Effective branching ratio of the RMD background as a function of the positron energy (δx) and gamma-ray energy (δy) [9].

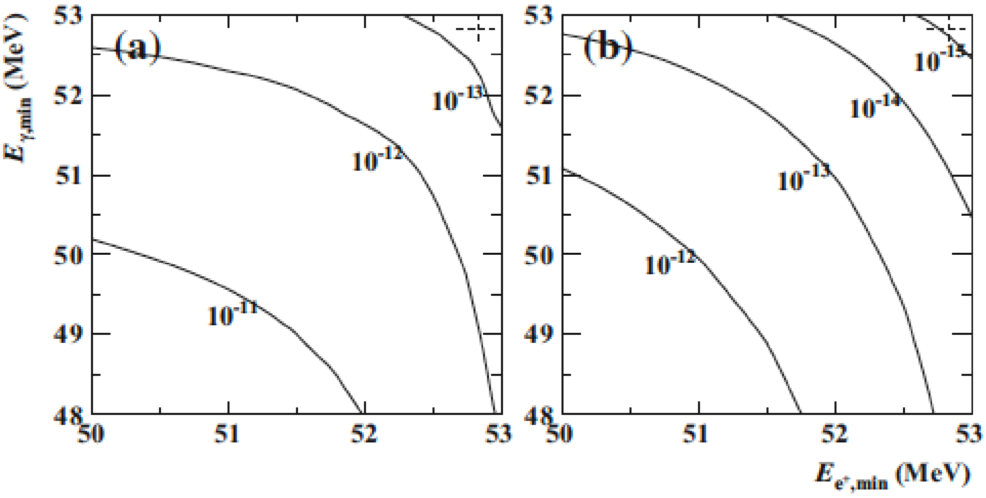

Fig. 2.3: Effective branching ratios of the accidental and RMD background into the kinematic window of MEG experiment defined by $E_{\mathrm{e^+},\mathrm{min}} < E_{\mathrm{e^+}} < 53.5$ MeV, $E_{\gamma,\mathrm{min}} < E_\gamma < 53.5$ MeV, $|t_{\mathrm{e^+}\gamma}| < 0.24$ ns and $\cos\Theta_{\mathrm{e^+}\gamma} < -0.9996$. (a) Accidental background from the side-band data. (b) RMD background calculated with the theoretical formula folded with the MEG detector response [1].

Accidental Background

Under the very high rate environment like the MEG and MEG II experiment, the accidental background becomes more important than the RMD background. Fig. 2.3 shows the effective branching ratio of the RMD and accidental background in the MEG experiment.

The accidental background rate (B_{acc}) can be estimated by:

$$B_{\mathrm{acc}} = R_\mu \cdot f_e^0 \cdot f_\gamma^0 \cdot \delta t_{e\gamma} \cdot \frac{\delta\omega_{e\gamma}}{4\pi}, \tag{2.6}$$

where R_μ is the muon beam rate, f_e^0 and f_γ^0 are the integrated fractions of the spectrum of the positron and the gamma-ray from the muon decay within the signal region, $\Delta t_{e\gamma}$ is the full width of the timing coincidence, $\Delta\omega_{e\gamma}$ is that of the angular constraint of the back-to-back kinematics.

The energy spectrum of the positron and gamma ray are shown in Fig. 1.3 and Fig. 1.4, respectively. f_e^0 can be estimated by integrating the flat part of the Michel spectrum ($x \approx 1$), yielding $f_e^0 \approx 2\delta x$. As for the gamma ray, if the main source of background gamma ray is the RMD[*2], it can be calculated by the integral of the spectrum over 2π for θ_γ and over the signal region for gamma ray energy. f_γ^0 is given by:

$$f_\gamma^0 \approx \int_{1-\delta y}^{1+\delta y} dy \int_0^{2\pi} d(cos\theta_\gamma) \frac{dB(\mu \to e^+\nu\bar{\nu}\gamma)}{dyd(cos\theta_\gamma)} \approx (\frac{\alpha}{2\pi})(\delta y)^2[\ln(\delta y) + 7.33]. \tag{2.7}$$

Given the angular resolution $\delta\theta_{e\gamma}$, the back-to-back resolution $(\Delta\omega_{e\gamma}/4\pi)$ can be presented by $(\delta\theta_{e\gamma})^2/4$.

From the above, the effective branching ratio of accidental background is given by:

$$B_{\mathrm{acc}} = R_\mu \cdot (2\delta x) \cdot [\frac{\alpha}{2\pi}(\delta y)^2(\ln(\delta y) + 7.33)] \cdot \frac{(\delta\theta_{e\gamma})^2}{4} \cdot 2\delta t_{e\gamma}. \tag{2.8}$$

Thus, the number of accidental background events can be written as follows:

$$\begin{aligned} N_{\mathrm{acc}} &= R_\mu \times T \times \Omega \times B_{\mathrm{acc}} \times \epsilon_\gamma \times \epsilon_e \\ &\propto R_\mu^2 \times \Delta E_\gamma^2 \times \Delta P_e \times \Delta\Theta_{e\gamma}^2 \times \Delta t_{e\gamma} \times T. \end{aligned} \tag{2.9}$$

where ΔE_γ, ΔE_{e^+} is the energy/momentum resolution for gamma-ray and positron, $\Delta\Theta_{\mathrm{e}^+\gamma}$ is the resolution for the opening angle between positron and gamma-ray, $\Delta t_{\mathrm{e}^+\gamma}$ is the resolution for the time difference between positron and gamma-ray.

2.1.3 Requirements

To maximize the N_{sig} in Eq. 2.1, it is important to increase the beam rate R_μ, the DAQ period T, the efficiency ϵ_γ, ϵ_e, ϵ_s and the detector acceptance Ω.

On the other hand, the accidental background events also increase quadratically with the increase of R_μ. In high rate experiments like the MEG II experiment, both the accidental overlap of a positron and a gamma-ray and the pileups of positrons (gamma-rays) in a detector have significant impacts. Detectors must separate the accidental background and must be tolerant for the pileups. Eq. 2.9 also indicates that having good resolutions of position, timing, angle, and energy is the key to reduce the background events.

Considering the realistic DAQ period (three-year for MEG II), the important points can be summarized as follows:

- Design the detectors, which are tolerable under high radiation and preserve good resolutions and high efficiencies under intense muon beam.
- Develop the reconstruction algorithms to cope with high pileup environment under intense muon beam and to preserve good resolutions and high efficiencies.

2.2 MEG Experiment

The most stringent upper limit on the $\mu \to e\gamma$ was established by the MEG experiment [1], $\mathrm{Br}(\mu \to e\gamma) < 4.2 \times 10^{-13}$ (90% C.L.).

[*2] Another main background source of the gamma-ray around the signal region is the AIF gamma-ray. However, the spectrum of the AIF gamma-ray depends on the material distribution of the experiments and difficult to discuss generally. In the MEG II experiment, the materials are reduced from the MEG experiment and the RMD events are dominant.

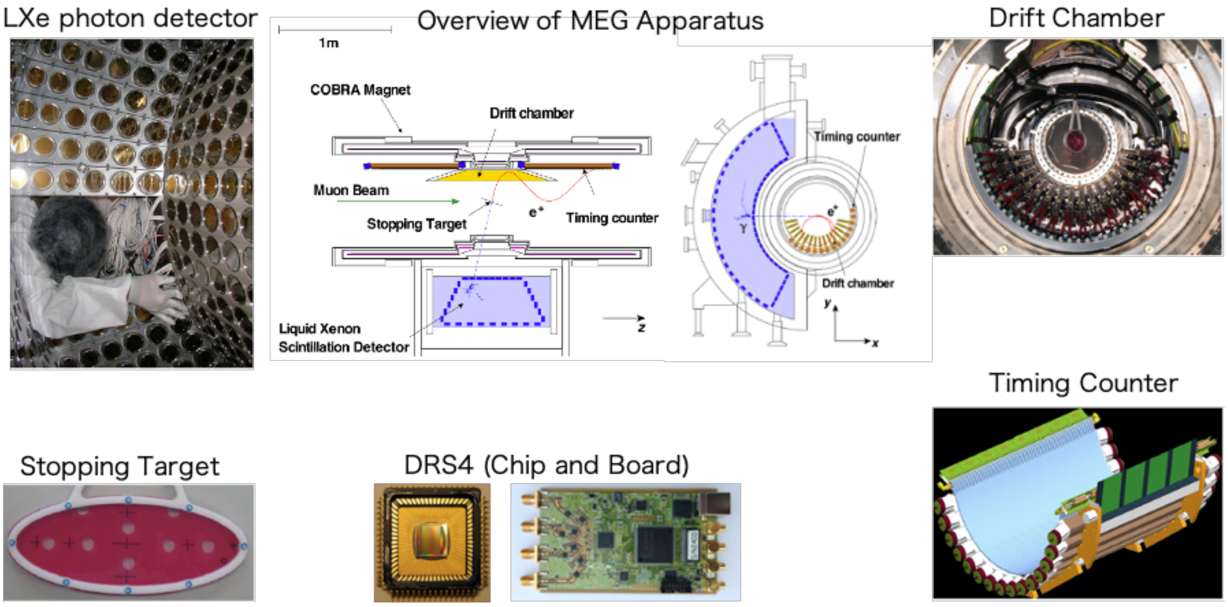

Fig. 2.4: The overview of the apparatus used in MEG experiment. The picture of DRS chip and board from [15]. The picture of the LXe from [3]. The other pictures and sketch from [1].

2.2.1 Apparatus

Fig. 2.4 summarizes the apparatus. The MEG experiment was conducted at the Paul Scherrer Institute with an intense continuous muon beam ($3 \times 10^7 \mu$ / s). Muons were stopped at a stopping target made of polyethylene and polyester. Gamma-rays were measured with a liquid xenon photon detector with 846 VUV sensitive photomultiplier tubes. Positrons were measured by a positron spectrometer, which was composed of 16 drift chamber modules and a timing counter made of the plastic scintillation bars. For the data acquisition, Domino-Ring-Sampler 4 (DRS4) chips [15] were used.

Table 2.1 shows the resolution and efficiencies achieved by MEG experiment (those proposed by the MEG II uprade are also shown). As for the detector performance of the positron detectors, the large scintillator used in the MEG timing counter ($4 \times 4 \times 80\mathrm{cm}^3$) caused the additional timing variation of scintillation photons by longitudinal propagation, incident angle, position dependence and so on. In addition, the performance of the PMTs used in the magnetic field were degraded during operation. The positron-crossing timing resolution achieved with the MEG timing counter ($\sigma_{\mathrm{TC}} \approx 70$ ps) was much worse than the designed value ($\sigma_{\mathrm{TC}} \approx 40$ ps). The event rate of the timing counter (1 MHz) also limited the beam rate of the MEG experiment.

The module-type drift chamber had mainly two crucial problems. Firstly, due to relatively large detector materials (including support structure and readout electronics of each module), the multiple scattering deteriorated resolutions and reconstruction efficiency. Secondly, the tracking volume and the number of layers were not enough to precisely associate the positron tracks with the hit positrons in the timing counters and with the vertex points on the stopping target, resulting in large uncertainties of the global tracking and lower reconstruction efficiency of 30%.

2.2.2 Result and Limitation

The MEG experiment finished data taking in 2013, and its final result with full data set was published in 2016 [1]. A maximum likelihood analysis is performed to obtain the number of the signal events in the analysis window based on

Table 2.1: The detector performance of MEG and expected performance of MEG II [3].

Resolution	**MEG**	**MEG II**
E_{e^+} [keV] (momentum of e^+)	380	130
θ_{e^+} [mrad] (Angle of e^+)	9.4	5.3
ϕ_{e^+} [mrad] (Angle of e^+)	8.7	3.7
z_{e^+}/y_{e^+} [mm] (Vertex position of e^+)	2.4/1.2	1.6/0.7
E_γ [%], $w < 2$ cm/$w > 2$ cm (Gamma energy)	2.4/1.7	1.1/1.0
$u_\gamma, v_\gamma, w_\gamma$ [mm] (Gamma position)	5/5/6	2.6/2.2/5
$t_{e^+\gamma}$ [ps] (Timing difference b/w $e^+\gamma$)	122	84
Efficiency(%)		
Trigger	99	99
γ	63	69
e^+	30	70

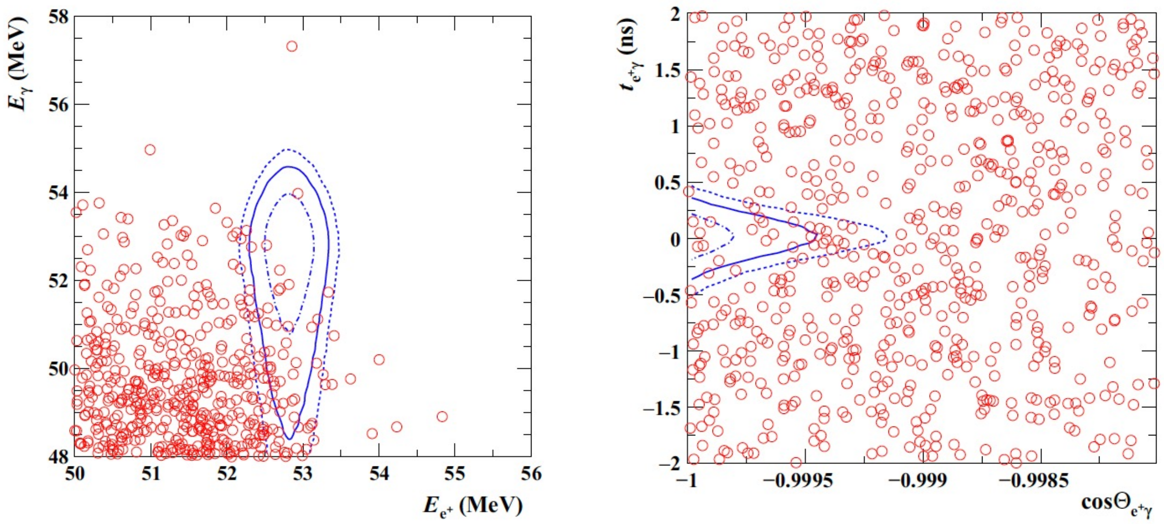

Fig. 2.5: Event distributions for the 2009 – 2013 full dataset on the (E_{e^+}, E_γ)-plane with the selections of cos $\Theta_{e^+\gamma} <$ -0.99963 and $|t_{e^+\gamma}| < 0.24$ ns (left), and $(\cos\Theta_{e^+\gamma}, t_{e^+\gamma})$-plane (right) with $51.0 < E_\gamma < 55.5$ MeV and $52.4 < E_{e^+} < 55.0$ MeV. The contours of the averaged signal PDFs (1σ, 1.64σ and 2σ) are superimposed [1].

the Probability Density Functions (PDFs) for signal, RMD, and accidental background events. Fig. 2.5 shows the event distributions for the 2009 – 2013 full dataset on the (E_{e^+}, E_γ) and $(\cos\Theta_{e^+\gamma}, t_{e^+\gamma})$ planes. The contours of the averaged signal PDFs are also shown. No significant excess was found within the signal contours, and the new upper limit for the branching ratio of $\mathrm{Br}(\mu^+ \to e^+\gamma) < 4.2 \times 10^{-13}$ (90% C.L.) was set as shown in Fig. 2.6, which improved the world record by a factor of 30 from the one set by the MEGA experiment [47].

The continuation of the MEG experiment is not realistic to achieve the $O(10^{-14})$ sensitivity. The single event sensitivity of the MEG experiment was 0.58×10^{-13}, while the upper limit of the branching ratio was 4.2×10^{-13}. These values mean that the sensitivity of the MEG experiment was limited not by the statistics but by the number of the accidental backgrounds. As shown in Fig. 2.6, the improvement of the upper limit in the MEG experiment got smaller and smaller as the DAQ time

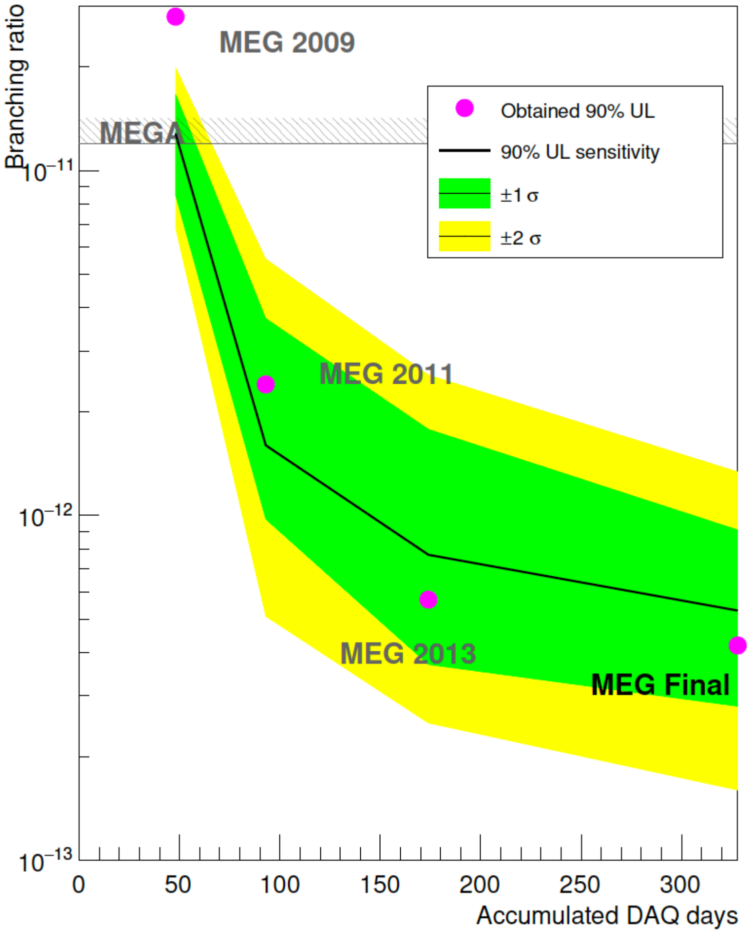

Fig. 2.6: The branching ratio sensitivity as a function of the DAQ days in the MEG experiment [4].

passed during 2009 – 2013. Assuming that the contribution from the number of the backgrounds improves by a square root of the statistics, it will take O(100) years to achieve 10 times better sensitivity from the MEG experiment. In addition, the MEG detectors were optimized for the MEG dedicated conditions (e.g. beam rate and experiment period). From the operation point of view, e.g. rate tolerance and radiation hardness, it is not realistic to continue the MEG experiment.

2.2.3 Proposal of the MEG II Experiment

An upgrade experiment, MEG II experiment, was proposed [21] in 2013, aiming at a branching ratio of O(10^{-14}) with the twice intense muon beam. Table 2.1 shows the resolution and efficiencies achieved by MEG experiment and those proposed for the MEG II upgrade. The positron reconstruction efficiency and resolution will be improved by a factor of ~2. This proposed performance is required to suppress the backgrounds which determined the limitation in the MEG experiment. The innovative positron spectrometer, which is composed of the highly segmented scintillation timing counter: pTC and ultra-low material drift chamber with large tracking volume: CDCH, was newly designed to achieve this goal. Table 2.2 summarizes the list of systematic uncertainties in MEG experiment. Alignment of stopping target was the largest uncertainty. Therefore, MEG II experiment will replace the stopping target system.

Table 2.2: The list of the systematic uncertainties considered in the physics analysis in the MEG experiment [4]. The fractions of "All the other" are also shown in parentheses.

PDF parameters	**Impact on sensitivity**
Alignment of stopping target	13%
All the other	<1%
Alignment of LXe detector - tracker	(37%)
E_γ scale	(23%)
Bias of center of $t_{e\gamma}$ PDF	(19%)
E_e bias	(11%)
Normalization	(7%)
Errors in event-by-event PDF	(3%)

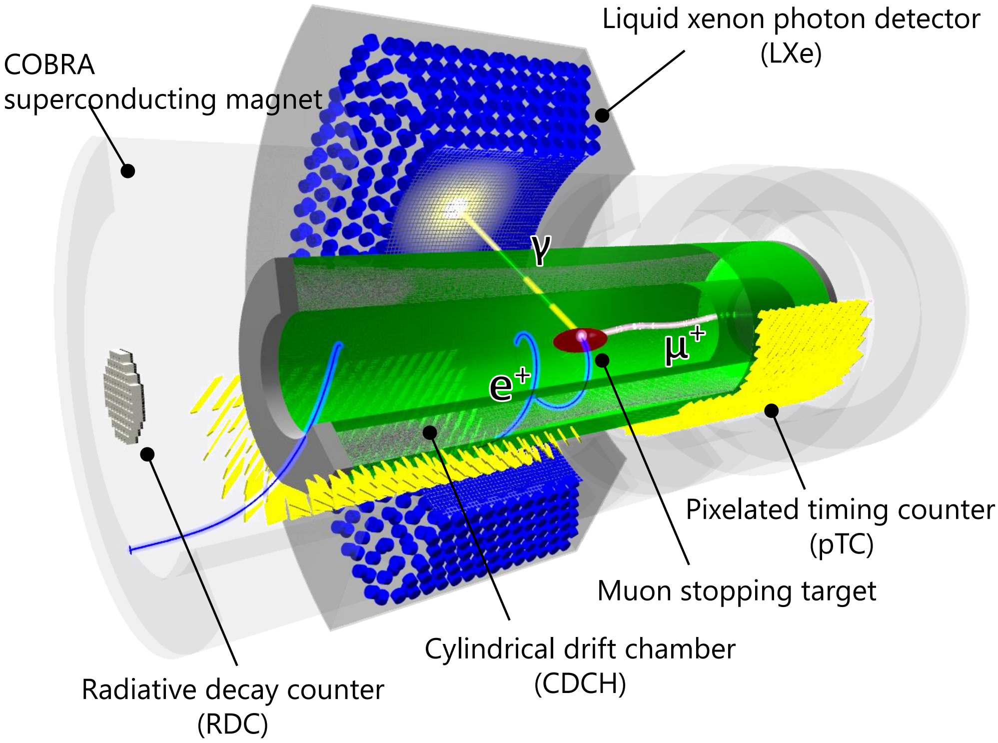

Fig. 2.7: The overview of the MEG II experiment [3].

2.3 MEG II Experiment

The apparatus of the MEG II experiment (except for the positron spectrometer explained in the next section) is described in this section [3].

The key points to reach O(10^{-14}) sensitivity are the increased beam rate (Sec. 2.3.2), and the higher performance of the detectors (Sec. 2.3.4, Sec. 2.3.5 and Sec. 2.4). In addition, the DAQ and trigger system (Sec. 2.3.6) are upgraded to cope

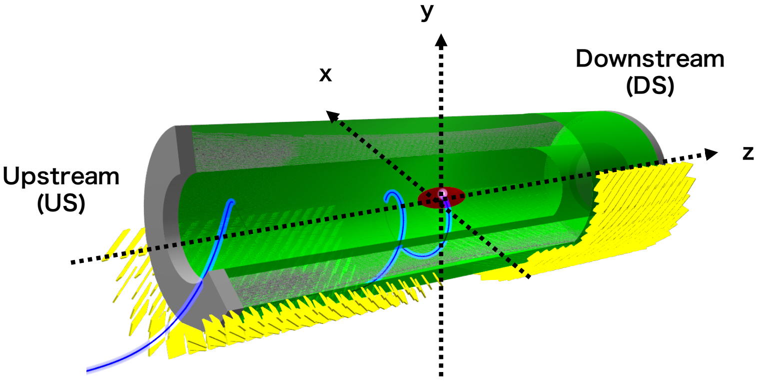

Fig. 2.8: The global coordinate system of MEG II positron spectrometer.

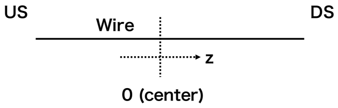

Fig. 2.9: The local coordinate on a CDCH wire.

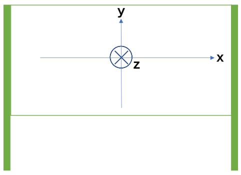

Fig. 2.10: The local coordinate of a pTC counter.

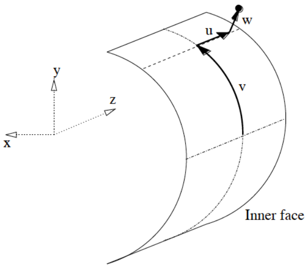

Fig. 2.11: The dedicated coordinate of the LXe detector (u, v, w) [16].

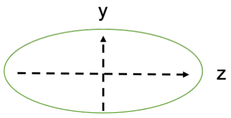

Fig. 2.12: The coordinate of the target ellipse.

with the higher number of readout channels and densities. The muon stopping target and the monitoring system (Sec. 2.3.3) are also upgraded to decrease the systematic uncertainties.

Fig. 2.7 shows the overview of the MEG II experiment. The positive muon beam is stopped at the stopping target at the center of the spectrometer magnet (Sec. 2.4.4). The positrons from the muon decays are measured by the new positron spectrometer and gamma-rays by the LXe gamma-ray detector, which is also upgraded from the MEG experiment. RDC is a new detector for background rejection. The requested period for the MEG II physics run is 20 week/year and for 3 years.

2.3.1 Coordinate systems

In the MEG II global coordinate system, we define the z-axis along the muon beam axis with the origin at the center of the COBRA. The y-axis is defined as the direction from bottom to top to direction and x-axis is defined as the rest direction in the right-handed coordinate system. Fig. 2.8 shows the coordinate systems of positron spectrometer.

When we reconstruct a hit in a counter of the pTC or on a wire of the CDCH, positron variables are described in the local coordinate system as defined in Fig. 2.9 and Fig. 2.10. The local coordinate of the LXe detector and the target, which are

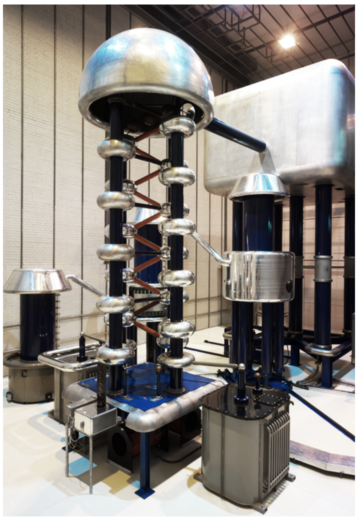

Fig. 2.13: The Cockcroft-Walton pre-accelerator [17].

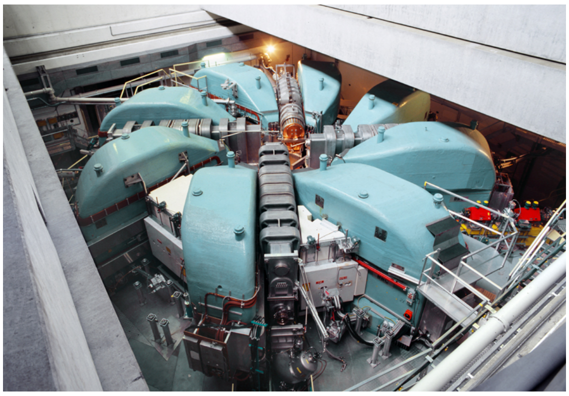

Fig. 2.14: The large proton ring accelerator [17].

shown in Fig. 2.11 and Fig. 2.12, respectively, are also used for the criteria in the track selection task.

2.3.2 Muon Beam Line

As described in the previous sections, an intense muon beam is necessary to accumulate N_{signal}. The $N_{\text{accidental}} \propto R_{\mu}^2$ indicates that a direct current (DC) muon beam is suitable instead of the pulsed muon beam. In addition, a positive muon beam should be used to avoid the formation of the muonic atoms which deteriorates the simple two-body decay kinematics. Currently the most intense DC muon beam in the world ($\sim 10^8\ \mu^+/\text{s}$) is available at Paul Scherrer Institut (PSI) in Switzerland.

The muon beam is produced at the proton cyclotron accelerator in the PSI. The protons from a hydrogen source are accelerated up to 590 MeV with the combination of the Cockcroft-Walton pre-accelerator (870 keV), the 4-sector injector 2 cyclotron (72 MeV) and the large 8-sector ring cyclotron (590 MeV). Fig. 2.13 and Fig. 2.14 show the Cockcroft-Walton pre-accelerator and the large proton ring accelerator, respectively. The proton beam (1.2 MW) is transported to the graphite target (the pion production target). The beam frequency is 50.7 MHz and the width of the beam bunch is 0.3 ns. This frequency (~20 ns interval) is short enough for the muon beam to be continuous compared with the pion lifetime (26 ns) and muon lifetime (2.2 μs). The surface muons [48], which originate from the stopped pions near the target surface, are collected and transported to the beamline (πE5) used by the MEG II experiment. The muons from the decays of the stopped pions, $\pi^+ \to \mu^+ + \nu_{\mu}$, have a sharp momentum spectrum around 29.8 MeV/c and are $\sim$ 100% polarized[*3].

Fig. 2.15 shows the schematic view of the πE5 beamline and the MEG beam transport system with MEG detectors. The production target is connected to the πE5 area by a quadrupole and hexapole channel in the direction of backward (165°). The muon beam is then transported through the beam transfer and contamination[*4] removal components: quadrupole triplet (Triplet I), the Wien-filter ($E \times B$ field separator), Triplet II, and a collimator system. Then, the muon beam goes through the Beam Transport Solenoid (BTS). BTS is a 2.8 m long iron-free superconducting solenoid to focus and transport the muon beam. The final muon momentum is adjusted by a degrader system in the BTS and finally, the muon beam is spotted on the MEG II target with a stopping rate of $7 \times 10^7 \mu^+/\text{s}$.

[*3] The 100% polarized muons have several scientific merits: for the possibility of the measurement of angular distribution of $\mu \to e + \gamma$, which may provide the crucial information of the new physics.

[*4] The contamination comes from mainly positrons generated by a Michel decay or pair creation of a photon from π^0 decay.

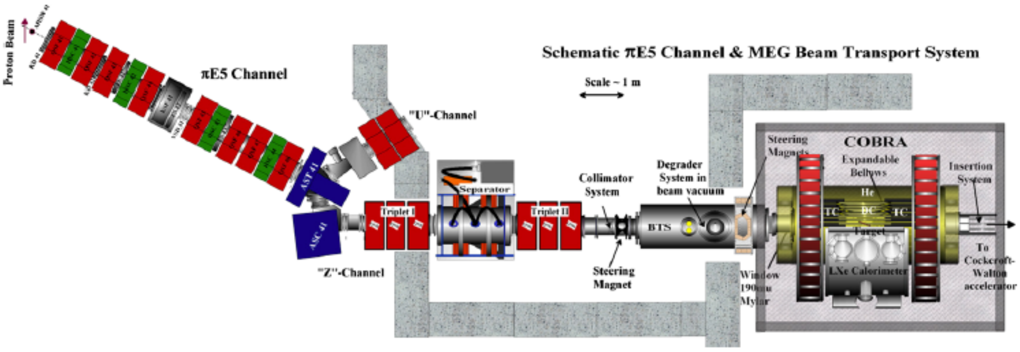

Fig. 2.15: The πE5 beam line [18].

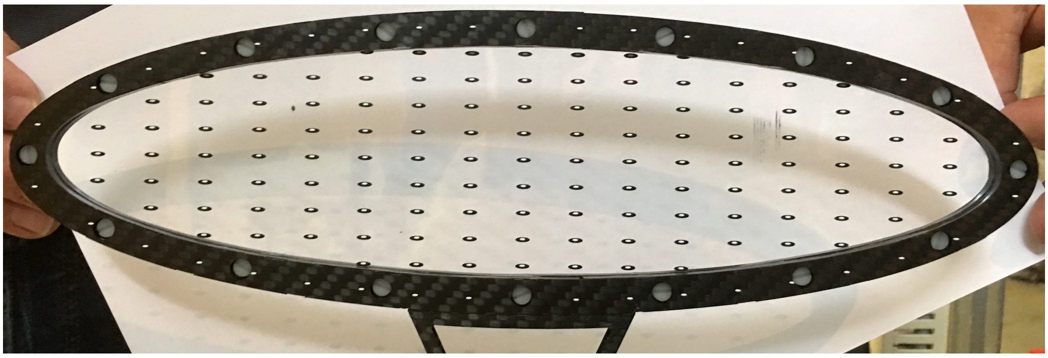

Fig. 2.16: The MEG II scintillator target [3].

2.3.3 Target

The main requirements for the MEG II target are as follows:

1. High muon stopping efficiency.
2. Low material budget to avoid multiple scattering, photon conversion, annihilation in flight (AIF), and bremsstrahlung.
3. Stable structure to reduce the systematic uncertainty.
4. Remotely movable structure for the insertion of the calibration targets.

For the MEG II target in the commissioning, a plastic scintillator target whose thickness is 174 μm was used. It was placed with the slant angle of 15.0° from the beam axis to achieve a longer effective thickness for muons (requirement 1.) and a shorter thickness for positrons (requirement 2.). The material is hard enough to avoid the deformation. The goal of the target alignment precision is $< 50\ \mu$m on the transverse direction and $< 100\ \mu$m on the axial direction.

To monitor the target position, pattern dots are printed for the CCD camera monitoring as shown in Fig. 2.16. By CCD camera monitoring of the patterned dots, we expect a $\sim 10\ \mu$m precision in the transverse coordinate and $\sim 100\ \mu$m in the axial coordinate [3].

In addition, the small holes will be made for the tracking-based alignment as in MEG. The tracking-based alignment was done by checking the positron track distribution at the vertex and the deficit of the distribution at the holes. Fig. 2.17 shows the example of the distribution from the MEG data.

The additional advantage of the scintillator material is the possibility of non-destructive measurements of the beam

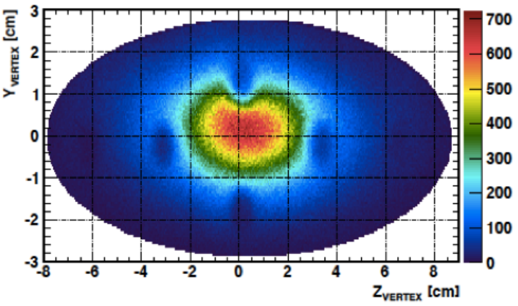

Fig. 2.17: The distribution of positron reconstructed position at the target with 2011 MEG data [3].

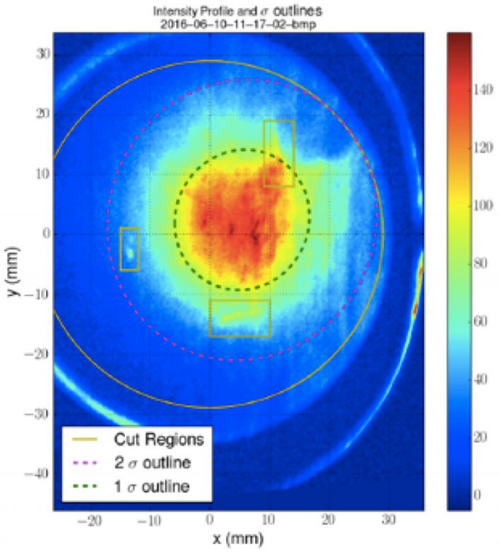

Fig. 2.18: The perspective corrected and 2D gaussian fitted beam image viewed originally under 15° to the target plane and taken in 2016 commissioning [3].

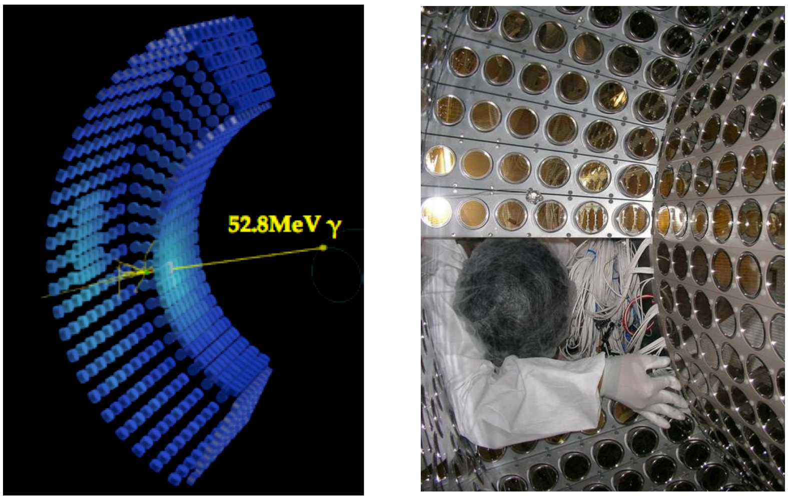

Fig. 2.19: The picture of the LXe photon detector [3].

intensity and profile with a CCD camera and dedicated optical systems. Fig. 2.18 shows the beam image taken with the CCD camera and optical system setup in the 2016 MEG II detector commissioning.

2.3.4 Liquid Xenon (LXe) photon Detector

The MEG II Liquid Xenon (LXe) photon detector is composed of ~900 L LXe as a liquid scintillator and photo-sensors. The LXe has the following advantages for precise photon measurement:

- Fast timing response,
- High stopping power,
- Large light yield,

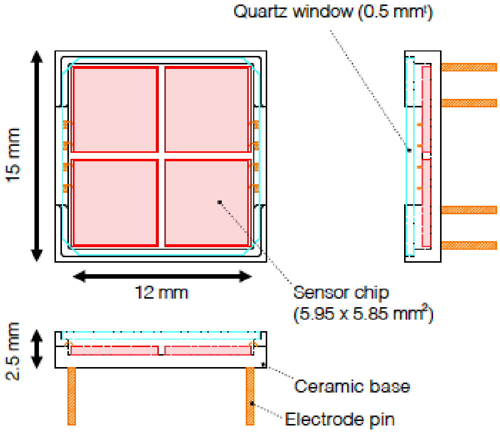

Fig. 2.20: The sketch of a large area VUV sensitive MPPC used in MEG II LXe photon detector [19].

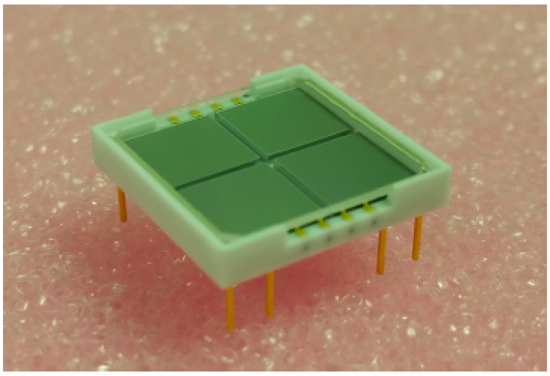

Fig. 2.21: A large area MPPC used in MEG II LXe photon detector [19].

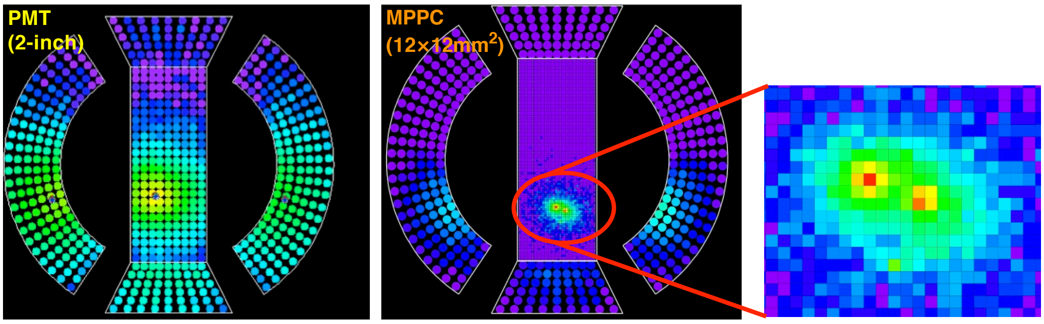

Fig. 2.22: Example of scintillation light distribution detected by PMTs (left) and MPPCs (right) for a same simulated event [3].

- Uniformity of the scintillation response,
- Radiation hardness.

On the other hand, it is expensive and a cryogenic system (∼165 K) is required for the detector operation. A major challenge is to detect the LXe scintillation light, which is in the vacuum-ultraviolet (VUV) range (175±5 nm). VUV-sensitive photo-sensors were developed in collaboration with Hamamatsu Photonics. In the MEG experiment, 846 2-inch PMTs (HAMAMATSU R9869) were used as shown in Fig. 2.19. The biggest issue was the non-uniformity of the PMT coverage in the inner face (photon entrance side). The collection efficiency strongly depended on the incident position due to this non-uniformity especially at the shallow region, and this dependence deteriorated the energy and position resolution in the MEG experiment. In MEG II, 216 PMTs on the inner face are replaced with 4092 SiPMs[*5].

A large area VUV enhanced MPPC[*6], shown in Fig. 2.20 (sketch) - Fig. 2.21 (picture), was developed. The detailed studies and mass tests are summarized in Ref. [19]. As a result, a high photon detection efficiency (PDE) up to 21%, a high gain, a low dark count rate, and a good single photoelectron resolution were achieved.

Fig. 2.22 shows a comparison of event displays with the MPPC readout case and the PMT readout case for a same

---

[*5] These replaced PMTs were re-used on the other face to replace the dead PMTs, and to further improve the uniformity of the readout by the optimized PMT layout.

[*6] Hamamatsu Photonics uses Multi-Pixel Photon Counter (MPPC) for their product name of SiPMs.

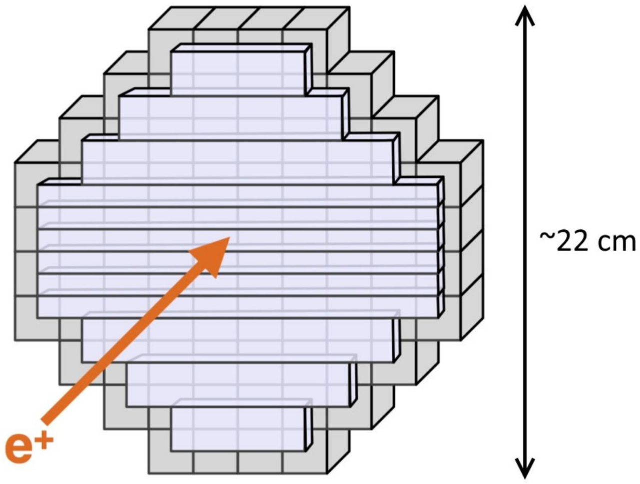

Fig. 2.23: The schematic view of the RDC. The horizontal long plates in front are the plastic scintillator bars and the cubes behind are the LYSO crystals [3].

simulated event. The imaging power is clearly improved by the higher granularity and uniform readout with MPPCs.

2.3.5 Radiative Decay Counter (RDC)

A gamma-ray from a RMD, which is a source of an accidental background event, can be identified by detecting a low momentum positron from the same decay. The low momentum positrons are swept away quickly through the small radius trajectory to either upstream (US) or downstream (DS), so the RDC is placed on the beam axis to detect those positrons and identify the RMD events.

They measure the coincidence of the positron timing with the photon in the LXe detector, and tag the RMD events. The energy measurement will help to separate the RMD positron and the accidental Michel positron whose energy is high enough to be distinguished.

DS-RDC

Fig. 2.23 shows the schematic view of the DS-RDC. DS-RDC is composed of the 12 plastic scintillation counters for the timing measurement and the 76 LYSO crystals for the energy measurement. Fig. 2.24 shows the distribution of the timing difference between the RDC and LXe detector. The peak in the red histogram corresponds to the RMD events, while the flat regions in both red and blue histograms correspond to the Michel events.

Fig. 2.25 shows the energy distribution at the RDC for RMD events with E_γ >48 MeV and Michel events. Typically the Michel positrons have higher energies and the energy measurement with LYSO crystals will help the identification.

US-RDC

The high transparency for the muon beam and the high detection efficiency for the RMD positrons must be demonstrated for a detector on the beam axis of the upstream side. In addition, the requirement for the radiation tolerance is severe under the intense muon beam.

For US-RDC, ultra-low mass Resistive Plate Chamber (RPC) is newly designed [49]. The test of the US-RDC prototype was conducted in December 2020 at PSI. Since the operation plan of US-RDC has not yet finalized, the contribution of the US-RDC is not included for the analysis in this thesis.

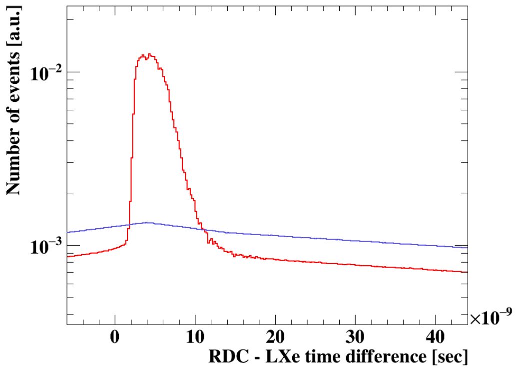

Fig. 2.24: The expected (MC) distribution of the timing difference between the RDC and LXe. Red line shows the accidental background events and blue line shows the signal events [3].

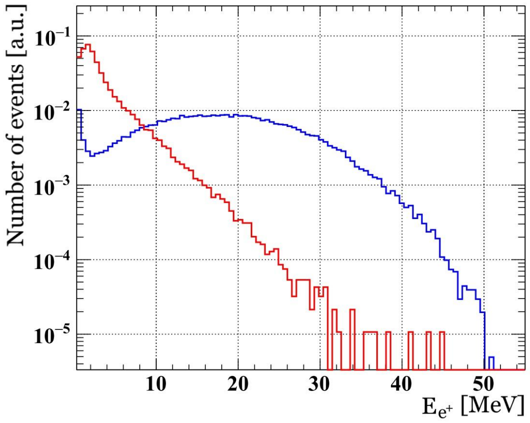

Fig. 2.25: The expected (MC) energy distribution at the RDC for RMD events with E_γ >48 MeV (red) and for Michel events (blue) [3].

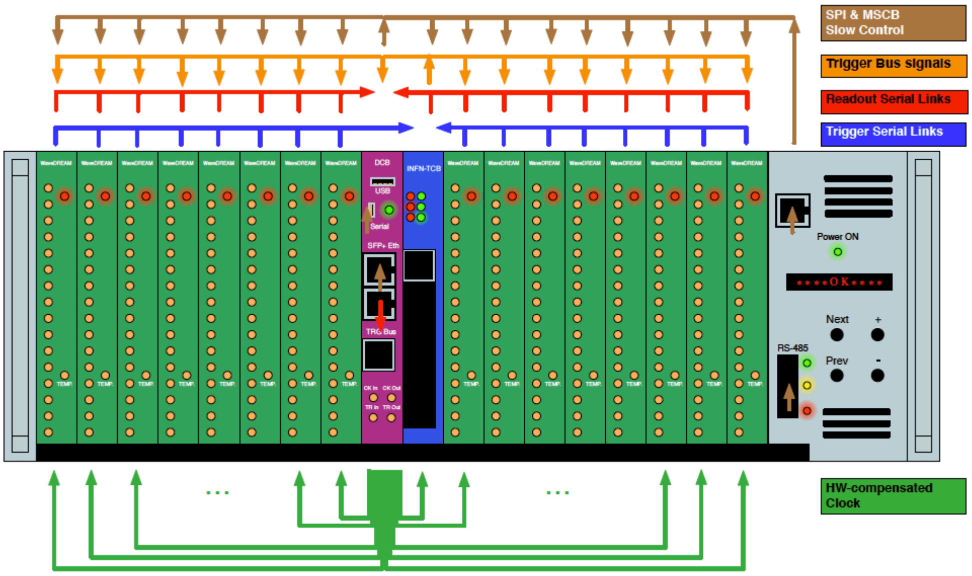

Fig. 2.26: The sketch of the single WaveDAQ crate [20]. The green boards are WDB, magenta DCB and blue TCB. CMB is drawn on the right side. Arrows show connections in the backplane: red arrows for data transmission to backend machines, blue for trigger serial links, orange to distribute back the trigger signal and green for hardware compensated clock distribution, and brown shows low level access for slow control and configuration.

2.3.6 Trigger and Data Acquisition (TDAQ) System

In the MEG II experiment waveform data is taken and stored for the offline analysis. For the efficient data accumulation and the limited space for the significantly increased number of channels (~9000 channels, which is ~3 times larger than MEG experiment), the new electronics, named Waveform Drs4 REadout Module Board (WaveDREAM Board, WDB) was developed.

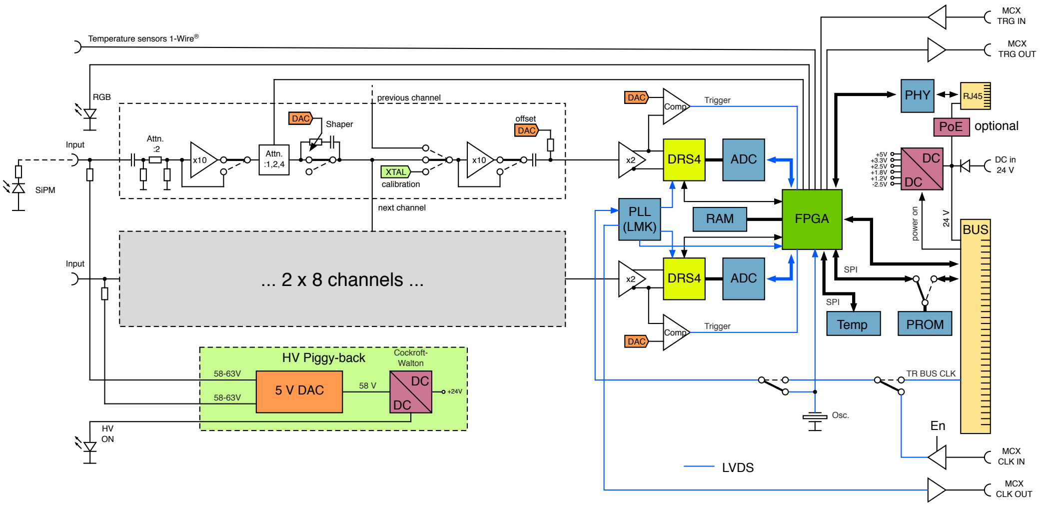

Fig. 2.27: The schematics of the WDB [3].

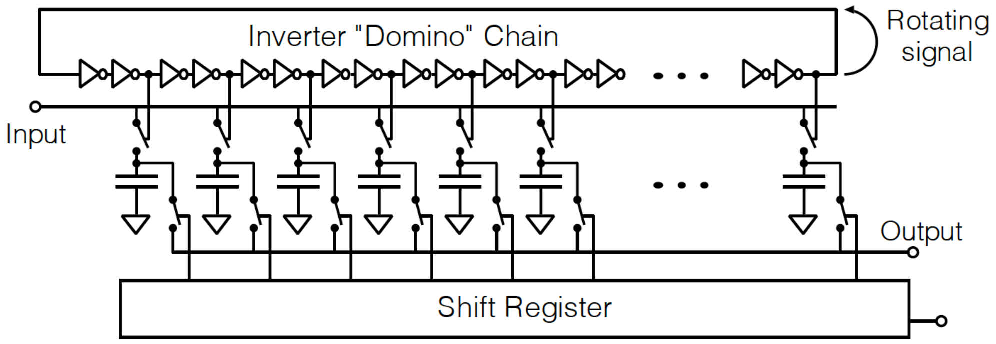

Fig. 2.28: The mechanism of the Domino Ring Sampler chip (DRS chip).

The WDB is inserted to the WaveDAQ crate with Data Concentrator Board (DCB) and Trigger Concentrator Board (TCB) in MEG II DAQ. Fig. 2.26 shows the single WaveDAQ crate. 16 boards (WDB) are connected to the 2 central slots (DCB and TCB) for the data and trigger processing, respectively. The power supply to the all boards and slow control are provideed by the crate management board (CMB) [3, 20].

WaveDREAM Board (WDB)

A WDB is an integrated DAQ electronics device: signal amplifier and shaper, high-voltage supply to the detectors, waveform digitizer, data transmission, and basic trigger functionalities are integrated on one board. Fig. 2.27 shows the schematics of the single WDB. A single WDB has 16 input channels, so the single crate has 256 readout channels at the maximum. The amplifier gain is adjustable in the range of 0.5–100. A waveform shaper is mounted and pole-zero cancellation can be applied to the waveform. A WDB contains two DRS4 chips whose sampling speeds can be adjusted in the range of 0.5-5 GSPS (Giga Samples Per Second) with 900 MHz bandwidth. The DRS4 chips [50] are connected to 80 MSPS Analog-to-Digital Convertors (ADCs). The scheme of the DRS chip is shown in Fig. 2.28. The voltage (amplitude) of the waveform is stored on 1024 capacitors as a charge by a logic wave propagating through the inverter domino chain (domino ring), and it is read out to the ADC by a shift register when the trigger is recieved. The sampling speed is flexible; 1.6 – 2.0 GSPS for pTC and 0.8 – 1.2 GSPS for the CDCH are used. This GSPS determines the timing window of one “event”: one sequential

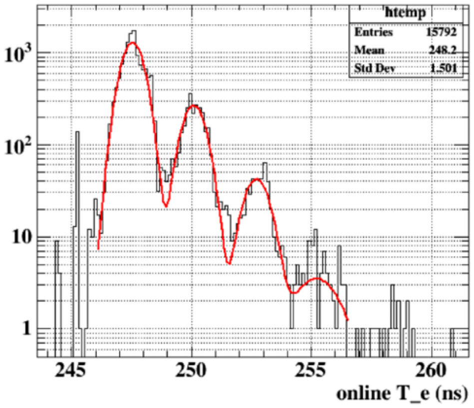

Fig. 2.29: The online timing distribution of positrons in MC (black) fitted with multiple gaussian function (red) [7].

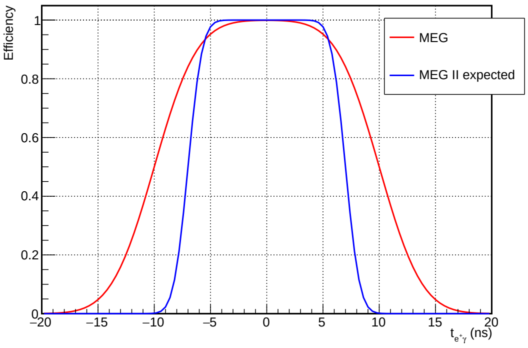

Fig. 2.30: The comparison of the online $t_{e^+\gamma}$ trigger selection efficiency of the MEG II expected (blue) timing window and the MEG (red) timing window. The width (FWHM) is reduced from 20 ns (MEG) to 14 ns (MEG II) [3].

waveform by one trigger[*7]. While the waveform is being sampled in the DRS4 chips, readout from sampling cells to the ADC is running in parallel and digitized data is transferred to an FPGA in which the dedicated trigger logics are implemented using digitized data and fast comparator outputs. The HV to the detectors is generated in an attachment board (HV piggy-back board), which has a 5V Digital-to-Analog Converter (DAC) and a Cockcroft-Walton voltage multiplier. The readout scheme guarantees a data transfer dead time of ~1 ms, which leads to a maximum DAQ rate of 100 Hz. Considering the muon beam rate, realistic data size, and online selection efficiency, the maximum trigger rate of the MEG II experiment is about 10 Hz.

Data Concentrator Board (DCB) and Trigger Concentrator Board (TCB)

The central 2 slots are reserved for special boards, which are responsible for the crate-level functions and for multi-board DAQ operation.

A DCB distributes the main reference clock and the trigger signal inside the crate. It is also responsible for the configuration in the crate and for the communication to the DAQ machines via the Gigabit Ethernet interface.

A TCB receives and handles all the trigger information from the WDB and judges the event of interest.

Trigger

The trigger processing will reject the background record by almost 6 orders of magnitude, resulting in a DAQ rate of ~ 10Hz. Online event reconstructions, such as the momenta, relative timing and direction, are performed based on the information from pTC and LXe[*8]. The necessary equation and lookup tables are implemented in the FPGA. The online reconstruction (timing/energy) of gamma-rays are performed from a sum of waveforms in the LXe detector. The online

---

[*7] The definition of "pileup" is overlapping of triggered positrons/gamma-rays and background positrons/gamma-rays in a analysis window. If more than one peak was found in one event (the timing window), the event can be counted as an event with pileups, as already explained in the first section of this chapter. The pileups by the background positrons/gamma-rays affects the reconstruction of the triggered positrons/gamma-rays by the baseline fluctuation (if the backgrounds come before the triggered one) or the overlapping of the peak position (if the timing is too close to be separated).

[*8] Since the drift time of CDCH is too long (in the range of several ns to O(100) ns), information from CDCH cells cannot be used for the online trigger. This makes the relative timing window wider since we cannot know the number of turns for positron track and obtain the TOF value from pTC to the vertex point.

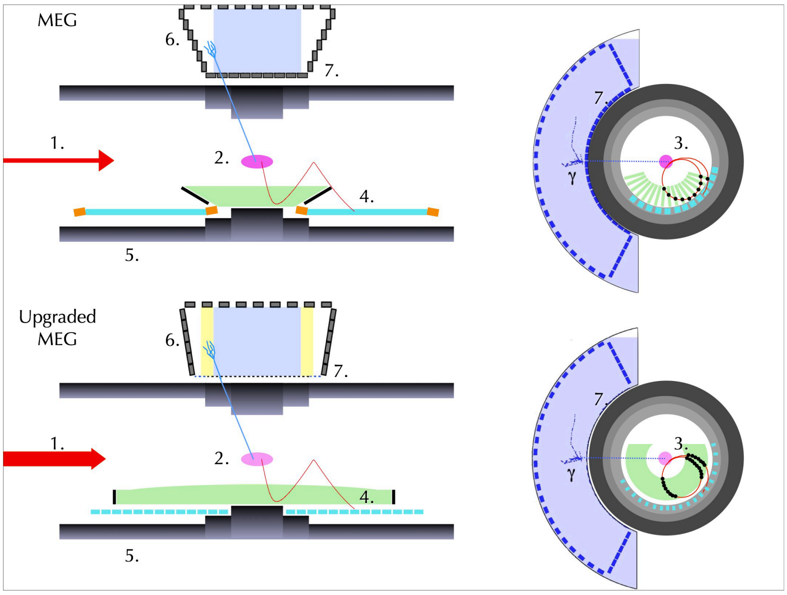

Fig. 2.31: The overview of the MEG (up) and MEG II (down) experiment [21]. The blue line shows the gamma ray and the red positron. The positron tracker volume (green region) was extended to the pTC interface, which increased the number of CDCH hits for one track and improved the trajectory and timing integration (matching efficiency). The timing counter (light blue region) was segmentalized into small pixels.

timing of positrons is defined from a pTC counter with the smallest $|z|$ position. The CDCH is not used for the online trigger due to its slow time response. The timing differences of positrons and gamma-rays at each channel are compared. Since the positron go into the pTC region after several turns as illustrated in Fig. 2.7 (e^+ reached at the pTC region at the second turn in this figure) but the number of turns cannot be reconstructed online, the coincidence width must be much wider than the online timing resolution (~450 ps). Fig. 2.29 shows the online timing distribution of positrons in the MC simulation. The difference by ~2.5 ns/turn can be observed thanks to the improvement of the online timing resolution from 2.5 ns (MEG) to 450 ps (MEG II). Fig. 2.30 shows the trigger selection efficiency as as function of the trigger timing window for the MEG II and the MEG experiment. The coincidence width (FWHM) is reduced from 20 ns to 14 ns without efficiency loss. In addition, the information on the opening angle between positrons and gamma-rays is available thanks to the highly segmented design of the pTC and the LXe readout.

2.4 Positron Spectrometer

The trajectory and the timing of the positron from $\mu \to e\gamma$ are measured by CDCH and pTC, respectively, in a gradient magnetic field generated by the spectrometer magnet named COnstant Bending RAdius magnet (COBRA). The requirement for the positron spectrometer is to reconstruct positron trajectories and timing, and to achieve two times better resolution and two times better efficiency under two times more intense muon beam. This requirement is achieved by the highly segmented design of the pTC and the ultra-low mass CDCH with the large number of layers in the large tracking volume.

2.4.1 Concept of Upgrade from MEG

For the $\mu \to e\gamma$ search, the positron measurement is crucial since the most dominant decay mode (Michel decay), $\mu \to e\nu\overline{\nu}$, emits positron around the signal energy.

The important requirements for the drift chamber are less material budget to avoid multiple scattering and very high

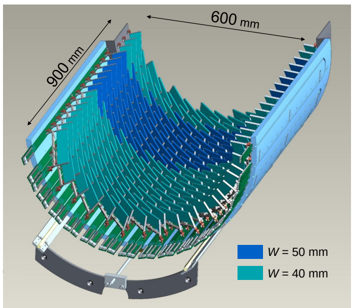

Fig. 2.32: The design of pTC detector [3].

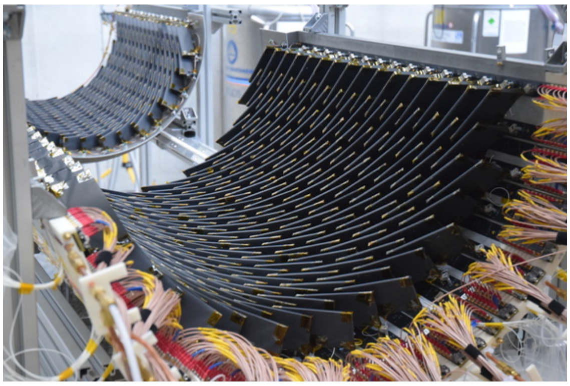

Fig. 2.33: The picture of pTC detector.

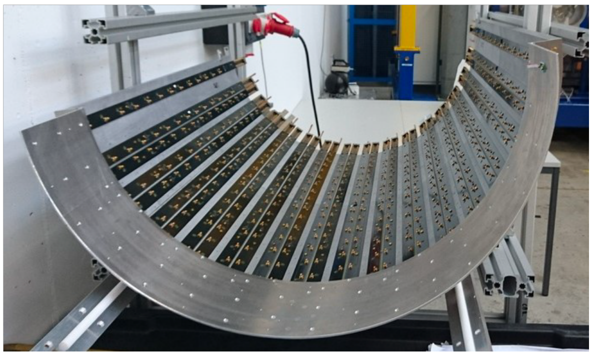

Fig. 2.34: The backplanes on the pTC support structure [7].

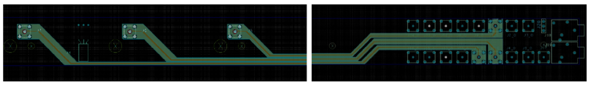

Fig. 2.35: The signal lines of the backplane [7].

granularity to be tolerant to the intense muon beam. Based on these requirements, a high-granularity ultra-low mass cylindrical stereo wire drift chamber has been considered.

The important requirement for the timing counter is a highly segmented and stacked design with small scintillators to improve the overall timing resolution using multi-hit measurements from one positron track. SiPMs were chosen for the photo-sensors of scintillation photons. This replacement solves the problem in MEG (PMT degradation) since SiPM is insensitive to the magnetic field. The time-offset calibration and uniform performance of the counters are crucial since the multiple-hit information, which is one of the most important concept of MEG II timing measurement, is used to achieve the target resolution. Several prototypes were tested with different scintillators and different SiPMs [23], and finally, the design of the MEG II timing counter was fixed [3].

2.4.2 Pixelated Timing Counter (pTC)

Design

Fig. 2.32 shows a CAD view of the pTC detector, and Fig. 2.33 shows the constructed pTC detector. The MEG II pTC is composed of 512 (256 for upstream and 256 for downstream) small scintillation counters. Each counter has 70 – 90 ps resolution with the double-side readout by 6 SiPMs connected in series at each side. The total capacitance becomes

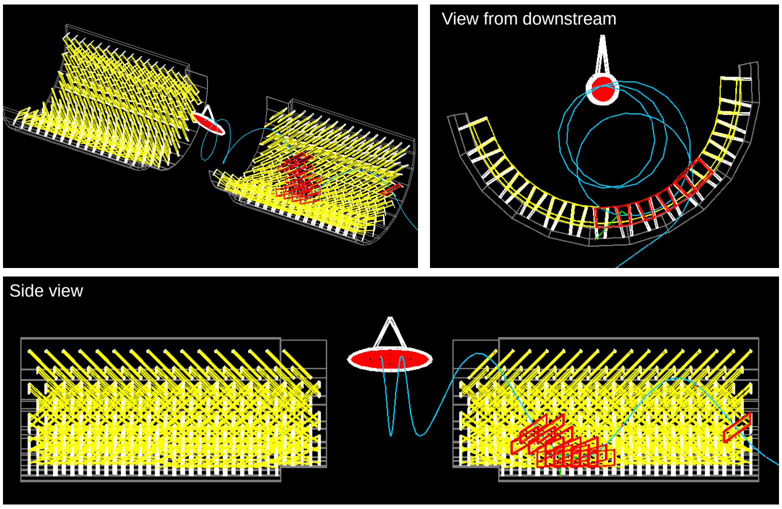

Fig. 2.36: A simulated signal positron trajectory (blue line) and the pTC counters (yellow). The positron crossed the red counters [3].

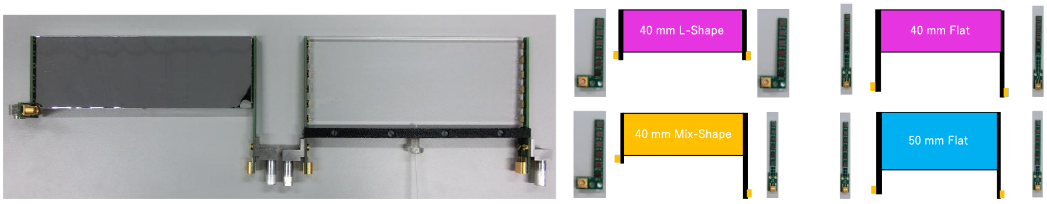

Fig. 2.37: (Left) The picture of single pTC counter. The picture of the two types of PCBs are also shown in right sketch [3]. (Right) The sketch of the counter design pattern. L-shape and mix-shape counters were designed to put counters on inner step of the support structure.

smaller by the series connection, resulting in the faster output pulse and better timing pick up. The counters are mounted on dedicated long (948×25 mm^2) PCBs called backplanes placed on a semi-cylinder-shaped aluminum support structure. The backplanes on the pTC support structure are shown in Fig. 2.34, and its drawing of the signal lines is shown in Fig. 2.35. The signals from the pTC counters are transmitted to the WDB with co-axial cables (RG178).

One positron with $\sim 45 - 50$ MeV momentum crosses eight counters on average. Fig. 2.36 shows an example of a simulated positron crossing the multiple pTC counters. The pTC achieves O(30 ps) timing resolution by using this multiple hits information. The detailed reconstruction algorithms are described in Chap. 6.

Components of Single Counter

Fig. 2.37 is the picture of the design models of counters. The main components of a counter are a scintillator tile, 12 SiPMs on two PCBs, an optical fiber and its support part, a reflector and a light shielding black sheet and connectors for backplane. They are summarized in Table 2.3.

Fig. 2.39 shows the pTC counter layout. The scintillator size and the alignment of counters were optimized by using a simulation. From the mechanical constraint, the PCB has the two types: flat-type and L-shaped type like the picture and the sketch. In total there are 4 design patterns on counters; flat-PCBs with 4 cm height scintillator (mainly used and illustrated with magenta in outer region of Fig. 2.39), L-shape PCBs with 4 cm (inner magenta) , L-PCB and flat-PBC (Mixed-PCBs) with 4 cm (yellow), and flat-PCBs with 5 cm (light blue). Positrons will cross the scintillator plate at almost right angle. 5

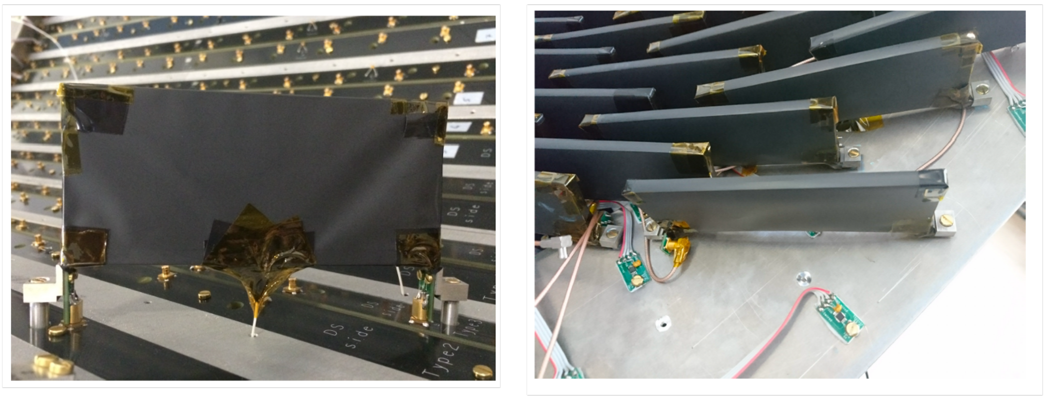

Fig. 2.38: (Left) A mounted flat-type counter on the backplane. (Right) Mounted L-shape counters on the inner step of the support structure [7].

Table 2.3: The materials for a pTC counter

Component	**Product**	**Note**	**Company**
Scintillator	BC422	40 or $50 \times 120 \times 5$mm^3	Saint-Gobain
SiPM	ASD-NUV3S-P High-Gain (MEG)	Used for main counters	AdvanSiD
SiPM 2	ASD-NUV3S-P	Used for spare counters. 40 or 50 μm pich	AdvanSiD
Reflector	ESR2 Film	32μm tickness, ≥ 98% reflection	3M
Light Shielding	Tedlar	25 μm tickness	DuPont

Table 2.4: The basic properties of BC-422 from the datasheet [5].

Property	**Values**
Light Output (% Anthracene)	55
Rise Time [ns]	0.35
Decay Time [ns]	1.6
Pulse Width (FWHM) [ns]	1.3
Bulk Light Attenuation Length [cm]	8

cm height counters are used since the typical radius of the positron trajectory becomes larger around the light blue region in Fig. 2.39. The Mixed-PCB counters and L-shaped PCBs are used due to the steps of the support structure. The other counters are composed of 4 cm height scintillator and flat-type PCBs. Fig. 2.38 shows the example of a mounted flat-type counter and mounted L-shape counters.

Scintillator

The rising part of the output waveform is crucial for timing measurement. The Saint-Gobain BC-422 scintillator whose rise time was ultra-fast (0.35 ns) was, therefore, chosen for pTC. The properties of BC-422 scintillator are summarized in Table 2.4.

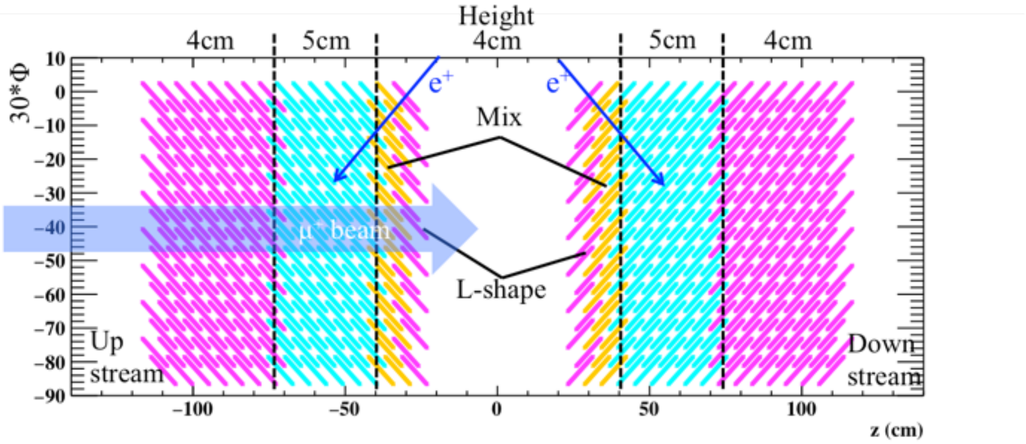

Fig. 2.39: The pTC counter map [22]. Counter region is ~20 –110 along the beam axis (z-axis) for both downstream and upstream.

Table 2.5: The datasheet values (provided by AdvanSiD [6]) of SiPMs used for the pTC ounter.

Type (Year)	**SiPM**	**Pixel Pitch**	V_{br} (20 °C)	V_{OV} from V_{br}	**# of Counters**
Type-I (2014)	ASD-NUV3S-P High-Gain (MEG)	50 μm	24 ± 0.3 V	+2 – +3.5	~448
Type-II (2015)	ASD-NUV3S-P	50 μm	26 ± 0.1[*9]V	+2 – +6	~ 48
Type-III (2018)	ASD-NUV3S-P	40 μm	26 ± 0.1 V	+2 – +6	~16

SiPM

The studies of readout configuration with SiPMs were conducted [23]. The series and parallel connection of SiPMs, which are well known as the advantageous method to increase the sensor coverage, were studied in the lab test. Those tests were carried out using SiPMs from different vendors. The total capacitance of series-connected SiPMs is smaller than that of a single SiPM, which results in the narrower output and faster rise time, while the wider output was measured with the parallel-connected SiPMs as shown in Fig. 2.40. The advantage on the rising part is especially crucial for the timing measurement, and finally, the series connection of 6 SiPMs from the AdvanSiD company was chosen for the pTC readout[*10]. Currently, 3 types of SiPMs (Type-I, II, III), as shown in Table 2.5, are used for pTC counters depending on the purchase period. Fig. 2.41 shows the timing resolution of single counter used until 2019.

Temperature and Humidity Control Systems

A stable detector operation is highly important for a long-term experiment. Especially, the relatively large temperature dependence of the SiPM performances affects the pTC timing resolution. A temperature control system is mandatory.

For pTC cooling, cooled water is circulated by a chiller machine (custom chill Model : CRAL300-230PE, 400W) through pipes of pTC support structure as shown in Fig. 2.42. When the pTC is operated in low temperature, for example 10°C,

---

[*9] The Min value of V_{br} is 24 V and The Max value is 28 V. 26 V is the typical value and ± 0.1 V is the 2 σ from the mean value in the same production lot.

[*10] In [23], the best timing resolution was obtained with the series connection of 3 SiPMs from the Hamamatsu Photonics. However, the AdvanSiD SiPMs were more reasonable than those, which means the number of SiPMs in one series-connection readout can be increased. The increase of the coverage was more crucial for the pTC performance than the performance of the single SiPM. Thus, the the series connection of 6 SiPMs from the AdvanSiD was adopted for the final design.

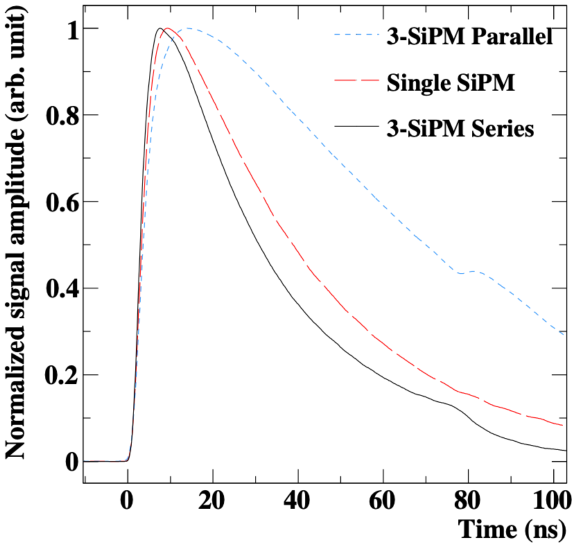

Fig. 2.40: The difference of the pulse shape with different connections of 3 SiPMs (3-SiPM parallel, single, and 3-SiPM series) with BC422 with HPK SiPM (S10362-33-050C) [23].

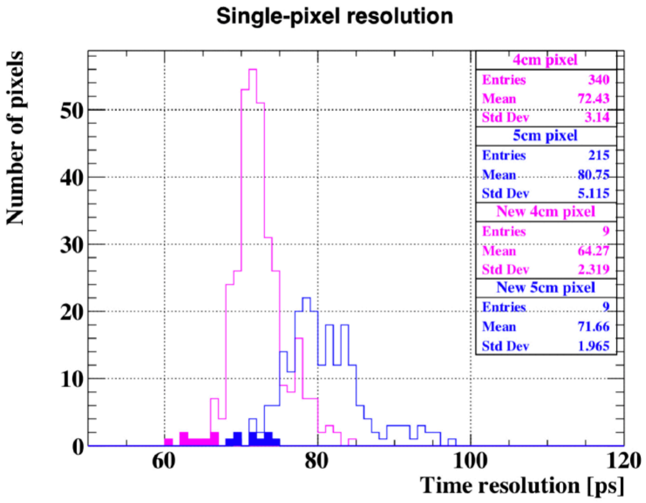

Fig. 2.41: The counter resolution measured in the lab-test with 4 cm counters (pink-line) and 5 cm counters (blue-line), which include type-I and type-II SiPMs [24]. The histograms filled with pink and blue show the resolution with type-III SiPMs for 4 cm and 5 cm counters, respectively.

dry-air from the PSI compressed air line flushes pTC to avoid the water condensation.

The pTC temperature and humidity are monitored with three thermal sensors and one humidity sensor on each backplane, respectively. The sensor positions are shown in Fig. 2.43. The operation test of the temperature control is explained in Sec. 3.4.4.

Laser-based Calibration System

To achieve the target performance of the pTC, the calibration of the time-offset of each counter is crucial. Two complementary methods were developed for the timing calibration: one is called laser-based calibration and the other is track-based

Fig. 2.42: The support structure viewed from the bottom side [7]. Cooling pipes and laser optical fibers can be seen.

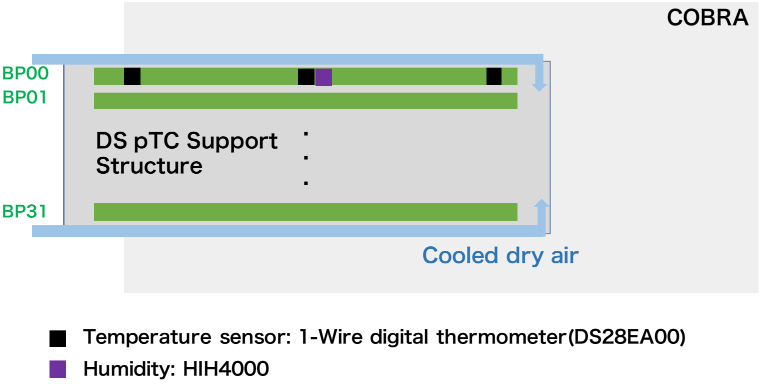

Fig. 2.43: The schematics of humidity and temperature sensor positions.

calibration. The details of the calibration algorithm are summarized in Chap. 6. In this subsection, the hardware of the laser-based calibration system is briefly explained.

The laser calibration system is shown in Fig. 2.44. The optical components selected based on the detailed studies [51] are summarized in Table A.1 in Appendix A. The optical length of these components were measured in advance. The pulse laser light, generated by PLP-10 from HAMAMATSU, is divided by optical splitters and injected into the counters simultaneously for a timing synchronization among counters. Since the laser power is not high enough to illuminate all (432) the counters simultaneously, an optical switch was installed to control the illumination to the counters.

2.4.3 Cylindrical Drift CHamber (CDCH)

Design

The design of the CDCH is inspired by the wire chamber used in KLOE experiment [52]. The MEG II CDCH has a 2 m-long single volume with a cylindrical shape. The inner radius is 17 cm, and the outer 29 cm. Low mass materials for the inner foil (aluminized Mylar foil) and outer support structure (carbon fiber) were used to lessen the effects of the multiple scattering. The filled gas is ultra-low mass mixture of helium and isobutane in the ratio 90:10. Fig. 2.45 shows the CDCH structure. The total radiation length for a positron track is $\sim 1.5 \times 10^{-3} X_0$ in the MEG II CDCH, while that was $\sim 2.0 \times 10^{-3} X_0$ in the MEG drift chamber.

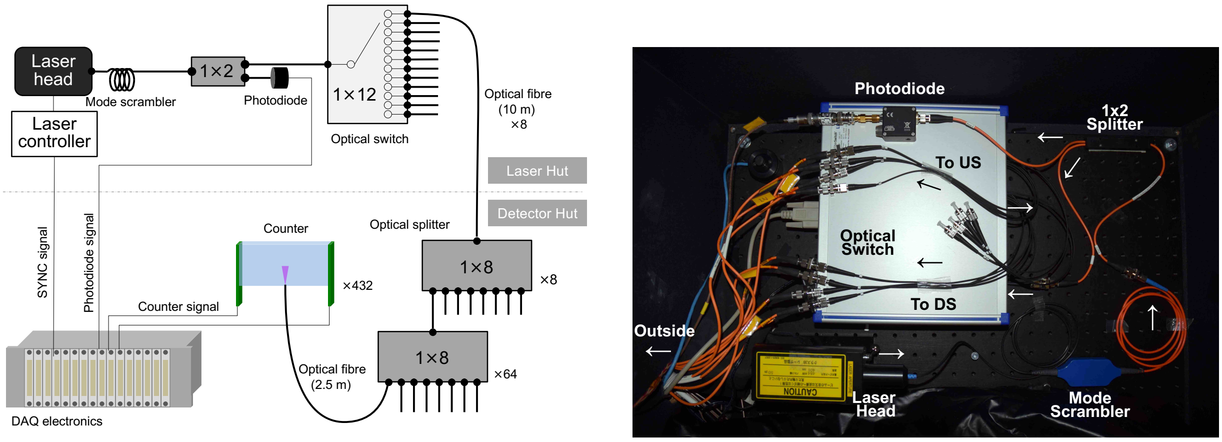

(a) (b)

Fig. 2.44: (a) Schematic and (b) picture of the laser-based calibration system for the MEG II pTC (from [25]). The individual components are described in the Table A.1.

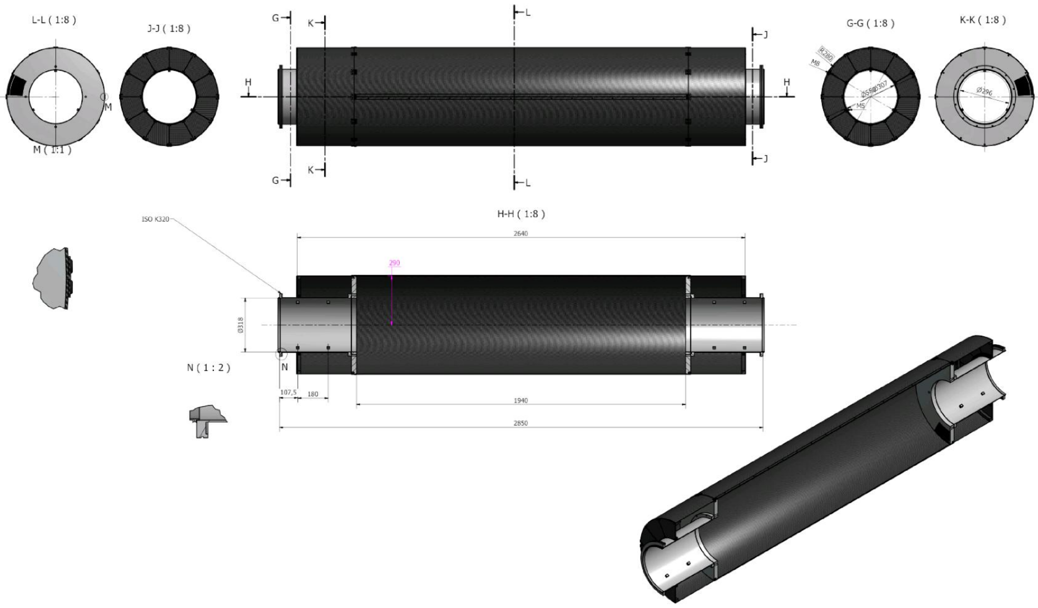

Fig. 2.45: The mechanical sketch of cylindrical drift chamber [3].

The long volume of the CDCH is installed in parallel to the muon beam inside the COBRA magnet and just inner area of the pTC. The layout of MEG II detectors is shown in Fig. 2.7 and Fig. 2.31. Since there is no large gap between the CDCH tracking volume and the pTC, the matching efficiency and flight time estimation are expected to be significantly improved.

The CDCH adopts a stereo-wire configuration with 9 layers for the precise z-determination. The stereo angle varies from 6° (inner most) to 8.5° (outer most), and wires in the continuous two layers were tilted in the opposite directions. Fig. 2.46 is the picture after the CDCH is fully wired.Due to the stereo angle tilting, not a cylindrical but a hyperbolic profile is seen.

Wires

Generally, a wire chamber is composed of three kinds of wires:

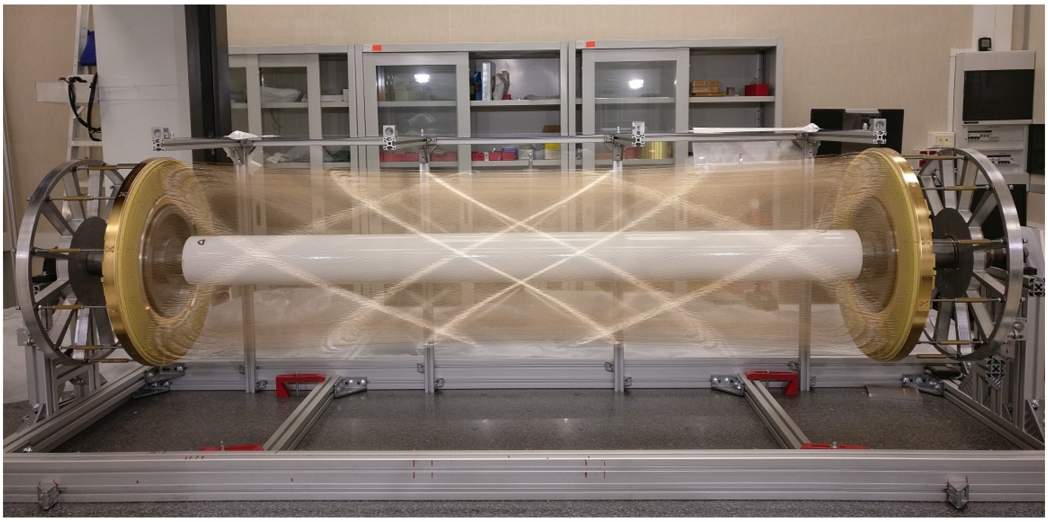

Fig. 2.46: The picture of CDCH mounted all wires [3].

Table 2.6: The CDCH wires.

Wires	**Material**	**Diameter**	Number of wires
Guard Field Wires	Al (Ag-plated)	50 μm	768
Cathode Field Wires	Al (Ag-plated)	40 or 50 μm	7680 (40 μm) /1728 (50 μm)
Anode Sense Wires	W (Au-plated)	20 μm	1728

- The guard field wires shape the electric field lines at the edge of the CDCH.
- The cathode field wires define the drift cells and make its ground mesh.
- The anode sense wires collect the charge induced by the positrons (i.e. detect the ionization of the gas through avalanche).

In total, 11904 wires are used to form 1728 drift cells (192 cells per layer) for the MEG II CDCH. The structure of layers in the CDCH is shown in Fig. 2.47, and the materials and diameter of these wires are summarized in Table 2.6*[11]. From the R&D studies [26], wires made of 5056 Al alloy*[12] (94.6% Al, 5.2% Mg, 0.1% Cr and 0.1% Mn) with diameters of 40 μm and 50 μm were chosen for the field and guard wires, respectively. The wire is silver-plated. The density is 3 g/cm^3 and its resistivity is 20 Ω/m. For the anodes, 20 μm pure-tungsten (W) wires with gold plate are used. The density is 19.25 g/cm^3 and resistivity 170 Ω/m. The nominal wire tension is defined as 50% of the wire elastic limit, +~4 mm.

The drift cells have almost square shapes whose side length is from 5.8/6.7 mm (at the center/endplate in the innermost layer) to 7.5/8.7 mm (in the outermost layer) as shown in Fig. 2.48, and its isochrone on the drift time in the cell is shown in Fig. 2.49. The average drift velocity measured with a test setup and a monitoring chamber is ~ 2 cm/μs, and the drift time is roughly in the range of 0 – 250 ns. The single-hit resolution in the cell is measured to be σ_r ~110 μm in the prototype test [54]. The higher granularity design will increase the number of hits per reconstructed track by a factor of four compared to the MEG experiment.

The wiring process, which includes the monitoring of the wire position, the alignment, the mechanical tension, and the quality of soldering between the PCB and wires, was conducted by a wiring robot [55].

---

*[11] The 10-layer design is illustrated in this figure, but we adopted the 9-layer design and the outermost layer was omitted for the real detector.

*[12] From California Fine Wire (CFW) company [53]

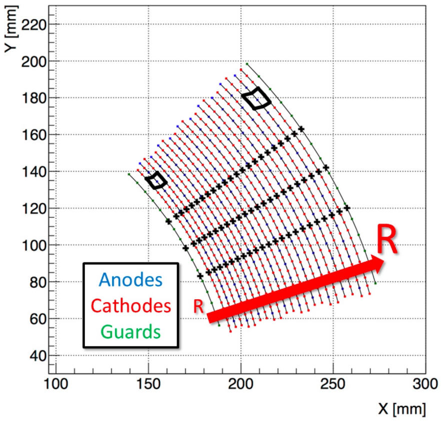

Fig. 2.47: The layer structure in the CDCH [26].

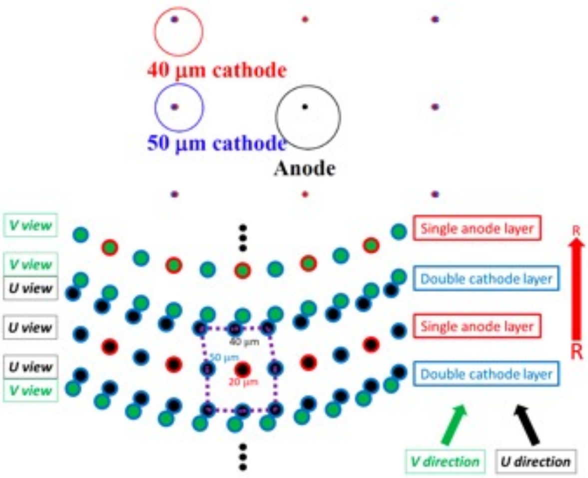

Fig. 2.48: Drift cell configuration of MEG II CDCH. Top: Simplified sketch of a single drift cell (an anode circle and cathode circles are depicted). Bottom: schematic view of the wires in the CDCH [26].

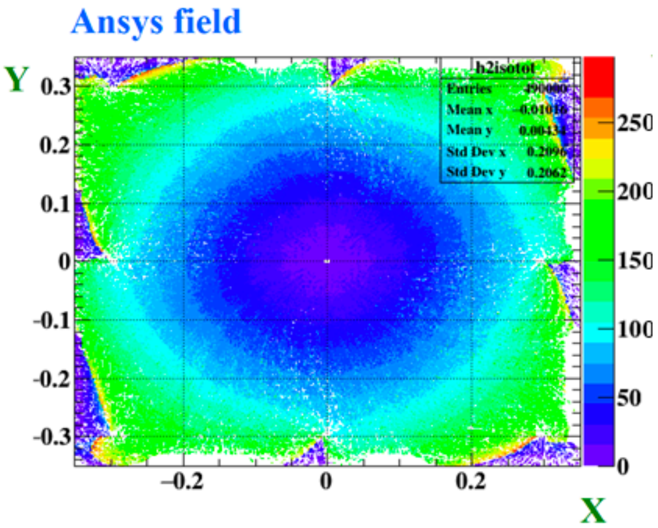

Fig. 2.49: Isochrones for a single 6 × 6 mm^2 drift cell [26]. The vertical color is ns. The drift lines are curved and the isochrone map is distorted by the magnetic field.

Gas

The CDCH uses a helium (He) based gas mixture. A small amount of isobutane (C_4H_{10}) is added as a quencher to avoid self-sustained discharge. The ratio of He:C_4H_{10} is 90:10. The advantage of He-based gas mixture is its large radiation length ($X_0 \sim 1300$ m), which minimizes multiple scatterings of the positrons. The drawback of this gas mixture is the high helium ionization potential of 24.6 eV, resulting in the small number of primary electron pairs, which potentially worsens the spacial resolution.

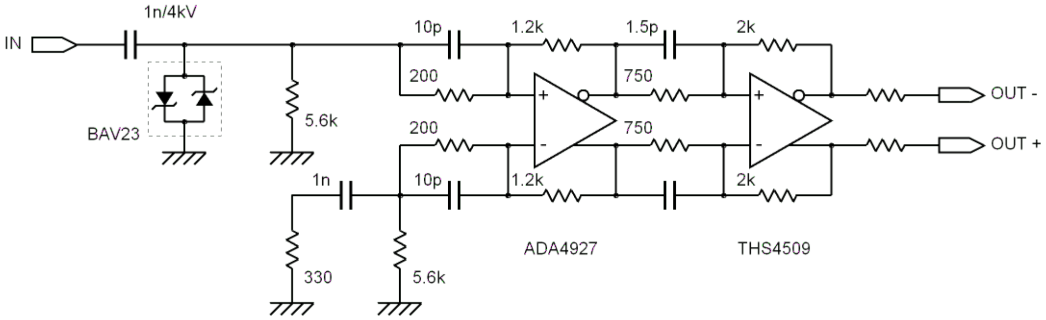

Fig. 2.50: Front-end electronics for CDCH [3].

Electronics

High speed signal processing is necessary for the better separation of single ionization clusters[*13], a better timing measurement at the two ends for z determination, and the cross-fitting waveform analysis algorithm (Sec. 7.1). A high performance 8-channel frontend electronics (FE) was developed for CDCH as shown in Fig. 2.50. The CDCH FE output is differential output (DIFF) to improve the noise immunity. The signal is transmitted to the dedicated WDB (differential readout) through 5m customized twisted-pair cables (Amphenol Spectra Strip SkewClear).

2.4.4 COnstant Bending RAdius (COBRA) Magnet

The COBRA magnet based on a superconducting solenoid was developed in the MEG experiment for the efficient $\mu \to e\gamma$ signal-like positron measurement [27], and is also used for MEG II experiment. The COBRA magnet generates a gradient magnetic field with 1.27 T at the center of the COBRA and 0.49 T at both ends. The layout of the COBRA magnet is shown in Fig. 2.51. The advantages of the COBRA gradient magnetic field compared to the uniform field are illustrated in Fig. 2.52. The positrons with the same momentum have the same projected bending radius (i.e. the dependence on the positron emission angle is small). The positrons with low-longitudinal momentum are swept away quickly and the unnecessary pileup can be avoided. Positrons with lower momentum have the smaller radius and do not reach the CDCH and pTC, which improves the high rate tolerance of the spectrometer.

Hit Rate of Positron Spectrometer with COBRA magnetic field

Due to the gradient magnetic field, the inner layer of the CDCH has a higher rate (1.8 MHz for each cell under the MEG II nominal beam intensity with the simulation) than the outer layers (0.8 MHz). The occupancy of the CDCH, which is the probability to have a hit in a cell in 250 ns, is expected to be 35% (inner layer) - 22% (outer layer), which is 3 - 4 times higher than the MEG experiment. As for the pTC, the rate itself is not so severe; less than 0.1 MHz. However, the same positron sometimes (2-3% from simulation) comes back into the pTC region more than twice. The algorithm for those events was developed and described in Chap. 6.

[*13] One of the largest motivation of this fast electronics is for cluster-counting technique proposed in [56]. This algorithm will further improve the impact parameter resolution, but currently it has not yet been implemented in the MEG II official analysis.

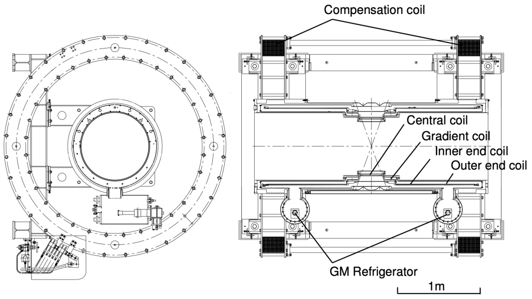

Fig. 2.51: COBRA magnet [27].

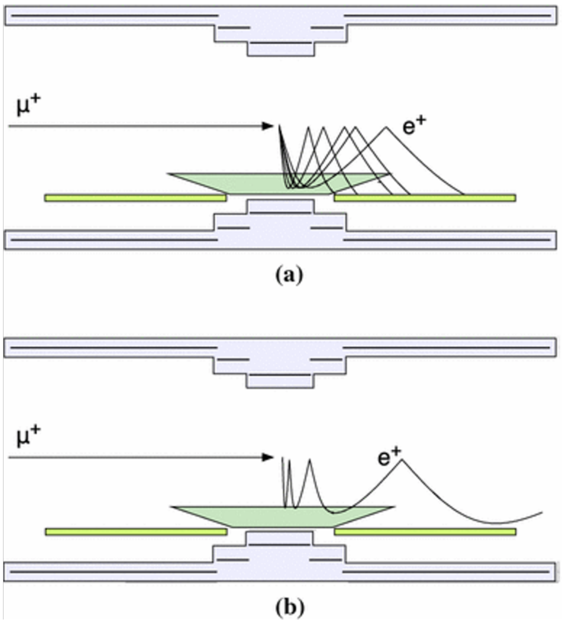

Fig. 2.52: The concept of the COBRA gradient magnetic field [1]. (a) Positrons with the same momentum have the almost same bending radius, even with the different emission angles. (b) Positrons with low longitudinal momentum are quickly swept away.

Chapter 3

Investigation of Radiation Damage for pTC

In the 2015 commissioning, an unexpected rapid current increase of pTC channels (~0.5 μA increase after just two days of irradiation) was observed, which was correlated with the beam irradiation. Fig. 3.1 shows a typical example of the current increase.

From the average current increase under the $7 \times 10^7 \mu$/s beam irradiation at 30 °C with the over-voltage $\sim$18 V, the dark current of each channel, a few μA before the exposure, is estimated to reach $\sim$100 μA after 3-year data taking period. The effects of the radiation damage in the pTC were investigated and mitigation strategies were studied, which are summarized in this chapter. The full details on this topic are published in [31].

3.1 Radiation Damage on Series Connected SiPMs

The degradation of SiPMs due to the radiation damage is a major concern especially for high intensity experiments or long-term experiments. Many studies on the radiation damage on SiPMs are reported as summarized in [57]. Nevertheless, the detailed studies on its effects on the timing resolution of a scintillation counter and impacts to series connected SiPMs have not been reported.

The series connection of multiple SiPMs shows some peculiar features. When n SiPMs with the identical electrical

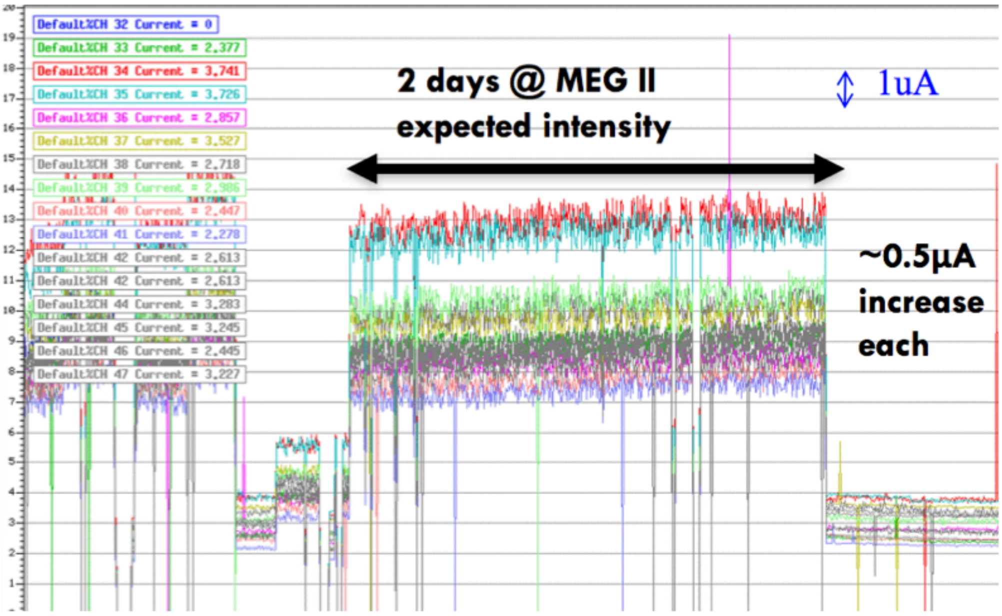

Fig. 3.1: The pTC current of each channel (16 channels are shown with colored lines) in 2015 commissioning.

Table 3.1: Summary of the damage level of the SiPMs.

SiPM	Φ_{eq} [$\mathrm{n_{1MeV}/cm^2}$]	note
#1 - #6	3×10^9	Electron irradiation with ^{90}Sr step by step
#7 - #8	8.7×10^8	Neutron irradiation at LENA
#9 - #10	5.5×10^9	Neutron irradiation at LENA
#11 - #14	0 (or negligible)	Re-used from broken pTC counters

properties (breakdown voltage, dark current etc.) are connected in series, the total capacitance and the effective charge gain become $\frac{1}{n}$, while the effective breakdown voltage, which is the voltage needed to apply the breakdown voltage to each SiPM, becomes n times higher. A common current flows through all the SiPMs connected in series, which results in different bias voltages for the individual SiPMs when the electrical properties of each SiPM are not identical.

3.2 Total Fluence

The estimated total fluence during the MEG II DAQ full period (20 weeks × 3 years) is $\sim 8\times10^{10}\mathrm{e^+/cm^2}$ at the high-rate region (~100 kHz) and this is equivalent to $\Phi_{eq} \approx 4\times10^9\mathrm{n_{1MeV}/cm^2}$ with the assumption of the effective Non Ionizing Energy Loss (NIEL) theory[*1] [59].

3.3 Irradiation on SiPMs

The main goal of the lab tests is:

- Study the radiation damage effect on series connected SiPMs.
- Evaluate the performance degradation after the 3-year data taking.
- Establish the strategy to mitigate the deterioration.

3.3.1 SiPM Irradiation

SiPMs from AdvanSiD (ASD-NUV3S-P High-Gain (MEG), type-I) were used for the evaluation. The SiPMs were irradiated at the different several dmage levels as summarized in Table 3.1. Six SiPMs (#1-#6) were irradiated with intense electrons from 37 MBq ^{90}Sr sources for 280 hours in total, which is equivalent to $\Phi_{\mathrm{eq}} \approx 3\times10^9\mathrm{n_{1MeV}/cm^2}$. The irradiation was separated into four steps, each 70 hours long, and no bias voltage was applied to the SiPMs during the irradiation.

The impact to the series connected SiPMs was evaluated with the different set of SiPMs irradiated with electrons and neutrons. The details of SiPM patterns and characteristics are summarized in Appendix B[*2]. Some characteristic phenomena by the series connection of differently damaged SiPMs were observed, and the dominant effect was the current increase, which is described in this chapter. Another effect by the hit position dependence is discussed in Sec. 6.5.6. In the appendix, the irradiation test of ASD-NUV3S-P model (type-II) at the Beam Test Facility (BTF) is also summarized.

[*1] Φ_{eq} is used for the comparison between the lab test in the following sections. Here the bulk damage, which is the silicon lattice defects and causes the dark current increase, was focused. The impact of the surface damage, which generates the charges in dielectric parts of SiPMs, was not focused since the pTC absorbed dose of ~ 20 Gy is small enough to be neglected by taking the result of Ref. [58] into account.

[*2] The combination of 6 SiPMs are classified into four groups: Pattern-A - Pattern-D in this appendix. In this section, all of the SiPMs were irradiated with electrons equally and this combination corresponds to “Pattern-D”.

3.4 Effect on pTC Performance by Dark Current Increase

The effect of the dark current increase by the radiation damage was evaluated with SiPMs which were irradiated with electrons step by step.

3.4.1 IV Curves for Each Damage Level

Figures 3.2a–e show the dark current I_{dark} versus bias voltage V_{bias} (I-V curves) of each of the six electron-irradiated SiPMs (taken at 0.1 V steps), and Fig. 3.2f shows the breakdown voltages of SiPMs at each irradiation step. The breakdown voltage V_{br} is calculated from the maximum point in the second-derivative of the logarithm of I_{dark} with three-point smoothing [60] and the systematic uncertainties are estimated from the change by different-point smoothings. The significant dark current increase was observed after each irradiation step, but no significant changes of the breakdown voltage and the IV-curve shape were observed. Figs. 3.2g–h show the I-V curves when they are connected in series. When SiPMs were cooled from 30°C to 10°C, the dark current increase by irradiation was mitigated.

3.4.2 Timing Measurement Setup

The deterioration of the timing resolution was evaluated using a test scintillation counter. Fig. 3.3 shows the test setup for the timing measurement. A scintillator and 6 SiPMs connected in series are aligned with a special jig made by a 3D printer. The electrical contacts with the SiPMs are made using spring probe pins so that the series circuit can be made each time without soldering. The electrons from a 3.7 MBq ^{90}Sr source are injected to the center of the test counter. The trigger signal is made by a small scintillation counter (a $5 \times 5 \times 5\mathrm{mm}^3$ scintillator (BC422) readout by a SiPM (Hamamatsu Photonics S10362-33-050C)), whose timing resolution is much better ($\sigma_t \sim 30$ ps) than that of a single counter with one-side readout ($\sigma_t \sim 100$ ps). The output signals were amplified and shaped through a two-staged voltage amplifier with a pole-zero cancellation (PZC) filter. The schematics of the amplifier is shown in Fig. 3.4. The signal waveforms were recorded using the DRS4 chip at 1.6 GSPS. The temperature of the MEG II pTC is controlled by the chiller systems. The test counter is put inside a thermal chamber and the measurements were performed at 30°C and 10°C, which correspond to the temperature in the experimental area and the temperature achieved with the chiller system, respectively. For the timing pick up, the digital constant fraction method (CFD) was applied to the waveforms. The timing when the waveform reaches a certain fraction (CFD fraction) of the peak point is extracted.

3.4.3 Deterioration of Time Resolution

Fig. 3.5 shows the example of the waveforms after each irradiation step. Clear increase of the baseline fluctuation by the dark noise was seen, but as for the signal height no significant change was observed (0.15 - 0.16 V from the most-probable value of its Landau-like distribution). Fig. 3.6 shows the results of bias voltage scan at each electron irradiation step. As explained above, the measurement was performed at 30°C and 10°C. The data were analyzed with a fixed CFD fraction of 20%. The resolution first improves with V_{bias} due to a higher gain and PDE, but at some voltage starts to deteriorate due to increased dark counts. As the fluence increases, the optimal voltage, where σ_t reaches the minimum, shifts to lower voltages.

Fig. 3.7 shows the timing resolution at three applied voltages around the optimal resolutions in the bias scan. The CFD fraction is optimized in steps of 10% from 10% to 60% for each dataset. As SiPMs are irradiated with more electrons and the dark current (I_{dark}) increases, the measured timing resolution (σ_t) becomes worse. The deterioration of the timing resolution is due to an increase of the baseline fluctuation caused by the dark noise: an increase of N_{RMS}. The correlation

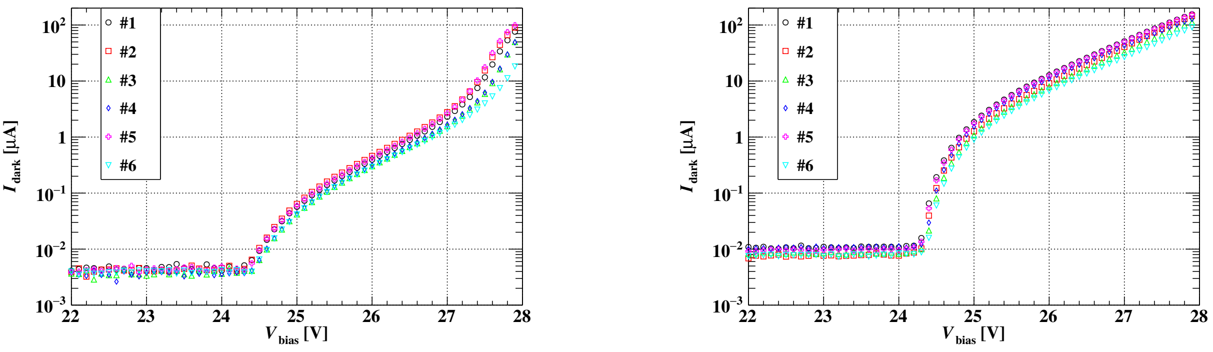

(a) Before irradiation.

(b) After 70 hours irradiation.

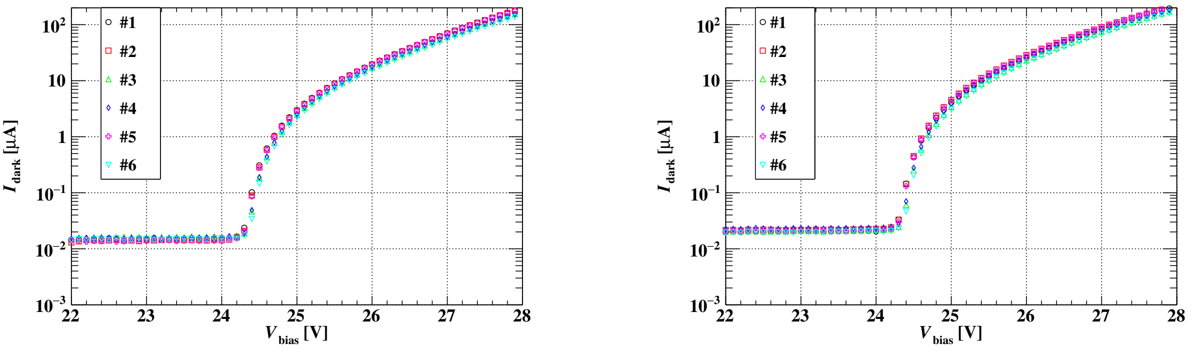

(c) After 140 hours irradiation.

(d) After 210 hours irradiation.

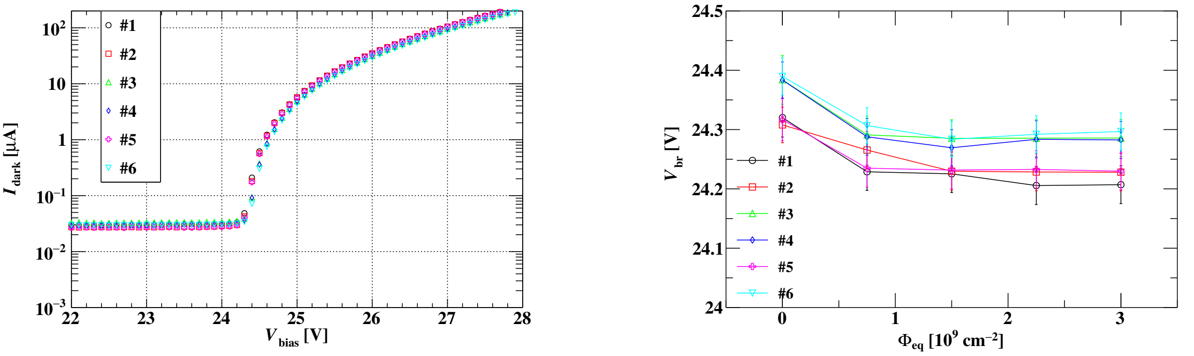

(e) After 280 hours irradiation.

(f) Breakdown voltages of single SiPMs versus fluence.

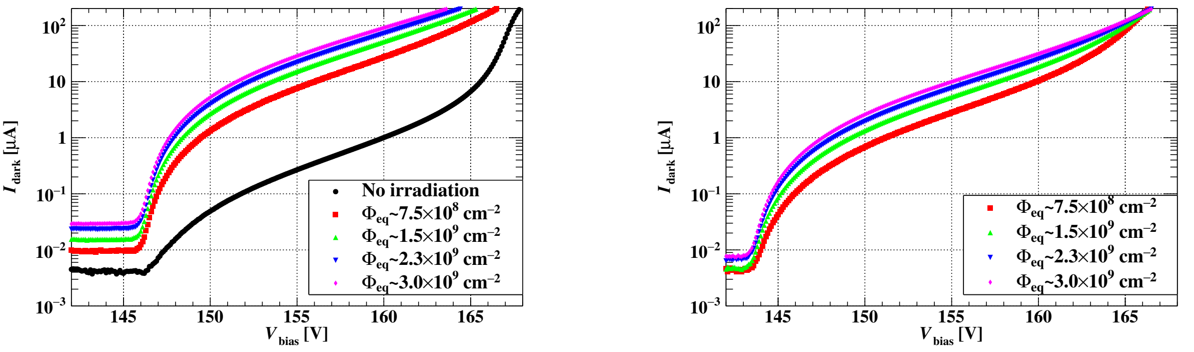

(g) Six series-connected SiPMs at each irradiation step at 30°C.

(h) Six series-connected SiPMs at each irradiation step at 10°C.

Fig. 3.2: The I-V curves of the six electron-irradiated SiPMs. The I-V data of each SiPM were taken at 30°C (a–e), and the breakdown voltages are plotted in (f). The I-V data of six series-connected SiPMs were taken at 30°C (g) and 10°C (h).

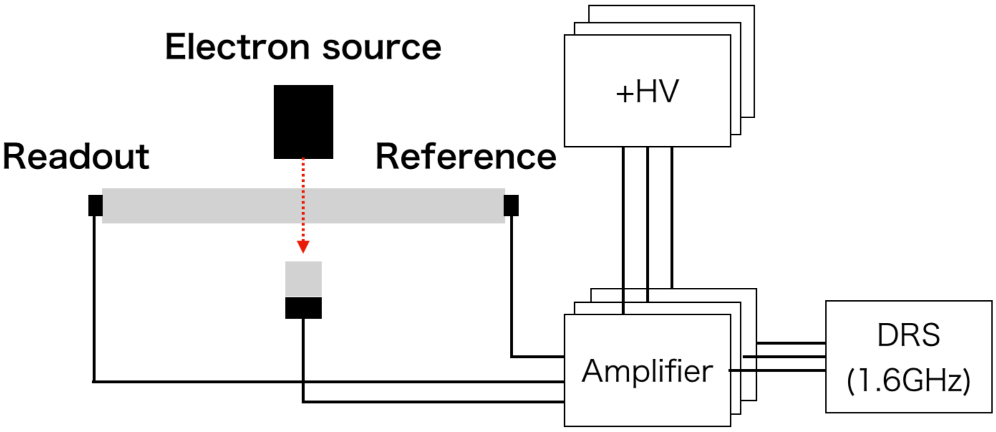

Fig. 3.3: The timing resolution measurement setup for the radiation tolerance test.

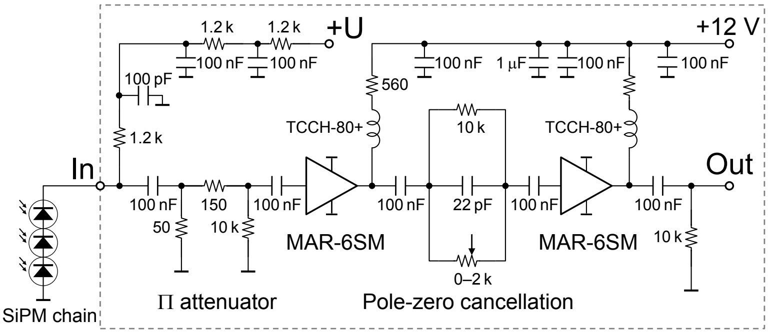

Fig. 3.4: The schematics of the amplifier [23]. The pole-zero cancellation filter can be applied by tuning the adjustable resistor in the circuit.

between I_{dark} and N_{RMS}, and that between N_{RMS} and σ_t are also shown in Fig. 3.8 and Fig. 3.9.

The measurement with $V_{\mathrm{over}} \approx 16$ V after the full irradiation (the marker with the largest I_{dark} in the same V_{over} in Fig. 3.7) for 3-year data taking with a typical hit rate region (~ 80 kHz) shows the expected deterioration of the pTC counters[*3] from the no-damaged measurement is 41% at 30 °C. The deterioration can be suppressed to 13% at 10°C. When 50 ps timing resolution of gamma-ray measurement and 35 ps timing resolution of positron measurement are assumed, the 41% deterioration of the positron timing measurement at 30°C will worsen $t_{e\gamma}$ from 61 ps to 70 ps, while at 10°C to 64 ps. In conclusion, operating the pTC at 10°C with the chiller system can be a reasonable solution to recover the timing resolution.

3.4.4 Cooling System for pTC

In the 2017 commissioning, the temperature control (cooling) system with chiller for pTC was installed and tested. The temperature and humidity were monitored by the sensors on the pTC backplanes as shown in Fig. 2.43. The goal of the operation temperature was 10°C. Since the water condensation was a crucial problem at the low temperature in 2017, the

---

[*3] Note that the double-side readout is adopted for the pTC counters, and the absolute resolution becomes $\sqrt{2}$ times better than the values in the figures.

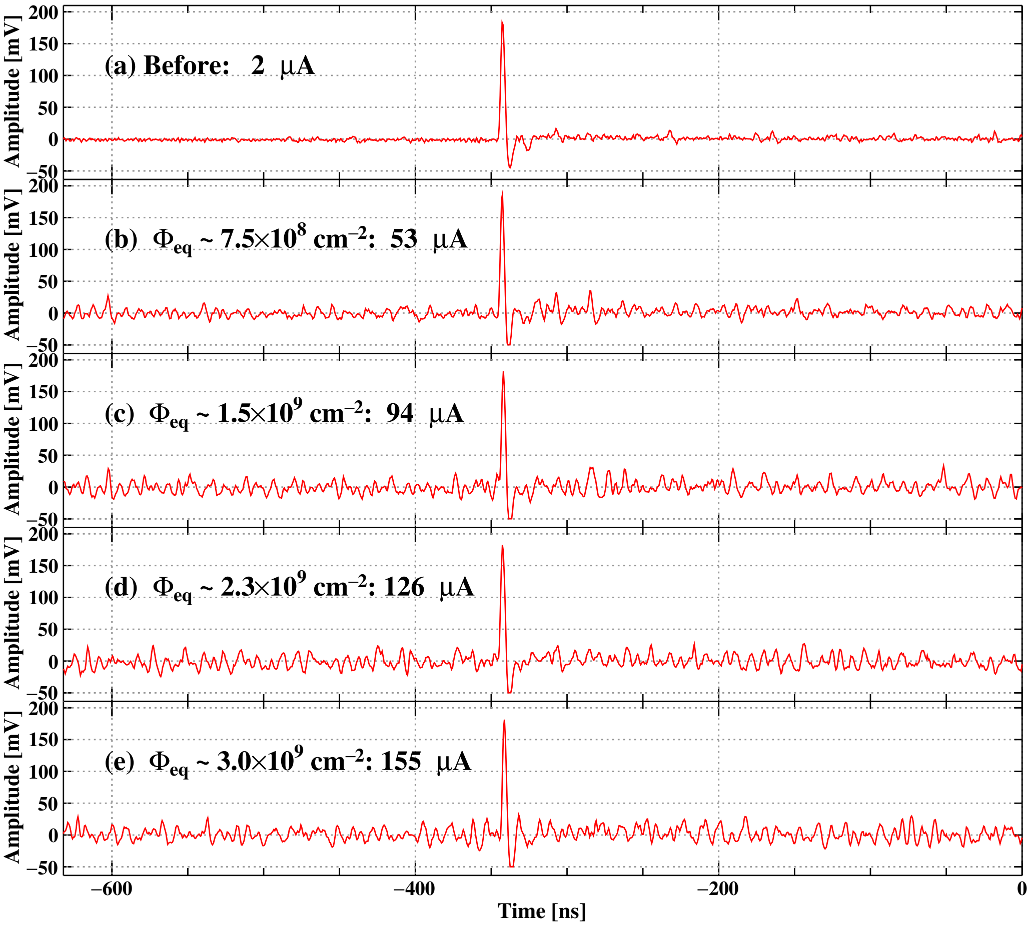

Fig. 3.5: The example of the waveform at each damage level.

operation temperature was 20°C in the 2017 commissioning.

In 2018, a flowing system of cooled dry air with a heat exchanger and a chiller was prepared and tested. The temperature was stable enough and the humidity became a safe level[*4]. The whole system in the experimental area is shown in Fig. 3.10. In 2019, the arrangement of air lines and water lines was improved, and the heat insulating materials were added for efficient cooling and to avoid water condensation around the pipes. Fig. 3.11 shows the insulated pipes and the flows of water and dry air.

Fig. 3.12 shows the monitored temperature and humidity on pTC in 2018 at 10°C setting. The humidity was in the safe level (∼ 50%) and the temperature was very stable around 10°C.

[*4] During the commissioning we set the safety threshold of the humidity for 70%.

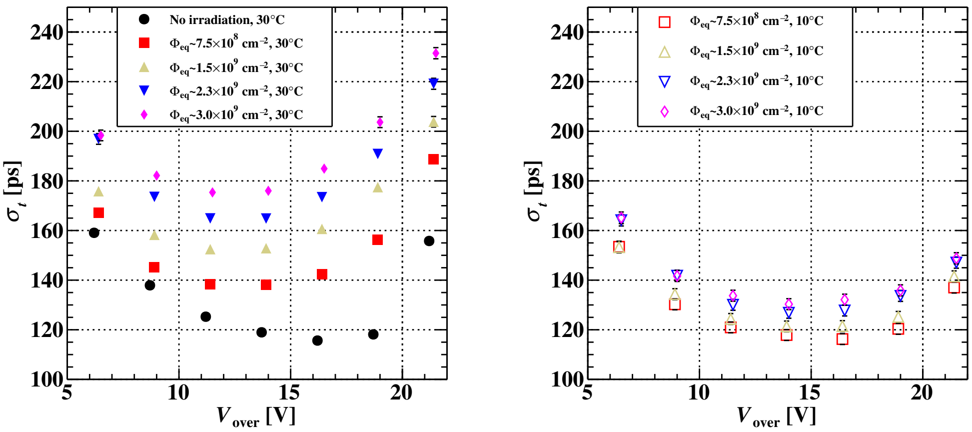

Fig. 3.6: Timing resolution versus over-voltage at 30°C (left) and 10°C (right). The CFD fraction is 20%.

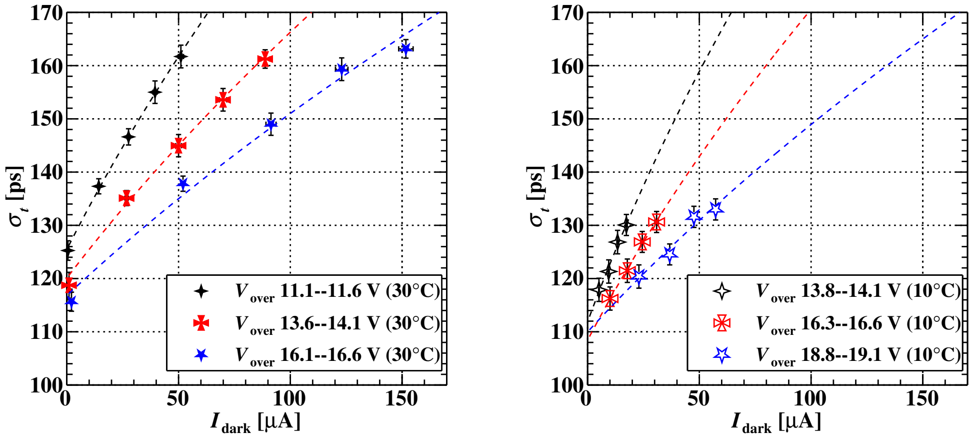

Fig. 3.7: The timing resolution with the different damage level at the fixed 3 applied voltage (157.5, 160 and 162.5 V). The dashed curves $\sigma_t = \sqrt{\beta I_{\mathrm{dark}} + \sigma_0^2}$ are fitted to the data.

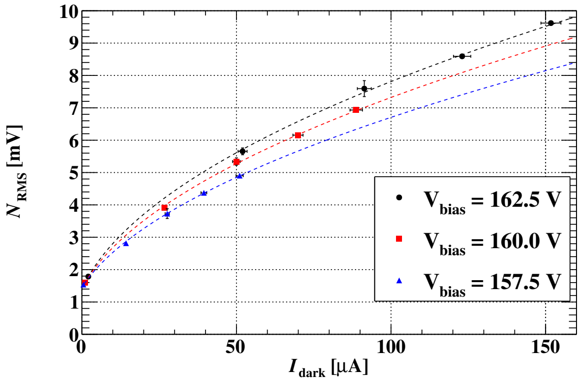

Fig. 3.8: Relation between the dark current and the RMS noise at 30°C for three applied voltages. The dashed curves $N_{\mathrm{RMS}} = \sqrt{\alpha I_{\mathrm{dark}} + N_0^2}$ are fitted to the data.

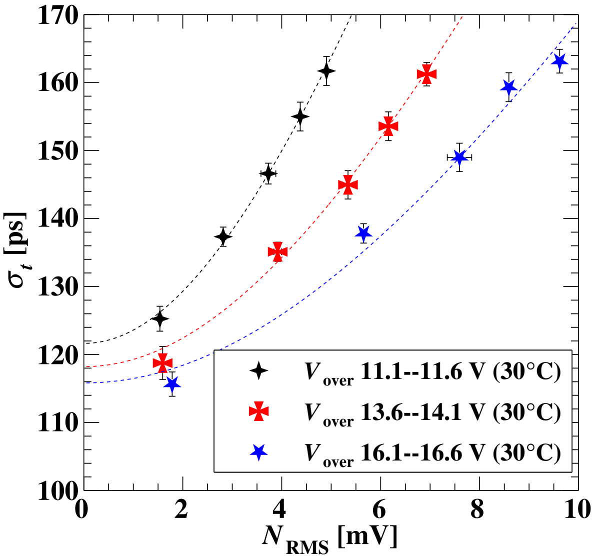

Fig. 3.9: Relation between the RMS noise and the timing resolution at 30°C for three applied voltages. The dashed curves are $\sigma_t = \sqrt{\gamma N_{\text{RMS}}^2 + \sigma_0^2}$ fitted to the data.

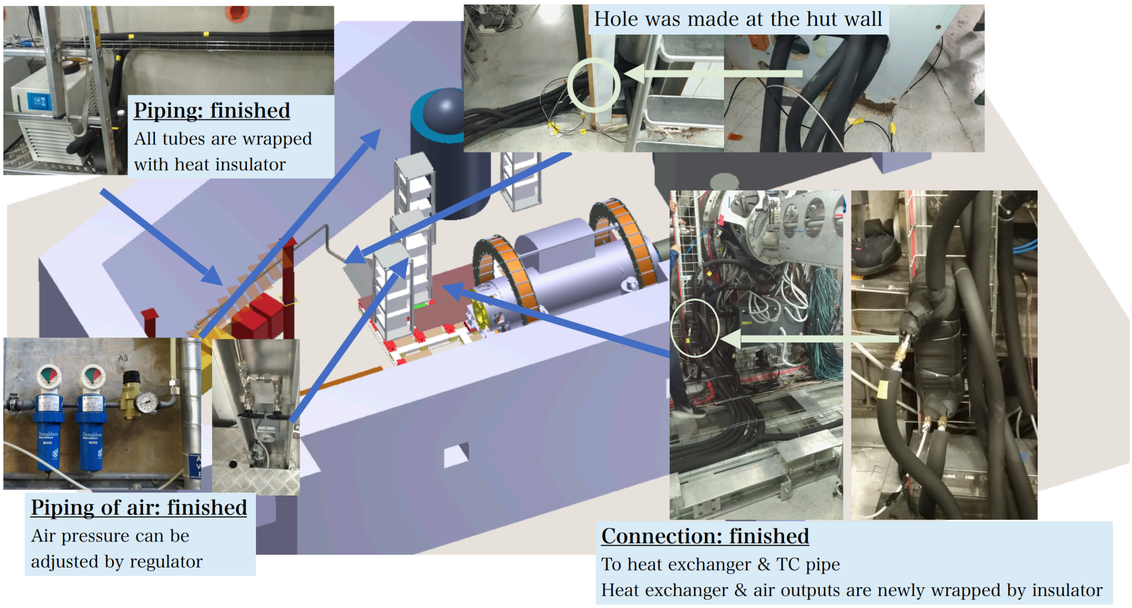
Piping: finished
All tubes are wrapped with heat insulator

Hole was made at the hut wall

Piping of air: finished
Air pressure can be adjusted by regulator

Connection: finished
To heat exchanger & TC pipe
Heat exchanger & air outputs are newly wrapped by insulator

Fig. 3.10: The system for pTC cooling. The pictures for a chiller, water pipes, a heat exchanger, air lines are also shown.

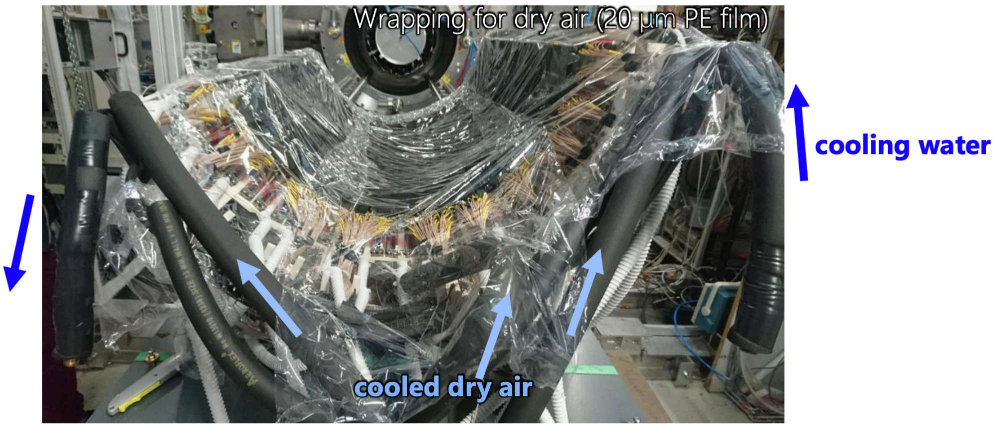

Fig. 3.11: The picture of pTC for the low temperature operation.

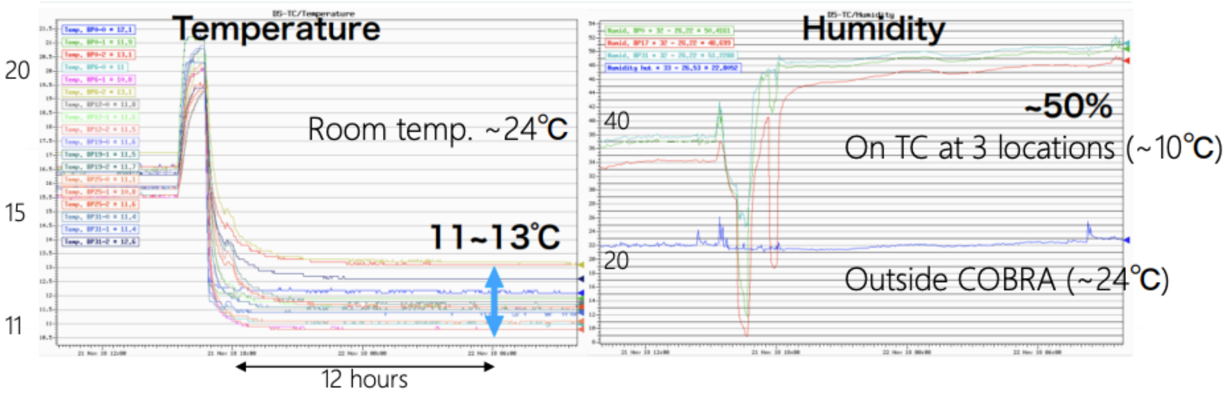

Fig. 3.12: The temperature and humidity measured on the pTC sensors.

Chapter 4

Commissioning Runs from 2017 to 2019

In this chapter, the commissioning of the positron spectrometer performed between 2017 and 2019 is summarized.

4.1 Commissioning Overview

Main topics in each year are summarized below:

- 2017: Test of the full pTC counters, performance evaluation with muon beam.
- 2018: First operation of the CDCH, preparation of the cooling system for pTC (stable 15°C operation).
- 2019: CDCH stability studies, stable 10°C operation of the pTC.

4.2 Status of Detectors

In 2017, the construction of the pTC counters was completed and the assembled detectors were installed in the experimental area to be tested with beam. The mock-up CDCH was also installed, which was made of the same materials as the real detector, 2 mm thick carbon fiber for the outer frame, 20 μm thick Mylar film for the inner frame, and one sector of the anode wires and related electronics. The same gas mixture was used during 2017 commissioning. 2017 was the only year in which both pTC (US / DS) were installed. However, up to 256 counters were readout at the same time due to the limited number of the readout electronics. In 2017, the pTC was operated at 20°C and in 2018 and 2019, it was operated at 10°C.

The CDCH was delivered to PSI[*1] and installed in 2018. In 2019, the design of the readout electronics for the CDCH was fixed and small number of the final version WDB was installed. However, due to the instabilities of the CDCH, data taking with the muon beam was not achieved. Instead, the data taking with cosmic rays was performed to obtain the waveform data. The number of the readout channels for each detector during the commissioning 2017 – 2019 is summarized in Table 4.1.

4.3 DAQ for Positron Spectrometer

In this section, the DAQ status of the positron spectrometer is summarized.

4.3.1 Readout Channels

The readout channels assigned for pTC and CDCH in each year are summarized in this subsection.

[*1] Considering the whole schedule of MEG II experiment, the wiring of the most outer layer (10-th layer) was omitted so that the construction can be completed by the beam time in 2018. The effect of losing one layer was an efficiency loss by roughly 10%, but this loss was found to be recovered by the analysis refinement and optimization.

Table 4.1: The number of the maximum readout channels for pTC and CDCH each year.

Year	pTC DAQ channels (counters)	CDCH cells
2017	512 (256)	N/A (mock-up CDCH)
2018	256 (128)	96 (prototype WDB)
2019 Oct	256 (128)	96 (prototype WDB)
2019 Nov	256 (128)	96 (prototype WDB) + 96 (final version WDB)

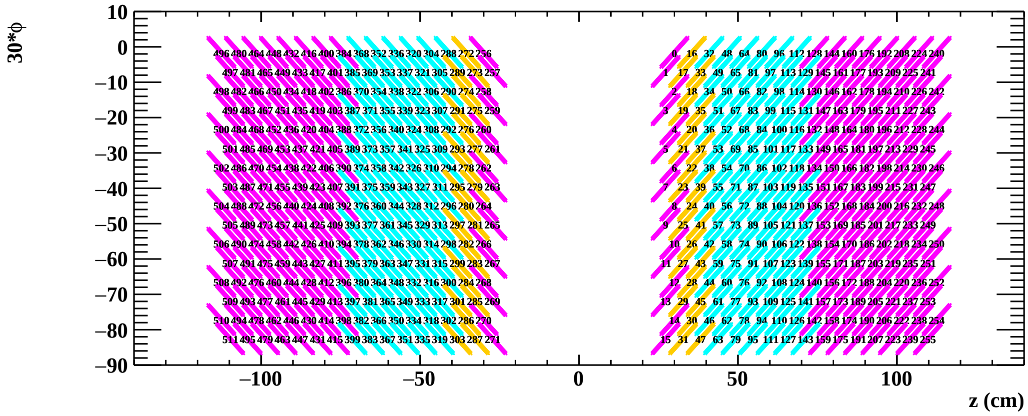

Fig. 4.1: The pTC counter map with identification number (0-511). In 2017, all of the counters (512) were tested, in 2018 and 2019 128 counters were tested (# 128 - 255 in 2018 and # 304 - 431 in 2019). The colors of the counters show the counter types (inner magenta: 4cm-L, yellow: 4cm-Mix, light blue: 5 cm-Flat, outer magenta: 4cm-Flat).

pTC Readout

In 2017, 512 WDB channels (for 256 counters) were assigned to the pTC, so the pTCs in the US and DS were tested separately. In 2018 and 2019, 256 WDB channels were assigned at the maximum, so the half of DS counters (# 128 - 255 in Fig. 4.1) in 2018 and the half of US counters (# 304 - 431 in Fig. 4.1) in 2019 were read for the data taking for the positron spectrometer. Fig. 4.1 shows the geometry net of pTC counters with the counter-identification number (# 0-255 for DS counters and # 256-511 for US counters).

In 2018 the readout counters of the pTC were selected based on z-position dependence on the CDCH hit rate. However, the reduction of gain at large z of CDCH was observed and the good positron tracks were less observed. In 2019, the central part of the upstream pTC counters were selected to maximize the number of the good positron tracks with the pTC readout and the CDCH hits in the smaller z region. Considering the test of pTC sub-systems (laser, cooling and installation materials), the US pTC was installed in 2019 since the test of the sub-system for DS pTC was performed in 2018.

pTC Operation Voltage and Temperature

The operation voltage of the pTC counters was tuned to be +$\sim$16 – 19 V from the breakdown voltage (equivalent to $\sim 4\mu$A dark current) for counters with type-I SiPMs, which gave the best timing resolution on average in the lab test. The counters with type-II SiPMs had the wider operation range than the type-I SiPM counters, and the operation range was tuned to be $\sim$22 – 23 V based on the results of the lab test. Since the cooling equipment (especially monitoring and humidity control system) was not sufficient in 2017, the operation temperature was controlled to be 20°C.

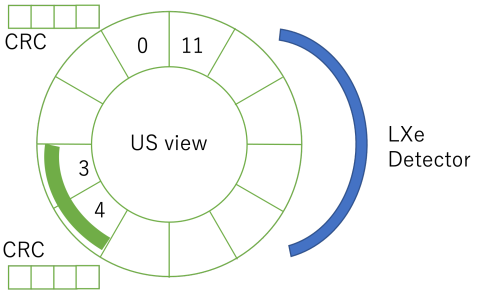

Fig. 4.2: The CDCH readout in 2018 commissioning [26]. Data acquisition was conducted with the readout in S3 (L1-3) and S4 (L1-3).

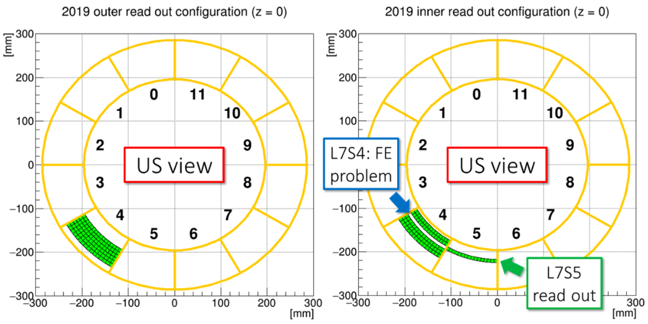

Fig. 4.3: The CDCH readout in 2019 commissioning [26]. Data acquisition was conducted mainly with the readout in S4 (L1 - 6).

In 2018, the cooling system was prepared and tested. The sensors for temperature and humidity were attached and monitoring system was prepared in the experimental area. However, it was soon found that the simple wrapping with 20μm PE film was not sufficient for the sealing, and the air flow was too weak to keep the safe humidity at 10°C. In addition, the water condensation around the water pipe was found during operation. The safe temperature for the pTC was 15°C in 2018.

In 2019, the flow rate of the dry air was increased by replacing the air tubes for the pTC and air pressures. The water pipes were wrapped with the thermal insulation tubes and tapes. The wrapping of the pTC with the PE film was also added to increase the airtightness. The pTC was operated at 10°C stably during the commissioning period.

CDCH Readout

The fraction of the CDCH readout channels was ~6% (96 wires) in 2018 and in the first period of 2019, and ~12% (192 wires) in the second period of 2019. The CDCH layer number was defined as L1 – L9 from the outer to the inner layer. The CDCH readout channels were divided into 12 sectors by every 16 channels. The sector number, S0 – S11, was defined counter-clockwise from the US-side view. The assigned readout cells for the 2018 and the 2019 commissioning (first half) are shown in Fig. 4.2 and Fig. 4.3. The additional 96 channels were assigned to S5, from L3 to L8.

In the first half of 2019, two configurations were prepared for the CDCH data taking. One is called outer-conf, which covers L1 – L6 in S4, and the other is inner-conf, which covers L4 – L6 and L8 – L9 in S4 and L7 in S5 (due to the FE issue). In the second half of 2019, the final version of WaveDREAM with the differential input[*2] from the CDCH readout, was finally installed and the readout channel increased from 96 to 96 (prototype) + 96 (final type). The additional 96 channels were assigned to S5, from L3 to L8 with the outer-conf channels. In this thesis, the outer-conf was used for the analysis of the cosmic-ray data. However, when the muon beam run was started, unexpected high current was observed in many channels. The detector commissioning in 2019 was, therefore, finished without the enough muon beam data taking. After the commissioning the detailed investigation for this abnormal current was conducted and the discharge problem was found.

[*2] To use the prototype WDB (with single-end input), we had to convert the differential (DIFF) output from the CDCH to the single-end (SE) input for the WDB. The DIFF-to-SE intermediate convertor was prepared and used in 2018 and 2019.

CDCH Operation Voltage

The nominal HV value set for 2018 run with a gas mixture He : iC_4H_{10} = 90 : 10 were 800V on outer guards, 1480V on L1 – L3, and 920V on L4 used as a guard layer[*3]. The applied voltage was scanned in the range of 1460 – 1540 V for the study of the gas gain and the stability check with several beam intensities (e.g. 6×10^6, 1.34×10^7, 3×10^7, and 7×10^7). The test with lighter gas mixture (He : iC_4H_{10} = 93 : 7) was also performed for the study of the gas gain [26].

After the 2018 commissioning, the extra wire stretching was performed to increase the cell stabilities. The nominal HV setting in 2019 was 1480 – 1400 V in L1 – L9 every 10V step, i.e. 1480V for L1, 1470V for L2, ..., 1400V for L9, and guard wires were 700V with a gas mixture He : iC_4H_{10} = 90 : 10.

4.3.2 Triggers for Positron Spectrometer

Trigger Muon Beam

The single-counter trigger is mainly used for the DAQ of the positron spectrometer, i.e. if there are hits in the pTC counters the waveform information from the DRS chips are recorded. Trigger rate was limited by the prototype data transfer system (around 3 – 5 Hz in 2017 and 5 – 6 Hz in 2018 - 2019 under the MEG II nominal intensity) , which will be improved to be 10 Hz in the future commissioning.

Trigger Cosmic Ray

The cosmic-ray counters (CRC), each of which is composed of a scintillation bar ($4.0 \times 4.0 \times 79.6\text{cm}^3$, Saint-Gobain BC404[*4]) and two photo-multipliers (R5934 HAMAMATSU) at both ends. These components were reused from the MEG timing counter. The cosmic ray tracks passing through the CDCH in the z-range of -40 cm – 40cm are triggered.

Other Triggers

In addition to the above triggers, a pedestal trigger, which is used for the study of the noise in the waveform baseline, and a laser trigger, which is used with the synchronization pulse from the laser controller for the laser-based calibration of the pTC (explained later), were used.

Synchronization between WDB

As described in Sec. 2.3.6, a main clock signal is distributed to each WDB from the ancillary board, and the PLL manages the synchronization with the accuracy of ~10 ps[*5]. Then the synchronization is refined in the offline analysis by using the sine waveforms from the PLL chips, resulting in 20 ps accuracy at 2 GSPS. The specific correction for the online synchronization in 2018 – 2019 is summarized in Appendix C.

4.3.3 Muon Beam Rate

The data taking under the muon beam was conducted in the πE5 beamline at PSI. The muon beam rate was measured at the center of COBRA for different beam-line configurations using a dedicated set-up at the beginning of each year of beam time and tuned by adjusting the beam slits. The muon stopping rate was calculated with the stopping efficiency in the MEG II target of 85% evaluated with a MC study. The beam rate was lower than expected in 2017 due to the removal of a target

---

[*3] For CDCH operation, the HV working point for the gas gain 5×10^5 with He : iC_4H_{10} = 90 : 10 is expected as the nominal setting. The typical HV values are around 1450 V with the +3.8 mm tension in 2018 as shown in [26], so the detailed analysis in the following chapter uses the data with the applied voltage of 1460 V.

[*4] https://www.crystals.saint-gobain.com/sites/imdf.crystals.com/files/documents/bc400-404-408-412-416-data-sheet.pdf

[*5] The actual accuracy of the online synchronization is limited by the jitter in the DRS chips and it will be ~60 ps.

in another line and a lower proton current (~1380 - 1500μA, while 2200μA was nominal assumption). To recover this effect the muon beam was tuned to be 30% higher than the nominal setting, resulting in $5.6 - 6.1 \times 10^7$ μ/s. On the other hand, the rate was higher in 2019 due to a problem with the beam blocker during the measurement, resulting in 10 - 20% higher rate than 2018.

4.3.4 Data Size

In 2017, the pTC data was accumulated about 10 days with MEG II nominal intensity. The accumulated data was about 2,000,000 events (~900,000 events for upstream and ~1,300,000 events for downstream), which were used for the analysis in the following chapter.

In 2018, the CDCH had many kinds of request related on the studies for the detector operation (current stability, gas gain study, and so on). So the beam condition (beam instensity, cosmic rays, or pedestal) and the CDCH settings (HV scan, gas type) were changed many times. The accumulated data for each settings were not so large, (O(1000) events – O(100,000) events) but sufficient to see the waveforms and S/N situation at each settings.

In 2019, the pTC and the CDCH data taking was performed about ~20 days. In this period, the muon beam was changed several times to study the gas gain, the stability of the detector, and so on. Due to the several instabilities, large noises, and readout problems, sufficient data acquisition with the 2019 muon data was not completed, and the most of the period was used to investigate the detector stabilities. The cosmic ray data was accumulated in the latter half of the period and analyzed to understand the noise situation of the CDCH with the final version electronics.

Chapter 5

Overview of Positron Analysis Flow

In this chapter, the overview of the positron analysis flow in the MEG II experiment is described.

5.1 Data Flow

The MEG II analysis framework with experimental data or MC samples is summarized in Fig. 5.1. The online DAQ system is based on Maximum Integrated Data Acquisition System (MIDAS) developed at PSI and TRIUMF [61]. Through the MIDAS system the experimental apparatus is operated and the experimental information is stored in a compressed data format. The offline software for MEG II is based on ROOT-based Object oriented MIDAS Extension (ROME) [62], which is developed in the MEG experiment and designed as a general purpose software for the experiment with the MIDAS system. The key concept of ROME is to generate most of the codes of a project except the algorithm part. The experimental framework is written in XML definition files compactly, and then ROME generates the specific class and framework out of it.

For the analysis of experimental data, the first step is the waveform analysis. Especially, noise reduction and clock synchronization are performed to the experimental data (.mid.gz file in the figure) and .root files (called raw files) are generated. This analysis part is separated from the other analysis chain since this part is applied to all the detectors and

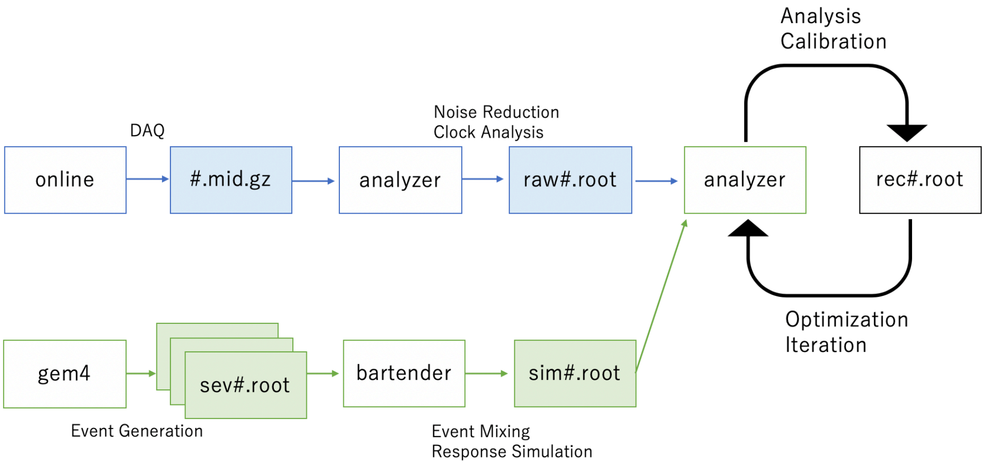

Fig. 5.1: The overview of the MEG II analysis framework.

not iterated so many times[*1]. By using the information from the raw file, reconstruction algorithms are applied and the necessary variables are extracted and stored in a .root file (called rec files).

For the analysis of simulation data, processes for event generation and event mixing are placed before the analysis of raw file.

5.2 Event Generation

The event generation framework is summarized in the following subsections.

5.2.1 Simulation of Interactions

For the event generation and the simulation of the physics interactions with the detector materials, the software called gem4 is used. Gem4 is based on the GEANT4 [63] (version 4.10 [64]), which is a toolkit for the simulation of particle interaction in matters written in C++. GEANT4 offers comprehensive physics processes, for example electromagnetic, hadronic, and optical processes over a wide energy range and with different kinds of materials and elements.

Gem4 simulates kinematics of muon decay events (Michel, RMD, and $\mu^+ \to \mathrm{e}^+\gamma$) and interactions between the detector materials and particles from those decays. The information of positrons, for example, the trajectory, momentum, timing, particle type, is recorded and used to evaluate the performance of the algorithms. This information is often called MC-truth or truth compared with the reconstructed information, and stored in the sev file (sub-events file).

5.2.2 Simulation of Detector Response

To simulate the detector response in a high rate environment, the $\mu^+ \to \mathrm{e}^+\gamma$ signal decays and Michel decays are generated separately with gem4, and then the Michel events are mixed into the $\mu^+ \to \mathrm{e}^+\gamma$ events at the equivalent rate of 7×10^7 Hz. The triggered-timing region in the waveform is defined by the signal decay and the background Michel positrons are randomly distributed over the time according to Poisson distribution, i.e. simulated signal waveform with background Michel positrons is counted as an “event”. The merged information file is called sim file, which contains the MC truth (kinematics at the vertex, incident point to the detectors, incident timing, positron sources - signal or Michel decay, and so on) for all of the positrons in events. The ionization process and its space-time relation in a CDCH cell is simulated with Garfield++[*2]. The response of the electronics is simulated with the SPICE software [65] and convoluted in the signal waveform. The noises are added at the end of the waveform generation. Currently, the white noise with 2 mV as mean amplitude, which was observed in the commissioning 2018, is added to the CDCH waveform simulation. As for the pTC noise simulation, the parameters of the dark count rate, the probabilities of the secondary noises (cross talk, after pulse, delayed cross talk), the recovery time of the SiPM were measured and implemented. The details of the measurement and the parameters are reported in my master thesis [28]. The simulated waveform data are stored in the raw file in a same format as the real data.

5.3 Positron Reconstruction Chain

Fig. 5.2 shows the overview of the positron reconstruction chain, which consists of pTC analysis, CDCH analysis, and pTC-CDCH combined analysis. The goal of the pTC analysis is to obtain the positron crossing timing, and that of the

---

[*1] In addition to the time saving, this process can be used for the physics analysis such as blind analysis. MEG II adopts the blind analysis and the collaborators must not access the MIDAS files.

[*2] Garfield/Garfield++ is developed at CERN for the detailed detector simulation based on ionization measurement in gases and semiconductors, `https://garfield.web.cern.ch/help/` (Garfield) and `https://garfieldpp.web.cern.ch/garfieldpp/` for Garfield++.

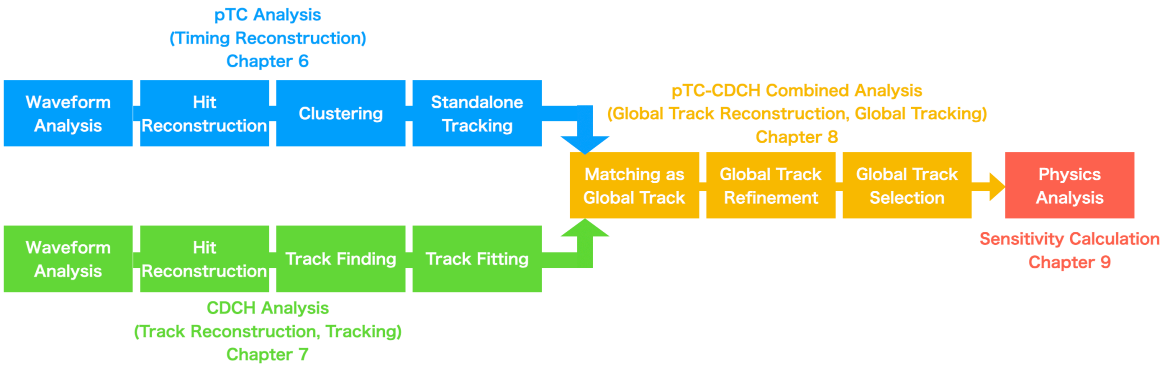

Fig. 5.2: The overview of the MEG II positron reconstruction algorithms.

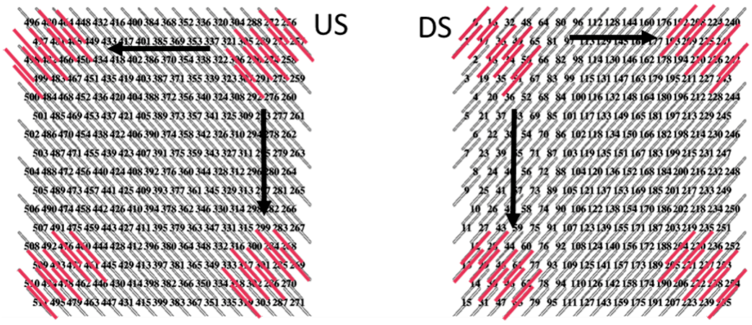

Fig. 5.3: The fixed combinations of counters used in [7] for the evaluation of the pTC resolution.

CDCH analysis is to obtain the "state" (i.e. best estimate of positron's kinematic parameters and those covariance) vector at the target. The pTC-CDCH combined analysis reconstructs "global tracks" from the pTC tracks and CDCH tracks. The quality of global tracks were then carefully checked with several criteria in the track selection for the physics analysis.

5.4 Updates from MEG II Official Previous Studies

In this thesis, the data from 2017 is mainly used for the pTC analysis and obtained performances are compared with the previous studies [7]. In the previous work, the timing resolution of the pTC was evaluated with "even-odd" analysis as the details are described in Sec. 6.4.1. The obtained resolution was 38.5 ps from the commissioning data in 2017 with the muon beam of MEG II nominal intensity. However, even though 512 counters were operated, the evaluation was performed with the limited combination of clusters as shown in Fig. 5.3 since there was no tracking information available due to missing pTC tracking algorithms. Only clean positron events, i.e. positrons crossed at the center of the first counter with the incident angle of 90° and successive counters from the center of the first counter (10 counters at the maximum), were selected for the evaluation. In addition, the timing resolution obtained from the simulation with the same method was 31.0 ps in the previous work, which is much better than the commissioning result. The deep understanding of the S/N was missing in previous work and simulations were not properly tuned to reproduce basic characteristics of the pTC. In this thesis, the main improvements of the pTC driven by the author are summarized as follows:

- Tracking algorithms were newly developed and the performance of the pTC was re-evaluated and demonstrated with the tracking information. This work evaluated the performance of the pTC with full combinations, which includes

Table 5.1: Data mainly used in the following chapters.

Detectors	**Year**	**Beam**	**Description**
pTC + Mock-up CDCH	2017	MEG II Nominal	pTC performance evalation
pTC + CDCH	2018	Low Rate (1.34×$10^7 \mu^+$/s) + MEG II Nominal	CDCH waveform analysis with beam
pTC + CDCH	2019	Cosmic	CDCH waveform analysis with the finalized WDB

the systematic uncertainty from the individual counter difference.

- The systematic difference between the simulation and the commissioning was investigated. Especially, the hit-position dependence in a counter and the difference of the evaluation method were investigated in detail.
- The uncertainty of the calibration methods were investigated. The breakdown of the uncertainty on the laser-based method was studied in detail. The track-based calibration method was established with newly developed tracking algorithm.
- The cooling system for 10°C operation to mitigate the radiation damage effect was prepared and the stable operation was confirmed in 2018 - 2019.
- The optimization methods for the operation voltage and the analysis parameter was developed in 2019.

The 2018 and 2019 data are mainly used for the CDCH waveform analysis. In [26] summarized the hardware status of the CDCH until 2019, and the first analysis on the gas gain, noise situation, waveform shape, and so on were studied. However, due to the large low frequency noise from the intermediate convertor for the prototype electronics, it was very difficult to extract the information for the performance evaluation of the spectrometer. In this thesis, the main upgrade of the CDCH analysis can be summarized as follows:

- The algorithm for the CDCH waveform analysis was updated and global tracking algorithms were developed using pTC and CDCH.
- Actual CDCH detector performance was taken into account. For example, S/N was found to be worse than the expectation. This deterioration was included in the simulation and the realistic performance was evaluated using newly developed algorithms.

The commissioning data used in this thesis in the following chapter is summarized in Table 5.1.

Chapter 6

Performance of the pTC

6.1 Goal of This Chapter

In this chapter, the analysis framework for the MEG II pTC was described. Then, the performance of the pTC was evaluated with the 2017 commissioning data.

6.2 Overview of Timing Reconstruction Algorithm

The goal of the pTC analysis is to obtain the positron crossing timing precisely from the counter hits. To achieve the target performance of O(30) ps, the multiple-hit information from one single positron track is needed. The timing reconstruction for the pTC is composed of the following algorithms:

- Waveform Analysis,
- Hit Reconstruction,
- Clustering,
- Standalone pTC Track Fitting (Tracking),
- Calibration and Refinement with Tracking Information.

6.3 Algorithms for pTC Analysis

In this section, the details of each algorithm for the pTC are described.

6.3.1 Waveform Analysis

Noise Reduction

Understanding the noise situation (signal-to-noise ratio, S/N) is crucial in the first step of the analysis. Since the signal cables, the readout electronics, and the detector components are gathered in the experimental area, unexpected noises are often picked up. Some of the noises caused by other electronics are periodical, and such noise components can be subtracted by making the template of the noise waveform. In the 2017 commissioning, the cross talk noise from the clock channel was observed. Fig. 6.1 shows the sine waveform in the clock channel for the WDB synchronization. The template noise waveform was made by summing up the pedestal data, and the example of the waveform is shown in Fig. 6.2. The results by the software noise reduction are shown in Fig. 6.3 and Fig. 6.4. The peak of the power spectrum around 100 MHz vanished, and the mean RMS-noise was reduced from 6.5 mV to 5.4 mV.

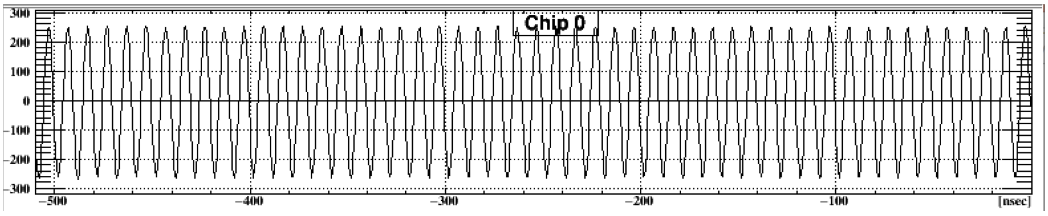

Fig. 6.1: The sine waveform in the clock channel for the pTC WDB synchronization.

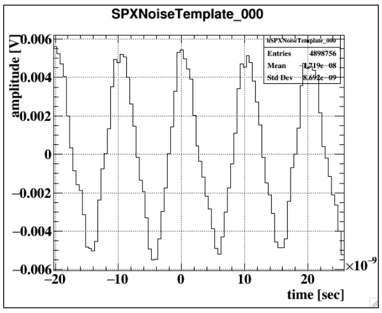

Fig. 6.2: The template noise extracted from the pedestal data taken in 2017 in the experimental area [28].

Signal Pulse Detection

Fig. 6.5 shows the example of the waveform from a single channel. To extract the timing information, the constant fraction method (CFD) is used in the pTC analysis. The analysis flow is as follows:

1. Pulse Search: a signal pulse whose height is over the threshold is searched.
2. Interpolation: The width of the waveform window and the sampling frequency are in the relation of trade-off. To obtain the comparable timing resolution to the higher sampling frequency, cubic interpolation between the sampling points is applied for the timing pickup*1.
3. Timing Pickup by CFD: the timing is picked up at the threshold defined as: (pulse peak) × (constant fraction (CF) value).

6.3.2 Hit Reconstruction

A timing coincidence, $|t_1 - t_2| < 20$ ns, is then taken between both sides of a counter. Note that the timing of each counter has an intrinsic time offset, t_{offset}, which is corrected in the calibration process. The reconstructed hit timing at each counter can be written as follows:

$$t_{\mathrm{measured}} = \frac{t_1 + t_2}{2} - t_{\mathrm{offset}}. \tag{6.1}$$

The x-coordinate of the hit position in a counter is reconstructed based on the time difference between the two channels:

$$x_{\mathrm{hit}} = \frac{(t_1 - t_2 - \Delta t)}{2} v_{\mathrm{eff}}. \tag{6.2}$$

The effective velocity v_{eff} and the difference in the internal time offset between both ends are obtained from the position calibration.

[*1] By cubic interpolation 2 GS/s (~ 500 ns timing window) is enough to obtain the comparable resolution with 5GS/s (~ 200 ns timing window) [23]

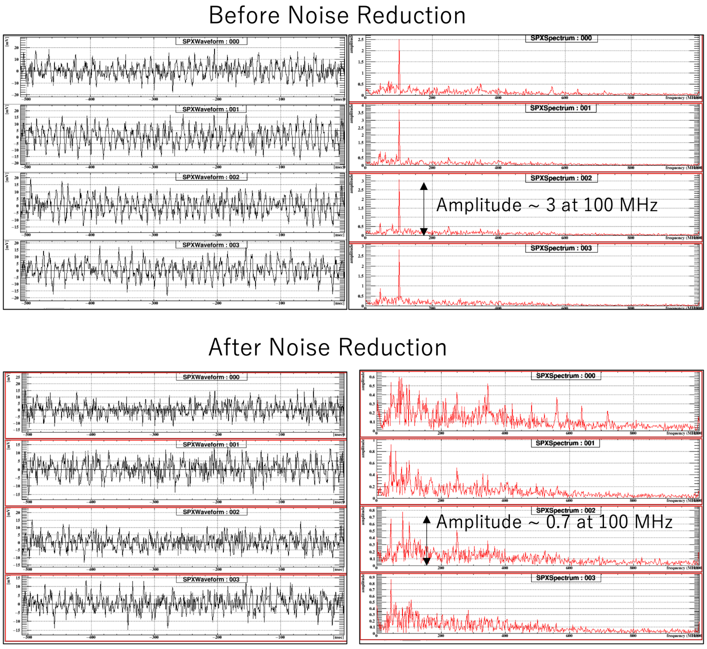

Fig. 6.3: The pedestal waveforms of the pTC (left black) and their amplitude of the power spectrum (right red) before / after the noise reduction (up / down) [28].

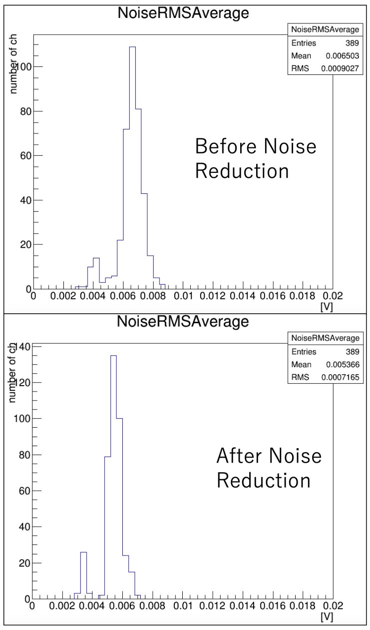

Fig. 6.4: The RMS-noise of each pTC channel with pedestal data before / after the noise reduction [28].

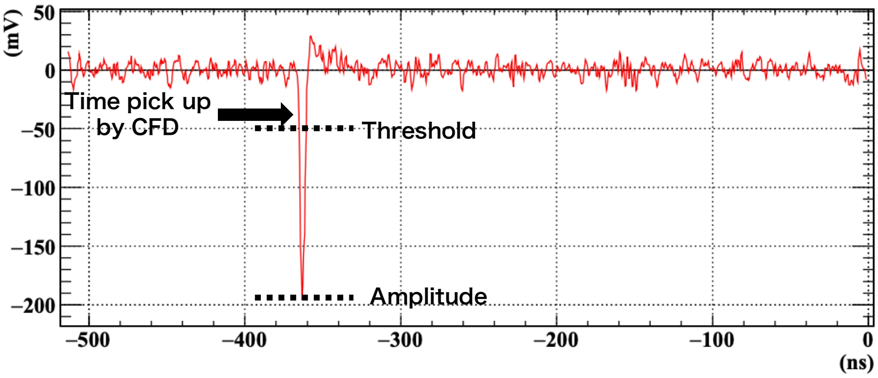

Fig. 6.5: The extracted waveform from a pTC counter [29].

Position Calibration

To reconstruct the hit x-position (longitudinal direction) in a counter, the relative time offset between two channels at the both side of a scintillator (intra-time offset) and the effective velocity of the scintillation light in a scintillator must be known beforehand. This is achieved by fitting the histogram of the x-position with the trapezoid and gaussian convoluted function, as shown in Fig. 6.6. The fitting parameters are the center position, the offset, and the length of the trapezoid function, and the deviation of the convoluted gauss function which can be interpreted as the position resolution:

$$f = \mathrm{trapezoid}(\mathrm{center}, \mathrm{length}, \mathrm{offset}) * \mathrm{gauss}(\sigma_{\mathrm{position}}). \tag{6.3}$$

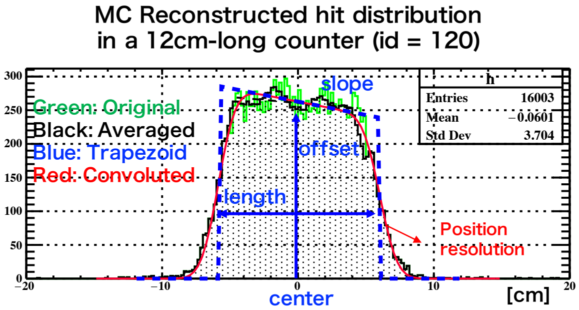

Fig. 6.6: An example of the x-position histogram of a counter. The green line is the original histogram, black after the moving average, blue-dashed the trapezoid function. The fitting result is shown with red line. The center of the fit result corresponds to the relative offset between the two channels [30].

Table 6.1: Parameters extracted from the position calibration.

Effective Velocity (data mean)	σ_{center}	σ_L	σ_{position}
12.4 ± 0.4 cm/ns	0.11 cm	0.27 cm	1.1 cm

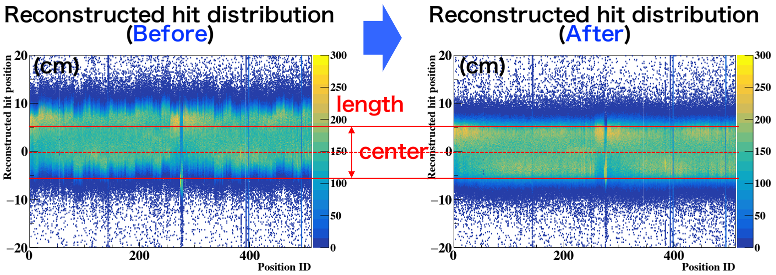

Fig. 6.7: The position distributions of counters before/after the calibration [30].

The effective velocity, v_{eff}, and the effective length, L ,can also be obtained from the length from the fitting with MC. The effective velocity in data can be corrected by:

$$v_{\text{eff data}} = \frac{L_{\text{MC}}}{L_{\text{data}}} v_{\text{eff MC}}. \tag{6.4}$$

The extracted parameters are summarized in Table 6.1. The estimated uncertainty of 0.11 cm for the center alignment satisfied our requirement for pTC counters (~ 1 cm). Fig. 6.7 shows the position distributions of counters before/after the calibration.

The position calibration is applied every year since 2017. Fig. 6.8 shows the difference of intra-time offset between 2017 and 2018 and examples of the two outliers: one is due to the bad fitting and the other is actually shifted. The difference between each year is rather small.

Energy Calibration

The energy deposit in a counter is calculated based on the pulse charge and an energy calibration factor C_E. C_E is extracted by the peak position of the distribution of the geometric mean of the integrated charge from simulations:

$$C_E = \frac{E^{\text{peak}}}{\sqrt{Q^{\text{peak}}_{\text{ch 1}} \cdot Q^{\text{peak}}_{\text{ch 2}}}}, \tag{6.5}$$

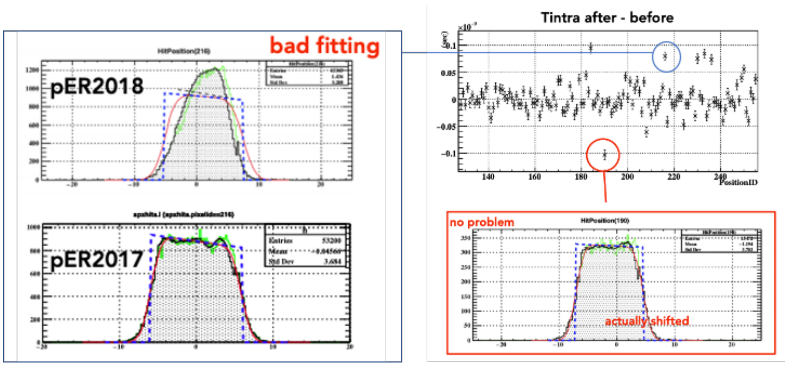

Fig. 6.8: The position calibration difference in 2017 and 2018, and the outlier examples.

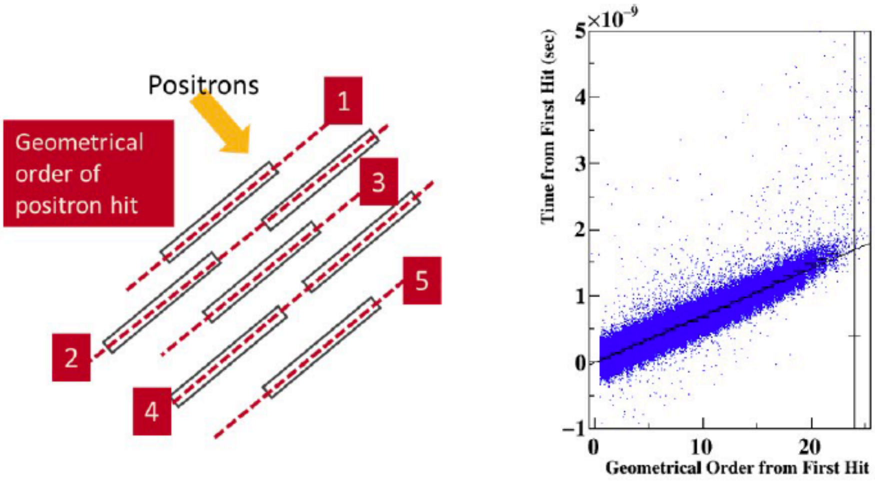

Fig. 6.9: The definition of the geometrical order in pTC (left) and the distribution of the geometrical order from the first hit and timing from the first hit [7].

where E^{peak} is the most probable value of energy deposit, $Q^{\text{peak}}_{\text{ch }1}$, $Q^{\text{peak}}_{\text{ch }2}$ are the most probable values of the reconstructed charges.

6.3.3 Clustering

The reconstructed pTC hits are then grouped into a cluster. To separate the hits from different particles, the geometrical order is defined as shown in Fig. 6.9. The reconstructed timing is projected on the geometrical order plane as shown in Fig. 6.9 (geometrical order from the first hit vs timing from the first hit), and by fitting the plot with a linear function and applying the correction, the timing distribution of pTC hits on the projected plane was obtained. Then the projected hits which have the close timing (±500 ps from a peak) are grouped into the clusters.

After several studies in the simulation, it was found that the inefficiency of the pTC clustering was mainly caused by positrons with a small turning radius after scattering. Fig. 6.10 shows an example of this event. The positron passed through the pTC counters in the orange region, and after a small turn, it soon came back into the pTC counters in the green region. To separate these clusters, the new position criterion (±10 cm from a peak position) is also implemented as shown in the same plot. By removing or separating the counters with tail hits from the cluster, the cluster's timing precision is recovered. This position information can also be used to add the hits to the cluster as shown in Fig. 6.11. If the hits in

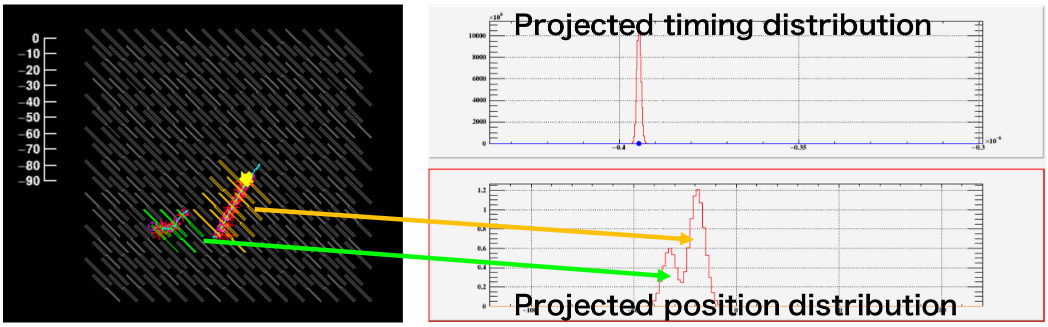

Fig. 6.10: A typical tail event of pTC cluster. After crossing a first cluster (orange), that positron loses the momentum by material effects and its turn radius becomes small, and it soon comes back to the pTC region (green).

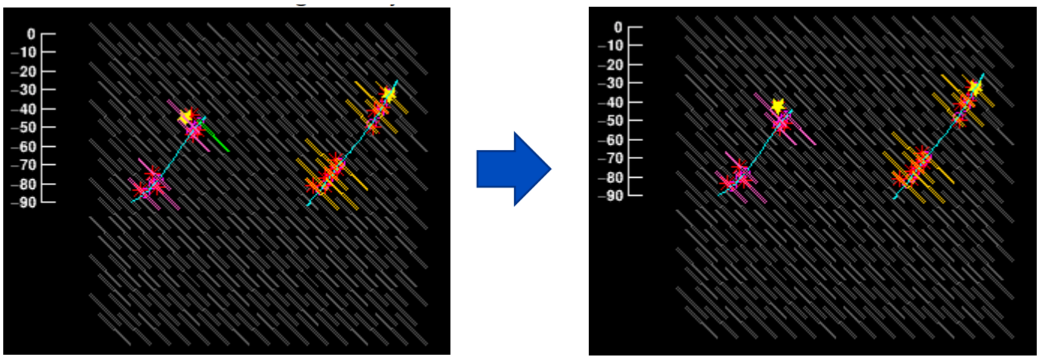

Fig. 6.11: The hit addition to the cluster by using the projected hit position. The green counter in the left plot cannot be assigned to the purple cluster only with the timing information, but it can be assigned to the purple cluster with the cross-check of the timing information and the position information. The positron passed through under the counters in the middle of the cluster.

the cluster are not consistent between timing-based and position-based, the algorithm will test again with wider acceptance (e.g. ±700 ps in the plot).

The hit qualities in a cluster are also checked with other criteria, the energy deposit in a counter should be higher than 0.5 MeV and the longitudinal hit position from the center should be within $\pm(6 \pm 5\sigma_{\text{position}}) \sim \pm 11$ cm, where σ_{position} is the resolution of the longitudinal position (local-x) reconstruction in a single counter (~1.1 cm). An additional algorithm to remove outlier hits from the cluster is implemented in the tracking process later.

6.3.4 Standalone pTC Track Fitting

To estimate the positron path length (and calculate the time of flight between counters), a track fitting process is performed. Combining the hits in a cluster and reconstructing a positron track gives a better estimation of hit positions in a counter. The standalone pTC track fitting is developed for a pTC track fitting without CDCH information. This algorithm enables us to reconstruct a part of positron tracks even under the limited (or no) CDCH information which was the case for the commissioning in 2017-2020. In addition, the independent tracks can be used for more reliable seeds in CDCH track finding process than seeds from only CDCH hits (this seeding method is explained in Sec. 7.5.2) since the tracks provide reliable information on the initial momenta and direction.

This algorithm is composed of three steps: the initial parameter estimation, the Kalman Filter (KF) fitting (the details of

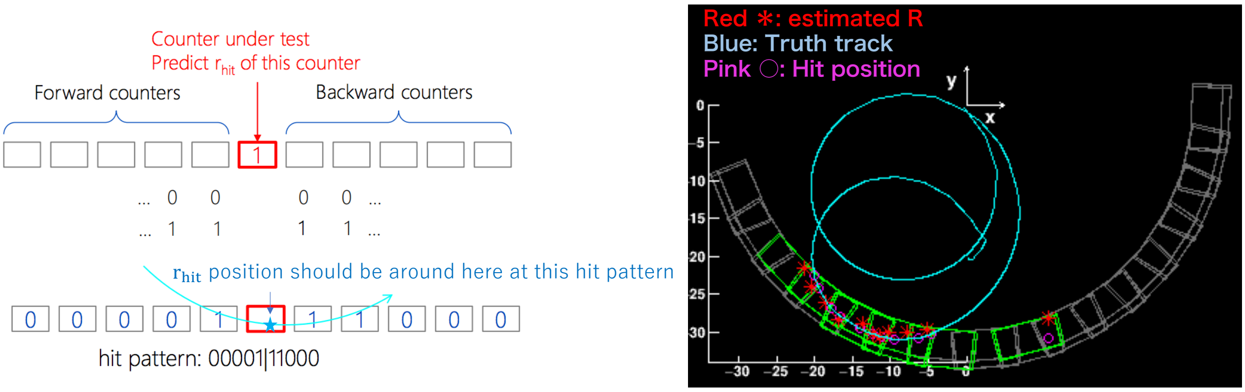

Fig. 6.12: The schematics of the y_{local} estimation algorithm (left) and its result (right).

the formulation is described in Appendix D), and the extrapolation to the CDCH. Using the extrapolated information from the pTC track will improve the track finding in the CDCH analysis thanks to the additional information on the track seed, as shown in Appendix E.

Initial Parameter Estimation

The KF algorithm is a recursive algorithm, so the initial input (3D position and momentum) is crucial for the fitting. Since the counter thickness is only 5 mm, the center of the counter is used as the local-z coordinate of the hit. The transverse (local-x) direction is reconstructed by using the timing difference between both ends with ∼11 mm resolution. As for the longitudinal direction (local-y), a dedicated algorithm was developed.

The concept of this algorithm is the classification of the cluster patterns. Fig. 6.12 shows the schematics of this algorithm. A single counter (shown red) is under the test, and 5 counter groups in front/behind that test counter in pTC geometrical order is defined. The hit or no-hit information in each group is recorded as the bit information and that 10-bit string represents the cluster pattern. The distribution of the local-y hit position on the counter under test for each pattern is in advance evaluated using a MC simulation and the mean and standard deviation are stored in a look-up table. The local-y hit position is set to the mean value for the hit pattern.

Another unknown initial parameter is the momentum (direction) information. The absolute value of the momentum can be estimated by the MEG II gradient magnetic field: the positrons above 45 MeV can reach the pTC. This value is used for the initial value of the KF calculation with a large initial uncertainty (~8 MeV). The direction can be estimated by the first two counters in the cluster.

Kalman Filter (KF) Fitting

The pTC hit clusters are then fitted with the KF algorithm. The KF is known as an efficient recursive algorithm to obtain the best estimate of a state vector[*2]. In the GENFIT package, a generic toolkit for track reconstruction for experiments in particle and nuclear physics [32], the KF algorithm and its extension algorithms like Deterministic Annealing Filter are available for the track fitting. Fig. 6.13 illustrates the KF algorithm overview. The detailed formulation is explained in Appendix D, and here the concept is briefly described. The key of the algorithm is to use both the estimation from the physics model (the positron's interaction among the materials with the gradient magnetic field) and measurement from the detectors. The KF starts from a certain state vector called seed. A seed state is important since it is the starting point of the recursive steps and a wrong initial state results in a wrong estimation. The state vector at the next step (or plane) is

---

[*2] In this case, the state vector contains the positron trajectory information, i.e. position, momentum, timing and covariance among them.

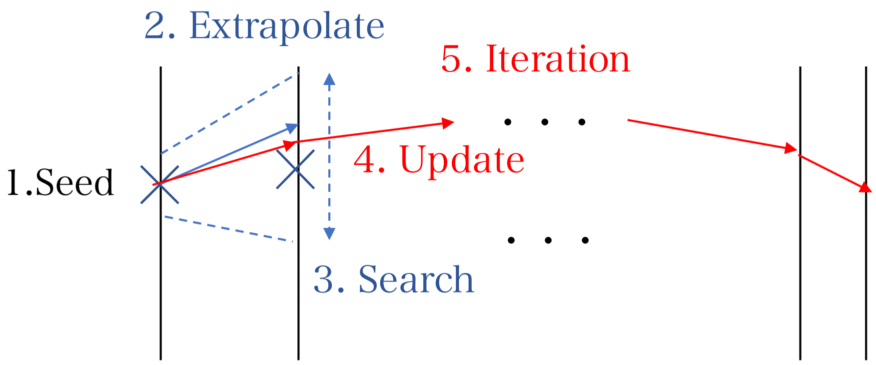

Fig. 6.13: The sketch of KF algorithm.

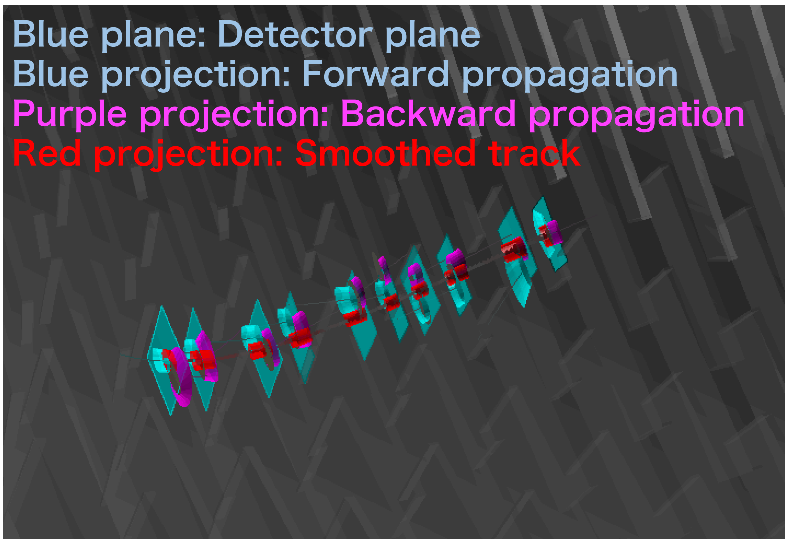

Fig. 6.14: The reconstructed positron track by GENFIT.

estimated from the previous state and its physics models, for example the extrapolation from the previous plane to the next plane. Then the estimated state and the measured state are combined with the factor called Kalman gain. After that the updated (combined) state is used for the next estimation step and these steps are repeated. Fig. 6.14 shows the reconstructed positron track in pTC region.

6.3.5 Timing Calibration

The timing calibration is the most crucial calibration for the analysis with the multiple counter hits. The reconstructed positron crossing timing at each counter can be written as follows:

$$t_{\text{rec}} = \frac{t_1 + t_2}{2} - t_{\text{offset}}, \tag{6.6}$$

where the first term is the average of the timings measured at both ends of the counter and the second term is the time offset of the counter. The time offset of the counter is defined as:

$$t_{\text{offset}} = \frac{l}{2v_{\text{eff}}} + t_{\text{SiPM}} + t_{\text{elec}}. \tag{6.7}$$

Table 6.2: The summary of the uncertainties for the laser-based calibration.

Item	Uncertainty [ps]
Reproducibility 4 cm/5cm counter	11/3.0
Measurement error (in lab test)	5.4
Statistics	1.0
Stability	8.8
Voltage correction	1.5
Time-walk correction	4.2
Waveform difference	4.3
Variation of transit time inside SiPMs	21
Total	27

The first term is the correction for the propagation time in a scintillator, where l is the longitudinal length of the scintillator, v_{eff} is the effective velocity of the light. t_{elec} is the signal transmission time in the electrical components (signal lines, cables and DAQ electronics lines and so on), t_{SiPM} is the offset from the SiPM chain's transit time.

Laser-based Calibration

The overview of the laser system and its concept are explained in Sec. 2.4.2. First, the time offset from the laser-based calibration is measured: the time offset of each counter is calculated by using the measured timing and the reference timing from the laser synchronized pulse. The light source generates a pulse signal synchronized with the laser light emission time, which is used as the reference signal to calculate the $t^{\mathrm{obs}}_{\mathrm{offset}}$,

$$t^{\mathrm{obs}}_{\mathrm{offset}} = \frac{t_1 + t_2}{2} - t_{\mathrm{SYNC}}, \tag{6.8}$$

where t_{SYNC} is the timing picked up by the laser synchronized pulse.

Compared to t_{offset}, $t^{\mathrm{obs}}_{\mathrm{offset}}$ includes the additional offset from the laser components (optical fiber, connection point, and laser light propagation), t_{laser}. This component is measured beforehand in the mass test process for the calibration system. The uncertainty of the laser-based calibration was evaluated in 2019 [8], and Table 6.2 summarized the uncertainties for the laser-based calibration measurement. The variations of the transit time inside the SiPMs are measured with the timing measurement setup similar to Fig. 3.4.2: the hit timing of electrons from ^{90}Sr was measured and its mean timing (time-center) was extracted, then the measurement was repeated for about 100 counters. The counter-by-counter variation of 21 ps, which includes the response of the SiPMs, is set as the upper limit of the variation of the transit time of SiPMs. The reproducibility of the light injection (i.e. time center at a counter) was evaluated by repeating the timing measurement 10 times by extracting and inserting the fiber every time. The measurement error of the effective optical length was calculated from the test of optical components for counters (the 1×8 optical splitters, the 2.5 m optical fibers, and the counter shown in Fig. 2.44). The stability, statistics, voltage correction, time-walk correction, waveform difference were studied with the data taken in during the detector commissioning. Especially, the monitoring precision is shown in Fig. 6.15, which shows the monitored time offset of a counter during 2017 commissioning. The RMS of the time offset monitored over a month was 8.8 ps on average. The monitoring precision better than 10ps, which can be obtained with 30min data-taking, is good enough for the detector operation.

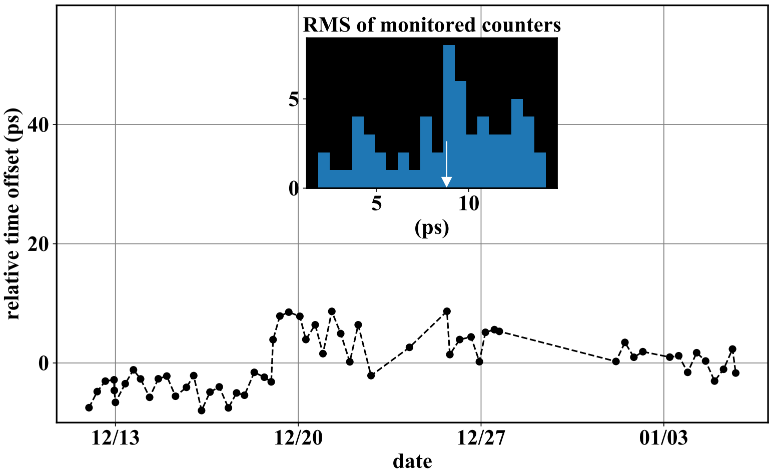

Fig. 6.15: The time offset history of a counter in a month [8]. The histogram of the RMS of monitored counters is also shown.

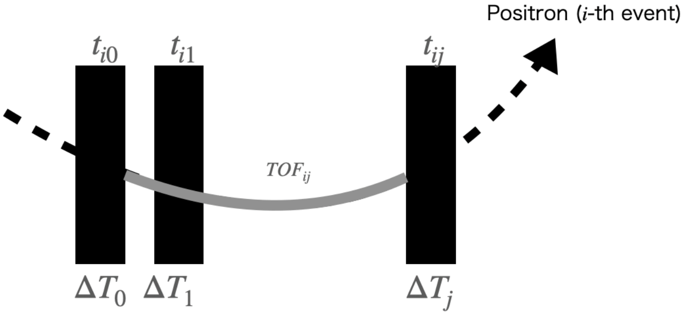

Fig. 6.16: The concept of track-based calibration.

Track-based Calibration

The concept of the track-based calibration is to obtain t_{offset} by minimizing the squared difference (defined as χ^2 below) between the measured timing and the calculated timing at each counter by using the information from a reconstructed track in the pTC region. The algorithm flow is as follows:

1. Track reconstruction: The reconstructed pTC hits are clustered, and then fitted with Kalman Filter algorithm and pTC tracks are obtained.
2. Calculation of the χ^2: By using the reconstructed information χ^2 defined as below is calculated:

$$\chi^2 = \sum_{i}^{N_{\text{tracks}}} \sum_{j}^{N_{\text{hit}}} \left(\frac{t_{\text{measured}} - t_{\text{calculated}}}{\sigma}\right)^2 \tag{6.9}$$

$$= \sum_{i}^{N_{\text{tracks}}} \sum_{j}^{N_{\text{hit}}} \left(\frac{t_{ij} - (t_{i0}^{\text{fit}} + TOF_{ij} + \Delta T_j)}{\sigma}\right)^2 \tag{6.10}$$

where N_{tracks} is the number of tracks from all events, N_{hit} is the number of hits (counters) in a track, σ is the timing resolution, and $t_{\text{measured}} = t_{ij}$ is the reconstructed timing at the j-th counter in the i-th track. $t_{\text{calculated}} = t_{i0}^{\text{fit}} + TOF_{ij} + \Delta T_j$ is the calculated timing at the j-th counter by using the first counter timing (t_{i0}^{fit}) in the i-th track

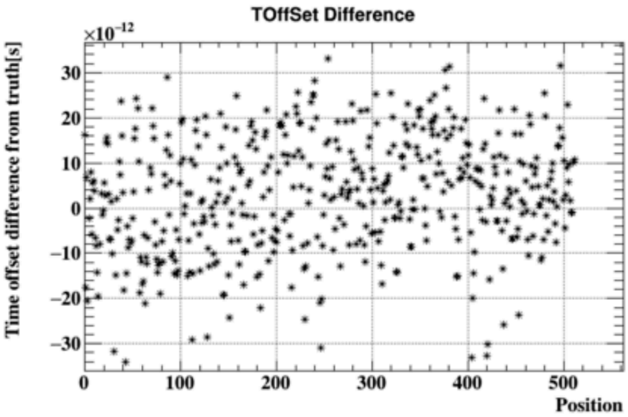

Fig. 6.17: The result of track-based calibration compared with the simulation random offset. The standard deviation is estimated to be ~13 ps.

Table 6.3: Comparison between two time calibration methods.

Item	**Laser-Based**	**Track-Based**
Position dependence	**No**	Yes
DAQ time	~ 30 **min.**	~2 days
Beam	**not necessary**	necessary
Coverage	84%	**100%**
Uncertainty	27 ps	**13 ps**
Strategy	Monitor Stability	Main Use

obtained by fitting, the flight time between the first counter and j-th counter (TOF_{ij}) in the i-th track and the intrinsic time offset of j-th counter (ΔT_j)[*3].

3. Minimization of χ^2: To obtain the best estimate of ΔT_j, the χ^2 is minimized by using the Millepede software[66], which is developed to solve the linear least squares problem with a simultaneous fit of all global and local parameters for efficient and fast alignment and calibration of large detectors[*4].

Fig. 6.16 illustrates these steps. For the estimation of the calibration uncertainty, we used a simulation. The random offset (± 100ps) is generated and added to the counters[*5]. Then the track reconstruction in pTC and the above track-based calibration algorithm are performed. The result is compared with the generated offset. A precision of ~13ps was achieved as shown in Fig. 6.17.

Strategy of Timing Calibration

Table 6.3 summarizes the comparison between the two methods. The basic strategy of the pTC time calibration is as follows: the time offset calculated from track-based calibration is mainly used, and its time-dependence during the data taking period is monitored by the laser-based calibration.

[*3] t_{i0}^{fit} is the local parameter (minimized track by track) and ΔT_j is the global parameter (common to all events) for fitting.

[*4] Software provided in [67] under the terms of the LGPLv2 license

[*5] When the time offset is calculated with the commissioning data, the time offsets from the laser-based calibration are used for the initial values, whose precision is 27 ps, and ± 100ps random offset is conservative enough for the evaluation of the algorithm.

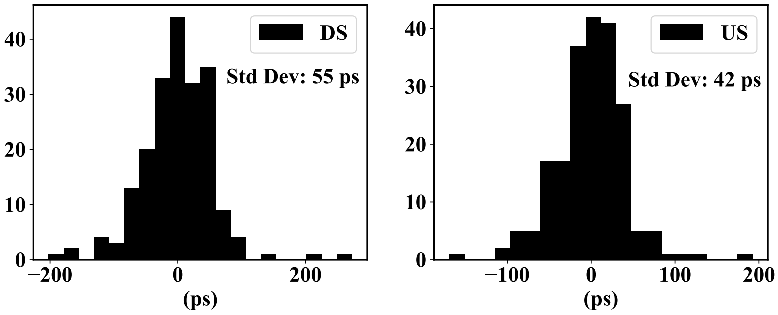

Fig. 6.18: The consistency between two pTC timing calibration methods with 2017 commissioning data [8].

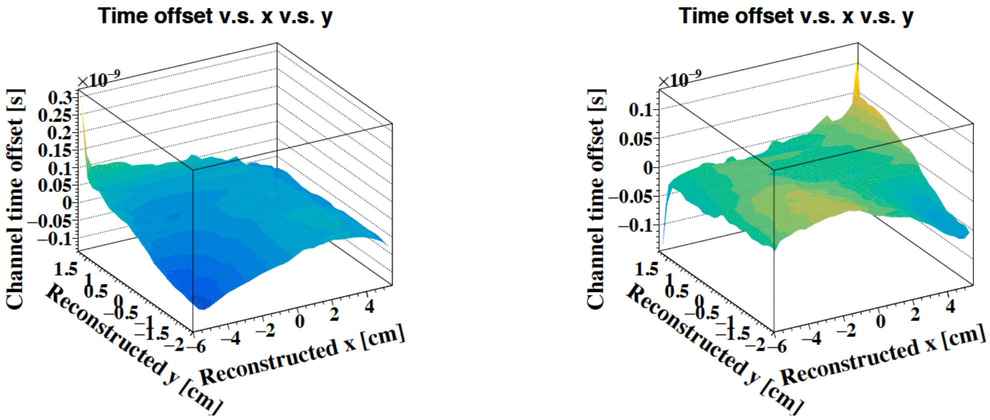

Fig. 6.19: The hit position dependence of the channel by channel time offset after the correction of the time offset in x direction for 4 cm counters [24]. The left plot shows channel 1, and right plot shows channel 2.

Application to Commissioning Data

To evaluate the real precision of the pTC timing calibration, the consistency between these two methods was compared. Fig. 6.18 shows the difference between the time offset values from the laser calibration and those from the track-based calibration. The estimated calibration precision was 42 ps for US pTC and 55 ps for DS pTC (48 ps on average). These values were worse than the estimated value from the simulation ($\sigma(t^{\text{laser}}_{\text{offset}}) \oplus \sigma(t^{\text{track}}_{\text{offset}}) \sim 30$ ps), and it may have a moderate effect on the pTC resolution. For example when 37 ps resolution was assumed with 9 counter hits, the effect of the calibration, whose uncertainties are random among counters, is $37 \oplus \frac{48}{\sqrt{9}} \approx 40$ ps conservatively.

6.3.6 Refinement of the Timing Reconstruction

After the track reconstruction and calibrations, the timing reconstruction is refined. The refinement is classified into two types: counter-level (inter-counter) for tracks and channel-level (intra-counter) for counters by using the energy deposit dependence and the position dependence of the timing measurement. The full details of the refinement are reported in [24]. These algorithms are applied to the 2017 commissioning data.

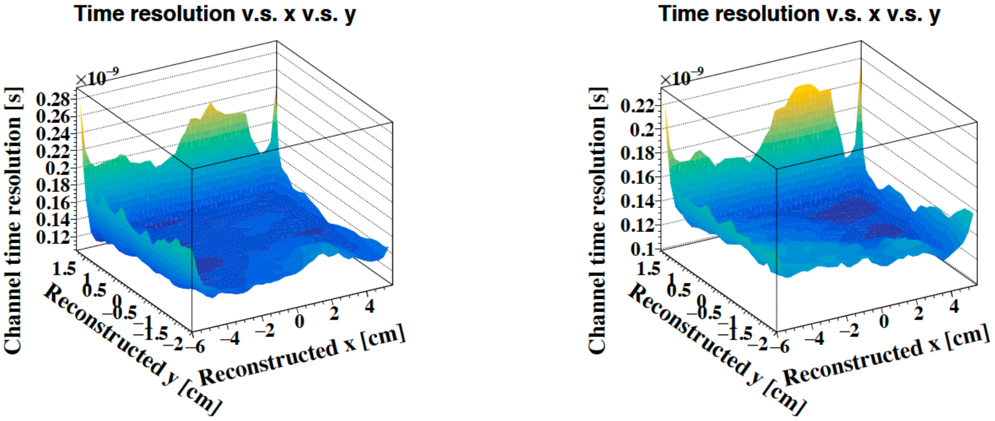

Fig. 6.20: The hit position dependence of the channel timing resolution (right) for 4 cm counters [24]. The left plot shows channel 1, and right plot shows channel 2.

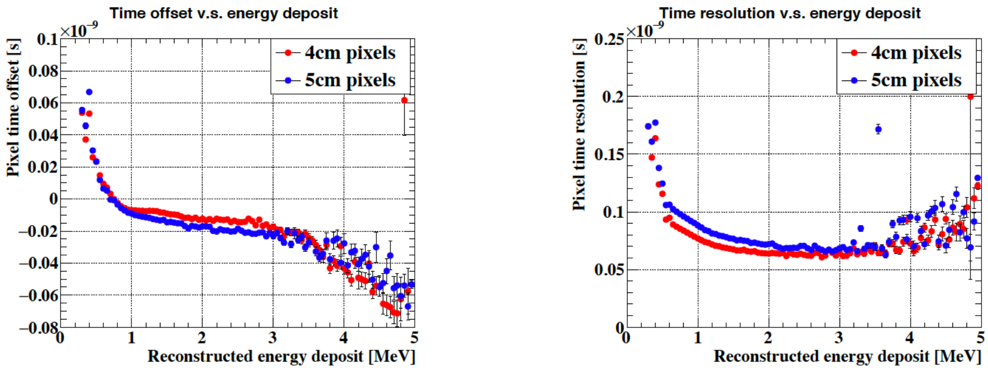

Fig. 6.21: The relation between the energy deposit and the time offset (left) and the timing resolution (right) [24].

Corrections (Channel-Level for Counters)

The channel by channel time offset, $t^{\mathrm{ch1}}_{\mathrm{offset}}$, at each (x, y) position in a counter is extracted as follows:

$$t^{\mathrm{ch1}}_{\mathrm{offset}} = t^{\mathrm{ch1}}_{i} - t_{\mathrm{ave}} - TOF_{1i} - \frac{\frac{l}{2} + x_i}{v_{\mathrm{eff}}}, \tag{6.11}$$

where t^{ch1}_{i} is the reconstructed timing at channel 1 of i-th counter, TOF_{1i} is the flight time between first counter and the i-th counter. Then the hit timing of the i-th counter is calculated with the weighted average of:

$$t_i = \frac{\frac{t^{\mathrm{ch1}}_{i} - t^{\mathrm{ch1}}_{\mathrm{offset}}}{\sigma^2_{\mathrm{ch1}}} + \frac{t^{\mathrm{ch2}}_{i} - t^{\mathrm{ch2}}_{\mathrm{offset}}}{\sigma^2_{\mathrm{ch2}}}}{\frac{1}{\sigma^2_{\mathrm{ch1}}} + \frac{1}{\sigma^2_{\mathrm{ch2}}}} \tag{6.12}$$

The position dependence of the timing offset and resolution in a counter after this correction for 4 cm counters are shown in Fig. 6.19 and Fig. 6.20, respectively.

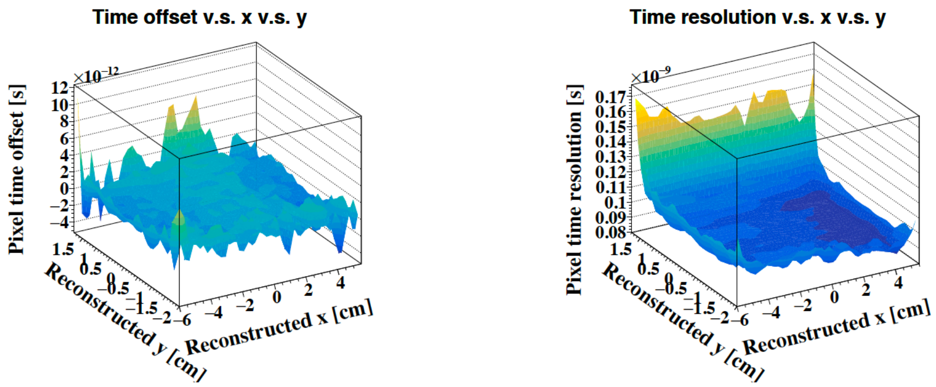

Fig. 6.22: The hit position dependence of the counter timing offset (left) and the timing resolution [24].

Corrections (Counter-Level for Tracks)

There is a correlation between the energy deposit and the timing resolution / measured timing offset ($t^{\text{cor offset}}$) for each counter, as shown in Fig. 6.21. This dependence is corrected with the following formula:

$$t_{\text{odd}} \text{ or } t_{\text{even}} = \frac{\sum_i^N \frac{t_i - TOF_{1i} - t_i^{\text{cor offset}}}{\sigma_i^2}}{\sum_i^N \frac{1}{\sigma_i^2}}, \tag{6.13}$$

where t_i is the reconstructed timing at i-th counter (i is odd number for t_{odd} and even number for t_{even}), TOF_{1i} is the flight time between first counter and the i-th counter, σ_i is the relative weight of i-th hit in the track, $t_i^{\text{cor offset}}$ is the energy-deposit dependent offset as shown in Fig. 6.21 and is extracted as the Gaussian mean of the following distribution:

$$t_i - t_{\text{ave}} - TOF_{1i}. \tag{6.14}$$

t_{ave} is the track timing calculated from:

$$t_{\text{ave}} = \frac{1}{N}\sum_i^N (t_i - t_1 - TOF_{1i}). \tag{6.15}$$

Fig. 6.22 shows the relation between the hit position and the time offset / timing resolution after the channel-level correction. The hit position dependence is also used for the counter-level weighted average with the same formulation as the energy deposit case.

6.4 Performance of pTC

In this section, the performance of the pTC is evaluated with the reconstruction algorithms explained in the previous sections. The pTC-standalone tracking algorithm enabled us to evaluate the performance of the full pTC counters. The development of the clustering algorithm, pTC tracking algorithm, and refinement algorithm contributed to the performance improvement of 15% from the previous work. In addition, the systematics of the counter hit position was newly discovered and studied in detail.

6.4.1 Even-Odd Analysis

The timing resolution of the pTC was evaluated with the even-odd analysis in the commissioning. The concept of this analysis is to use the timing from the i_{even}-th hits and i_{odd}-th hits as the reference timing of each other. This can be described

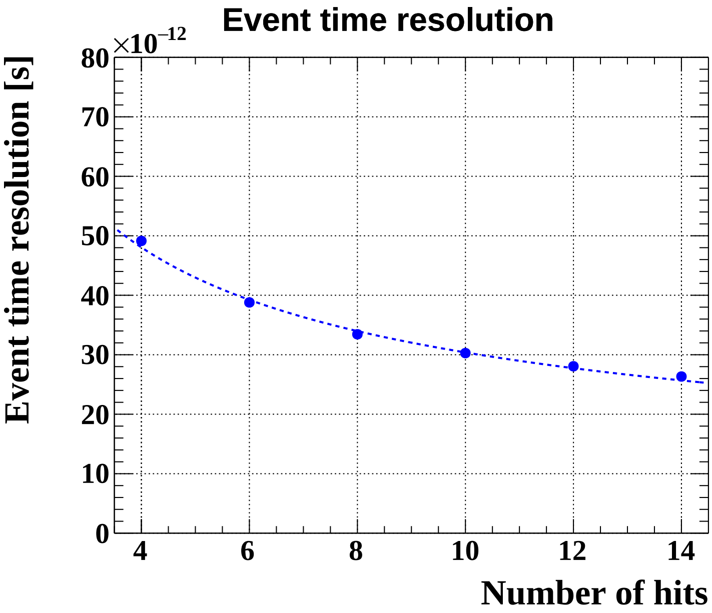

Fig. 6.23: The timing resolution from even-odd analysis with 2017 commissioning data with the latest analysis.

as follows:

$$\sigma_{\mathrm{pTC}}(N_{\mathrm{hit}}) = \frac{1}{2}(t_{\mathrm{odd}} - t_{\mathrm{even}}) \tag{6.16}$$

$$= \frac{1}{2}\left(\frac{1}{N_{\mathrm{odd}}}\sum_{i}^{N_{\mathrm{odd}}}(t_{2i-1} - TOF_{1(2i-1)}) - \frac{1}{N_{\mathrm{even}}}\sum_{i}^{N_{\mathrm{even}}}(t_{2i} - TOF_{1(2i)})\right) \tag{6.17}$$

$$= \frac{1}{N}\left(\sum_{i}^{N/2}(t_{2i-1} - TOF_{1(2i-1)}) - \sum_{i}^{N/2}(t_{2i} - TOF_{1(2i)})\right), \tag{6.18}$$

where t_i is the reconstructed timing at i-th counter, TOF_{1i}^{rec} is the reconstructed time of flight from the first counter to the i-th counter. N is the number of the pTC hits in the cluster (or track), $N_{\mathrm{odd}} = N_{\mathrm{even}} = \frac{1}{2}N$, note that N must be an even number.

6.4.2 Overall Timing Resolution

Fig. 6.23 shows the timing resolution of pTC tracks extracted by the even-odd analysis as a function of the number of hits. The overall timing resolution of pTC was estimated by using the distribution of the number of pTC hits for signal positrons. This distribution was obtained by using the MC, as shown in Fig. 6.24. The overall resolution is calculated as follows:

$$\sigma_{\mathrm{pTC}} = \sum_{N_{\mathrm{hit}}}^{N_{\mathrm{max}}} P(N_{\mathrm{hit}}) \times \sigma_{\mathrm{pTC}}(N_{\mathrm{hit}}), \tag{6.19}$$

where N_{hit} is the number of pTC hits, $P(N_{\mathrm{hit}})$ is the probability for a signal positron crossing N_{hit} counters. $\sigma_{\mathrm{pTC}}(N_{\mathrm{hit}})$ is the extracted resolution from the even-odd analysis as shown in Fig. 6.23 and fitted with:

$$\sigma_{\mathrm{pTC}}(N_{\mathrm{hit}}) = \sqrt{\frac{\sigma_1^2}{N_{\mathrm{hit}}} + \sigma_2^2}, \tag{6.20}$$

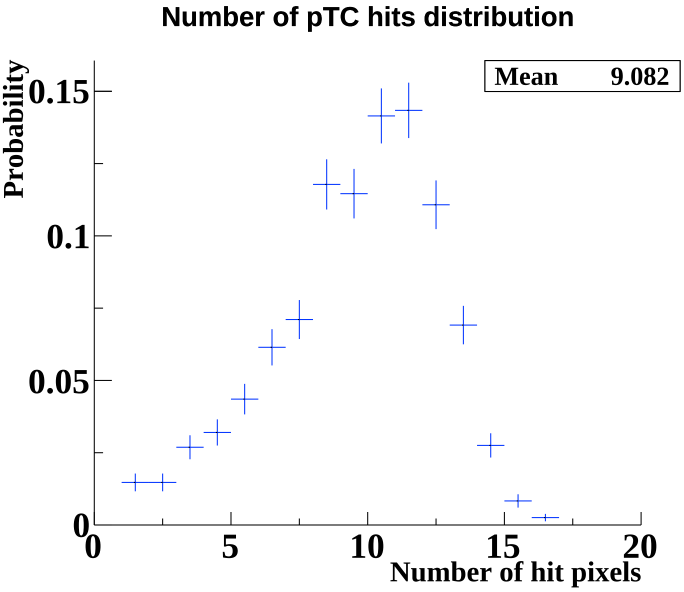

Fig. 6.24: The probability distribution of the number of pTC hits for signal positrons.

Table 6.4: The pTC performance evaluation with the commissioning data: comparison of the updated studies and previous studies.

Algorithm	σ_{pTC}	$\sigma_{\text{TOF CDCH}}$ (MC)	σ_{e^+} (Expected)
Previous [7]	38.5 ps	14.8 ps	41.2 ps
Updated	34.3 ps	6.9 ps	35.0 ps

where σ_1 is equivalent to an averaged single-pixel resolution, whose contribution scales with the square root of the number of counters ($\frac{1}{\sqrt{N_{\text{hit}}}}$)[*6]. σ_2 is the other contributions which do not scale with the number of hits[*7].

The overall timing resolution was evaluated to be 34.3 ps with 2017 commissioning data. Combined with the flight time uncertainty of 7 ps inside the CDCH region (Sec. 7.5.3), the positron timing measurement on the target with a precision of 35.0 ps was obtained. The timing resolution was estimated 41.2ps in previous studies [7]. The improvement is summarized in Table 6.4. 15% of improvement was achieved thanks to the new algorithms, i.e. the standalone pTC tracking, update of the clustering, and the refinement algorithms. The TOF calculation in CDCH is also optimized by using the KF fitting iteration, resulting in the improvement by a factor of two as described in Sec. 7.5.3. Now the overall timing resolution for $\mu \to e\gamma$ measurement $\sigma_{t_{e^+\gamma}}$ is calculated to be 68 ps with the assumption of $\sigma_{t_\gamma} = 58$ ps. This value is much better than the design value of 84 ps and the MEG value of 122 ps.

6.5 Performance Studies Using MC Simulations

To verify the estimated performance of the pTC, the comparison of the evaluation methods with MC data was performed. Table 6.5 summarizes the results of the resolution estimated by various methods in MC (even-odd or truth-based) and the

---

[*6] For example, the single counter resolution, the calibration precision, and the electronics jitter are contained in σ_1.

[*7] For example, the multiple scattering, the secondary particle effects, and the systematic time spread from the hit position dependence in counters are contained in σ_2.

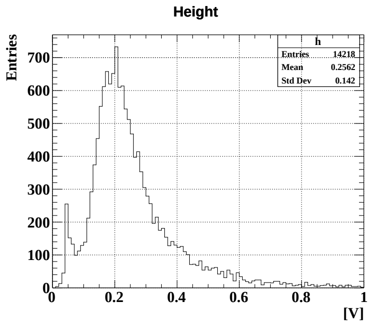

Fig. 6.25: 2017 pTC amplitude.

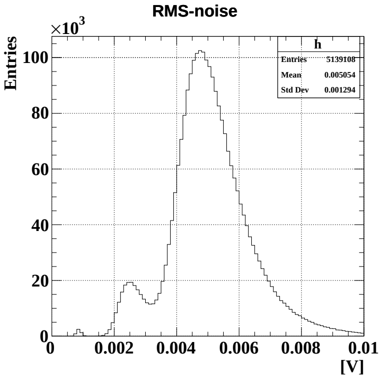

Fig. 6.26: 2017 pTC RMS-noise .

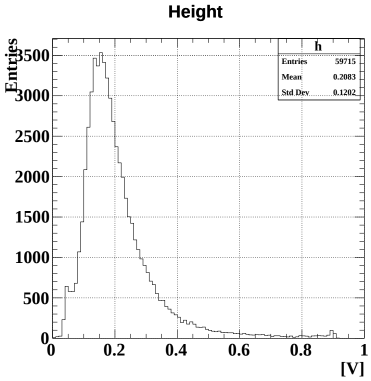

Fig. 6.27: pTC amplitude (MC).

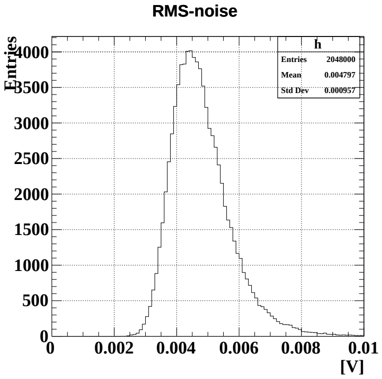

Fig. 6.28: pTC RMS-noise (MC).

hit position dependence.

6.5.1 Tuning of S/N

As discussed in Sec. 3.4.3, the timing resolution of the pTC counter is predominantly affected by the S/N. Fig. 6.25 and Fig. 6.26 show the observed amplitude and RMS-noise of pTC waveforms, and Fig. 6.27 and Fig. 6.28 show the ones for MC. The mean value of the height in the commissioning was higher than the MC mainly due to the difference of the operation temperature and the over-voltage; the 2017 commissioning was performed at 20°C while the MC was tuned with $30°C$ condition (this difference was equivalent to the over-voltage $\sim$ 1.2V). Also, the small amount of the counters with type-II SiPMs had higher gain and lower noise.

6.5.2 Hit Rate

The hit rate of the pTC counters was calculated from the number of pulses outside the trigger timing (pedestal region). The example of the timing distribution is shown in in Fig. 6.29. Assuming the Poisson distribution:

$$P(X = k) = \frac{R^k e^{-R}}{k!}, \tag{6.21}$$

then the expected value of the hit rate at each counter, R, can be calculated as follows:

$$R = -\ln(\frac{N_{\text{Pedestal}}}{N_{\text{All}}\ T}), \tag{6.22}$$

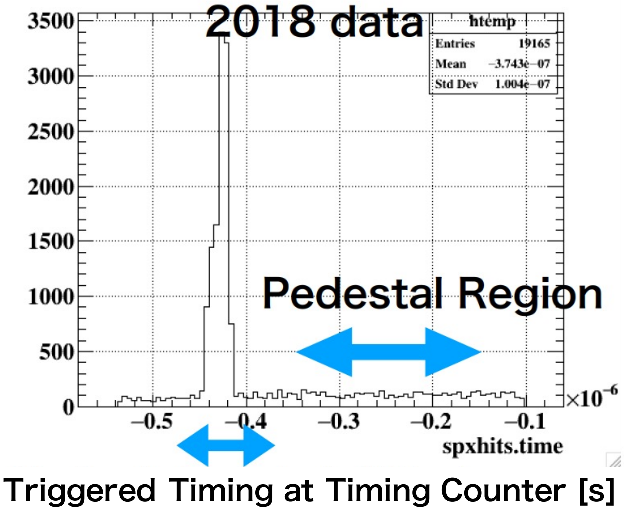

Fig. 6.29: The timing distribution of the pTC hits in 2018 data with the muon beam. Triggered events can be seen around 410 ns – 430 ns. For the rate calculation, the flat region (pedestal region) is used with the assumption of the Poisson distribution.

where N_{Pedestal} is the number of the off-trigger timing events (no pulses in the trigger-timing region, $k = 0$), N_{All} is the total number of the events, and T is the timing window of the pedestal region. The comparison of the hit rate of each counter was already checked in the previous study [7], as shown in Fig. 6.30 with 2017 commissioning data. The hit rate is consistent between the MC and the real data around $|Z| <\sim 100$. Hit rate around $|Z| >\sim 100$ is different between real data and simulations, which is considered due to the material difference between the mock-up CDCH (2017 commissioning) and the CDCH (MC).

Fig. 6.31 shows the average hit rate of the counters at each z-position including the 2018 and the 2019 commissioning data. As discussed above, there is discrepancy between the 2017 data and the MC. In contrast, the tendency (sharp drop around $|Z| \sim 100$) is the same between the MC and the 2018 data since the CDCH material settings became consistent between the real and the MC. Considering the beam rate difference between the 2017 and the 2018 ($7 \times 10^7/6 \times 10^7$), we can conclude that the hit rate is reproduced well by the MC simulations.

6.5.3 Tracking Quality

The tracking efficiency and the resolution were studied with MC and data. The tracking efficiency was estimated as follows:

$$\mathrm{Efficiency} = \frac{N_{\mathrm{Fitted}}}{N_{\mathrm{Cand}}}, \tag{6.23}$$

where N_{Cand} is the number of the candidate events for tracking (pTC clusters with $4 \leq N_{\mathrm{hits}} \leq 14$), and is the number of the fitted events (fitting converged with $\chi^2/\mathrm{dof} \leq 25$). The extracted efficiency was 98.6% for the data in 2017 and 95.1% for the MC. The estimated y_{local}-position (described in Fig. 6.12) was also checked with MC. Fig. 6.32 shows the relation between the resolution of the estimated position at the i-th counter. No significant bias was observed in the estimation and the resolution of y_{local}-position was ~8 mm.

Table 6.5: The pTC performance evaluation with the commissioning data and MC.

Data	σ_{pTC} (Even-Odd)	σ_{pTC} (Truth-Based)
Commissioning	34.3 ps	-
MC	34.7 ps	37.4 ps
MC (position dep. + irradiation)	37.7 ps	42.6 ps

6.5.4 Position Dependence of Tracks

Fig. 6.33 and Fig. 6.34 show the timing resolution from even-odd analysis (6 – 10 hits) with 2017 commissioning data and MC at several $|z|$ region, respectively. $|z|$ of track is defined as the mean position of the counters. Tracks in 40 cm $\leq |z| \leq$ 75 cm have slightly worse resolution than the average ("all" in the figure) since 5 cm counters are mainly used in that region, while tracks in 75 cm $\leq |z|$ have slightly better resolution than the average. The discrepancy between the data and MC is within a few ps at the maximum. The comparison between MC and Data shows that the resolution of the data is very well reproduced by the MC simulations, which verifies the reliability of MC simulations.

6.5.5 Evaluation with MC Truth

In the MC, the precise evaluation of the reconstructed parameters is possible using "true" timing information (truth-based method). The deviation of the following distribution is calculated:

$$\sigma_{\mathrm{pTC}}(N_{\mathrm{hit}}) = \frac{1}{N_{\mathrm{hit}}}\sum_{i}^{N_{\mathrm{hit}}}((t_i^{\mathrm{rec}} - TOF_{1i}^{\mathrm{rec}}) - (t_i^{\mathrm{true}} - TOF_{1i}^{\mathrm{true}})) \tag{6.24}$$

$$= \frac{1}{N_{\mathrm{hit}}}\sum_{i}^{N_{\mathrm{hit}}}(t_1^{\mathrm{calc}} - t_1^{\mathrm{true}}), \tag{6.25}$$

where t_i^{rec} is the reconstructed timing at i-th counter, t_i^{true} is the true (or reference) timing generated in MC. TOF_{1i}^{rec} is the reconstructed time of flight from the first counter to the i-th counter, and TOF_{1i}^{true} is that of MC truth. t_1^{calc} is the calculated timing at the first counter by using $t_i^{\mathrm{rec}} - TOF_{1i}^{\mathrm{rec}}$.

The obtained performance from the commissioning data and the MC data with the same method (even-odd) was consistent, while that from the even-odd for data and the truth-based method for MC was not as shown in Table 6.5. Our interpretation was that the even-odd analysis partially cancel out the systematics of the hit-position by subtracting the adjacent counters, resulting in the better timing resolution than the truth-based method.

6.5.6 Implementation of Systematics by Hit Position

The study on the systematics of timing measurement by the hit position in the counter was possible with the standalone pTC tracking (Sec. 6.3.4). The timing center is defined as $t_{\mathrm{ch1}} - t_{\mathrm{ave}} - \mathrm{TOF}$, and its dependence on the hit position is shown in Fig. 6.35 with the 2017 commissioning data. To extract the dependence from the commissioning data, the correction (in Sec. 6.3.6) was not applied here.

This effect is implemented as the time offset between adjacent SiPMs to reproduce the dependence of Fig. 6.35. As a conclusion, 60 (4 cm counters)/75 ps (5 cm counters) time offset between adjacent SiPMs are used to reproduce the dependence as shown in Fig. 6.36. The contribution to the pTC performance by this new systematics is estimated to be 2%.

Table 6.6: The pTC performance.

Items in Commissioning 2017	Updated	Previous [7]
Obtained Performance from Even-Odd	34.3 ps	38.5 ps
Evaluation	Full combinations	Fixed combination
New Algorithms (% : improvement)	tracking (new)/clustering (2-3%)/refinement (5%)	-
New Systematics Studies		
Systematics (% : deterioration)	Evaluation (8%)/Hit position (2-14%)	No systematics
With Systematics (At Commissioning 2017)	37.0 ps	-
With Systematics (Full Radiation, 10°C)	47.6 ps	-

Increase of Systematics by Radiation Damage

The effect by the non-uniformed radiation damage after 3-year data taking is estimated by using the 6 damaged SiPMs chain (comparable damage level to the MEG II expected dose) and damage-free new SiPMs chain. The damaged chain was composed of; two electron irradiated SiPMs with the fluence level of $\Phi_{eq} \approx 3 \times 10^9 \mathrm{n_{1MeV}/cm^2}$ (used in Chap. 3) and four neutron irradiated SiPMs, two with the fluence level of $\Phi_{eq} \approx 8.7 \times 10^8\ \mathrm{n_{1MeV}/cm^2}$ samples and the other two with $\Phi_{eq} \approx 5.5 \times 10^9\ \mathrm{n_{1MeV}/cm^2}$ ones. Fig. 6.37 shows the position dependence of the hit position with lab test setup (same to Sec. 3.3.1). The detail of each pattern in the plot is explained in Appendix B, and the above pattern which should be focused here is "pattern C (reverse)". Fig. 6.38 shows the position dependence of the damage-free SiPMs with lab test setup. Comparing the dependence of Fig. 6.38 and Fig. 6.37, the factor for the position dependence of time center by the radiation damage can be extracted: ~1.8, i.e. 60 (4 cm counters)/75 ps (5 cm counters) time offset should be 108 / 135 ps. The simulated time center dependence at the edge is shown in Fig. 6.39, and the difference of the performance by this time-offset is summarized in Table 6.5. The effect on the timing resolution from position dependence and irradiation is estimated to be 14%.

6.6 Performance of pTC

With the novel tracking algorithm in the pTC, performance evaluation with full counters and full combinations became possible. 15% better than the previous value (from 38.5 ps to 34.3 ps) thanks to the new algorithms (especially clustering, tracking, and refinement) compared with the previous work in [7]. The MC was updated for the study of the systematics from the evaluation method and the positron trajectory (i.e. hit position in pTC counters). The hit position dependence of the time center was confirmed both from the lab-test and the commissioning data. We found that the obtained performance from the even-odd could be 8% better than the true performance as shown in Table 6.5. Considering these updates, the conclusion of the pTC performance is summarized in Table 6.6. The performance with systematics, 37.0 ps, is calculated with the correction by the evaluation method (8%). The performance after the three-year running, 47.6 ps, is also shown, which is calculated with the correction by the evaluation method, the position dependence (from 2% to 14% by the irradiation), and the dark noise increase by the radiation damage (13%).

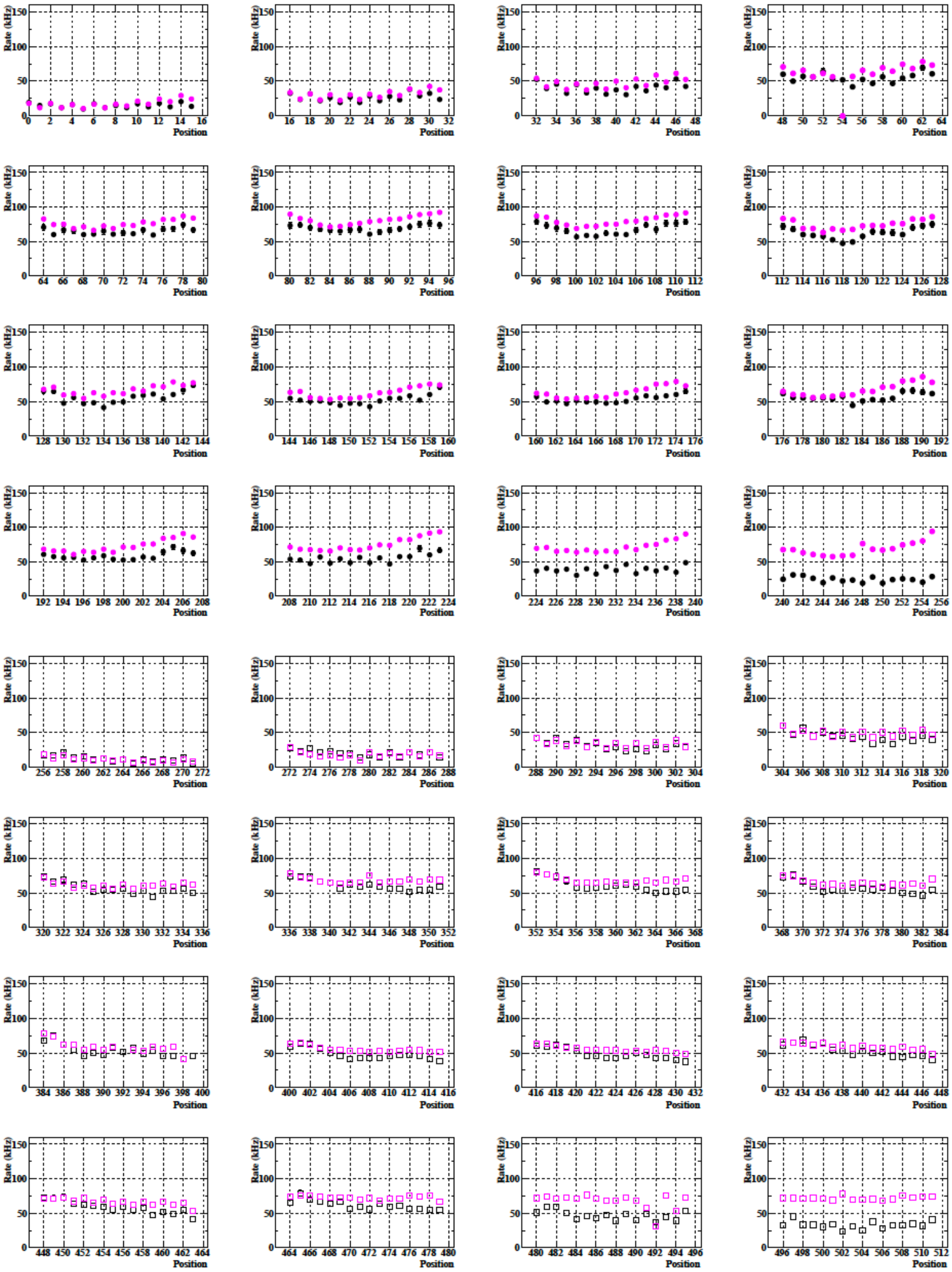

Fig. 6.30: Hit rates calculated with 2017 data (magenta) and MC (black) with MEG II nominal beam rate settings [7]. Larger discrepancy between the MC and the data was observed in the large |Z| region (position ~200 - 256/~450 - 512).

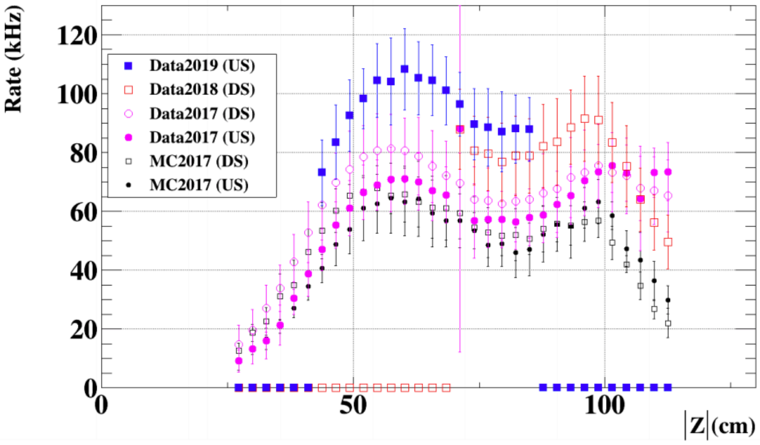

Fig. 6.31: Hit rates calculated with 2017, 2018, and 2019 data with MEG II nominal beam rate settings each year.

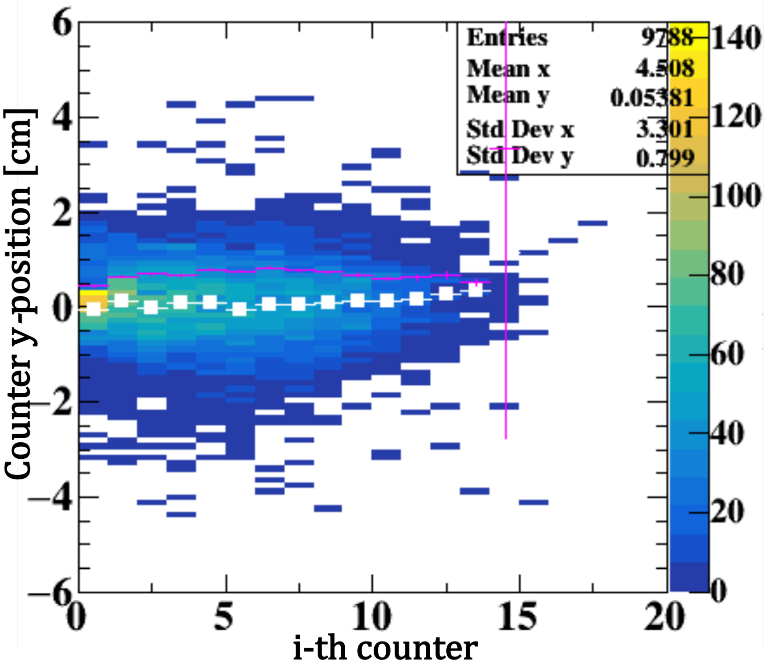

Fig. 6.32: The 2D scatter plot of the difference between the estimated position and the MC truth. The magenta line shows the resolution, white square shows the mean of the distribution at each counter.

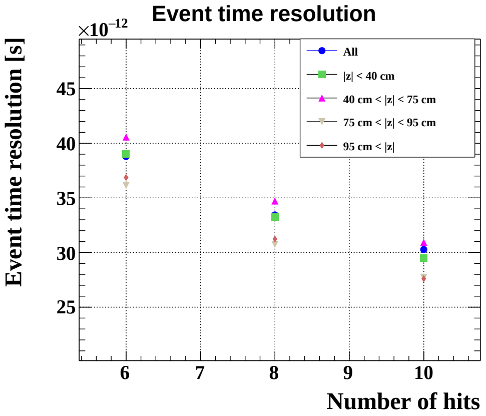

Fig. 6.33: Timing resolution from even-odd analysis with 2017 commissioning data at several $|z|$ position of tracks.

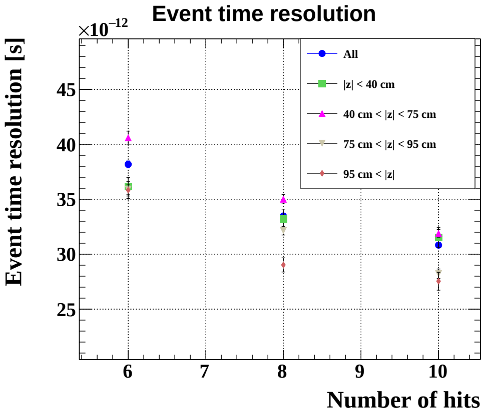

Fig. 6.34: Timing resolution from even-odd analysis with MC at several $|z|$ position of tracks.

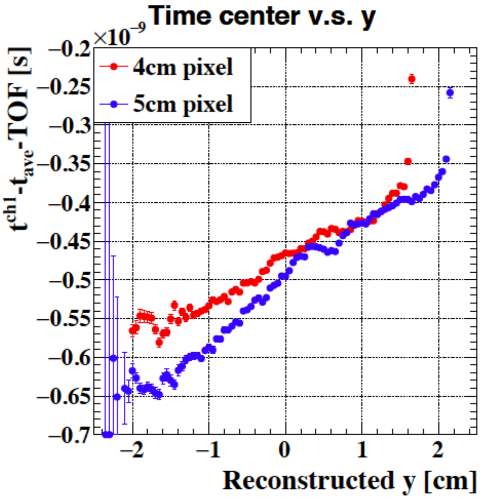

Fig. 6.35: The y-dependence of the timing center in a counter at the edge ($x_{\mathrm{hit}} > 5$ cm) with 2017 data [24].

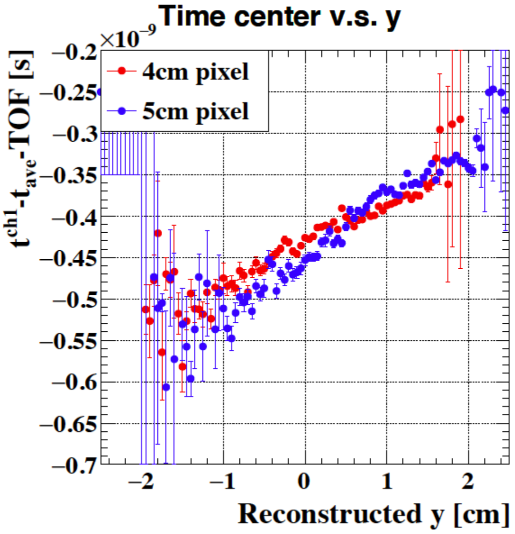

Fig. 6.36: The y-dependence of the timing center in a counter at the edge ($x_{\mathrm{hit}} > 5$ cm) with MC to reproduce the 2017 data [24].

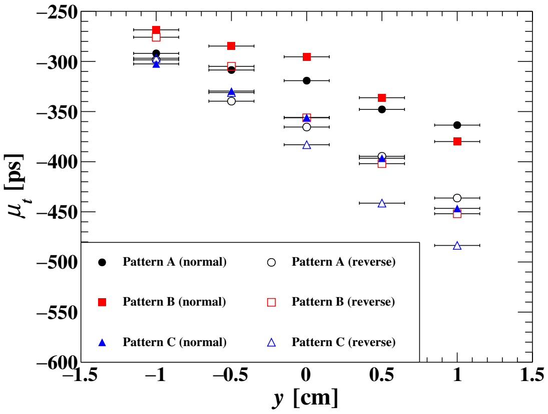

Fig. 6.37: Position dependence of the time center in a counter at $x = -4.25$ cm. The applied voltage was fixed to 162.5 V at 30°C [31].

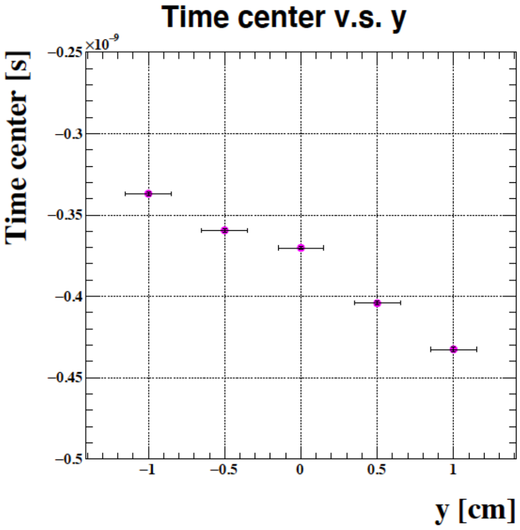

Fig. 6.38: The y-dependence of the timing center in a counter at $x = -4.25$ cm [24].

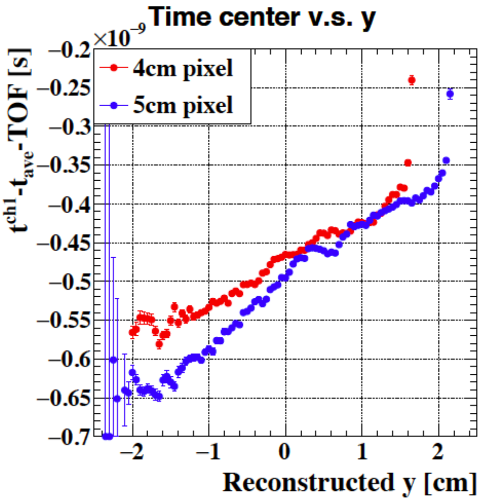

Fig. 6.39: The y-dependence of the timing center in a counter at the edge ($x_{\mathrm{hit}} > 5$ cm) with 1.8 times increased dependence, i.e. 108 (4 cm counters)/135 ps (5 cm counters) time offset between adjacent SiPMs [24].

Chapter 7

CDCH Analysis

In this chapter, the waveform analysis of the MEG II CDCH is described. Then, the comparison between the commissioning data in 2018 and the simulation is discussed. The CDCH tracking algorithms are explained based on the updated simulation.

7.1 Waveform Analysis of CDCH

When positrons pass through the CDCH cells, the noble gas particles in the mixture (He) are ionized and the electrons move toward an anode wire and are then amplified by the avalanche process around an anode wire. The nominal gas gain for MEG II CDCH is 5×10^5[*1]. The signal of CDCH is induced by those electrons. The average hit rate of CDCH cells(~ 1 MHz) is one order higher than pTC (~ 100 kHz), and especially inner layers are more severe (~ 1.8 MHz) due to the gradient magnetic field. The number of ionization clusters is different event by event, and signal height also differs due to the fluctuation in the avalanche process and the space-charge effect. The average cluster densities of the gases are $N_{\mathrm{He}} = 7.4$ /cm and $N_{\mathrm{Iso}} = 54$ /cm. The slow drift velocity of the ionized clusters (~ 2 cm/μs) limits the time resolution of the wire measurement. To reconstruct CDCH data in such severe conditions, a novel algorithm of the CDCH waveform analysis was developed. The CDCH waveform analysis is mainly composed of two steps.

7.1.1 Signal Search

Signal pulses are searched for in a predefined timing window (~ 300 ns from the trigger timing, which is the maximum drift time for a hit). The pulse search threshold is defined from the RMS noise value calculated from the baseline region and default value is $5 \times N_{\mathrm{RMS}}$. The pulse information such as the edge timing, the peak timing and so on is calculated from the sampling points of the waveform crossing the threshold and recorded for the next step.

7.1.2 Cross-Fitting

The idea of the cross-fitting algorithm is to use the waveform from one wire end as the template of the waveform and to fit the waveform of the other end using template from one wire end. This procedure is expected to improve the signal finding efficiency. In addition, the timing difference and height difference between both ends are used for the local-z reconstruction.

The shape of the signal waveforms obtained at the two ends is assumed to be the same except for the pulse amplitude and the timing offset. The χ^2 to be minimized is defined as below:

$$\chi^2 = \int \frac{(f(t) - c \times g(t+\tau))^2}{\sigma^2} dt, \tag{7.1}$$

[*1] The gas gain value can be tuned with the applied voltage, but the operation with too high applied voltage will result in the fast aging of the wire chamber, for example, loss of gain, loss of response uniformity, and electrical instability. The detailed study on the aging for MEG II CDCH is reported in [68].

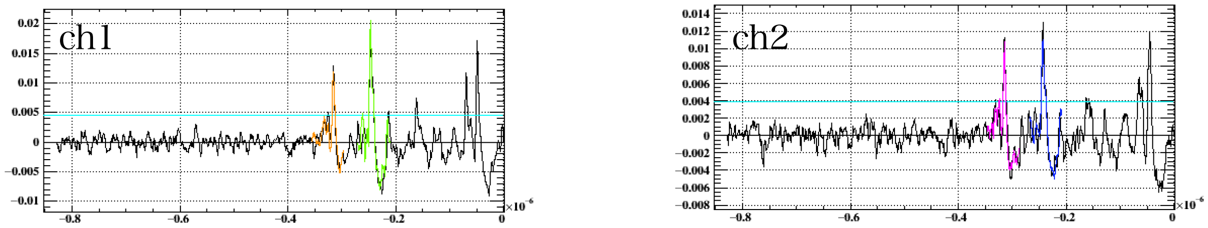

Fig. 7.1: The example of the simulated CDCH waveforms and the cross-fitting algorithm. The sky-blue horizontal line shows the threshold for the signal finding, and the orange, green, magenta, and blue lines on the waveform shows the fitted results, respectively.

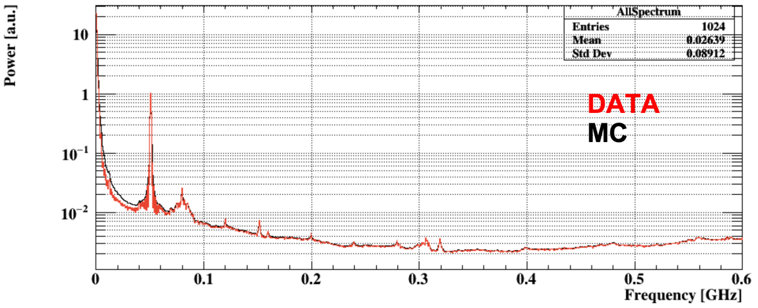

Fig. 7.2: The noise spectrum of the CDCH noise in 2018.

where $g(t)$ is the fit function (the waveform from one end), $f(t)$ is the waveform from the other end, τ is the fitting parameter for the time difference. and c is also the fitting parameter to scale the pulse amplitude. When a signal was found in one end, the waveform was stored within a pulse packet range (-20 ns – +40 ns in a figure) and used for the χ^2 calculation with MINUIT[*2]. Fig. 7.1 shows the example of the waveform from two ends of a wire. This cross-fitting finds the CDCH pulses with “OR” logic of the two ends. Under the severe S/N condition, this method drastically recovers the pulse finding efficiency compared to the algorithms used in [7]. The efficiency of track reconstruction for signal positrons without pileups is improved from 13% (27% for hit reconstruction) to 80% (69% for hit reconstruction) with the updated simulation.

7.2 Analysis of Low Rate Data

The algorithm for the CDCH waveform analysis applied to the commissioning data taken in 2018 (with 1.34×10^7 muon beam) and 2019 (cosmic rays).

7.2.1 Noise Reduction

Fig. 7.2 shows the power spectrum of the periodical noises observed in 2018 in the experimental area, and the typical waveforms taken in the 2018 commissioning are shown in Fig. 7.3. There were two major sources of the noises in the CDCH as shown in Fig. 7.2: the low-frequency noise from the intermediate DIFF-to-SE converters which were used in the prototype electronics in the 2018-2019 commissioning and the 50 MHz noise from the ground loop of the signal cables, which might be related to the accelerator frequency (RF frequency). Fig. 7.4 shows the example of the 50 MHz strong noise (black lines) observed in 2019. The red lines are the fitted results with sine functions. The subtraction of 50 MHz

---

[*2] MINUIT in C++ implementation from ROOT reference guide [69].

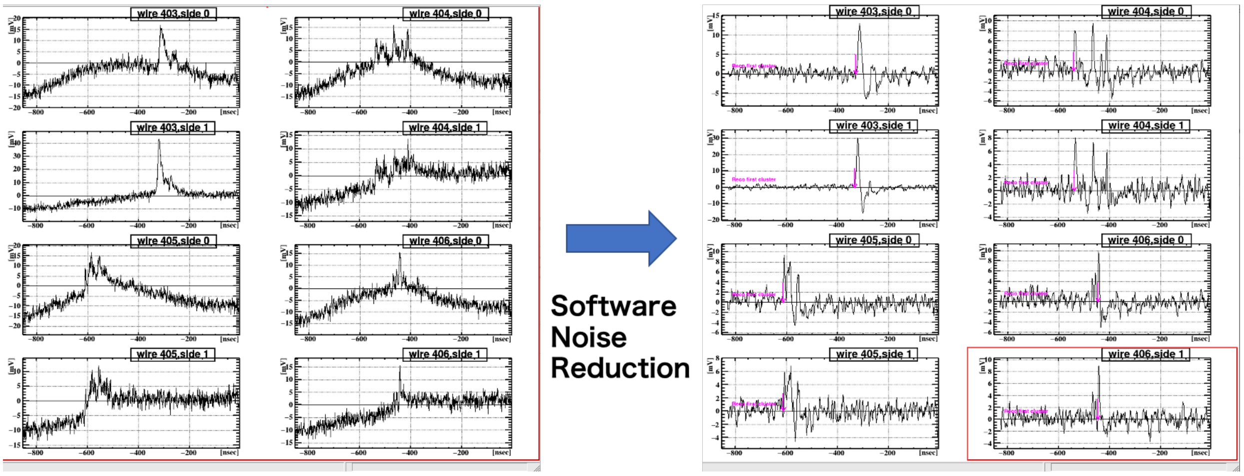

Fig. 7.3: The example of the CDCH waveform with the muon beam rate of 1.34×10^7 taken in 2018 commissioning.

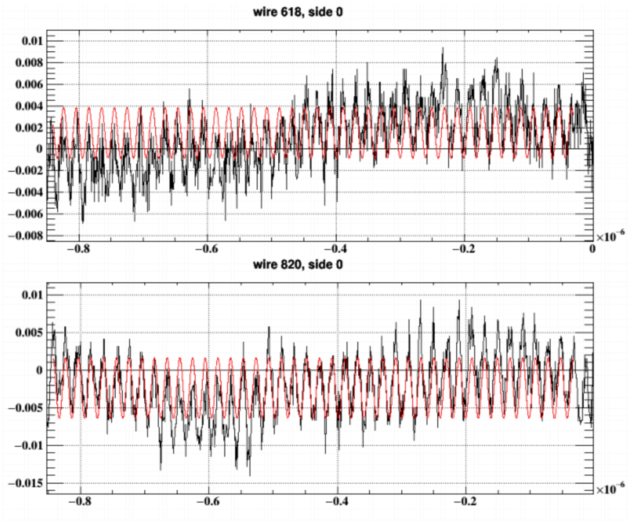

Fig. 7.4: (Black) The observed 50 MHz noise in the 2019 commissioning. (Red) The template noise spectrum extracted from the waveform themselves by the sine fitting.

noise was not applied to the data taken in 2018, since the digital filter (described below) was sufficient to reduce the noise in 2018. The DIFF-to-SE intermediate converter will not be used in the future (the differential input is adopted for the final version of the WDB for CDCH), and the ground loop of the signal is solved after the commissioning, so these problems will not be crucial for the future operation (the noise situation in 2020 is shown in Appendix F). As for the solution in 2018 and 2019, the noise reduction by the digital filter was found to be effective. Fig. 7.3 shows the comparison of the typical waveforms before/after the software noise reduction. The digital filter was composed of two types of the moving average filter: a smoothing filter with 5 points, i.e. the 5 points including the target point are averaged, and a high-pass filter with 31 points, i.e. the average of the 31 points before the target point are subtracted from the target point. The high-pass filter removed the low frequency large noise and the moving average filter reduced the RMS-noise from 2 mV to 1 mV at the peak region of the distributions.

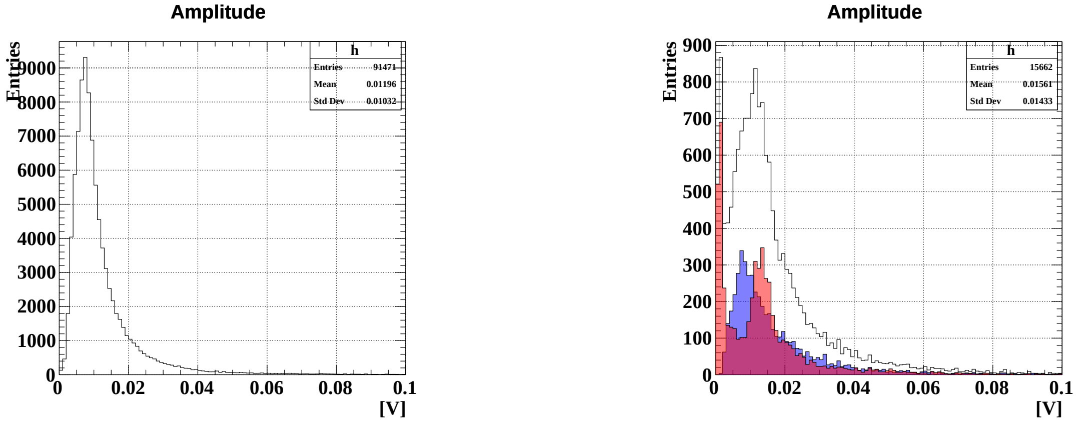

(a) 2018 CDCH amplitude ($1.34 \times 10^7 \mu$/s).

(b) 2019 CDCH amplitude (Cosmic). Red: Final Electronics, Blue: Prototype only.

Fig. 7.5: The signal amplitude histograms from the commissioning data taken in 2018 and 2019.

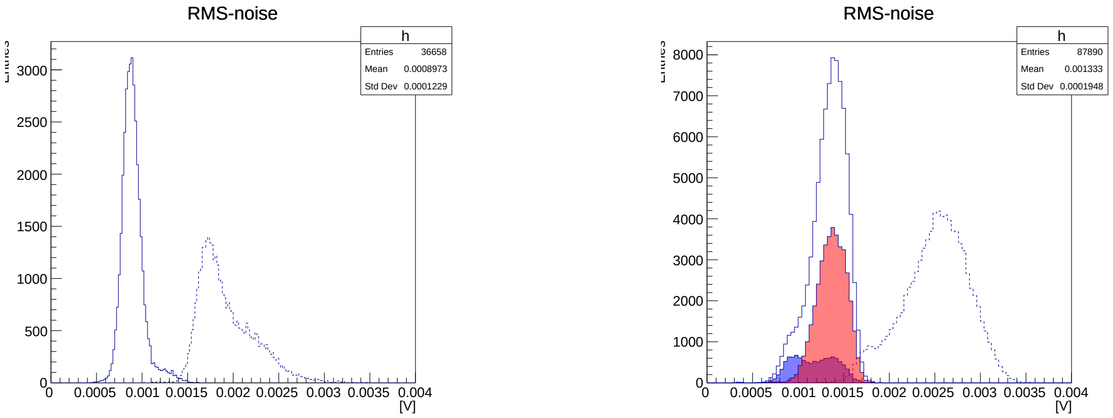

(a) 2018 CDCH RMS-noise ($1.34 \times 10^7 \mu$/s).

(b) 2019 CDCH RMS-noise (Cosmic). Red: Final Electronics, Blue: Prototype only.

Fig. 7.6: The RMS-noise histograms from the commissioning data taken in 2018 and 2019. The dashed line shows the RMS-noise calculated from the raw waveform and the solid line shows that after the noise subtraction by the moving average filter.

7.2.2 Observed S/N

After the noise reduction, the S/N of the CDCH waveform was extracted as shown in Fig. 7.5 and Fig. 7.6. The final version electronics (filled with red) seem to have slightly higher amplitude than the prototype (filled with blue) thanks to the differential readout. As for the RMS-noise, the distribution before the noise reduction (dashed line) and that after the noise reduction (solid line) are shown. The noise reduction algorithm significantly reduced the RMS-noise of the CDCH. In 2018, the RMS-noise had a long tail at larger side due to the large low frequency noise. In 2019, the peak of the RMS-noise became larger than 2018 due to the strong 50 MHz noise from the ground loops. The intrinsic component of the detector

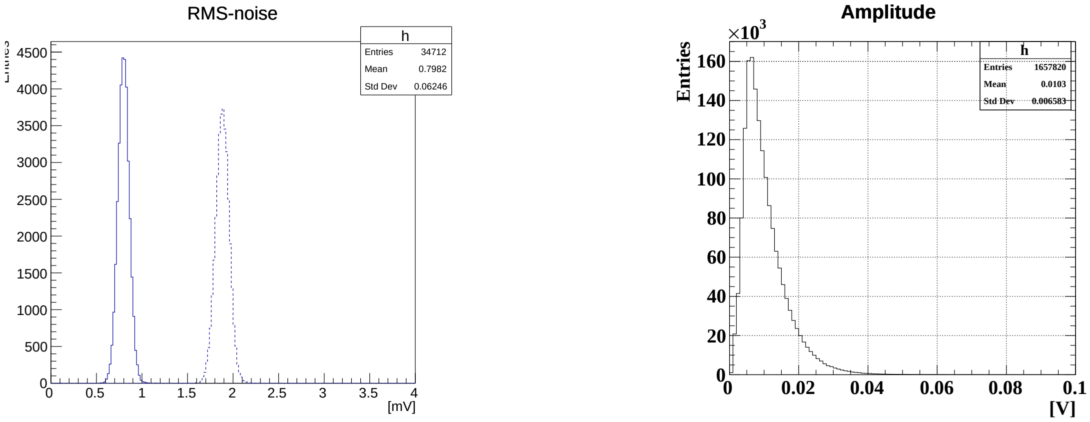

(a) CDCH RMS-noise (MC).

(b) CDCH amplitude (MC).

Fig. 7.7: The distributions of simulated RMS-noise (dashed line: before noise subtraction, solid line: after noise subtraction) and signal amplitude.

Table 7.1: The major updates of the CDCH waveform analysis after 2018 [7].

Settings	Before	Update	Note
Pulse Shape	Parametric	SPICE	S slightly decreased (~ 2/3)
Amp Gain [mV/fC]	0.545	0.146	S decreased by a factor of 3.7
RMS-noise [mV]	1	2	White-Gauss / 2020 noise spect (Appendix F)
Z-Dependence	None	Implemented	60% gain decrease at the edge
Diffusion	Per cluster	Per electron	Drift time fluctuation for each electron
Space-Charge	None	Implemented	Described in the next subsection
Number of Layer	10	9	~10% efficiency drop

white noise (the peak region of the RMS-noise distribution in 2018) is extracted to be ~ 2 mV before the noise subtraction and ~ 1 mV after the noise subtraction. The S/N of the CDCH (S (10 mV) /N (1 mV) $\approx$ 10) was much worse compared with the pTC (S (200 mV) /N (5 mV) $\approx$ 40).

7.3 Reproduction of Commissioning Data by MC Simulations

In this section, the major updates of the simulation from previous studies [7] are summarized.

7.3.1 Update of Simulation

The major updates from previous studies [7] are summarized in Table 7.1. Fig. 7.7b and Fig. 7.7a show the simulated S/N of the CDCH waveform. Fig. 7.8 shows the correlation of signal amplitudes at two ends before (left) and after (middle) the updates. The correlation in the real data from 2018 commissioning is also shown in right of Fig. 7.8. The correlation seen in real data is well reproduced by the updates of simulations (middle). The newly introduced SPICE-based signal shape contributed to a slight decrease in the signal size. The amp-gain of the CDCH frontend was modified from the design value to the actual value; the signal height became ~1/3.7.

As for the noise simulation, two choices were prepared: one is to use the white Gaussia noise with 2 mV mean, the other

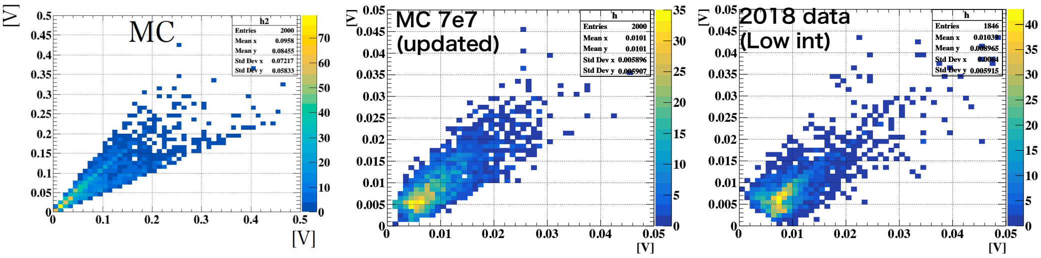

Fig. 7.8: The scatter plots of the simulated signal amplitude at ch1 (x-axis) and ch2 (y-axis). Left plot is before the update of the gain parameters, center plot is after the update, and right plot is from the commissioning data in 2018 (1.34×10^7 rate at 1460V). Note that the scale of the axis is one-order different between left plot and center/right plot.

is to use the noise spectrum observed during the commissioning. Since the difference of the two options was less than 1% on the efficiency, as described in Appendix F, the first option was used for the performance evaluation in the following chapters.

Based on the results of the gas-gain measurement from the prototype [26], the z dependence (described as quadratic function) was implemented. The diffusion was implemented per-electron level and each electron has its own drift time fluctuation due to diffusion. In addition, the space-charge effect was implemented to simulate the high-rate environment in the CDCH. The detail of the model was explained in the following subsection.

7.3.2 Space-Charge Effect for High Rate Environment

At the high gain in the CDCH, ions produced in the avalanche around the wire screen the electric field, and reduce the gain for electrons arriving later. This phenomenon is known as a "space-charge" effect. To extend the MEG II simulation to the high rate environment, this effect was newly implemented in 2019.

If a cluster produces a charge Q in an avalanche, a cluster arriving after a time $\Delta t < \frac{r_0}{v_0}$ is affected by the space charge:

$$Q^{\mathrm{SC}} = Q_0 \frac{r_0 - v_0 \Delta t}{r_0}, \tag{7.2}$$

with the assumption that the avalanche happens uniformly within the distance r_0, the avalanche has a lateral extension l_0, and ions move out from the wire with a velocity v_0. Then the electric field is reduced according to the following equation:

$$E = E_0 - \frac{\sum_i Q^{\mathrm{SC}}}{2\pi\epsilon r_0 l_0}. \tag{7.3}$$

Finally, gain is decreased as follows:

$$G = e^{\frac{E}{E_0}\log G_0}. \tag{7.4}$$

7.4 Comparison between MC and Commissioning Data at MEG II Beam Rate

Fig. 7.9a and Fig. 7.9b show the signal amplitude and the RMS-noise at each operation voltage in the 2018 commissioning with the muon beam of the MEG II intensity. The MC waveforms have the consistent amplitudes around the peak region (0 - 0.03V) with the commissioning data, where operation voltage was around 1520 V and gas gain was $\sim 1 - -2 \times 10^5$ [26]. The small discrepancy was seen in the region above 0.04 V, and the commissioning data had larger amplitudes than the MC.

As for the RMS-noise, the commissioning data in 2018 had the larger values than the MC due to the contribution from the intermediate converter and the ground loops, which will be disappeared in the future. In the MC, the contribution from these

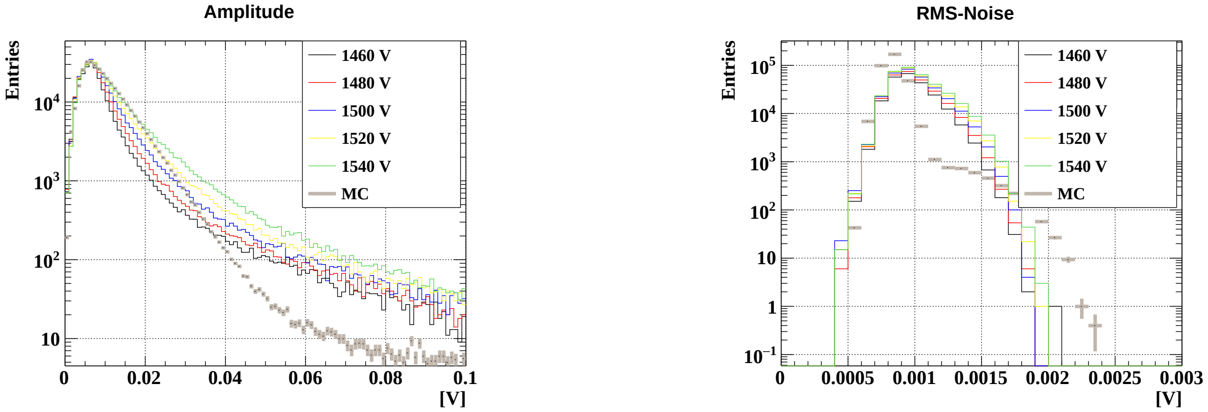

(a) The signal height with several operation voltages and the simulation after the noise reduction under the MEG II nominal beam rate. The number of entries for the MC was scaled to the number of the commissioning data at 1520 V.

(b) The RMS-noise with several operation voltages and the simulation after the noise reduction under the MEG II nominal beam rate. The number of entries for the MC was scaled to the number of the commissioning data at 1520 V.

Fig. 7.9: The signal height and the RMS-noise under the MEG II nominal beam rate.

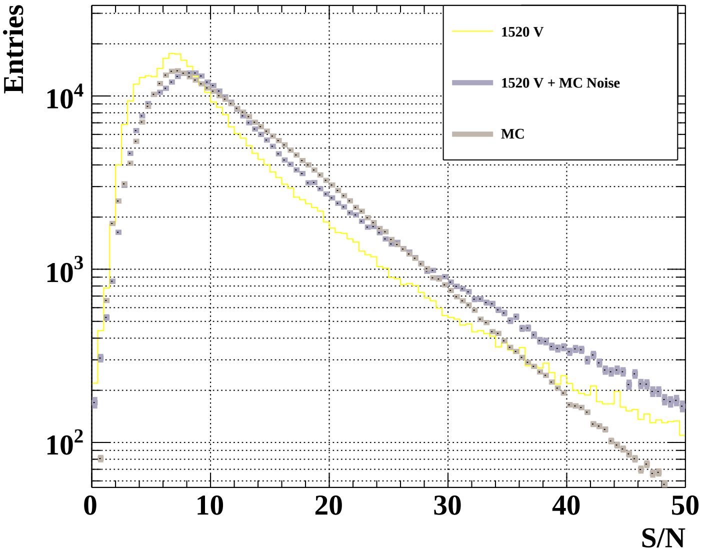

Fig. 7.10: S/N distributions from the commissioning data and the simulation. S from the commissioning data and N from the simulated mean (0.8 mV) is also shown.

equipment were removed and the 2 mV white noise was added instead. Fig. 7.10 shows the S/N of each waveform with three patterns; S/N from the commissioning data (yellow), S/N from the simulation (brown), and S from the commissioning data and N from the simulated mean, 0.8 mV (purple). Since the noise problems in CDCH were already fixed, higher tail in the RMS-noise will disappear in the future. Therefore, consistency between MC and 1520V+MC noise shows that the updated MC simulations are reliable enough. The S/N is one-order worse than the expectation in previous works [7].

7.5 CDCH Tracking Algorithms

In this section, the algorithms for the CDCH analysis after the waveform analysis, which are hit reconstruction, track finding, and track fitting, are described with MC. The goal of CDCH analysis is to reconstruct the positron tracks and estimate the state vector at the vertex on the stopping target. The state vector includes the kinematic variables related to the $\mu \to e\gamma$ search, i.e. position's momentum (angle) and timing information. Also, the covariance between the variables is calculated and used for the positron selection for physics analysis.

7.5.1 Hit Reconstruction

The CDCH hit reconstruction is performed based on the waveform analysis at the two ends.The important information of the CDCH hit is the local-z position on the wire and its impact parameter (b)[*3]. The target resolution of the z reconstruction is 10 cm, and b estimation 110 μm. For the local-z reconstruction, two methods have been developed.

Charge Division

The conventional charge division method has been adopted for the reconstruction of the z-coordinate on the wire [70]. By measuring the charge asymmetry between the two ends, the local-z can be measured as below:

$$z = \frac{G\frac{Q_{\mathrm{up}}}{Q_{\mathrm{down}}} - 1}{G\frac{Q_{\mathrm{up}}}{Q_{\mathrm{down}}} + 1}\left(\frac{Z}{\rho} + \frac{L}{2}\right), \tag{7.5}$$

where the first factor is the charge asymmetry calculated from the charges at both ends, the latter factor correspond to the effective wire length. The input impedance of the readout preamplifier circuit is typically 360 Ω and the wire resistivity is 175 Ω/m. G is the gain ratio between the two ends, which must be calibrated with the data.

Time Difference

The arrival timing difference between the two ends can be used to determine the z position. This is called the timing difference method. The local-z can be calculated as follows:

$$z = \frac{(t_{\mathrm{up}} - t_{\mathrm{up\ offset}}) - (t_{\mathrm{down}} - t_{\mathrm{down\ offset}})}{2} v_{\mathrm{eff}}, \tag{7.6}$$

where the t_{up}, t_{down} are the reconstructed timing at the two ends, v_{eff} is the effective velocity of the signal propagation on a wire. $t_{\mathrm{up\ offset}}$, $t_{\mathrm{down\ offset}}$ are the timing offset of the two ends.

Fig. 7.11 and Fig. 7.12 show the difference between the reconstructed z and the MC truth for the single Michel positron and the Michel positron with pileup positrons at the MEG II nominal intensity of the muon beam, respectively. The estimated resolutions of the core component (obtained fitting with mean$\pm 1\sigma$) are 3.2 cm from the time difference method and 11.5 cm from the charge division method under the muon beam intensity expected in the MEG II. The consistency between two methods, $z_{\mathrm{time\ diff}} - z_{\mathrm{charge\ div}}$, is also shown in the plots. The width is 11.8 cm, and the mean value is slightly shifted (~ -1 cm, which is due to the bias in the charge division method). The time difference method is much more precise than the charge division method and we use the z from time difference in the reconstruction procedure.

[*3] The positron track information or assumption is needed to calculate the impact parameter b as described in Sec. 7.5.2. Even if the local-z and b are obtained, there is still an ambiguity on whether a positron passed the left side of a wire or the right side. This ambiguity is iteratively solved in the track fitting process.

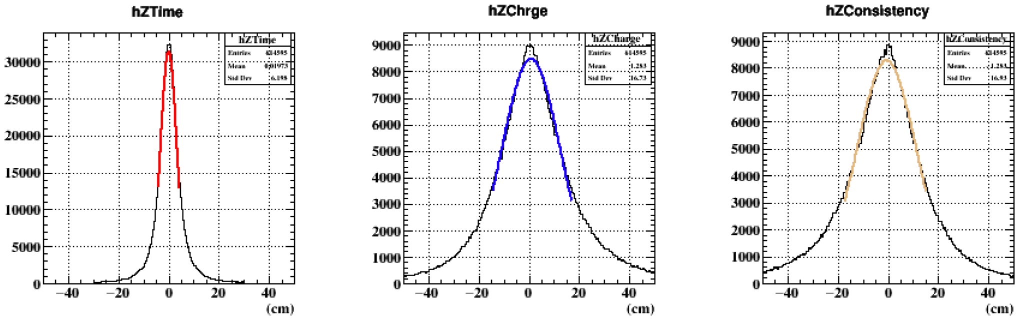

Fig. 7.11: The difference in z between the MC truth and the reconstruction (left: time difference, center: charge division). The right histogram shows the consistency between the two methods under the MEG II expected muon decay rate (7×10^7).

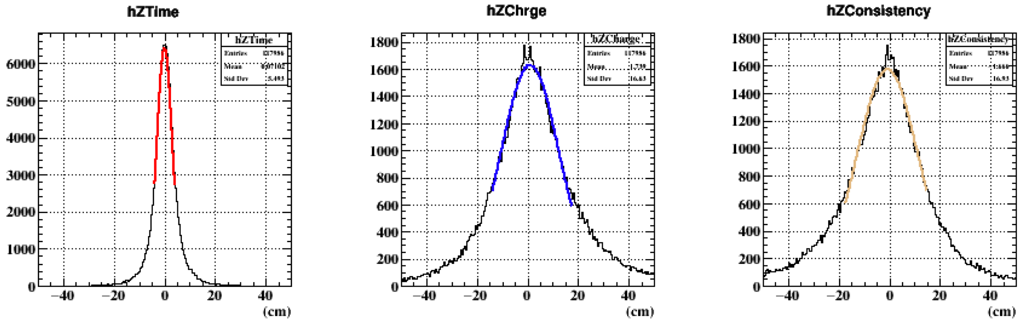

Fig. 7.12: The difference in z between the MC truth and the measurement (left: time difference, center: charge division). The right histogram shows the consistency between the two methods under the single Michel decay.

7.5.2 Track Finding

The nearby reconstructed hits are then clustered to reconstruct the positron track. This process is often called pattern recognition, or track finding in the field of particle physics. For the track finding algorithm, there are two major categories: one is the local following method and the other is the global following method. The concepts are summarized as follows:

- Local Following: Starting from a reliable track seed, nearby hits are added step by step. For example, Kalman Filter technique, local clustering.
- Global Following: All hits are treated equally and simultaneously at the process of clustering. For exmaple, Neural Net, circle fits.

In MEG II track finding, the local following algorithm based on the Kalman Filter technique is adopted. The algorithm starts from making seeds, and then those seeds are prolongated to tracks. The algorithm and codes are partially based on the Alice Offline Project (AliRoot) [71] and are developed by the MEGII CDCH tracking project.

The basic procedure of the MEG II track finding is as following:

- Calculate drift time for CDCH hits from the pTC clusters,
- Construct possible seed tracks from the outer layers,
- Extrapolate seed tracks,
- Compute track qualities.

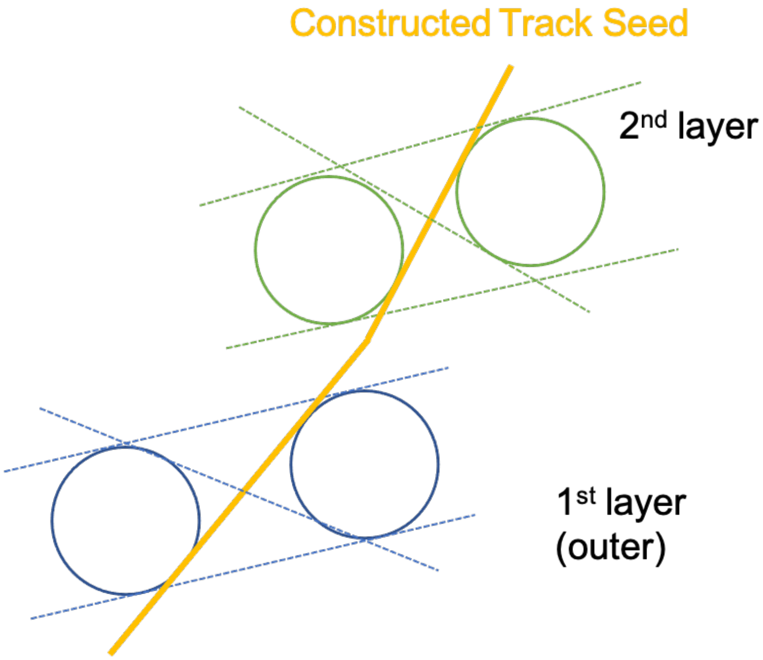

Fig. 7.13: The illustration of the CDCH seeding procedure. The blue and green circles show the drift circle, and the dashed lines are the candidate of the track (left-right for each circle). The yellow line shows the constructed track seed.

Fig. 7.13 shows the seeding procedure. To calculate the drift time and the impact parameter, the timing from pTC cluster is mainly used as the reference timing, T_0. The initial drift time is calculated as $t_{\mathrm{hit}} - T_0$[*4]. The coordinate of pTC clusters can be also used to filterate the initial CDCH hits for the seed to ~1/4 of CDCH full volume. Since the wire measurement is the 1-D measurement, it is impossible to know whether a positron passed through the left side or the right side of a wire only from the wire measurement. To solve this "left-right" ambiguity, a part of track has to be assumed from the possible patterns. The track seeds are mainly formed by two consecutive hit-pairs in two layers. The possible left-right patterns of the two hits are all checked in the same layer to estimate the direction, and the direction compatibility is checked with $|\Delta\cos(\phi(\mathrm{direction}) - \phi(\mathrm{position}))| < 0.2$. The difference between the reconstructed z position and the stereo-crossing z position, Δz, is also used for the consistency check of the two pairs. The pre-determined criteria for z consistency is $\Delta z^2 < 9 * 2 * \sigma_z^2$. σ_z can be optimized based on the data. In this thesis, fixed value of 10 cm was implemented. The reconstructed track seeds are then prolongated by the iteration of the extrapolation, hit addition and the Kalman Filter fitting. After the prolongation over a single turn, then the seeding and prolongation at the next turn region are tried.

The output of the pattern recognition has the many track candidates, including the ghost tracks. The quality factor, Q, is defined and calculated for each track candidate:

$$Q = l_{\mathrm{dense}}\, d_{\mathrm{max}} + n_{\mathrm{hit}} + 0.2\, n_{\mathrm{hit}}\, p(\chi^2, n_{\mathrm{dof}}), \tag{7.7}$$

where l_{dense} is the length (the number of the continuous layers) of the densest area of hits, d_{max} is the maximum density of the hits, n_{hit} is the number of hits in the candidate, $p(\chi^2, n_{\mathrm{dof}})$ is the probability value of the χ^2 with the degree of freedom n_{dof} from the track fitting. The first term means that the more continuous tracks have higher weight, the second term means the bigger tracks have the higher weight, and the third term means the tracks with the better χ^2 have the higher weight. The

---

[*4] At the seeding level, the averaged drift velocity of ~2.7 cm/μm is used for the calculation. The more precise b calculation is performed with the pre-calculated table of time-xy relation (t-xy table), the incident angle, and the TOF correction by the track information after completing the pattern recognition.

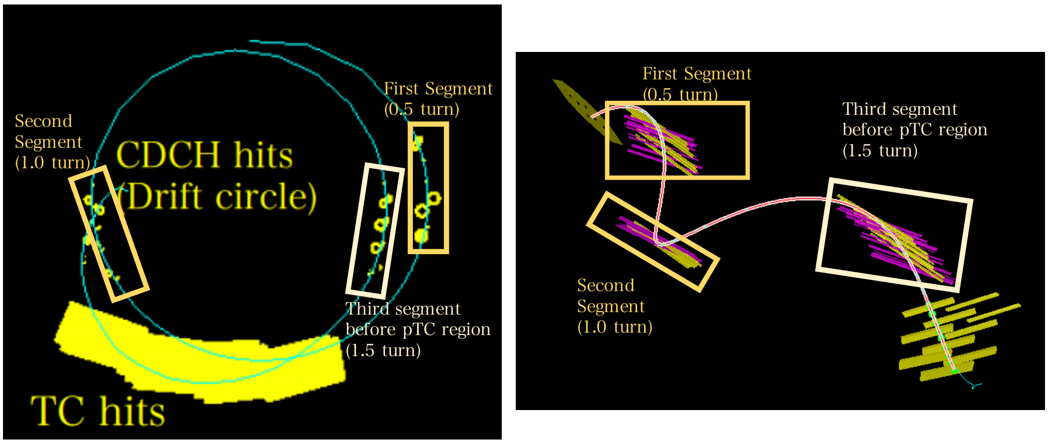

Fig. 7.14: Event monitor with a simulated signal positron from the x-y projected view (left) and the 3-D monitor from the top view (right).

factor 0.2 was manually tuned to maximize the reconstruction efficiency in the simulation. The tracks are removed from the output when they have 30% of hits who are already associated by the better quality track.

7.5.3 CDCH Track Fitting

In the final step of CDCH analysis, the positron tracks are reconstructed by using the fitting algorithms, and the best estimate of the state vector at the vertex is obtained. This task is composed of three steps: the DAF fitting, the turn merge and the extrapolation.

The track fitting of CDCH hits are performed with the DAF algorithm implemented in GENFIT. DAF (Deterministic Annealing Filter) algorithm is an extension of the Kalman Filter (KF) technique with the re-weighted (assignment) measurement and the outlier hypothesis. The probabilities of the measurements, which are the “left” measurement and the “right” measurement on a wire measurement case, are assigned. Those measurements then compete each other during the iteration process of the KF technique. The higher assignment measurement will survive the fitting iteration, and the lower assignment measurement will be frozen out[*5]. The sum of probabilities on a detector plane can be < 1, which means the inconsistent measurement can have the small probability. Such inconsistent measurements can be removed. These characteristics are suitable for the fitting with wire measurements.

Then the fitted tracks from different turns are merged. The typical positron trajectory has 1.5 turns before entering pTC as illustrated in Fig. 7.14, and crosses the CDCH active volume three times (leaves three track segments). To achieve the target resolution, these all segments must be merged for fitting. This turn merge is based on the consistency of position and timing between the state vectors extrapolated to the plane defined at the center of the two segments. The turn merge criteria should be wider than the resolution since the number of hits and the path length is not large enough with the only single segment. For example, the momentum matching $|\Delta p| < 5$ MeV, the timing matching $|\Delta t| < 20$ ns, the position matching $|\Delta z| < 10$ cm and $|\Delta r| < 10$ cm, the angle matching $|\Delta\theta| < 0.2$ rad and $|\Delta\phi| < 0.2$ (outer) or $|\Delta\phi| < 0.5$ (inner) rad. If multiple tracks become the candidates for one segment, the χ^2 values, which are calculated from the DAF fittings are compared and the best pair is accepted. After the fitting again with full segments, the track state vector is extrapolated by the Runge-Kutta algorithm to the stopping target to find the vertex position. The flight time from the vertex to the pTC

[*5] The DAF procedure can be considered as the thermodynamical approach since its assignment probability is the function of a parameter, T, which can be considered as the temperature. The freezing out up to “hard” ($T = 0$) is equivalent to χ^2 cut.

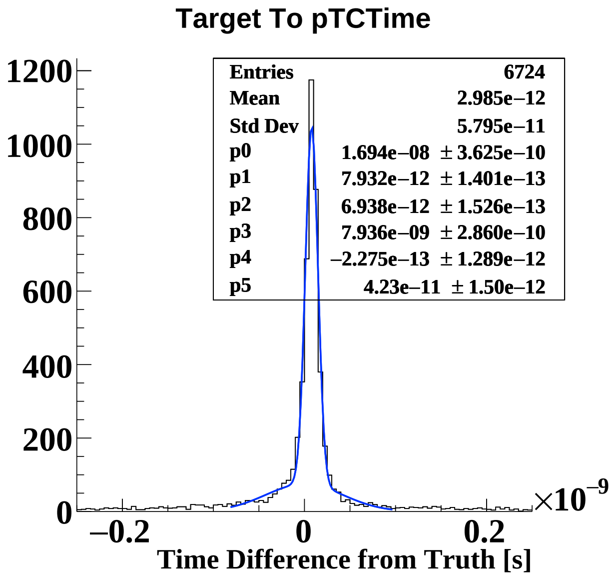

Fig. 7.15: The estimated flight time precision ($\sigma_{\mathrm{TOF}} \approx 6.9$ ps) in the CDCH region with the simulation.

(i.e. inside the CDCH region) is calculated from the path length of the reconstructed track divided by the speed of light. Fig. 7.15 shows the estimated flight time precision, 6.9 ps, which is twice better than 14.8 ps from [7] since not only the information from the forward propagation but also that from the backward propagation of the KF algorithm was utilized in this thesis. The formulation of the KF algorithm is explained in detail in Appendix D.

Chapter 8

Performance of Positron Spectrometer

The pTC and CDCH algorithms were described in the previous chapters. In this chapter, the pTC and the CDCH combined algorithms, which are developed for the performance evaluation of the positron spectrometer, are described. The resolutions of the positron spectrometer had not been evaluated with realistic MEG II conditions in previous studies [7]. In this thesis, the performance of the positron spectrometer is evaluated based on the MEG II simulations tuned by the commissioning data.

8.1 CDCH-pTC Combined Analysis for Global Tracking

The goal of the CDCH-pTC combined analysis is to reconstruct the global positron tracks and obtain the refined information at the vertex. This analysis is composed of two steps; the CDCH-pTC Matching and the pTC-CDCH Global Tracking.

8.1.1 CDCH-pTC Matching

The reconstructed positron track in CDCH is extrapolated to the pTC and associated with the pTC cluster, and then the pTC hits are re-fitted by the DAF algorithm using the momentum information from the CDCH tracking. The state vector from the CDCH track fitting is extrapolated to the pTC clusters, and the matching between the extrapolated position and the pTC counter position is tested. Fig. 8.1 shows the difference between the pTC hit position and the CDCH extrapolated position. The criteria for the position difference is 5σ for the pTC local-x direction (i.e. $x_{\mathrm{extrapolated}} - x_{\mathrm{counter}} < 5.5$ cm) and 10 cm for the 3D distance (i.e. $\sqrt{(x_{\mathrm{extrapolated}} - x_{\mathrm{counter}})^2 + (y_{\mathrm{extrapolated}} - y_{\mathrm{counter}})^2 + (z_{\mathrm{extrapolated}} - z_{\mathrm{counter}})^2)} < 10$ cm) . The difference between T_0 of the CDCH track and the pTC timing is also checked (± 15 ns timing window). The distribution

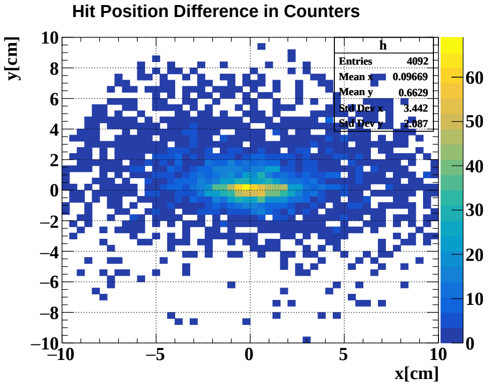

Fig. 8.1: The difference between the pTC hit position and the CDCH extrapolated position.

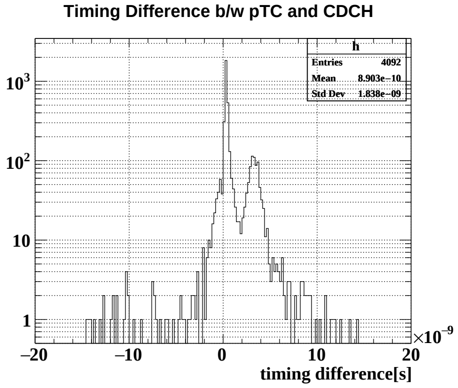

Fig. 8.2: The timing difference between the pTC clusters and the CDCH tracks. ±15 ns timing window for the matching is applied.

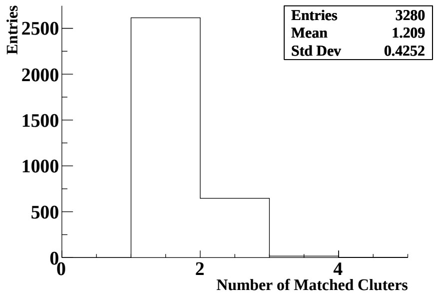

Fig. 8.3: The number of matched cluters for one CDCH track.

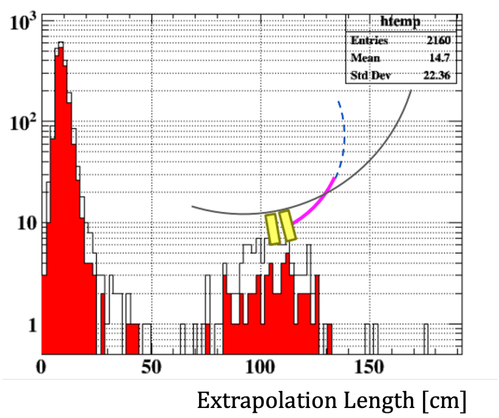

Fig. 8.4: The propagation length from the CDCH region to the pTC counter which is illustrated in the histogram: the length of the pink line is the propagation length, the black circle is the CDCH outer foil, and yellow boxes are pTC counters. The red histogram shows the after 5σ resolution cut.

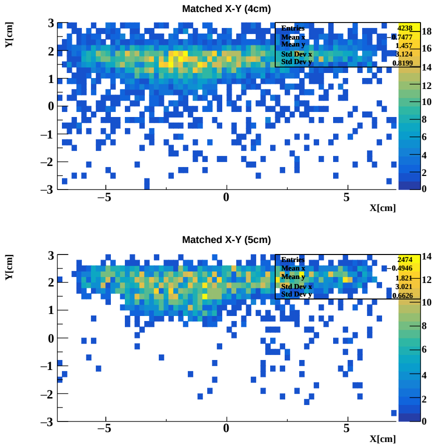

Fig. 8.5: The distribution of (x, y) matched positions in the counter local coordinate. Up: 4cm counters (the counter region is ±6 cm for x and ±2 cm for y), down: 5 cm counters (±6 cm for x and ±2.5 cm for y).

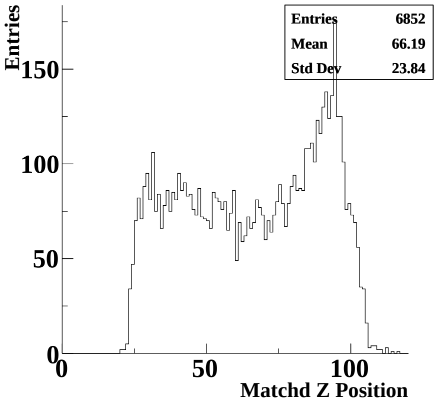

Fig. 8.6: The matched $|z|$-position.

of the timing difference after the matching is shown in Fig. 8.2. If the multiple CDCH tracks match with one pTC cluster, the extrapolation lengths are compared since the large distance of the extrapolation increase the uncertainty, resulting in the worse path-length estimation. For example, Fig. 8.3 shows the number of the matching with pTC clusters for one CDCH track. Fig. 8.4 shows the extrapolation length of CDCH tracks (black histogram). The tracks within the 5σ from the truth are also shown (red histogram). Most of the good resolution tracks have shorter extrapolation length, since they have the

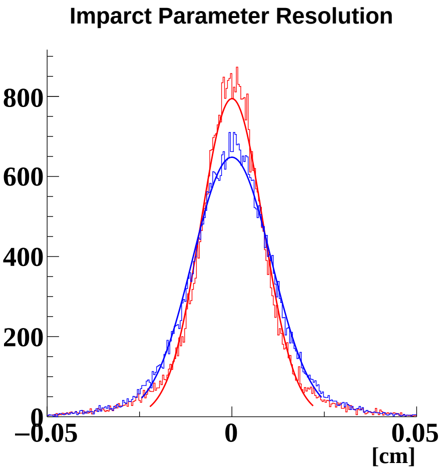

Fig. 8.7: The impact parameter resolutions with a simulated signal positron. The blue histogram was updated to the red histogram by the pTC-CDCH track re-fitting. The resolution changed from 106 μm to 85 μm (the standard deviation from 123 μm to 112 μm).

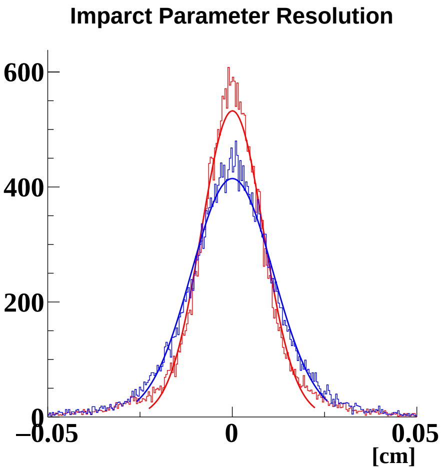

Fig. 8.8: The impact parameter resolutions with a simulated signal positron and 7×10^7 Michel positrons. The blue histogram was updated to the red histogram by the pTC-CDCH track re-fitting. The resolution changed from 111 μm to 84 μm (the standard deviation from 130 μm to 114 μm).

track segment just before the pTC region as shown in Fig. 7.14. For these reasons, the pair with the shortest distance is selected. Fig. 8.5 shows the (x, y) distribution of the extrapolated CDCH tracks for matched positrons in the counter local coordinate, and Fig. 8.6 shows that of the $|z|$ matched position in the global coordinate. Since one positron crosses 8 – 9 counters on average, the first matched counter tends to have high y-position.

8.1.2 pTC-CDCH Global Track Refinment

The positron track information in the CDCH and the timing information in the pTC are now available. The next step is the refinement of the positron global tracks by utilizing both information.

Track Refinement by pTC Timing

The timing information from the pTC is used for the re-calculation of the drift time. The accuracy of the timing at each CDCH hits are not so good (~ ns) before the refinement. The positron crossing timing at each cell, T_0, should be refined with the reconstructed pTC timing and CDCH TOF information. The drift time $t_{\rm drift}$ is calculated as follows:

$$t_{\rm drift} = t_{\rm CDCH\ Hit} - (t_{\rm pTC\ cluster} - \Delta T_{\rm Path}), \tag{8.1}$$

where $t_{\rm CDCH\ Hit}$ is the measured time of the CDCH hit on the wire, $t_{\rm pTC} - \Delta T_{\rm Path}$ is the refined T_0 with the pTC timing from the pTC cluster ($t_{\rm pTC\ cluster}$) and the flight time calculated by the path length from the pTC counter to the track point in the hit cell ($\Delta T_{\rm Path}$). Fig. 8.7 and Fig. 8.8 show the impact parameter resolution before (blue) / after (red) the refinement[*1]. The impact of the refinement is ~20% improvement for σ_r.

[*1] The refinement is effective when the track is combined with the correct cluster. When the track parameter is refined with the wrong cluster, the impact parameter resolution will be deteriorated. In principle, the matching criteria is severe enough to avoid the wrong matching of signal-like positrons, however, this should be noted for the background analysis.

Table 8.1: The timing resolution (calculated from the pTC performance in Table 6.6 and the path length estimation of the CDCH in Fig. 7.15) at the vertex.

With CDCH Information from Simulation	Updated	Previous [7]
TOF Resolution in CDCH	6.9 ps	14.8 ps
Resolution At Vertex (2017)	37.6 ps	44.1 ps (41.2 ps in [7])
Resolution At Vertex (Full Radiation, 10°C)	48.1 ps	55.4 ps
Resolution At Vertex (Full Radiation, 30°C)	59.8 ps	68.3 ps

Timing Reconstruction by Global Tracking

The timing of the matched point of the tracks from the CDCH and the pTC (t_{pTC}) is calculated by using all the hit timings (t_i, i = 1, 2, ... n) in the pTC track with the correction for TOF from the first hit counter to the i-th hit counter (TOF_i):

$$t_{\mathrm{pTC}} = \Sigma_i^n \frac{1}{n}(t_i - \mathrm{TOF}_i). \tag{8.2}$$

The timing at the target is then calculated by using the flight length from the target to the matched point ($\mathrm{L}_{\mathrm{CDCH}}$):

$$t_{\mathrm{vertex}} = t_{\mathrm{pTC}} - \mathrm{L}_{\mathrm{CDCH}}/c. \tag{8.3}$$

Table 8.1 summarized the timing resolution at the vertex (σ_t) combined with the pTC resolution ($\sigma_{t_{\mathrm{pTC}}}$) and the CDCH path length estimation ($\sigma_{L_{\mathrm{CDCH}}/c}$) as follows:

$$\sigma_t = \sqrt{\sigma^2_{t_{\mathrm{pTC}}} + \sigma^2_{L_{\mathrm{CDCH}}/c}}. \tag{8.4}$$

8.2 Positron Spectrometer Performance

The improvements of the positron reconstruction efficiency and the detector resolution are the crucial updates in the MEG II experiment. In this section, criteria of the performance evaluation for the positron spectrometer is described.

8.2.1 Definition of Reconstruction Efficiency

The denominator of the efficiency is the total number of the events, where the gamma-ray from signal decay enters the LXe detector acceptance ($|u| < 23.9$ cm, $|v| < 67.9$ cm). The numerator of the efficiency is the number of the selected signal events with the following conditions.

8.2.2 Global Track Selection

Most of the triggered events include more than one positron track due to high beam rate. The best candidate for the positron track has to be selected. The selection task, which is the final step of the global tracking chain, is composed of the following components:

- Track pre-selection,
- pTC track selection,
- Quality selection,
- Track selection.

Track pre-selection

In the actual physics analysis, the raw data size will be huge and a pre-selection will be applied to reduce the data size and calculation time. The pre-selection criteria is summarized below:

- Propagation to the pTC region and back-propagation to the target from CDCH tracks is succeeded,
- 40 MeV $< P_{\rm rec} <$ 65 MeV,
- -12 ns $< \delta t_{e\gamma} <$ 12 ns,
- -1 $< \cos(\delta\theta_{e\gamma}) <$ -0.9,

where $P_{\rm rec}$ is the reconstructed momentum at the target, $\delta t_{e\gamma}$ is the timing difference between a gamma-ray and a positron, $\delta\theta_{e\gamma}$ is the opening angle between a gamma-ray direction and a positron direction. The reconstruction and selection of the gamma-ray in the triggered event is completed before the positron track pre-selection. The rate of high energy gamma-rays are lower than that of high energy positrons, and a signal like gamma ray can be well separated from the pile up gamma-rays. Note that a pre-selection with too strong criteria will cause a selection bias and the criteria should be loose enough compared to the region of interest. For example, the $\mu \to e\gamma$ blinding box of $\delta t_{e\gamma}$ in MEG experiment was -1 ns $< \delta t_{e\gamma} <$ 1 ns and timing sideband was -0.7 ns $< \delta t_{e\gamma} \pm 2 <$ 0.7 ns, which were determined by the detector resolution and the range of the likelihood analysis. Pre-selection should be much wider than these values. In addition, the momentum values from the Michel positrons will be used to extract the momentum resolution of the spectrometer, as described in Appendix G. The wide range is needed for the pre-selection, and the above criteria was set in this thesis.

pTC Track Selection

The CDCH tracks can match more than one pTC cluster, so we should select the best pTC track (i.e. choose the best positron timing measurement). The first cluster, i.e. pTC cluster in the smallest $|z|$ region, is selected. This is because that the latter clusters are more affected by the scattering and energy loss from materials (first pTC cluster, CDCH outer foil, wires and so on). The resolution of the path length also becomes worse due to the large propagation length.

Quality Selection

The quality of the reconstructed CDCH track is checked. The "quality" does not depend on the event types (signal or Michel background events). In the KF fitting, the χ^2/dof represents the quality of track fitting. The following criteria are checked in the quality selection:

- $N_{\rm CDCH\ hit} \geq 9$: require more than one hits per layer on average.
- $0 \leq N_{\rm CDCH\ turns} \leq 10$: reject tracks with too many turns.
- $\sigma_P^{\rm track} <$ 1 MeV: reject the tail tracks.
- $\sigma_\phi^{\rm track} <$ 30 mrad: reject the tail tracks.
- $\sigma_\theta^{\rm track} <$ 20 mrad: reject the tail tracks.

where $N_{\rm CDCH\ hit}$ is the number of the hits in the CDCH track, $N_{\rm CDCH\ turns}$ is the number of turns on a CDCH track, $\sigma_P^{\rm track}$, $\sigma_\phi^{\rm track}$, $\sigma_\theta^{\rm track}$ are the square root of the corresponding diagonal component of the covariance matrix from a state vector of the starting point on the track.

Fig. 8.9 shows the number of positron tracks in each event (black), one after the track pre-selection (purple), and one after the track quality selection (red). Most of the low quality tracks are rejected by up to the quality selection, and the events which still have more than two tracks are only a few %.

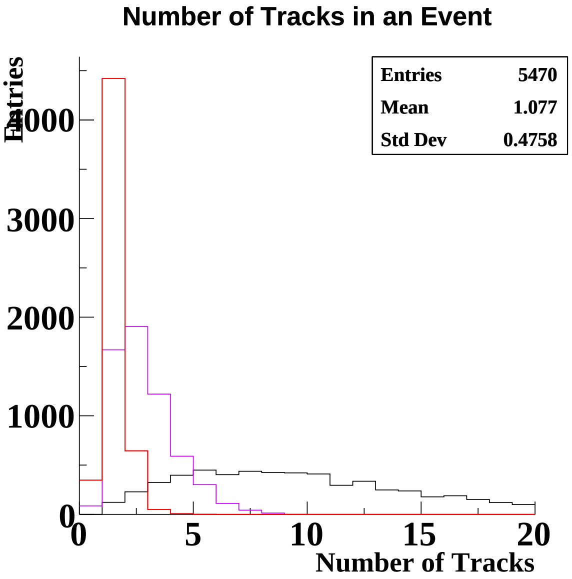

Fig. 8.9: The number of positron tracks in each event with no selections (black), those with the track pre-selection (purple), and those with the track quality selection (red).

Track Selection

A track selection is applied on the qualified CDCH and pTC track pair to select the best track to be used in the physics analysis. The track selection is composed of the following steps:

1. Target volume check
2. Acceptance check
3. Covariance check
4. Ranking

All of the positron tracks used for the physics analysis must come from the target. The target fiducial area is defined as the ellipse:

$$\frac{(y - y_{\mathrm{offset}})^2}{y_{\mathrm{target}}} + \frac{(z - z_{\mathrm{offset}})^2}{z_{\mathrm{target}}} = 1. \tag{8.5}$$

Where y_{offset} and z_{offset} are the offset values for the target center position, y_{target} and z_{target} are the semi-minor and semi-major axes of the target ellipse. The reconstructed position, $(y_{\mathrm{rec}}, z_{\mathrm{rec}})$, must be inside the target fiducial area.

The second step is to check whether the positron track is in the acceptance range or not. The positron acceptance for $\mu^+ \to e^+\gamma$ search is defined with the LXe detector acceptance ($|u| < 23.9$ cm and $|v| < 67.9$ cm). From the vertex position, the state vector is extrapolated linearly opposite to the positron emission direction. When that state vector is inside the fiducial volume at R = 64.84 cm, the event is accepted for physics analysis.

The third step is to check the values in the covariant matrix of the track at the vertex position. Since the tracking algorithm adopts the KF technique and we have the covariance matrix on each track, the per-track error (per-error, σ') can be defined as the diagonal components of the covariance matrix at the vertex point. If the per-error is large, that track is not used for the physics analysis. Fig. 8.10 shows the distribution of each per-error. The per-error criteria is determined by the distribution of as follows:

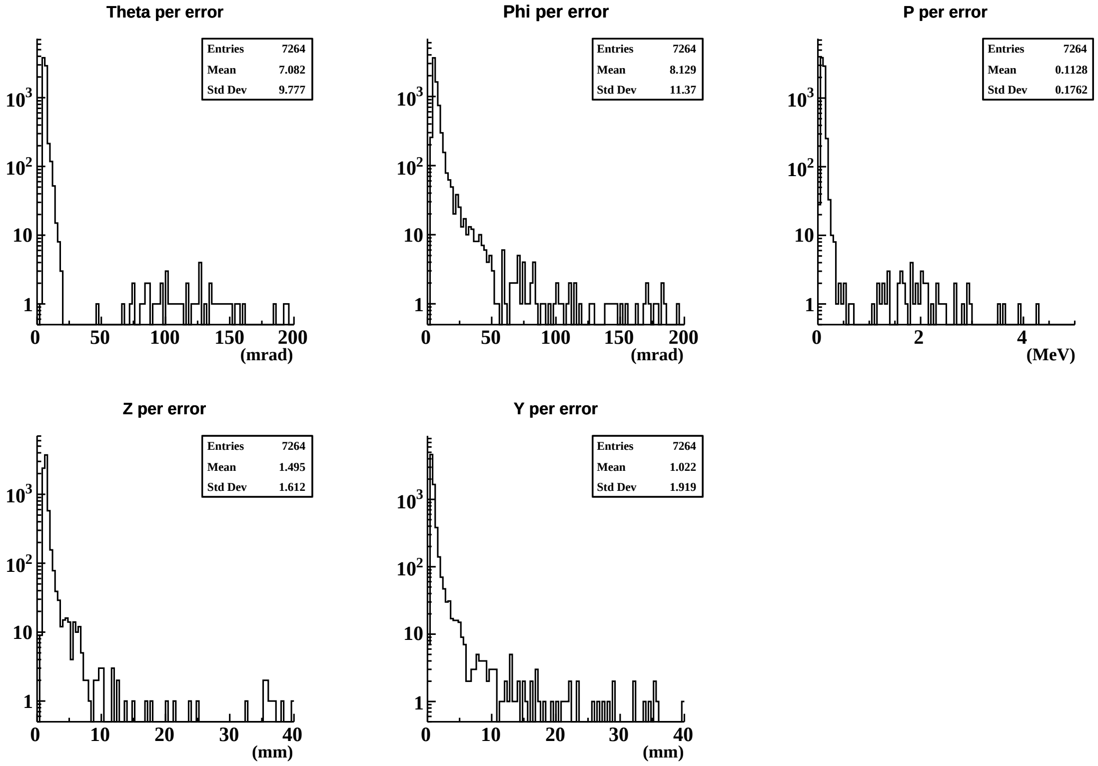

Fig. 8.10: The distribution of the per-errors of MEG II kinematic parameters.

- $\sigma'_P < 1$ MeV
- $\sigma'_\phi < 30$ mrad
- $\sigma'_\theta < 20$ mrad
- $\sigma'_z < 1$ cm
- $\sigma'_y < 1$ cm

The final step is the ranking. Based on the ranking value (currently just the reduced χ^2 value of each track), the best track in an event is selected. The distribution of χ^2/dof is shown in Fig. 8.11. The distribution of tracks after the all selections including the tail cut is also shown in the histogram filled with red.

8.2.3 Truth Check

The MEG II simulation file is made by mixing a single signal event and Michel events with the rate of $7{\times}10^7$e$^+$/s. After the track selection, the selected track is checked whether it is really a signal event or not by using the MC truth information.

8.2.4 Tail Cut

The track parameters (vertex, angle, and position) are checked by using the MC truth. If the reconstructed value is consistent with the MC truth within 5σ, that event is used for the physics analysis. This 5σ region is defined as Table 8.2.

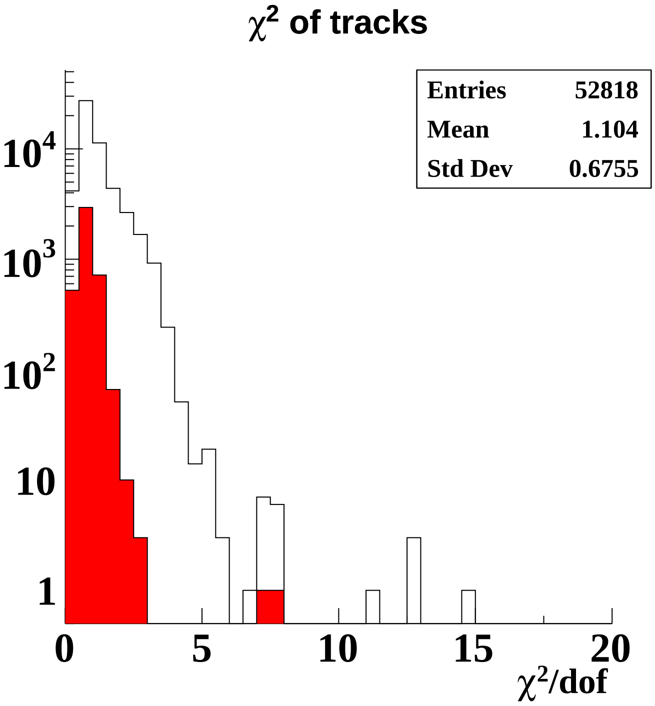

Fig. 8.11: The distribution of the χ^2 of tracks (black) and selected tracks with good quality (red, within 5σ tail cut).

Table 8.2: The criteria for the 5σ efficiency cut.

Variable	σ	5σ
θ [mrad]	6.1	30.5
ϕ [mrad]	5.6	28.0
P [MeV]	0.09	0.45
z [mm]	1.5	7.5
y [mm]	0.76	3.8
t [ps]	40	200

8.2.5 Angle Correlation Correction

The correlation of the parameters, as shown in Fig. 8.12 in the signal region, is corrected. The correlation is obtained from the 2D plot of θ and ϕ, and the projected resolution of ϕ (σ_ϕ) is calculated with the slice of each θ. The weighted average value of the σ_ϕ with each slice is quoted. The projected σ_ϕ is 4.9 mrad (σ_ϕ without the correction was 6.2 mrad) with the pileup of 7×10^7e$^+$/s.

8.2.6 Resolution and Efficiency

The resolutions and efficiency evaluated with the MC for five cases are summarized in Table 8.3. The four cases correspond to one signal in one event without backgrounds, and with muon rates at 3×10^7, 5×10^7, and 7×10^7. The last case ”Optimistic” assumes that the signal gain of the CDCH is recovered to the design value.

The difference between the MC truth and the reconstructed kinematics with the pileup of 7×10^7e$^+$/s are shown in

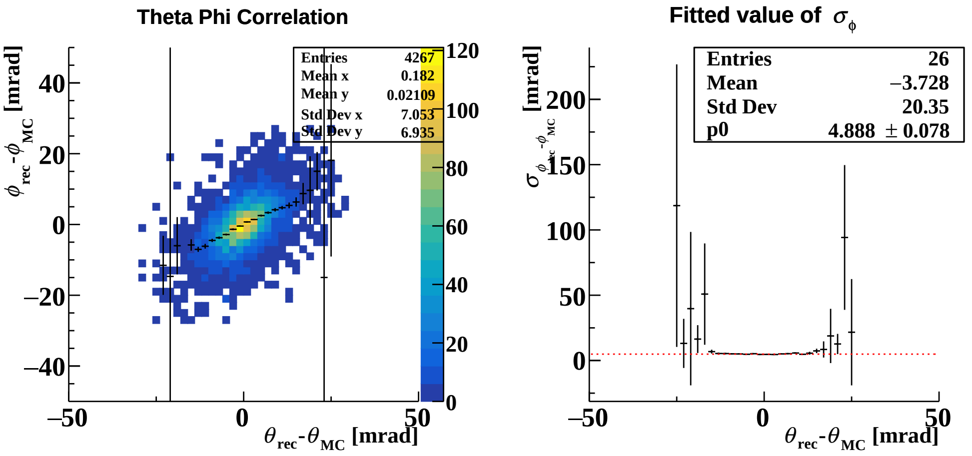

Fig. 8.12: The relation between the θ and ϕ.

Table 8.3: The performance of the positron reconstruction under the several beam rates. The "optimistic" case uses the 3.7 times better S/N condition.

Variable	Signal Single	3×10^7	5×10^7	7×10^7	7×10^7(Optimistic)
θ [mrad]	6.0	6.2	6.3	6.5	6.1
ϕ [mrad]	4.5	4.6	4.7	4.9	4.7
P [MeV]	79	82	86	91	84
z [mm]	1.5	1.6	1.5	1.7	1.5
y [mm]	0.7	0.7	0.8	0.8	0.7
t [ps]	40	42	42	41	41
Efficiency [%]	79.8	75.3	70.5	65.2	67.7

Fig. 8.13. The obtained reconstruction efficiency with the pileup of $7 \times 10^7 e^+/s$ is 65.2%. Two times better efficiency than that of the MEG experiment (30% with the pileup of $3 \times 10^7 e^+/s$) is obtained with the two times intense muon rate. However, this value is slightly worse than the expected value in the design (70%). There is still room for the improvement by studying cases of inefficiency events. As for the resolutions, the angular resolutions are 23 – 32% worse than expected due to the worse reconstruction of the CDCH hits by the worse S/N, while the momentum resolution is 30% better due to the improvement of the fitting algorithms (the DAF fitting with GENFIT, the turn merge algorithm, and so on). The results with 3.7 times higher gain for the CDCH is also shown in Table 8.3 as the "optimistic" scenario[*2], which is an optional setting for CDCH electronics prospected after the 2019 commissioning. Recovery of the resolutions, especially angle and momentum resolutions, can be seen. The efficiency also slightly increased: 65% to 68%.

8.2.7 Breakdown of Inefficiency

Table 8.4 shows the breakdown of the inefficiency of the positron measurement. The breakdown study suggests that the inefficiency is caused by the bad tracking quality: failure of turn merge of the CDCH tracks ("Quality Selection") and track extrapolation from the CDCH region to the pTC region ("pTC-CDCH Matching"), and reconstruction of the signal

---

[*2] The optimistic scenario means the noise is constant (2 mV white noise) and simply S/N is improved by a factor of four.

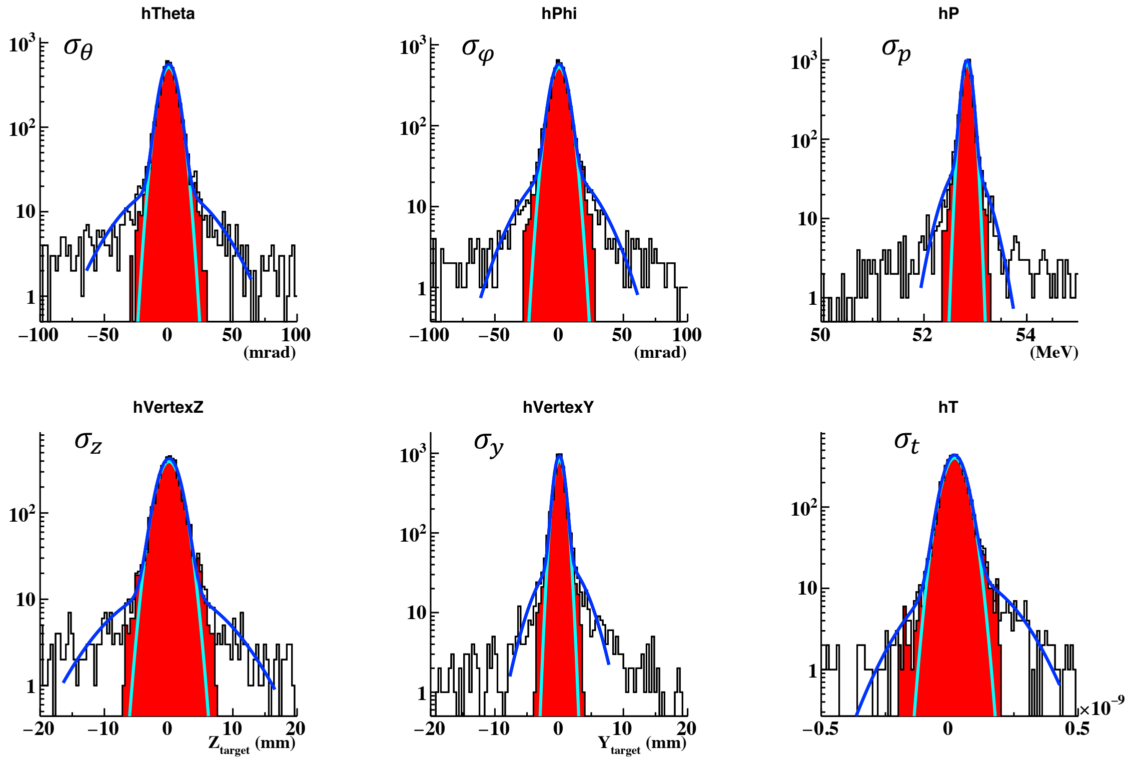

Fig. 8.13: The difference between the MC truth and the reconstructed kinematics with the pileup of $7 \times 10^7 e^+/s$. The red region contains the effective events after the tail cut. The tail cut will reduce the efficiency 10% (75.5% → 65.2%) at this rate. The blue line shows the double-gaussian fitting without tail cut, and the light blue shows the single gaussian fitting after the tail cut. The resolution is extracted from the σ of the latter fitting.

Table 8.4: The breakdown of the inefficiency of the positron measurement with pileups of $7{\times}10^7$ Michel positrons.

Item	Single	7×10^7	Main Reasons for Inefficiency at 7×10^7
Within LXe Acceptance	100%	100%	Definition of denominator, 10000 events for this test in total
Within pTC Acceptance (pTC Hits)	90.8%	90.8%	Scattered by CDCH materials, Annihilation
Quality Selection	88.5%	83.6%	Small number of hits for one track (failure of turn merge)
pTC-CDCH Matching	86.0%	78.2%	Failure of propagation
Pre-Selection	85.6%	77.9%	Out of pre-selection window
Selection	85.1%	75.5%	Cut and selection based on signal kinematics
Tail Cut	79.8%	65.2%	Lower tracking efficiency
Efficiency [%]	79.8±0.5%	65.2±0.4%	-

kinematics (“Tail Cut”).

8.2.8 Rate Dependence of pTC and CDCH Efficiencies

The rate dependence of the tracking (CDCH) and the timing reconstruction (pTC) efficiency for a signal positron is evaluated. The acceptance cuts are same to Table 8.4. The tracking efficiency includes the tail cuts for the kinematics except for the timing, and the timing reconstruction includes the tail cut for the timing.

Table 8.5 shows the efficiency at each step; at CDCH tracking reconstruction, CDCH-pTC matching, and the pTC timing

Table 8.5: The efficiency of CDCH tracking, CDCH-pTC matching, and pTC timing reconstruction under the beam of the MEG II intensity.

Item	Efficiency at 7×10^7	Efficiency at Each Step
Within Acceptance	90.8%	$P(\text{Acceptance}\mid\text{All}) = 90.8$
Tracking Rec.	69.6%	$P(\text{Tracking}\mid\text{Acceptance}) = 76.7$
CDCH-pTC Matching	67.9%	$P(\text{Matching}\mid\text{Tracking}) = 97.5$
Timing Rec.	65.7%	$P(\text{Timing}\mid\text{Matching}) = 96.9$

Table 8.6: The rate dependence of CDCH tracking, CDCH-pTC matching, and pTC timing reconstruction efficiency.

Item	Signal Only	3×10^7	5×10^7	7×10^7
$P(\text{Tracking}\mid\text{Acceptance})$	92.8	87.9	82.5	76.7
$P(\text{Matching}\mid\text{Tracking})$	97.7	97.3	97.4	97.5
$P(\text{Timing}\mid\text{Matching})$	97.3	97.6	97.2	96.9

reconstruction, and Table 8.6 summarizes the rate dependence of those. The reconstruction efficiency of pTC clusters is scarcely affected by the increase of the beam rate, while that of CDCH tracks is significantly affected.

The maximum hit rate of the pTC counters is less than 100 kHz even at the MEG II nominal intensity. The S/N of the pTC waveform (≈ 40) is good enough to be detected. Sharp waveforms by the series connection of the SiPMs and stabilized baseline by the pole-zero cancellation also help the reconstruction at each counter. The contribution from the accidental pileups in the pTC waveform ($\sim$500 ns) is negligible. Most of 2% inefficiency of pTC clusters come from the scattered particles and secondary particles, which is difficult to recover.

The deterioration of the CDCH tracking efficiency is due to the deterioration of CDCH hit reconstruction efficiency. At high muon rate, space-charge effects and pileup effects are getting severe and cross-fitting and hit reconstruction (explained in Sec. 7.1 and Sec. 7.5.1, respectively) become more difficult. The reconstruction efficiency of CDCH hits is affected by $\sim$10% as the beam rate increases, as shown in Fig. 8.14. The denominator of the hit efficiency is the total number of hits for the signal positron, and the numerator is that of reconstructed hits. The z-position and timing criteria between the MC truth and reconstructed hits, i.e. $z_{\mathrm{MC}} - z_{\mathrm{rec}} < 30$ cm and $t_{\mathrm{MC}} - t_{\mathrm{rec}} < 5$ ns is applied to reject the low-quality or inconsistent hits.

Fig. 8.15 shows an example of an event that fails turn merge. If the turn merge fails, especially the merged segment is less than three, most of the tracks are rejected by the tail cut due to the less number of hits as shown in Fig. 8.16. The failure of the turn merge was caused by not optimized conditions for the turn merge and the propagation failure of each segment due to the short tracking length (i.e. the number of CDCH hits in one segment is small). If we could solve the failure of the turn merge, the inefficiency from the propagation failure and the quality ($\sim$8% at the maximum) might be recovered.

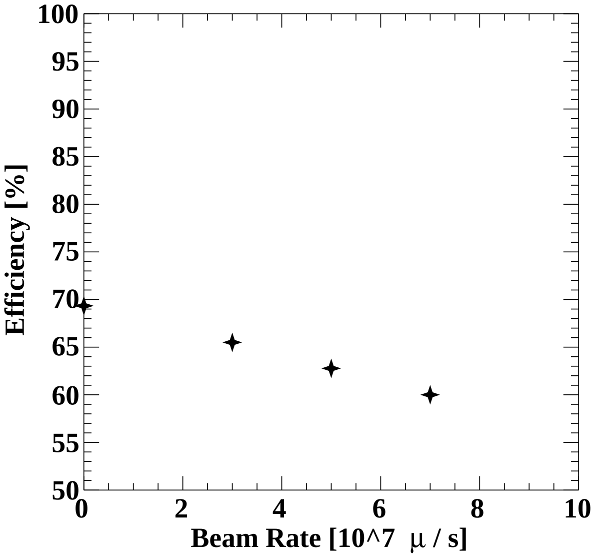

Fig. 8.14: The relation between the efficiency of the hit reconstruction by signal positrons and the beam rate.

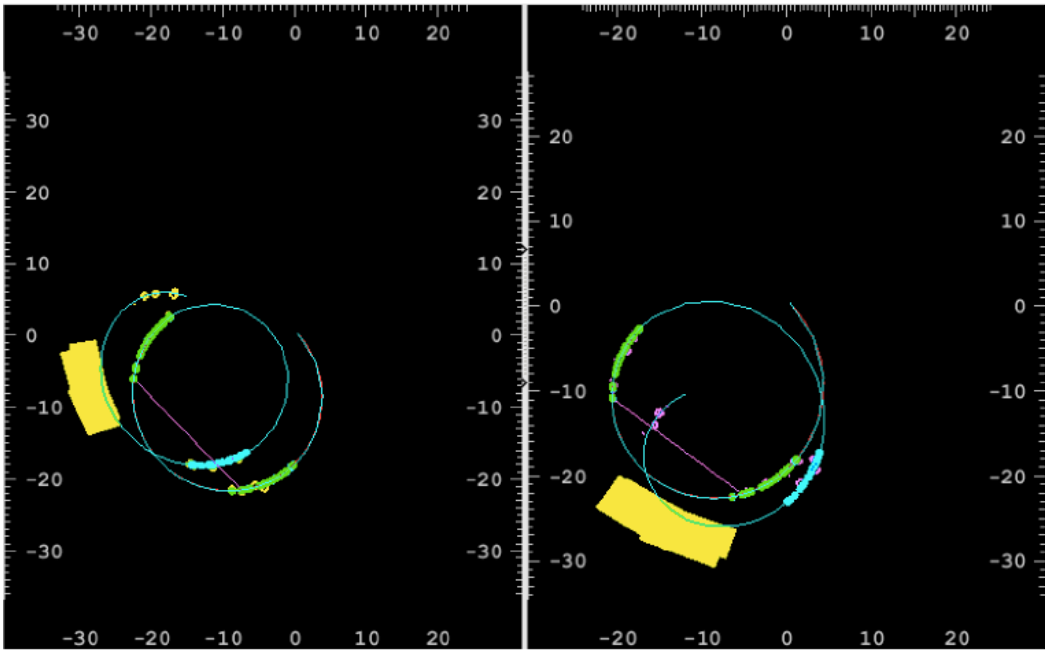

Fig. 8.15: An example of an inefficiency event by turn merge failure from ± stereo view. The green-dot segment and the blue-dot segment were not merged.

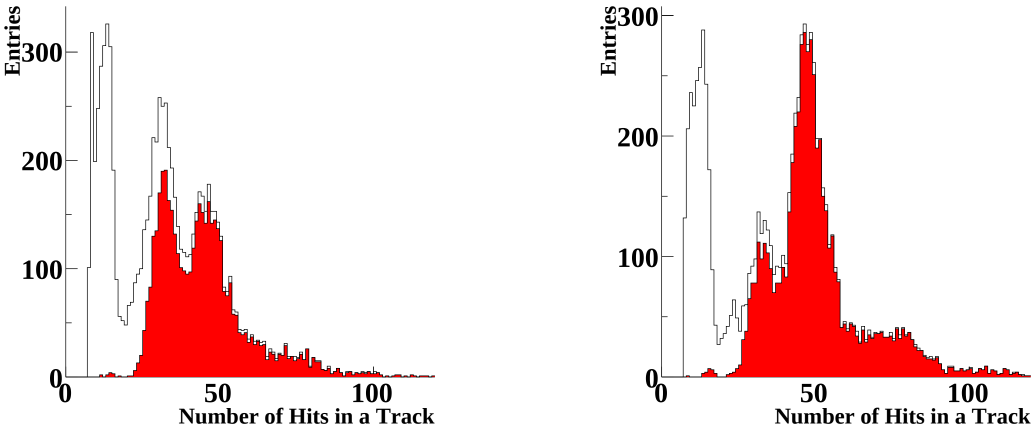

(a) MEG II nominal rate.

(b) Signal Only.

Fig. 8.16: Distribution of the number of hits in one signal track under the MEG II beam intensity before (black) and after (red) the tail cut. One track segment has ~20 hits (first peak), and these segments are merged to improve the quality of the tracks.

Chapter 9

Projected Sensitivity of MEG II

Based on the results described in Chap. 8, the projected sensitivity of the MEG II experiment is calculated in this chapter.

9.1 Maximum Likelihood Fit

The MEG II collaboration employs the Maximum Likelihood Fit (ML-Fit) to estimate the number of $\mu^+ \to \mathrm{e}^+\gamma$ events, N_{sig}. The improved detector resolution in MEG II will give us better signal/background separation, and the improved reconstruction efficiency will give us larger statistics. Based on the current best understanding on the detector performance, the projected sensitivity of the MEG II experiment will be discussed.

9.1.1 Maximum Likelihood Function

The likelihood function, $L(\theta|X)$ where θ is the target parameters to be estimated and X is the obtained data set, can be written as below:

$$L(\theta|X) = \prod_{i}^{N_{\mathrm{obs}}} p(x_i|\theta), \tag{9.1}$$

where N_{obs} is the number of events observed in the experiment, $p(x_i|\theta)$ is the probability density function of each event for a given set of parameters θ, and x_i is the discriminant variables of the i-th event. The likelihood function can be extended [72] with the Poisson distribution of N_{obs}:

$$L(\theta, N|X) = \frac{e^{-N} N^{N_{\mathrm{obs}}}}{N_{\mathrm{obs}}!} \prod_{i}^{N_{\mathrm{obs}}} p(x_i|\theta), \tag{9.2}$$

where N is the sum of the expected numbers of the three event types; the accidental background events (N_{acc}), the RMD events (N_{RMD}) and N_{sig}:

$$N = N_{\mathrm{sig}} + N_{\mathrm{acc}} + N_{\mathrm{RMD}}. \tag{9.3}$$

So $L(\theta, N|X)$ can be written as $L(N_{\mathrm{sig}}, N_{\mathrm{acc}}, N_{\mathrm{RMD}}|X)$. For simplicity we describe $L(N_{\mathrm{sig}}, N_{\mathrm{acc}}, N_{\mathrm{RMD}}|X)$ as L.

9.1.2 Probability Density Function

To formulate the likelihood function, the probability density function (PDF) $p(x_i|N_{\mathrm{sig}}, N_{\mathrm{acc}}, N_{\mathrm{RMD}})$, hereafter denoted as p, must be described properly. From the definition of PDF, there are relations below:

$$p(\mathrm{sig}) + p(\mathrm{acc}) + p(\mathrm{RMD}) = 1, \tag{9.4}$$

$$p(\mathrm{sig}|x_i) + p(\mathrm{acc}|x_i) + p(\mathrm{RMD}|x_i) = 1, \tag{9.5}$$

where $p(\mathrm{sig})$, $p(\mathrm{acc})$, $p(\mathrm{RMD})$ is the PDF of a signal, accidental or RMD event, and $p(\mathrm{sig}|x_i)$, $p(\mathrm{acc}|x_i)$, $p(\mathrm{RMD}|x_i)$ is the PDF of a signal, accidental or RMD event at the observation of x_i. From the Beyes' theorem, there is the relationship below:

$$p(\mathrm{sig}|x_i) = \frac{p(x_i|\mathrm{sig})p(\mathrm{sig})}{p(x_i)}, \tag{9.6}$$

the same relation can be written on accidental and RMD events. The PDF can be written down as below:

$$p(x_i|N_{\mathrm{sig}}, N_{\mathrm{acc}}, N_{\mathrm{RMD}}) = p(x_i|\mathrm{sig})p(\mathrm{sig}) + p(x_i|\mathrm{acc})p(\mathrm{acc}) + p(x_i|\mathrm{RMD})p(\mathrm{RMD}) \tag{9.7}$$

The signal, accidental and RMD PDF are denoted as below:

$$S(x_i) = p(x_i|\mathrm{sig}),\ A(x_i) = p(x_i|\mathrm{acc}),\ R(x_i) = p(x_i|\mathrm{RMD}). \tag{9.8}$$

Then the event-by-event PDF function can be formulated as below:

$$p = S(x_i)\frac{N_{\mathrm{sig}}}{N} + A(x_i)\frac{N_{\mathrm{acc}}}{N} + R(x_i)\frac{N_{\mathrm{RMD}}}{N}. \tag{9.9}$$

Also, from the sideband of the signal box region, the N_{acc} and N_{RMD} can be estimated and can be included in the likelihood function as μ_{acc} and μ_{RMD}. In conclusion, the MEG II likelihood function can be written down:

$$L = \frac{e^{-N}}{N_{\mathrm{obs}}!}\exp(\frac{(N_{\mathrm{acc}} - \mu_{\mathrm{acc}})}{2\sigma_{\mathrm{acc}}^2})\exp(\frac{(N_{\mathrm{RMD}} - \mu_{\mathrm{RMD}})}{2\sigma_{\mathrm{RMD}}^2})\prod_{i}^{N_{\mathrm{obs}}}(S(x_i)N_{\mathrm{sig}} + A(x_i)N_{\mathrm{acc}} + R(x_i)N_{\mathrm{RMD}}), \tag{9.10}$$

where σ_{acc}, and σ_{RMD} are the uncertainties of the numbers of the accidental background events and the RMD events from the sideband of the signal box region.

9.1.3 Discriminant Variables

The discriminant variables for ML fitting are described in $\vec{x_i}$:

$$\vec{x_i} = (E_{\gamma}, E_{\mathrm{e}^+}, t_{\mathrm{e}^+\gamma}, \Phi_{\mathrm{e}^+\gamma}, \Theta_{\mathrm{e}^+\gamma}, t_{\mathrm{rdc}}, E_{\mathrm{rdc}}). \tag{9.11}$$

The analysis regions are summarized as follows:

- Gamma energy: $48 < E_{\gamma} < 55$ MeV,
- Positron energy: $52.2 < E_{\mathrm{e}^+} < 53.5$ MeV,
- Time difference between gamma ray and positron $|t_{\mathrm{e}^+\gamma}| < 0.25$ ns,
- Relative angle of flipped positron direction with reference to gamma direction: $|\Theta_{\mathrm{e}\gamma}| < 40$ mrad and $|\Phi_{\mathrm{e}\gamma}| < 40$ mrad.

This analysis region includes enough signal and background regions for the fitting, and is wider than the signal region, e.g. described in Sec. 2.1.2. The regions become narrower significantly compared with MEG thanks to the improved resolutions of the positron spectrometer*[1]. The PDF functions $S(x_i)$, $A(x_i)$ and $R(x_i)$ are calculated from the theoretical expectations and the measured detector responses. For example, A(E_{e^+}) is constructed from the measurement of the Michel spectrum, and S(E_{e^+}) is constructed from the function of the energy resolution (PDFs are shown in Fig. 9.3 and Fig. 9.4 in the latter section). S($t_{\mathrm{e}^+\gamma}$) becomes the combination of the positron timing resolution and the gamma-ray timing resolution. The resolution of $t_{\mathrm{e}^+\gamma}$ is calculated from the obtained resolutions in this thesis, but this value is measured by the peak of the RMD events in the real experiment.

Table 9.1: Default values for the sensitivity calculation of MEG II experiment.

Variables	Values
R_μ	$7 \times 10^7 \mu/s$
T	20 weeks / year × 3 year (84% live fraction)
Ω	10.8%
ϵ_γ	69 %
ϵ_e	70%
ϵ_s	91%
N_{obs}	$1.01 \times 10^{14} \mu$

9.1.4 Expected Number of Muon Decays

To estimate the probability of $\mu \to \text{e} + \gamma$, the estimation of the total number of the muon decay observed in the experiment (normalization factor, N_{obs}) is needed. This can be calculated as follows:

$$N_{\text{obs}} = R_\mu \times T \times \Omega \times \epsilon_\gamma \times \epsilon_e \times \epsilon_s, \tag{9.12}$$

the definition of each variable is the same in (2.1). For the MEG II sensitivity calculation, values summarized in Table 9.1 were used[*2].

9.1.5 Systematic Uncertainty

In the MEG experiment, the impact of systematic uncertainties on the sensitivity was small (less than 1%) except for the uncertainties for the target deformation, as shown in Table 2.2. As for the alignment of the target which had 13% impact on the sensitivity, the dedicated systems (hard-material target, pattern dots, and camera system) are installed and it is expected that this uncertainty will decrease a lot. Therefore, this uncertainty is neglected in the estimation of MEG II sensitivity at this moment. Even though muon intensity will be twice higher, other uncertainties related to the detector performances and reconstruction under high rate are assumed to be negligible in this sensitivity estimation.

9.1.6 Confidence Interval and Sensitivity

The MLFit gives the best estimate of N_{sig} from a given dataset of an experiment. The best estimate of $\text{Br}(\mu \to \text{e}\gamma)$ is then given as $N_{\text{sig}}/N_{\text{obs}}$. We adopt an asymptotic approach in [73] to calculate the confidence interval of N_{sig} (or Br) at 90% confidence level in this thesis.[*3]

The "sensitivity" of an experiment is defined here as the median of the upper limits of the confidence intervals for an ensemble of "pseudo-experiments" with the null-signal hypothesis. The pseudo-experiment is a statistical dedicated simulation of the experiment to study the statistical behavior of the experiment. It is used in the sensitivity calculation because the full simulation takes too much time and it is not realistic to use the full simulation for the statistical estimations. It does not simulate the actual physics interaction, digitization of the detected information and so on, but generates the

---

[*1] The analysis region in the MEG experiment was as follows: $48 < E_\gamma < 58$ MeV, $50 < E_{\text{e}^+} < 56$ MeV, $|t_{\text{e}^+\gamma}| < 0.7$ ns, $|\Theta_{\text{e}\gamma}| < 50$ mrad and $|\Phi_{\text{e}\gamma}| < 75$ mrad in [4].

[*2] In the real experiment, the efficiencies and the stopping rate can be changed during the data taking. In the MEG experiment, the total number of decayed muons (normalization farctor) was calculated by two independent methods; counting the Michel positrons and the RMD events [1]. The uncertainty of the total number of decayed muon was 3.5%.

[*3] In the MEG experiment, a full frequentist approach was adopted.

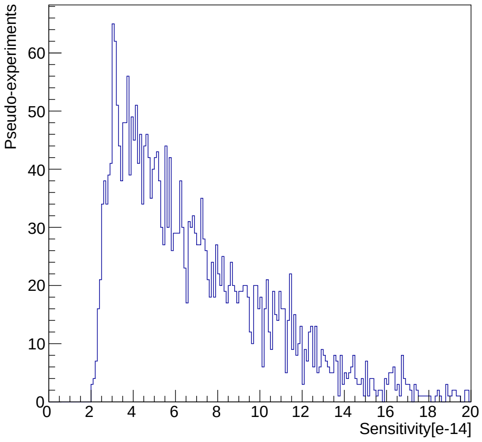

Fig. 9.1: The distribution of the upper limits of $N_{\rm sig}/N_{\rm obs}$ at 90% C.L. for 3000 pseudo-experiments with null-signal hypothesis. The obtained median is $N_{\rm sig}^{\rm median} = 5.6$, and the sensitivity is 6.0×10^{-14}.

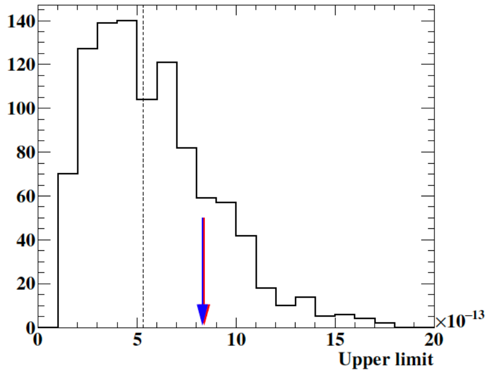

Fig. 9.2: The distribution of the upper limits of seudo-experiments in the MEG experiment [4]. Vertical dashed line shows the search sensitivity from the median calculation (5.3×10^{-13}), and two arrows show the upper limits obtained from the timing sidebands.

Table 9.2: The number of background events obtained in the MEG experiment, and that expected in the MEG II experiment.

Variable	$N_{\rm ACC}$	$\sigma_{N_{\rm ACC}}$	$N_{\rm RMD}$	$\sigma_{N_{\rm RMD}}$	$N_{\rm obs}$
MEG Data (Analysis Region) [4]	7739.1	37.7	624.6	28.4	$1.711{\times}10^{13}$
MEG II Design [3]	4793.6	28.6	57.2	5.7	$1.01{\times}10^{14}$
Previous work [7]	3639.7	24.6	41.0	4.1	$7.23{\times}10^{13}$
Updated	4746.3	28.1	53.4	5.3	$9.43{\times}10^{13}$

variables used for the discrimination of the event type[*4]. The accidental background and the RMD background events are generated including the statistical fluctuations. Table 9.2 shows the examples of the generated number of events for the pseudo-experiments in the fitting region. The projected sensitivity of the MEG II experiment was calculated from at least O(1000) pseudo-experiments. Fig. 9.1 shows the distribution of the upper limits with updated parameters of the positron spectrometer in this thesis. The median value is 6.0×10^{-14}. Fig. 9.2 shows that in the MEG [4], 5.3×10^{-13} ($N_{\rm sig} \approx 9.1$). The total statistics in the MEG II experiment becomes $9.43{\times}10^{13}/1.711{\times}10^{13} \approx 5.5$ times larger than that in the MEG, while the number of signal-like background events ($N_{\rm sig}$ in the null-hypothesis) becomes $9.1/5.6 \approx 1.6$ times smaller, resulting in the net improvement of the sensitivity by a factor of $5.5 \times 1.6 \approx 9$.

9.2 Comparison with MEG Experiment

The performance of the MEG positron spectrometer and the MEG II positron spectrometer (design values: Design column and updated values: 7×10^7 column) are summarized in Table 9.3. The performance of the MEG II positron spectrometer at the halved rate (3.5×10^7) and with the additive gases to stabilize the CDCH (O_2 addition) are also shown. The timing resolution of "7×10^7" is calculated from the gamma-ray timing resolution (50 – 58 ps is expected, and here 55 ps [16] is

---

[*4] For example, some detector resolutions themselves are not used for the ML-Fit analysis, but that information is necessary to simulate the events in the pseudo-experiment properly.

Table 9.3: The input parameters of the positron spectrometer for the likelihood analysis with several possible scenarios.

Variable	MEG	Design	7×10^7	3.5×10^7 (Half rate scenario)	0.5% O_2 addition to 7×10^7
θ [mrad]	9.4	5.3	6.5	6.2	6.7
ϕ [mrad]	8.7	3.7	4.9	4.7	4.6
P [keV]	380	130	91	82	95
z [mm]	2.4	1.6	1.7	1.6	1.8
y [mm]	1.2	0.7	0.8	0.8	0.8
$t_{e\gamma}$ [ps]	122	84	70	69	70
Efficiency [%]	30	70	65.2	74.0	62.4

used) and the positron timing resolution (37.6 – 48.1 ps as shown in Table 8.1). The $t_{e\gamma}$ is calculated to be 67 – 73 ps. Here 70 ps is used for the input.

9.2.1 Extension of MEG Experiment

Before discussing the MEG II update, the extension of the MEG experiment is discussed. In the MEG final result[1], the single event sensitivity was 0.58×10^{-13} while the upper limit sensitivity was 4.2×10^{-13}. This means that the sensitivity of the MEG final result was limited not by the statistics but by the number of the accidental backgrounds. The contribution to the sensitivity from the background is improved by a square root of the statistics. With this assumption, three-year extension of the MEG experiment will achieve $\sim 3 \times 10^{-13}$.

9.2.2 Several Upgrade Cases from MEG Experiment

The first case is that the LXe detector performance is upgraded for MEG II [16], and that the position spectrometer performance and the timing resolution of $t_{e\gamma}$ are assumed to be unchanged from the MEG performance. In this case, the sensitivity after the three-year running will reach 2.2×10^{-13}. It is better than the simple MEG extension, however, it is still far from the sensitivity below $O(10^{-14})$.

The second case is that the timing resolution is updated in addition to the LXe detector update, and the other resolutions and the efficiency of the spectrometer are unchanged from the MEG. In this case, the the sensitivity after the three-year running will reach 1.9×10^{-13} by the improvement from $\sigma_{t_{e\gamma}} = 122$ ps to 70 ps.

The third case is to consider the upgrade of CDCH performance. The projected sensitivity of 6.0×10^{-14}, which was one order better than the MEG experiment, will be achieved thanks to the improved detector resolutions and efficiency of the MEG II positron spectrometer. Considering the positron reconstruction efficiency was 30% in the MEG experiment, the achieved 65% reconstruction efficiency is significantly better. As for the resolution, improvement of the momentum resolution is significant by a factor of 4. The timing resolution, 70 ps, is also much better the MEG case (122 ps).

9.3 Comparison with MEG II Design Values

9.3.1 Sensitivity with Design Values

The sensitivity has been studied with updated performance of the LXe detector and RDC, but with the designed values of the positron spectrometer in Ref. [16]. The designed performance of the positron spectrometer is summarized again in Table 9.3 (“Design”). The effect of the US-RDC has not been taken into account. The branching ratio sensitivity of the

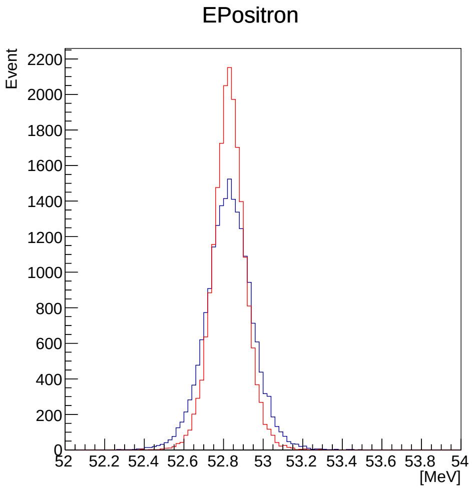

Fig. 9.3: The generated signal event in the pseudo-experiments. Red histogram is made with the assumption of σ_p = 93 keV and blue histogram σ_p = 130 keV.

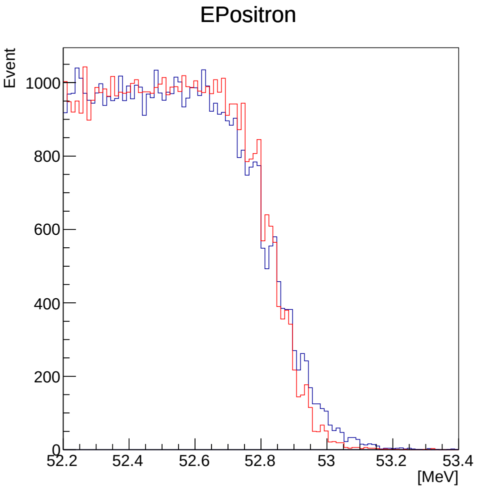

Fig. 9.4: The generated background event in the pseudo-experiments. Red histogram is made with the assumption of σ_p = 93 keV and blue histogram σ_p = 130 keV.

MEG II experiment is calculated to be $(5.9 \pm 0.1) \times 10^{-14}$.

9.3.2 Impact of Update

Momentum Resolution

The improvement of the momentum resolution ($\sigma_p \sim 90$ keV) is one of the largest changes from the design value (130 keV). This improvement is due to the usage of GENFIT in the tracking algorithm and the improvement of the turn merge algorithm. Fig. 9.3 and Fig. 9.4 shows the generated signal and background events for the pseudo-experiments, respectively, with the momentum resolution 93 keV (red) or 130 keV (blue). The positron momentum measurement is especially important for the improvement of the signal/background separation. The detector acceptance at the low momentum region (45 – 50 MeV) was also largely improved from the MEG experiment and the acceptance curve around the signal region became flat[*5]. However, the impact on the sensitivity is almost negligible because the likelihood fit is performed in a narrow p_{e^+} range of 52.2-53.5 MeV. In conclusion, the expected improvement in the projected sensitivity by the update of the positron momentum resolution is 9% from the design ($5.4{\times}10^{-14}$ when only the momentum resolution was updated).

Update of Angular Resolutions

The angular resolutions (6.5/4.9) became worse than the design values (5.3/3.7) due to the worse S/N of waveforms and the lower single-hit resolution of CDCH. The deterioration of the sensitivity by the angular resolutions is 8% from the design ($6.4{\times}10^{-14}$ when only the angular resolutions were updated).

9.4 Comparison with Previous Works

The comparison with previous work [7] is summarized Table 9.4. There are three points to be mentioned as the major updates.

[*5] The detail of the acceptance is described in Appendix G (Michel-Fit).

Table 9.4: Summary of the contribution for the results in this thesis.

Update	[7]	This Thesis
Calculation of Resolution (CDCH)	MEG-based MC in 2013	MEG II updated MC
Calculation of Resolution (pTC)	From fixed-pattern of data	From tracks of data
Efficiency (Initial Design Simulation)	~ 50% (56% at 10 layers)	-
Efficiency (Updated Simulation)	-	65%
$t_{e\gamma}$ (Without Radiation, σ_γ = 50 ps)	67 ps	63 ps
$t_{e\gamma}$ (Full Radiation at 10°C, σ_γ = 58 ps)	80 ps	75 ps
Projected Sensitivity	7.6×10^{-14}	6.0×10^{-14}

- evaluation of the CDCH tracking resolution with the updated MEG II simulation while previous work used the MEG simulation results,
- evaluation of the positron reconstruction efficiency with the newly developed simulation and algorithms, while previous work used the initial MEG II design simulation,
- updates of the pTC timing resolution and the detailed studies of the systematics and the radiation damage effects, which resulted in even better performance as in Table 9.4.

In [7] 56% of efficiency was obtained. However, this efficiency was based on the initial MEG II design simulation (i.e. one-order better S/N for CDCH and 10 layers instead of 9 layers). The MEG II simulation was updated to be based on the measured S/N and 9 layer configuration of the CDCH in this thesis. When the algorithms used with the initial MEG II design based MC is applied to the updated S/N conditions, the efficiency becomes much worse. If the cross-fitting step is omitted from the current algorithm, the reconstruction efficiency became only 13% even without pileup case as explained in Sec. 7.1. Without the all updates of the algorithms and with pileups, it will be less than 10%. Therefore, improvement to 65% with updated simulation is due to the refinement algorithms of CDCH tracking, pTC tracking, and global tracking.

When we assume that 50% (or 56%) efficiency and 80 ps timing resolution in the previous study, the projected sensitivity for three years becomes 8.2×10^{-14} (7.2×10^{-14}), while that is 6.3×10^{-14} with 65% in this thesis. As for the timing resolution, the timing resolution was improved from 67 ps to 63 ps without radiation damage and from 80 ps to 75 ps after the 3-year irradiation at 10°C, which corresponds to the sensitivity from 5.9 - 6.3×10^{-14} to 5.7 - 6.1×10^{-14} at the 65% efficiency.

In conclusion, the improvement from the previous work is 21% for three-year data taking.

9.5 Possible Other Scenarios

The projected sensitivity was updated based on the realistic conditions. Here, several possible updates are considered, which will be achievable before the physics data taking starts.

9.5.1 Gain Improvement and Software Optimization

The CDCH FE pre-amp gain can be increased by a factor of four. Of course, the S/N does not increase simply by a factor of four since the electrical noise will also be increased. However, combined with the noise reduction algorithms, the single hit reconstruction may be significantly improved. The study on the effect of the different gain on the performance is in progress using commissioning data in 2020. As an example, the efficiency is 80%, which is the value of the “signal only” case and considered as the limit of the current reconstruction algorithms, the final sensitivity will be improved to 5.2×10^{-14}.

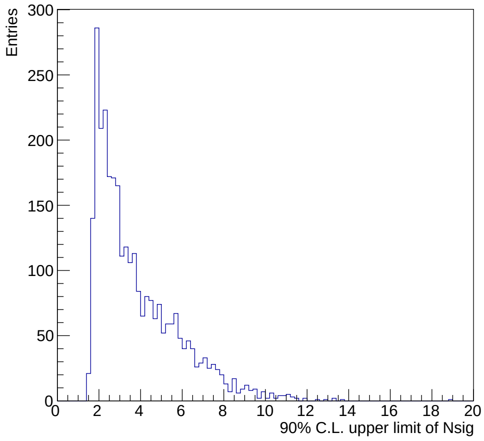

Fig. 9.5: The distribution of the upper limits of N_{sig} at 90% C.L. for 3000 pseudo-experiments with null-signal hypothesis at a half rate beam. The obtained median is $N_{\mathrm{sig}}^{\mathrm{median}} = 3.2$.

9.5.2 Additive Gas Impact

In the 2020 commissioning, the additive gases, especially small fraction (0.5 – 2%) of O_2, were found to be effective for the stable CDCH operation. The detailed effect of the additional gas is under study, but preliminary results suggest a slight performance degradation by the change of waveform shape, number of the ionized electrons per track, and the gas-gain, as summarized in Table 9.3. The effect on the projected sensitivity is ~3%, which is not crucial.

9.5.3 New Detector Installation: CDCH II/US-RDC

All of the MEG II detectors were already installed in 2018, however, there will be other updates of the MEG II detector: the new detector (US-RDC), and the new CDCH (CDCH-II).

The expected improvement by the US-RDC is roughly 2 – 9%, although the introduction of the US-RDC has not been decided yet. The CDCH II may adopt thick cathode wires (for example, 60 μm) to mitigate the wire breaking problems, which may result in slight (~ 4%) degradation of the reconstruction efficiency. On the other hand, CDCH II can be assembled with 10-layer configuration, which will improve the reconstruction efficiency roughly by 10% and result in the better sensitivity.

9.5.4 Reduced Muon Stopping Rate

The MEG II data taking is supposed to be performed with the muon stopping rate of 7×10^7, but it is likely that the rate will be adjusted to maximize the sensitivity for the given detector performance. As already discussed, the PDE decrease of the LXe VUV-MPPC can be a crucial problem at this beam rate. The running of the MEG II at a half rate (3.5×10^7) is under consideration to mitigate the effect of the PDE decrease.

An estimation of the sensitivity at the reduced beam rate has already been done in Ref. [16], but the better performance of positron reconstruction at reduced rate has not been taken into account.

As described in the previous chapter, the positron spectrometer performance is largely affected by the pileups. If the half rate is adopted, the efficiency will be improved from 65% to 74%, and the angular and momentum resolutions will be improved by 5/4% (θ/ϕ) and 10%, respectively. Fig. 9.5 shows the distribution of the upper limits of N_{sig}, and Fig. 9.6

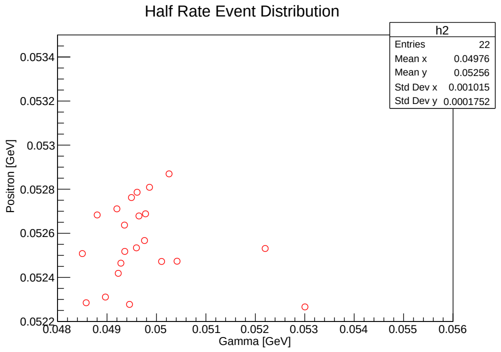

Fig. 9.6: The example event distribution within 1.64σ angles, positions, and timing resolution at half rate beam. $N_{\text{sig}} = 2.2$ was obtained in this pseudo-experiment.

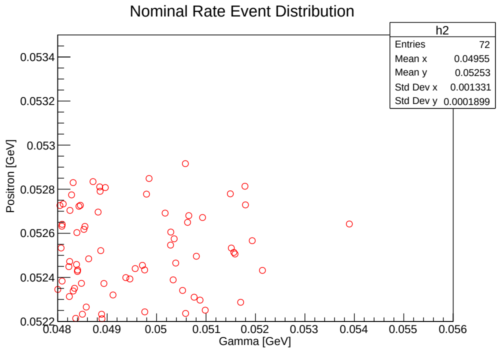

Fig. 9.7: The example of event distribution within 1.64σ angles, positions, and timing resolution at MEG II nominal beam. $N_{\text{sig}} = 7.4$ was obtained in this pseudo-experiment.

shows the example of generated event distribution in the analysis region (with 1.64σ resolution cut). Compared with the nominal beam case, Fig. 9.1 and Fig. 9.7, the significance of the signal/background separation will be improved. Including the positron spectrometer update, the projected sensitivity with the half rate becomes $(6.0 \pm 0.1) \times 10^{-14}$ which is 9% better than the result in [16]. In addition to the reconstruction performance, there are other advantages on the hardware operation by reducing the beam rate; less radiation damage on pTC, less wire aging for CDCH, and so on.

The expected sensitivity as a function of the running period at each beam rate is shown in Fig. 9.8. The up-to-date estimation with the updates on the positron spectrometer performance achieved the projected sensitivity of 6.0×10^{-14}, which is one-order better than the MEG experiment. As described in Sec. 1.5, the $\mu \to e\gamma$ search with the sensitivity of $O(10^{-14})$ is an attractive probe for the new physics, especially SUSY-GUT theories with heavy right-handed neutrinos. The results reported in this thesis extended the accessible parameter space around O(10 TeV), where it is difficult to be accessed by the direct search experiment and has significant impact on the BSM theories. The beam rate for the MEG II experiment will be decided in the end of 2021 engineering run, considering all the detector conditions.

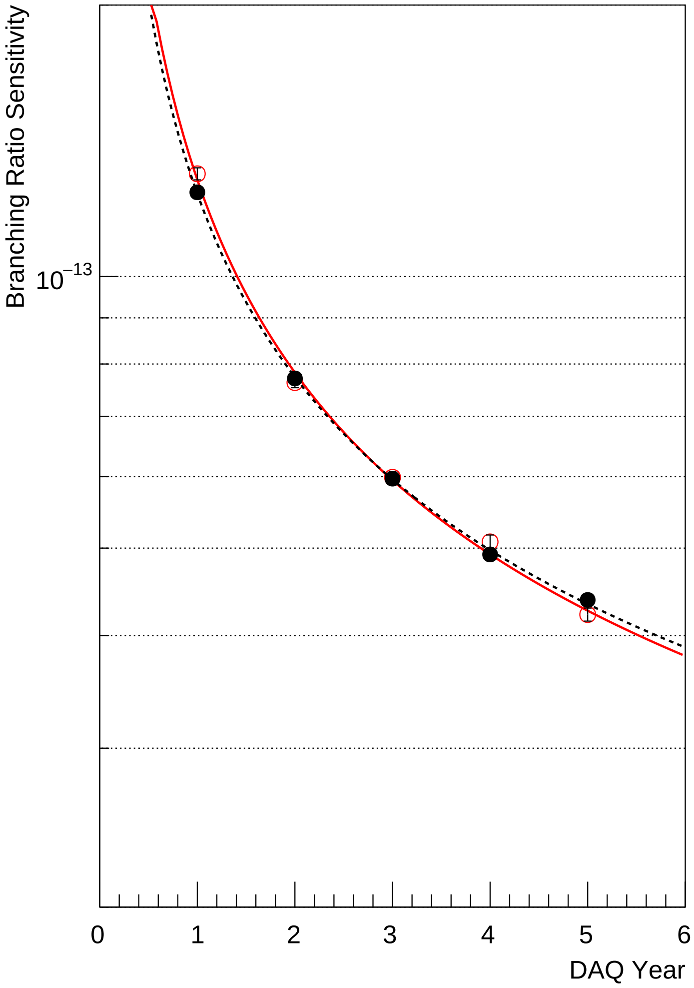

Fig. 9.8: The branching ratio sensitivity as a function of the DAQ years. (Black) With the updated resolutions under $7 \times 10^7 \mu$/s. (Red) With the updated resolutions under $3.5 \times 10^7 \mu$/s.

Chapter 10

Conclusions

An innovative positron spectrometer has been developed for a $\mu^+ \to e^+\gamma$ search with a branching ratio sensitivity of $O(10^{-14})$ in the MEG II experiment. Commissioning of the detectors with the muon beam at PSI has been performed over the past five years to demonstrate the detector performance and the stable operation. The pTC measures the positron timing with a precision of 35.0 ps by using the multiple-hit information, which is 15% better than the previous studies. The radiation damage to the pTC SiPMs has a significant impact on the stable operation of pTC and the time resolution. A detailed study of the effect of radiation damage was conducted and new dedicated cooling system has been developed to mitigate the deterioration of the pTC performance. Stable operation at 10°C was established, which mitigates the deterioration of the timing resolution by a factor of three. The MC simulations were developed based on the results from the analysis of the commissioning data, for example, S/N tuned to the observed CDCH waveform (one-order decrease of the S/N), new 9 layer configuration of CDCH, and space-charge effect of the CDCH. With the updated simulation, the efficiency of the positron spectrometer was evaluated to be 65%, which is twice better than the MEG (30%) and 9% better than the previous studies. The momentum resolution is 30% better than the design value thanks to the refinement of the track fitting algorithm. The projected sensitivity of the MEG II experiment was evaluated based on the updated performance of the positron spectrometer, and we conclude that the MEG II experiment can reach a sensitivity of 6.0×10^{-14} in three years of data collection. The contribution to the sensitivity is 21% improvement from the previous studies, which extends the accessible parameter space around O(10 TeV) energy scale in the new physics models. The engineering run for the MEG II experiment will start with the full detectors and the full readout electronics in 2021, followed by the physics data-taking.

A

Laser components

The optical components for the laser calibration system (shown Fig. 2.44a) are summarized in Table A.1.

Table A.1: Optical components used in the laser calibration system [8]

Item	**Model** (Manufacturer)	**Specifications**	**Pieces** (spares)	**Ref.**
laser	Picosecond Light Pulser PLP-10 (HAMAMATSU PHOTONICS K.K.)	Wavelength 401 nm, pulse width 60 ps, peak power 200 mW	1	[74]
optical fibre (2.5 m)	QMMJ-31-IRVIS-50/125-1HYWT-2.5-SP (OZ OPTICS)	High power GI multimode, core/clad 50/125 µm, NA 0.2, 400–2000 nm, 1 mm jacket	432 (+129)	[75]
optical fibre (10 m)	MMJ-33-IRVIS-50/125-3-10 (OZ OPTICS)	GI multimode, core/clad 50/125 µm, NA 0.2, 400–2000 nm	8 (+6)	[76]
mode scrambler	ModCon Mode Controller (Arden PHOTONICS)	Insertion loss < 3 dB at 850 nm	1	[77]
1×2 splitter	FUSED-12-IRVIS-50/125-50/50-3S3S3S-3-0.25 (OZ OPTICS)	FBT multi-mode coupler, 400–1600 nm, excess loss < 1.0 dB for 480–700 nm	1	[78]
1×8 splitter	MMC-18-A-EVEN-1-A-30CM-R-1 (Lightel Technologies Inc.)	FBT multi-mode coupler, insertion loss ≤ 11.5 dB	70 (+11)	[79]
photodiode	DET02AFC (THORLABS)	400–1100 nm, bandwidh 1 GHz, rise time 1 ns	1	[80]
optical switch	fibre Optical Switch mol 1×12-50 µm (LEONI)	Insertion loss < 2.0 dB for 5–16 output channels	1	[81]

B

Radiation damage with differently damaged SiPMs

In this chapter, the study of the radiation damage effect with differently damaged SiPMs in series is summarized. The full detail of this section is published in [31]. The position dependence and the effect on the timing resolution are already described in Sec. 6.5.6. Here, the information of the irradiation levels of the SiPMs, their alignment (pattern A–D), and the IV-curves are shown and explained.

The radiation damage effect with new type of SiPMs is also summarized (the detail is reported in [28]).

B.1 SiPMs Irradiation

Six SiPMs (#1-#6) were irradiated with intense electrons from 37 MBq ^{90}Sr sources for 280 hours in total, which is equivalent to $\Phi_{\mathrm{eq}} \approx 3 \times 10^9 \mathrm{n}_{1\mathrm{MeV}}/\mathrm{cm}^2$. The irradiation was separated into four steps, each 70 hours long, and no bias voltage was applied to the SiPMs during the irradiation.

In addition, a set of SiPMs, which was irradiated with neutrons with kinetic energies ranging from 0.5 MeV to 16 MeV using the reactor neutron facilities at the Laboratory of Applied Nuclear Energy (LENA) of the University of Pavia, was prepared. Among them, two samples with $\Phi_{\mathrm{eq}} \approx 8.7 \times 10^8\ \mathrm{n}_{1\mathrm{MeV}}/\mathrm{cm}^2$ (#7, #8) and two with $\Phi_{\mathrm{eq}} \approx 5.5 \times 10^9\ \mathrm{n}_{1\mathrm{MeV}}/\mathrm{cm}^2$ (#9, #10) were picked up for this study.

B.2 Patterns for SiPMs Connection

The specific concern on the series connection of SiPMs arises from the difference of the radiation damage levels depending on the SiPM position in the counter. The difference is caused by the gradient magnetic field of COBRA, and the hit rate of a top part of a counter is ~2 times larger than that of a bottom. Different combinations of SiPMs were used for these tests as summarized below:

Pattern A Two electron irradiated SiPMs (#1, #2 [or #5[*1]]) and four non irradiated SiPMs (#11 – #14).

Pattern B Four electron irradiated SiPMs (#1 – #4 [#5]) and two non irradiated SiPMs (#11, #13).

Pattern C Two electron irradiated SiPMs (#1, #2 [#5]) and four neutron irradiated SiPMs, two with the fluence level of $\Phi_{\mathrm{eq}} \approx 8.7 \times 10^8\ \mathrm{n}_{1\mathrm{MeV}}/\mathrm{cm}^2$ samples (#7, #8) and the other two with $\Phi_{\mathrm{eq}} \approx 5.5 \times 10^9\ \mathrm{n}_{1\mathrm{MeV}}/\mathrm{cm}^2$ ones (#9, #10).

Pattern D Six electron irradiated SiPMs (#1 – #6). The dose level is specified in the sentence or figures if necessary. If omitted, the SiPMs after full irradiation ($\Phi_{\mathrm{eq}} \approx 3 \times 10^9 \mathrm{n}_{1\mathrm{MeV}}/\mathrm{cm}^2$) are used for the measurement.

Pattern D is used to evaluate the radiation damage and current increase effects on timing resolution step by step, as

---

[*1] SiPM #2 was broken during the measurement and was replaced with #5, which has the same damage level and the I-V characteristics as #2.

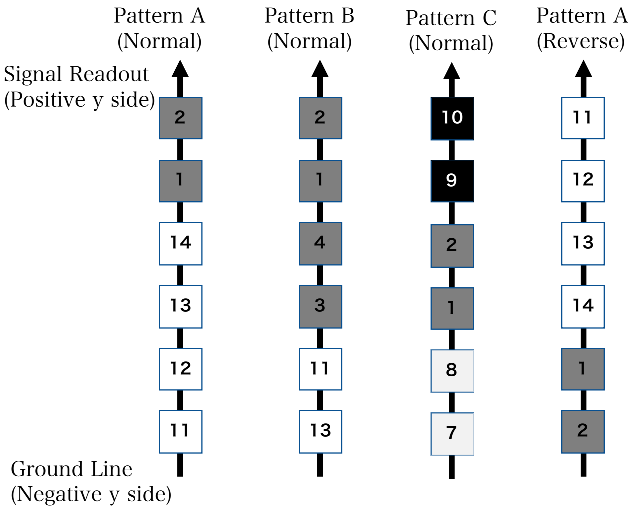

Fig. B.1: Schematic of SiPMs' pattern A, pattern B, pattern C in normal order and pattern A in reverse order. The SiPMs with highest dark currents are in black, those with lowest in white.

already described in this thesis. Pattern A and Pattern B are considered as extreme cases to highlight the effects of the position dependence of the irradiation, while pattern C simulates a gradient damage level closer to a realistic condition.

The SiPMs under test are located at the negative x side of the test counter; the signal is extracted from the positive y side, while the negative y side is connected to the ground line. The more highly-damaged SiPMs were located at larger y position: this configuration of SiPMs is called "normal order". Data were taken also with SiPMs ordered in the opposite way along the y direction: this configuration is called "reverse order". Figure B.1 illustrates the layout of each pattern[*2].

B.3 IV Curves for Each Pattern

Figures B.2–B.4 show the I-V curves of individual SiPMs used in patterns A, B, and C. Figures B.5 and B.6 show the I-V curves in series measured at 30°C and 10°C, respectively. The breakdown voltages of patterns A and B turned out to be shifted to values higher than that of pattern D. This "shift of the breakdown voltage" is one of the characteristic behaviors for the series connection with differently damaged SiPMs.

When the I-V characteristics of series-connected SiPMs differ, the applied voltage to each SiPM is automatically adjusted to flow a common current. As a consequence, the over-voltages for the six SiPMs differ from one another; even when the total applied voltage is below the breakdown voltage of the series-connected SiPMs, voltages applied to non-damaged SiPMs may result to be higher than their breakdown voltages to flow the same dark current as that of the damaged SiPMs below the breakdown. This mechanism causes a breakdown voltage shift as illustrated in Figure B.7. Table B.1 summarized the breakdown voltages of pattern A, pattern D, and the sum of the breakdown voltages of the single SiPM used for those patterns. A shift of ~1.5 V is found between Pattern A and Pattern D, and this shift is not recovered by cooling.

B.4 New SiPM test

As explained in Sec. 2.4.2, ASD-NUV3S-P model is also used in addition to ASD-NUV3S-P High-Gain (MEG). The radiation tolerance of this model is also checked with a beam test at Beam Test Facility (BTF) in Italy, Frascatti. The beam

---

[*2] The pTC is designed with the readout from the larger radius side (i.e. negative y-side), which corresponds to the reverse order case in this study.

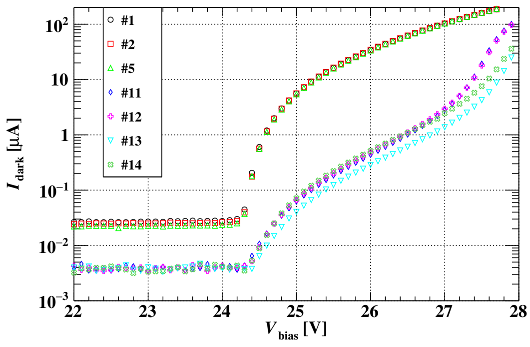

Fig. B.2: I-V curves of each SiPM used for pattern A.

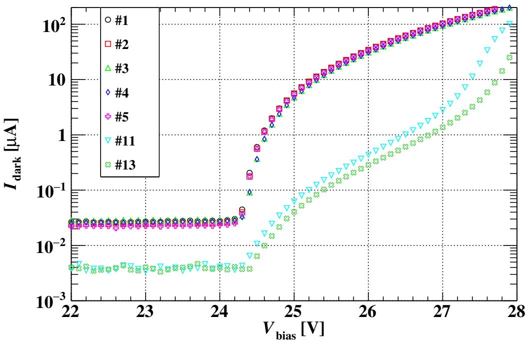

Fig. B.3: I-V curves of each SiPM used for pattern B

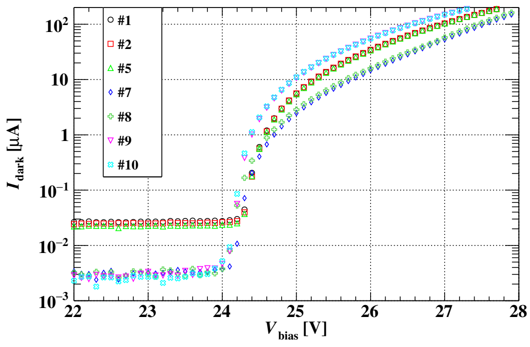

Fig. B.4: I-V curves of each SiPM used for pattern C.

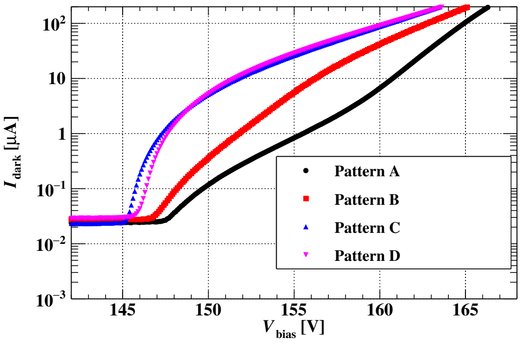

Fig. B.5: I-V curves of several patterns of series-connected SiPMs measured at 30°C.

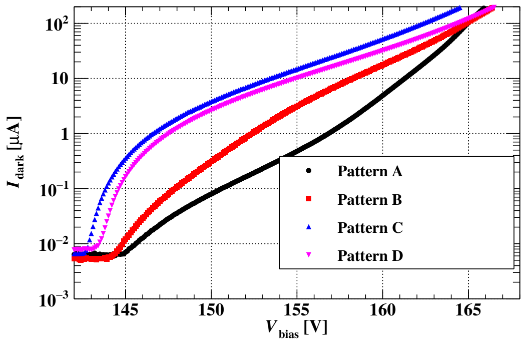

Fig. B.6: I-V curves of several patterns of series-connected SiPMs measured at 10°C.

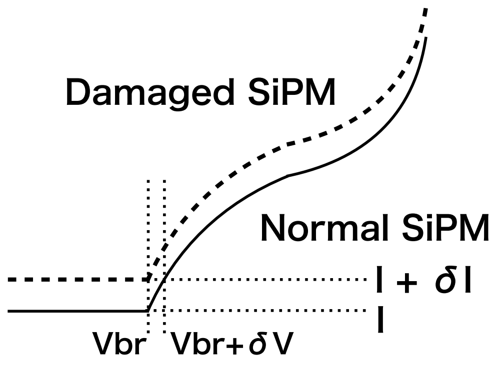

Fig. B.7: The explanation of breakdown voltage shift arising from the difference in dark currents. If n SiPMs have the same dark current I at the breakdown voltage $V_{\rm br}$, the breakdown voltage of the series-connected SiPMs is expected to be $n \times V_{\rm br}$. In pattern A, the breakdown voltage becomes $6 \times V_{\rm br} + 4 \times \delta V_{\rm br}$, and in pattern B, $6 \times V_{\rm br} + 2 \times \delta V_{\rm br}$ to accommodate the same current $I + \delta I$ at the breakdown voltage.

Table B.1: V_{br} values of Pattern A and Pattern D.

SiPM	V_{br} (V)
Sum of #1 - #6	145.5 ± 0.2
Sum of #1, #2, #11 - #14	145.7 ± 0.2
Pattern D (30°C)	145.94 ± 0.05
Pattern A (30°C)	147.51 ± 0.05
Pattern D (10°C)	143.43 ± 0.05
Pattern A (10°C)	144.89 ± 0.05

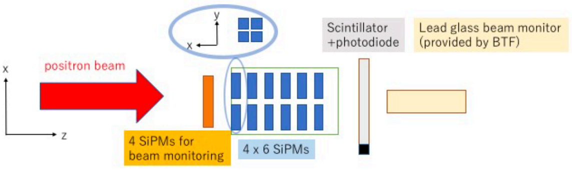

Fig. B.8: The irradiation test setup at BTF.

irradiation setup is shown in Fig. B.8. In this test, 24 type-II SiPMs (50 μm pitch) were irradiated. The calculated fluence was $1.1 \times 10^{12} \mathrm{e}^{+}/\mathrm{cm}^{2}$, which was roughly one order higher than the highest total dose expected in MEG II.

In spite of such a severe damage on SiPMs, the current level and the timing resolution measured were not bad, or even better at 10°C than the type-I SiPMs as shown in Fig. B.9 and Fig. B.10. In conclusion, the radiation damage on ASD-NUV3S-P models will not be a problem.

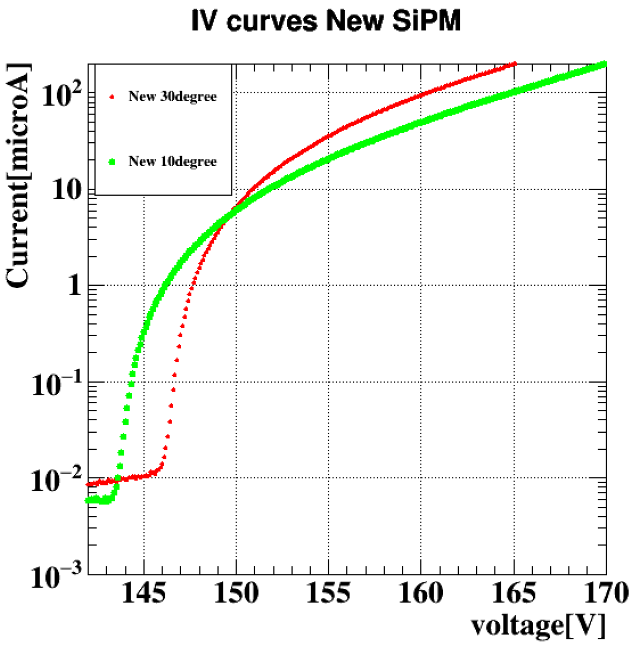

Fig. B.9: The IV curves of the SiPMs after irradiation at 10°C and 30°C. The type-II SiPMs shown in ”New”.

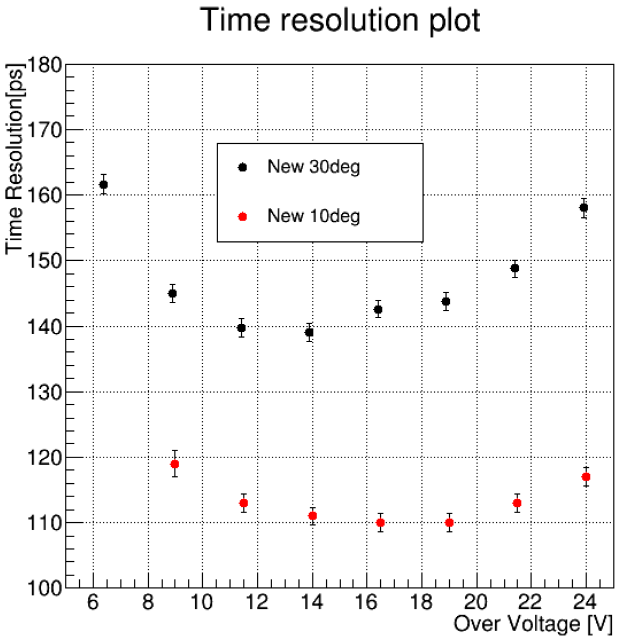

Fig. B.10: The bias scan of the timing resolution of type-II SiPMs (shown as “New”) after irradiation at 10°C and 30°C.

C

Online Synchronization in 2018 - 2019

C.1 Analysis of Online Synchronization

The data quality on the synchronization were checked with 2018 - 2019 commissioning data, and the correction was applied to the data.

C.1.1 Clock Analysis

The same 80 MHz sine waves are recorded at all the DRS chips to align the phase of different DRS chips in the offline analysis.The start cell (cell-zero) of DRS is adjusted and aligned by fitting the sine waves around the signal timing. The DRS cell cycle is locked with the output signal (square wave with 1.95 MHz at 2GSPS case) of the phase-lock loop (PLL) in WaveDREAM board (see Fig. 2.27). The relationship among the clock signal, PLL output, and DRS cycle is illustrated in Fig. C.1. For the evaluation of the timing synchronization, signals of the square pulses from a function generator (5 V peak to peak divided into 8 channels with 1 MHz) were used as the input, and then the deviations of the timing difference between two channels were checked. The online cell-zero adjustment jitter was ~ 60 ps in the 2017 case, and combining the offline analysis the synchronization consistency became ~ 20 ps at 2 GSPS.

Two problems on the online synchronization happened in 2018 and 2019: "12.5 ns jump" and "out-of-synchronization".

C.1.2 12.5 ns Jump

Fig. C.2 shows the effect of this 12.5 ns jump on the time-difference method of the CDCH hit reconstruction. There are sometimes 12.5 ns unphysical differences in the data from the different chips. Fig. C.3 shows the time difference between cell-zero chip id and the reference chip. It seemed that the synchronization sine wave was sampled at two different clock cycles and this cycle difference (1/80MHz ~ 12.5 ns) caused the timing jump in the different chips. In many cases, this 12.5 ns jump happened only when the run started or ended (i.e. this jump was not observed during one run), so this jump is corrected in the offline analysis.

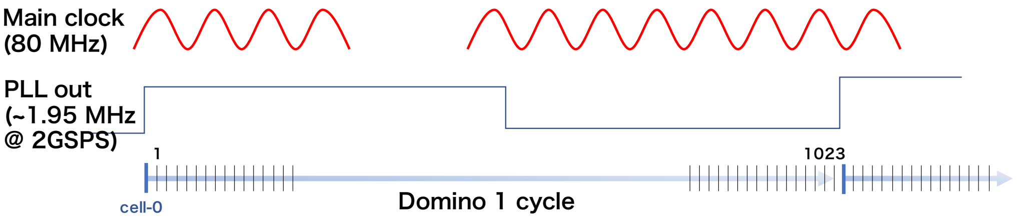

Fig. C.1: The relation among the clock, PLL and DRS cycle.

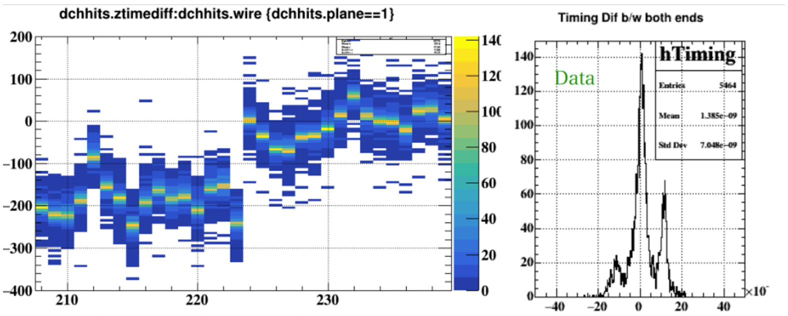

Fig. C.2: The reconstructed hit positions on CDCH wires (left) and the timing difference between both ends (right). Clearly unphysical jump can be seen.

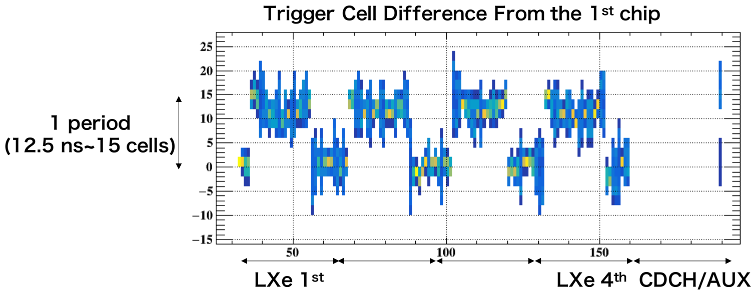

Fig. C.3: The cell-zero chip-id difference from the reference chip. If the synchronization completely works and no trigger jitter, the difference should be zero.

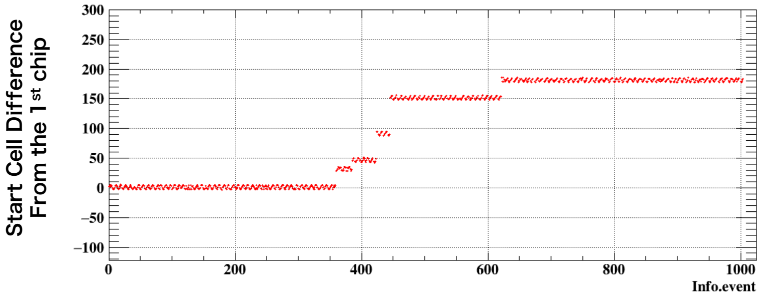

Fig. C.4: Drift of the difference of the cell-zero from the reference chip during a run which caused the out-of-synchronization problem. The cell-zero id of the chip drifted to the one direction.

C.1.3 Out-of-synchronization

In some runs, a drift of the cell-zero was observed as shown in Fig. C.4. It seemed that the sampling point of the synchronization signal failed to be fixed, and the cell-zero continued to drift. The correction of these runs is much more difficult than the 12.5 ns jump since this drift happened suddenly during the same run and the numbers of drift cycles (12.5 ns × cycles) were not fixed even among the runs with the same number of events. The runs with out-of-synchronization were not used for the analysis. These jumps and drifts were modified in the final version of electronics in 2019 latter half. The problems of the jump and drift were solved.

D

Kalman Filter Algorithm

D.1 Kalman Filter Formalism

The Kalman Filter (KF) is a powerful algorithm to obtain the best estimation of the state, and used for the positron tracking in the MEG II analysis. In this chapter, the schematics of the KF algorithm is described based on [32] and [82].

The states of the positron tracks at each point can be expressed by the five parameters (one for the momentum, two for the direction, and two for the position) in GENFIT [32]:

$$\vec{x}_k = \left[\frac{q}{|\vec{p}|}, \frac{du}{dw}, \frac{dv}{dw}, u, v \right]^T , \tag{D.1}$$

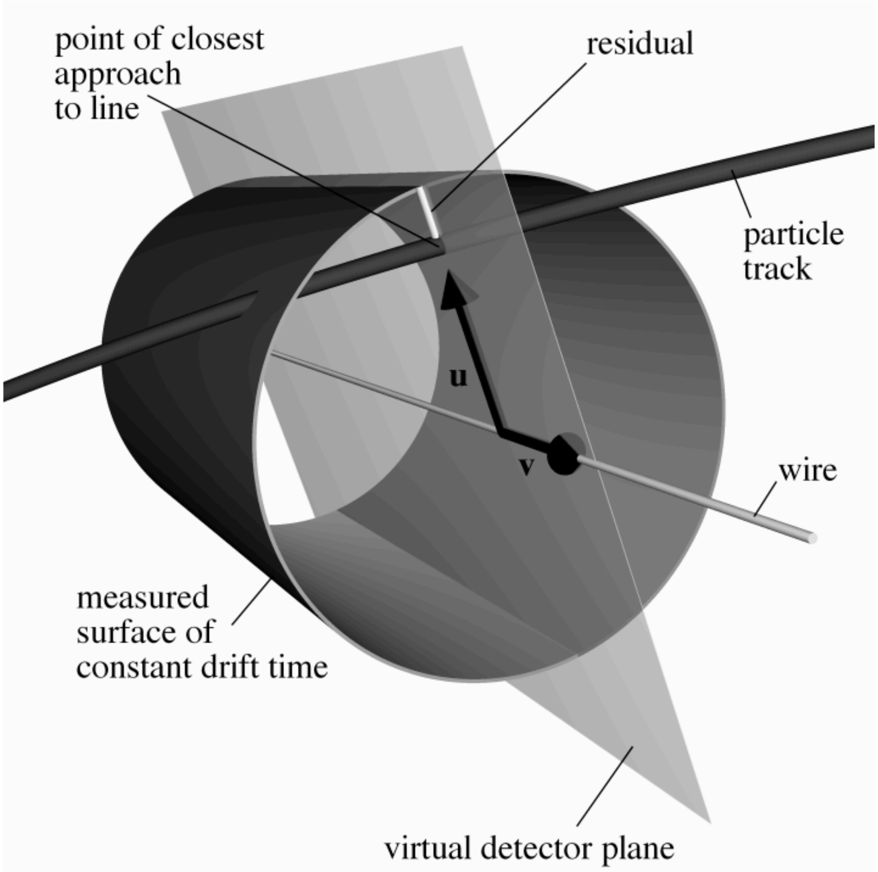

Fig. D.1: The coordinate system of the wire measurement in GENFIT [32].

where k is the index of the measurement (hit index in the track), $\vec{x}_k$ is the state of k-th measurement, q is the particle charge, p is the moentum. u, v, w is the coordinate system on the detector plane defined in the GENFIT, as shown in Fig. D.1.

The k-th state of the positron track is estimated by using the information of the $(k-1)$-th state:

$$\vec{x}_k = \mathbf{f}_{k-1}(\vec{x}_{k-1}) + \vec{w}_{k-1}, \tag{D.2}$$

where $\mathbf{f}_{k-1}$ is a transport matrix from the $(k-1)$-th state to the k-th state, w_{k-1} is the white noise[*1]. The measurement state,$\vec{m}_k$, can be described with the projection matrix $\mathbf{H}_k$:

$$\vec{m}_k = \mathbf{H}_k\vec{x}_k + \vec{\epsilon}_k, \tag{D.3}$$

where the $\vec{\epsilon}_k$ is the measurement uncertainty. The contribution of the multiple scattering, bremsstrahlung, and the other stochastic processes are taken into account in $\vec{w}_{k-1}$.

The KF algorithm performs the two steps recursively; "prediction step" with the mathematical model and "update step" with the measurement information. The schematics is described in Fig. 6.13. This recursive characteristics is suitable for the particle tracking: the k-th state include all of the information up to the $k-1$-th state.

The prediction step estimates the k-th state from the $k-1$-th state which already include all of the information till the $k-1$-th measurement and described as $x_{k-1|k-1}$. The predicted state, $\vec{x}_{k|k-1}$, and its covariance, $\mathbf{C}_{k|k-1}$, are calculated as following:

$$\vec{x}_{k|k-1} = \mathbf{f}_{k-1}(\vec{x}_{k-1|k-1}), \tag{D.4}$$

$$\mathbf{C}_{k|k-1} = \mathbf{f}_{k-1}\mathbf{C}_{k-1|k-1}\mathbf{f}_{k-1}^T + \mathbf{Q}_{k-1}, \tag{D.5}$$

where the $\mathbf{Q}_{k-1}$ is the covariance matrix of $\vec{w}_{k-1}$.

Then the predicted state is updated to $\vec{x}_{k|k}$ and the covariance to $\mathbf{C}_{k|k}$ with the information of the k-th measurement:

$$\vec{x}_{k|k} = \vec{x}_{k|k-1} + \mathbf{K}_k\left[\vec{m}_k - \mathbf{H}_k\vec{x}_{k|k-1}\right], \tag{D.6}$$

$$\mathbf{C}_{k|k} = \left[\mathbf{I} - \mathbf{K}_k\mathbf{H}_k\right]\mathbf{C}_{k|k-1}, \tag{D.7}$$

where $\mathbf{K}_k$ is the Kalman Gain matrix, which determines the best weight for the measurement and the prediction. The $\mathbf{K}_k$ is described as following:

$$\mathbf{K}_k = \mathbf{C}_{k|k-1}\mathbf{H}_k^T\left[\mathbf{H}_k\mathbf{C}_{k|k-1}\mathbf{H}_k^T + \mathbf{V}_k\right]^{-1}, \tag{D.8}$$

where $\mathbf{V}_k$ is the covariance matrix of $\vec{\epsilon}_k$.

One more important information for the positron tracking is the calculation of χ^2 for the track. The χ^2 value at each point after the update step, χ^2_k, can be calculated as following:

$$\chi^2_k = \vec{r}^{\,T}_{k|k}\mathbf{R}^{-1}_{k|k}\vec{r}_{k|k}. \tag{D.9}$$

The $\vec{r}_{k|k}$ is the residual of the state vector after the k-th update step, $\mathbf{R}_{k|k}$ is that of the covariance matrix:

$$\vec{r}_{k|k} = \vec{m}_k - \mathbf{H}_k\vec{x}_{k|k}, \tag{D.10}$$

$$\mathbf{R}_{k|k} = \mathbf{V}_k - \mathbf{H}_k\mathbf{C}_{k|k}\mathbf{H}_k^T. \tag{D.11}$$

[*1] The KF algorithm assumes the linear dynamic system, but the particle representation under the magnetic field is not a linear system. In this case, the system equation is approximated by a linear function with the Taylor expansion. This extended algorithm to the non-linear system is called "Extended Kalman Filter".

The χ^2 of the positron track is obtained by the sum of χ^2_k at each step.

After completing the iteration to the final state, the KF performs the same iteration from the last state to the first state (backward steps). This process is called the "smoothing step". The weight for the smoothing step at k-th state, $\mathbf{A}_k$, is described as following:

$$\mathbf{A}_k = \mathbf{C}_{k|k}\mathbf{F}_k^T\mathbf{C}^{-1}_{k+1|k}. \tag{D.12}$$

After the smoothing step, the state, covariance matrix, and residuals can be calculated as following, respectively:

$$\vec{x}_{k|n} = \vec{x}_{k|k} + \mathbf{A}_k\left[\vec{x}_{k+1|n} - \vec{x}_{k+1|k}\right], \tag{D.13}$$

$$\mathbf{C}_{k|n} = \mathbf{C}_{k|k}\mathbf{A}_k\left[\mathbf{C}_{k+1|n} - \mathbf{C}_{k+1|k}\right]\mathbf{A}_k^T, \tag{D.14}$$

$$\vec{r}_{k|n} = \vec{m}_k - \mathbf{H}_k\vec{x}_{k|n}, \tag{D.15}$$

$$\mathbf{R}_{k|n} = \mathbf{V}_k - \mathbf{H}_k\mathbf{C}_{k|n}\mathbf{H}_k^T, \tag{D.16}$$

as described in [82].

D.2 Deterministic Annealing Filter (DAF)

DAF is the extension of the KF algorithm to guard against the wrong measurement assignment in the same layer. For exmaple, one CDCH hit has the two competing hits in the same (virtual) layer: a "left-measurement" and a "right-measurement" (one is the true measurement and the other is the wrong measurement). Here, the DAF algorithm is briefly described based on Ref. [83] and [33].

The concept of the DAF is to use the predicted residuals of the measurement for the re-weighted observations. The prolongation part is actually identical to the KF case, but the assignment probabilities of all competing measurements can be computed in every layer. Let us assume that there are n_k measurements in the layer k, and their index is written with i, like $\vec{m}_k^i$ (i = 1, ... n_k). The prediction, $\vec{x}_{k|k-1}$, is updated with the observation, $\vec{m}_k^i$, with the assignment probability of p_k^i:

$$\vec{x}_{k|k} = \vec{x}_{k|k-1} + \mathbf{K}_k\sum_{i=1}^{n_k} p_k^i\left[\vec{m}_k - \mathbf{H}_k\vec{x}_{k|k-1}\right]. \tag{D.17}$$

To allow the zero-weights of the measurements, the Kalman gain matrix has to be written in terms of inverse covariance (or weight matrix):

$$\mathbf{K}_k = \left[\mathbf{C}^{-1}_{k|k-1} + p_k\mathbf{H}_k^T\mathbf{V}_k^{-1}\mathbf{H}_k\right]^{-1}\mathbf{H}_k^T + \mathbf{V}_k^{-1}, \tag{D.18}$$

where p_k is the sum of all weights p_k^i. The covariance matrix of the updated state is given by:

$$\mathbf{C}_{k|k} = \left[\mathbf{C}^{-1}_{k|k-1} + p_k\mathbf{H}_k^T\mathbf{V}_k^{-1}\mathbf{H}_k\right]^{-1}. \tag{D.19}$$

After the smoothing step, the prediction $x^*_{k|n}$ using the all measurements except the ones at k-th layer can be obtained along with its covariance $\mathbf{C}^*_{k|n}$. By using this prediction and covariance matrix, the assignment probabilities of the measurements can be computed as following:

$$p_k^i \propto \phi(\vec{m}_k^i; \mathbf{H}_k\vec{x}^*_{k|n}, \mathbf{V}_k + \mathbf{H}_k\mathbf{C}^*_{k|n}\mathbf{H}_k^T). \tag{D.20}$$

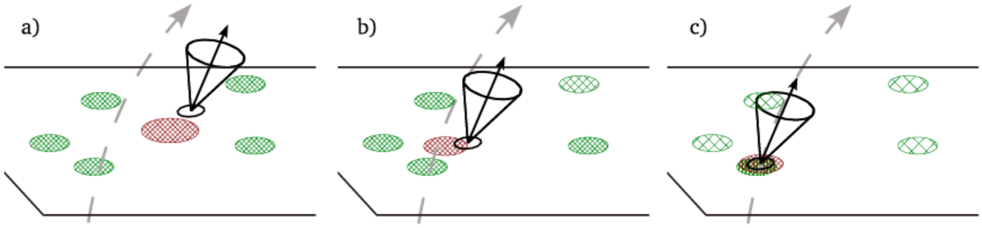

Fig. D.2: Illustration of the probability assignment with deterministic annealing filter [33]. (a) The algorithm starts with high temperature and all measurements (green circles) in the same layer have the similar weight. (b) At the lower temperature, the measurements far from the estimate obtain the lower assignment probabilities. (c) Finally, the assignments are frozen out.

where ϕ(measurement; mean, covariance) means the multivariate gaussian probability function. An even simpler formula can be obtained if the covariance matrix after the smoothing step is neglected[*2]:

$$p_k^i \propto \phi(\vec{m}_k^i; \mathbf{H}_k \vec{x}^*_{k|n}, T\mathbf{V}_k) \equiv \phi_k^i, \tag{D.21}$$

the $\mathbf{V}_k$ is replaced with $T\mathbf{V}_k$, where T is the parameter to control the global optimization of the assignment probabilities and called "temperature". Practically, the weights are normalized as following:

$$p_k^{i\,*} = \frac{\phi_k^i}{\Lambda(T, \lambda) + \sum_{j=0}^{n_k} \phi_k^j}. \tag{D.22}$$

where λ is the parameter which defines the cut-off value[*3].

The meaning of the temperature is illustrated in Fig. D.2. The algorithm starts from the high temperature, resulting in the similar weights for all measurements. Then the update step is iterated at the lower temperature, and finally, the assignments will be frozen out.

[*2] This is natural approximation since the covariance with all the information in the track should have much smaller values than that of the single measurement.

[*3] At the very low temperature, this is equivalent to the χ^2 cut.

E

Track Extrapolation from pTC to CDCH

In Sec. 6.3.4, it was written that the pTC-self tracking is composed of three steeps: the initial parameter estimation step, the Kalman Filter (KF) fitting step, and the extrapolation to the CDCH step. The final step may be especially important to improve the positron reconstruction efficiency by the additional track seeding in the track finding process. The detail of the extrapolation process and the hit finding test from the pTC to the CDCH with MC simulation is described in the following section.

E.1 Extrapolation

The final step of the pTC independent tracking task is extrapolating the track to the outer surface of the CDCH defined as a cylinder along the z-axis with R = 27 cm. In GENFIT package the Runge-Kutta algorithm including a full material model is implemented. The extrapolation is performed step by step from the initial state obtained by the KF fitting, with the correction of the energy loss and the multiple scattering.

By extrapolating the state vector near the CDCH hits, the track finding in CDCH outer region becomes possible by checking the consistency of the drift time, the phi-position, the position from the CDCH wire measurement and the stereo crossing point of two layers. Fig. E.1 shows the example of the track fitting results with pTC hits and CDCH outer (layer 1

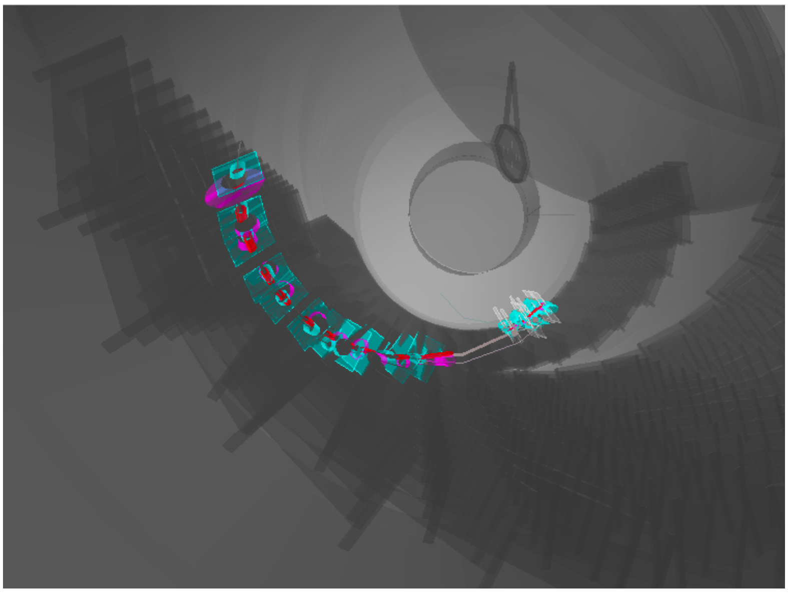

Fig. E.1: A positron partial track reconstructed with pTC hits and CDCH hits (MC). Blue rectangular planes show pTC hits, blue cylinders show drift circles of CDCH hits, and gray planes show CDCH hits.

– 4) hits.

This partial tracking algorithm is used to estimate the z-resolution on wires and the matching efficiency between the CDCH and pTC with the commissioning data. One more important application of this extrapolated state is to be used as the seed state for CDCH track finding process. A partial track has much more information and reliability than a pTC cluster, these additional information will further improve the track finding quality and the reconstruction efficiency. This additional seeding method is currently still under development.

F

Noise Spectrum from Commissioning 2020

In this section, the latest noise situation from the 2020 commissioning is used for the preliminary study.

F.1 Noise Spectrum and Noise Level

Fig. F.1 and Fig. F.2 shows the spectrum and the RMS-noise, respectively. In 2020, the higher gain FE cards (×2 and ×4 from the standard one) were also prepared and tested, but in this appendix, only the results with the standard FE cards were shown. There still remains the 50 MHz noise and the unknown high frequency noise (300 MHz). As expected, the noise

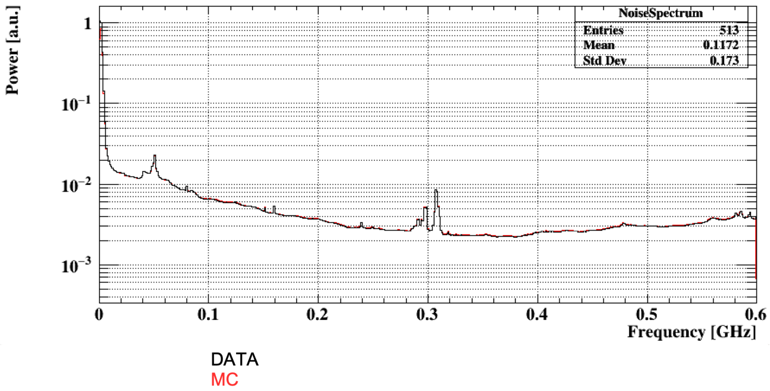

Fig. F.1: The noise spectrum observed in 2020 with the standard FE card.

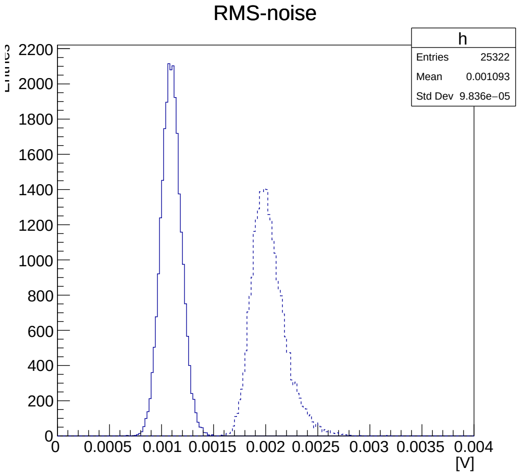

Fig. F.2: The RMS-noise sin 2020 with the standard FE card. The muon rate is MEG II nominal (7×10^7/s)

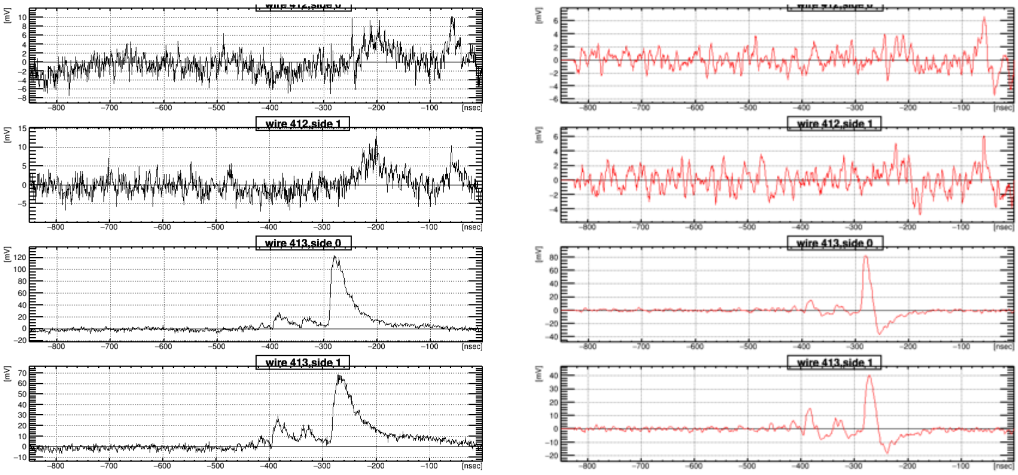

Fig. F.3: The waveforms in the 2020 commissioning under the muon beam. (Left) before the noise subtraction, (right) after the noise subtraction.

Table F.1: The positron reconstruction resolution under the several beam rates.

Variable	Signal Single	Signal Single+O_2	Pile-up 7×10^7	Pile-up 7×10^7+O_2
θ [mrad]	6.0	6.2	6.7	6.7
ϕ [mrad]	5.5	5.9	6.7	6.2
P [MeV]	80	82	96	95
z [mm]	1.5	1.6	1.7	1.8
y [mm]	0.7	0.7	0.8	0.8
t [ps]	45	47	45	46
Efficiency [%]	80.0	77.5	64.6	62.5

level before the subtraction is ~2 mV, and after the subtraction is ~1 mV. The examples of the waveforms from the 2020 commissioning are shown in Fig. F.3. Clearly, the low frequency noise became smaller than the 2018 situation (Fig. 7.3).

F.2 Expected Performances

The expected performance of the positron spectrometer with the 2020 noise situation is summarized in Table F.1. The effect of the additive gas (0.5% O_2) is also summarized[*1].

The conclusion in Chap. 9 takes the additive gas effect and the noise spectrum into account in “case-8”. Even with the latest operation situation, 6×10^{-14} is still the reasonable goal.

[*1] These values do not include the effect of “angle correlation correction” and “pTC-CDCH track-selection”.

G

Performance Evaluated with Reconstructed Kinematics

G.1 Performance Evaluated with Reconstructed Kinematics

The resolutions and efficiency of the positron reconstruction were evaluated by using the MC truth in Chap. 8. In this appendix, the performance of the positron spectrometer evaluated with the reconstructed variables under the actual condition, i.e. without MC truth information, will be described.

As for the evaluation of pTC timing resolution the even-odd analysis is used. Its concept and detail are already shown in the sentences. In this chapter, the algorithms for the tracking evaluation, which could not be performed with the commissioning data due to the limited readout channels, are mainly summarized.

G.1.1 CDCH Tracking Resolution

For the evaluation of the tracking performance, two methods are inherited from the MEG experiment (evaluation with MEG 2013 data is shown in [4]): double turn analysis and Michel-Fit. Generally, the extracted resolutions and the resolutions from MC truth do not completely agree with each other. The extracted values from the real data will be scaled by using the values from MC to obtain the detector performance.

Double Turn Analysis

To extract the energy resolution, angular resolution and position resolution of the track, double-turn analysis is used. Double-turn analysis uses track segments for the positron with $N_{\mathrm{Turn}} \geq 2$. An imaginary vertex plane is assumed between the first turn and second turn. The first turn segment and second turn segment are fitted separately and each turn segment is extrapolated to that plane. The difference in each variables (θ, ϕ, z, y, E_e) between both turns is calculated and fitted with the double-gaussian function. Fig. G.1 shows the fit result for each variable and Table G.1 summarized the extracted values.

Table G.1: The extracted and estimated resolutions for the detector.

Variable	MC (Signal)	7×10^7
θ [mrad]	6.5	7.7
ϕ [mrad]	6.2	6.9
P [keV]	91	118
z [mm]	1.7	1.6
y [mm]	0.8	0.85

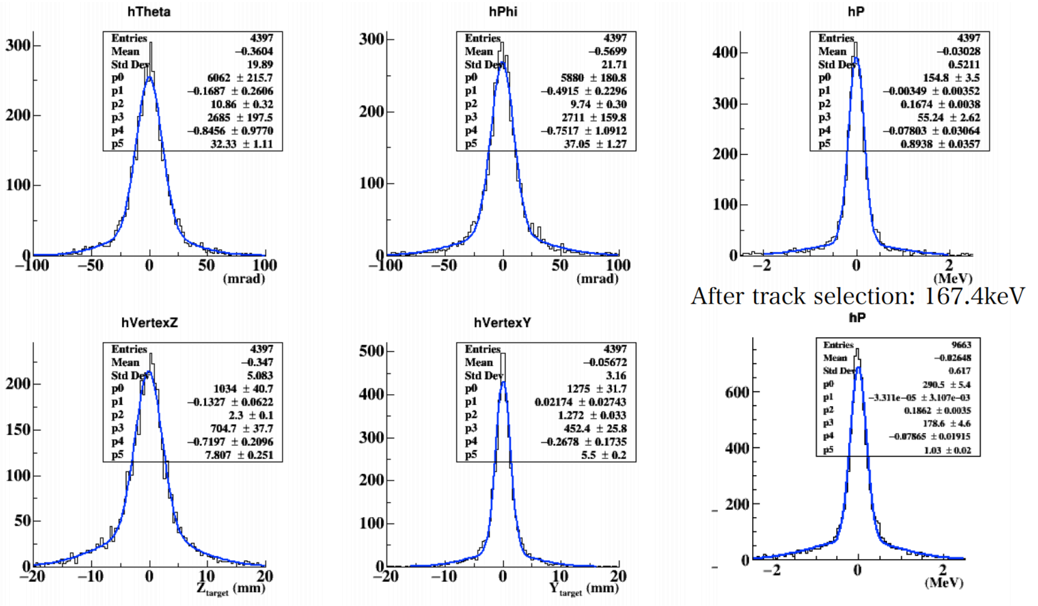

After track selection: 167.4keV

Before track selection: 186.2 keV

Fig. G.1: The distributions of CDCH tracks between the first turn and the second turn.

Table G.2: Comparison of the results from Michel-Fit with MEG II expected and MEG 2013 data.

Parameter	**Michel Fit with 2013 data**	**Michel Fit with MEG II expected (MC)**
σ_{core} [keV]	325	110
σ_{tail} [MeV]	1.91	2.28
f_{core}	0.852	0.911
$\mu_{\mathrm{acceptance}}$ [MeV]	49	46.9
$\sigma_{\mathrm{acceptance}}$ [MeV]	2.5	2.4

Since the double turn analysis uses not typical 1.5-turn events but only 2(or more than 2)-turn events for the evaluation, the extracted resolution may not agree with the results from MC truth completely. Though the double turn analysis algorithm works fine, further study to optimize the event selection criteria[*1] is needed.

Michel-Fit

As for the momentum resolution, another method called “Michel-Fit” is also used. The theoretical energy spectrum from the Michel decay, $S_{\mathrm{theo}}(E_e^{\mathrm{param}})$, is well known [41]. The reconstructed Michel energy spectrum, $S_{\mathrm{rec}}(E_e^{\mathrm{rec}})$, can be fitted with the following formula:

$$S_{\mathrm{rec}}(E_e^{\mathrm{rec}}) = \Sigma(S_{\mathrm{theo}} \times F_{\mathrm{acceptance}})(E_e^{\mathrm{param}}) * R_{\mathrm{response}}, \tag{G.1}$$

[*1] Currently the same event selection criteria to the signal case is applied for event selection except for the number of turns ($N_{\mathrm{Turn}} \geq 2$) and the timing coincidence (±12 ns) between the gamma ray.

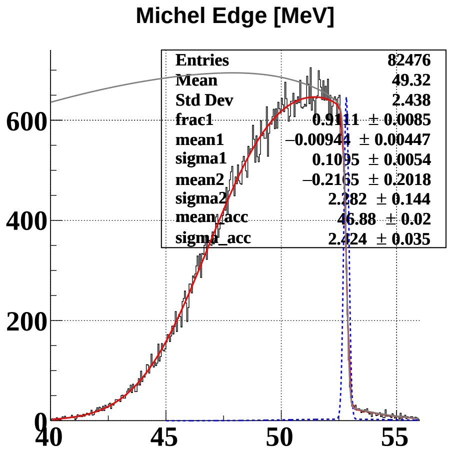

Fig. G.2: Michel-Fit with the reconstructed energy spectrum (MC). The grey line shows the theoretical Michel spectrum, the blue dashed line response function, and the red line is the fitting result.

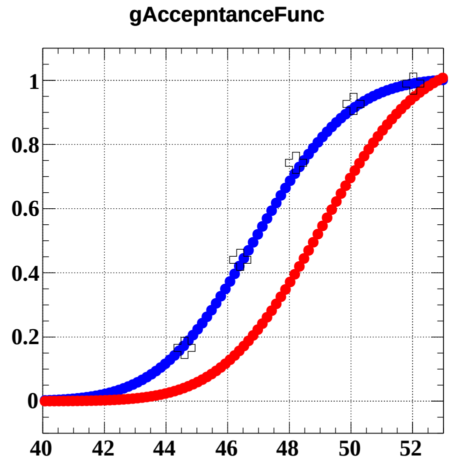

Fig. G.3: The acceptance function of MEG II (MC, blue) and MEG 2013 data (red) normalized at 52.8 MeV. The relative efficiency (normalized at 52.8 MeV) from the reconstructed tracks in the range of 43 – 53 MeV/2 MeV is also shown with cross marks.

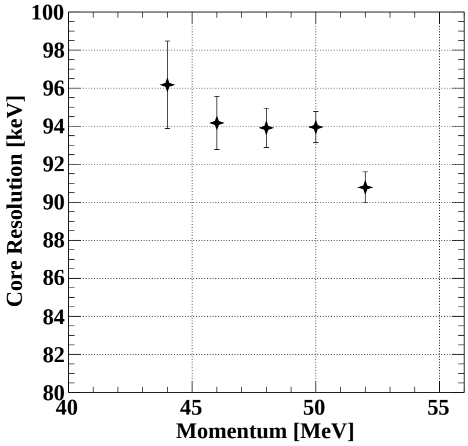

Fig. G.4: The momentum dependence of the momentum resolution with Michel positrons.

where $F_{\text{acceptance}}$ is the acceptance function of the positron spectrometer, which describes the relative efficiency of the positron spectrometer as a function of the positron momentum. $F_{\text{acceptance}}$ is defined with an error function as follows:

$$F_{\text{acceptance}} = \frac{1 + \text{erf}(\frac{E_e^{\text{param}} - \mu}{\sqrt{2}\sigma})}{2}. \tag{G.2}$$

R_{response} is the response function defined with the double gaussian function:

$$R_{\text{response}} = f_{\text{core}} \times \text{gaus}_{\text{core}} + (1 - f_{\text{core}}) \times \text{gaus}_{\text{tail}}. \tag{G.3}$$

f_{core} is the fraction value for the core component of distribution.

Fig. G.2 shows an example of the Michel-Fit, and Table G.2 shows the values from the fitting. Fig. G.3 shows the obtained acceptance functions in MEG II MC and MEG 2013 data. The relative reconstruction efficiency calculated from the reconstructed tracks and normalized at the signal energy bin (52 MeV) is also shown. The acceptance around the signal region is clearly improved from the MEG experiment. The momentum resolution extracted from the Michel-Fit was worse than the case of the evaluation with MC-truth. The same trend was obtained from the double turn analysis (118 keV). This difference comes from the difference of the Michel events and the signal events, especially the difference of the momentum of positrons. Fig. G.4 shows the momentum dependence of the momentum resolution with Michel positrons. The MEG II positron spectrometer is optimized for the detection of the signal-like (around 52.8 MeV) positrons. The resolution with lower-momentum Michel positrons becomes slightly worse than the signal positrons case. However, this dependence is too small to explain the worse resolution extracted from the Michel-Fit. Other possibilities are the systematics from the track selection for the Michel events and the intrinsic systematics of the method, but the reason of the worse resolution is not understood[*2].

[*2] Actually, if this worse resolution comes from not a physics nor a software reason but just systematics of the methods, it is not a big problem; we can just scale the parameter.

Acknowledgments

First of all, I would like to thank Prof. Toshinori Mori and Prof. Wataru Ootani for giving me a great opportunity to join the MEG II experiment. I would like to thank all members of the MEG II pTC group, especially, Prof. Wataru Ootani, Dr. Yusuke Uchiyama, Dr. P.W. Catttaneo, Dr. Matteo De Gerone, Dr. Miki Nishimura, Dr. Mitsutaka Nakao, Mr. Kosuke Yanai, and Mr. Taku Yonemoto for working together. Prof. Wataru Ootani kindly supervised me and gave me lots of advices. I learned lots of things from Dr. Yusuke, not only the hardware and the software, but also the mind as a researcher. Without his teaching, this work would not be completed. I would like to thank to all members of the MEG II positron analysis group, especially, Dr. Francesco Renga, Dr. Cecilia Voena, Dr. Marco Chiappini, Mr. Mannuel Meucci, Dr. Fedor V. Ignatov, Dr. William R. Molzon, Mr. Dylan Palo, and Mr. Patrick Schwendimann. I strongly wanted to join the engineering run for the positron spectrometer, however, I am sure that the MEG II positron analysis group will obtain the promising and excellent results in 2021.

I would also like to express my great thanks to the collaborators, especially, Dr. Toshiyuki Iwamoto and Dr. Kei Ieki, who supported not only my research but also my daily life in Switzerland, Dr. Miki Nishimura, Dr. Shiji Ogawa, Dr. Mitsutaka Nakao, Mr. Satoru Kobayashi, Ms. Rina Onda, Mr. Kosuke Yanai, Mr. Kazuki Toyoda, who shared the wonderful time in Switzerland. Especially, Dr. Nishimura Miki was always kind and helpful, Dr. Mitsutaka Nakao gave me lots of supports and advices for the research life in the doctor course, and I worked on many pTC studies and tasks with Mr. Kosuke Yanai.

Finally, I would like to thank my family for their constant support and encouragement.

Reference

[1] A. M. Baldini *et al.*, Search for the lepton flavour violating decay $\mu^+ \to e^+\gamma$ with the full dataset of the MEG experiment, The European Physical Journal C 76 (8) (2016) 434, doi:10.1140/epjc/s10052-016-4271-x.

[2] P. A. Zyla *et al.*, Review of Particle Physics, Progress of Theoretical and Experimental Physics 2020 (8) (aug 2020), doi:10.1093/ptep/ptaa104.

[3] A. Baldini *et al.*, The design of the MEG II experiment, European Physical Journal C 78 (5) (2018), doi:10.1140/epjc/s10052-018-5845-6.

[4] D. Kaneko, The final result of $\mu^+ \to e^+\gamma$ search with the MEG experiment, Ph.D. thesis, The University of Tokyo (2016).

[5] BC422 property from Saint-Gobain. available at https://www.crystals.saint-gobain.com/products/bc-418-bc-420-bc-422-bc-422q(accessed on 2021-05-04) .

[6] The homepage of AdvanSiD. available at http://advansid.com/home(accessed on 2021-05-04) .

[7] M. Nishimura, Positron Timing Measurement to Search for Lepton Flavor Violating Decay in MEG II, Ph.D. thesis, The University of Tokyo (2018).

[8] G. Boca *et al.*, The laser-based time calibration system for the MEG II pixelated Timing Counter, Nuclear Instruments and Methods in Physics Research, Section A: Accelerators, Spectrometers, Detectors and Associated Equipment 947 (2019) 162672, doi:10.1016/j.nima.2019.162672.

[9] Y. Kuno, Y. Okada, Muon decay and physics beyond the standard model, Reviews of Modern Physics 73 (1) (2001) 151–202, doi:10.1103/RevModPhys.73.151, arXiv:9909265.

[10] T. Mori, W. Ootani, Flavour violating muon decays, Progress in Particle and Nuclear Physics 79 (2014) 57–94, doi:https://doi.org/10.1016/j.ppnp.2014.09.001.

[11] S. Antusch *et al.*, Impact of θ_{13} on lepton flavour violating processes within SUSY seesaw, Journal of High Energy Physics 2006 (11) (2006) 090–090, doi:10.1088/1126-6708/2006/11/090.

[12] T. Moroi, M. Nagai, T. Yanagida, Lepton Flavor Violations in High-Scale SUSY with Right-Handed Neutrinos, Physics Letters B 728 (may 2013), doi:10.1016/j.physletb.2013.11.058.

[13] Hirao, Kaigo and Moroi, Takeo, Leptonic CP and Flavor Violations in SUSY GUT with Right-handed Neutrinos (2021). arXiv:2102.04070, arXiv:2102.04070.

[14] V. Andreev *et al.*, Improved limit on the electric dipole moment of the electron, Nature 562 (7727) (2018) 355–360, doi:10.1038/s41586-018-0599-8.

[15] DRS Chip Home Page. available at https://www.psi.ch/en/drs(accessed on 2021-05-04) .

[16] S. Ogawa, Liquid xenon detector with highly granular scintillation readout to search for $\mu^+ \to e^+\gamma$ with sensitivity of 5×10^{-14} in MEG II experiment, Ph.D. thesis, The University of Tokyo (2020).

[17] The PSI proton accelerator. available at https://www.psi.ch/en/media/the-psi-proton-accelerator(accessed on 2021-05-04) .

[18] J. Adam *et al.*, The MEG detector for $\mu^+ \to e^+\gamma$ decay search, European Physical Journal C 73 (2013) 2365, doi:10.1140/epjc/s10052-013-2365-2.

[19] K. Ieki *et al.*, Large-area MPPC with enhanced VUV sensitivity for liquid xenon scintillation detector, Nuclear Instruments and Methods in Physics Research Section A: Accelerators, Spectrometers, Detectors and Associated Equipment 925 (2019) 148–155, `doi:https://doi.org/10.1016/j.nima.2019.02.010`.

[20] M. Francesconi *et al.*, The WaveDAQ integrated Trigger and Data Acquisition System for the MEG II experiment (2018), `arXiv:1806.09218`.

[21] A. M. Baldini *et al.*, MEG Upgrade Proposal (2013), `arXiv:1301.7225`.

[22] M. Nakao, MEG II positron timing counter - construction, calibration, and performance evaluation by using high intensity muon beam (in Japanese), Master's thesis, The University of Tokyo (2017).

[23] P. W. Cattaneo *et al.*, Development of High Precision Timing Counter Based on Plastic Scintillator with SiPM Readout, IEEE Transactions on Nuclear Science 61 (5) (2014) 2657–2666, `doi:10.1109/TNS.2014.2347576`.

[24] Y. Kohei, Research on Long-term Operation and Analysis Method of Positron Timing Counter in MEG II Experiment, Master's thesis, The University of Tokyo (2020).

[25] M. Nakao *et al.*, A Laser-based Time Calibration System for the MEG II Timing Counter, in: 2018 IEEE Nuclear Science Symposium and Medical Imaging Conference Proceedings (NSS/MIC), 2018, pp. 1–3, `doi:10.1109/NSSMIC.2018.8824370`.

[26] M. Chiappini, The construction and commissioning of the ultra low mass MEG II drift chamber for the search of the $\mu^+ \to e^+\gamma$ decay at branching ratios below 10^{-13}, Ph.D. thesis, University of Siena and INFN Pisa (2019).

[27] W. Ootani *et al.*, Development of a thin-wall superconducting magnet for the positron spectrometer in the MEG experiment, IEEE Transactions on Applied Superconductivity 14 (2) (2004) 568–571, `doi:10.1109/TASC.2004.829721`.

[28] M. Usami, Research on radiation tolerance and long-term stable operation of MEG II positron timing counter (in Japanese), Master's thesis, The University of Tokyo (2018).

[29] M. Nishimura *et al.*, Full system of positron timing counter in MEG II having time resolution below 40 ps with fast plastic scintillator readout by SiPMs, Nuclear Instruments and Methods in Physics Research Section A: Accelerators, Spectrometers, Detectors and Associated Equipment 958 (2020) 162785, `doi:https://doi.org/10.1016/j.nima.2019.162785`.

[30] M. Nakao on behalf of MEG II collaboration, Commissioning of positron timing counter for MEG II Experiment in 2017: Calibration (Japanese Canference), The Physical Society of Japan 73rd Annual Meeting (2018).

[31] G. Boca *et al.*, Timing resolution of a plastic scintillator counter read out by radiation damaged SiPMs connected in series, Nuclear Instruments and Methods in Physics Research Section A: Accelerators, Spectrometers, Detectors and Associated Equipment 999 (2021) 165173, `doi:https://doi.org/10.1016/j.nima.2021.165173`.

[32] C. Höppner *et al.*, A novel generic framework for track fitting in complex detector systems, Nuclear Instruments and Methods in Physics Research Section A: Accelerators, Spectrometers, Detectors and Associated Equipment 620 (2) (2010) 518–525, `doi:https://doi.org/10.1016/j.nima.2010.03.136`.

[33] S. Fleischmann, Track Reconstruction in the ATLAS Experiment The Deterministic Annealing Filter, Ph.D. thesis, Bergische Universität Wuppertal (2006).

[34] G. Aad *et al.*, Observation of a new particle in the search for the Standard Model Higgs boson with the ATLAS detector at the LHC, Physics Letters, Section B: Nuclear, Elementary Particle and High-Energy Physics 716 (1) (2012) 1–29, `doi:10.1016/j.physletb.2012.08.020`, `arXiv:1207.7214`.

[35] S. Chatrchyan *et al.*, Observation of a new boson at a mass of 125 GeV with the CMS experiment at the LHC, Physics Letters, Section B: Nuclear, Elementary Particle and High-Energy Physics 716 (1) (2012) 30–61, `doi:10.1016/j.physletb.2012.08.021`, `arXiv:1207.7235`.

[36] Y. Fukuda *et al.*, Evidence for oscillation of atmospheric neutrinos, Physical Review Letters 81 (8) (1998) 1562–1567, `doi:10.1103/PhysRevLett.81.1562`, `arXiv:hep-ex/9807003`.

[37] S. P. Martin, A Supersymmetry Primer, in: G. L. Kane (Ed.), Advanced Series on Directions in High Energy Physics, Perspectives on Supersymmetry II, 2010, pp. 1–153, `doi:10.1142/9789814307505_0001`.

[38] H. Goldberg, Constraint on the Photino Mass from Cosmology, Physical Review Letters 50 (19) (1983) 1419–1422, `doi:10.1103/PhysRevLett.50.1419`.

[39] J. Ellis *et al.*, Supersymmetric relics from the big bang, Nuclear Physics B 238 (2) (1984) 453–476, `doi:https://doi.org/10.1016/0550-3213(84)90461-9`.

[40] T. Aoyama *et al.*, The anomalous magnetic moment of the muon in the Standard Model, Physics Reports 887 (2020) 1–166, `doi:https://doi.org/10.1016/j.physrep.2020.07.006`, `arXiv:2006.04822`.

[41] T. Kinoshita, A. Sirlin, Radiative Corrections to Fermi Interactions, Phys. Rev. 113 (6) (1959) 1652–1660, `doi:10.1103/PhysRev.113.1652`.

[42] M. Aaboud *et al.*, Search for supersymmetry in final states with two same-sign or three leptons and jets using 36 fb^{-1} of $\sqrt{s}$ = 13 TeV pp collision data with the ATLAS detector, Journal of High Energy Physics 2017 (9) (2017) 84, `doi:10.1007/JHEP09(2017)084`.

[43] V. Khachatryan *et al.*, Search for supersymmetry in pp collisions at $\sqrt{s}$ = 13TeV in the single-lepton final state using the sum of masses of large-radius jets, Journal of High Energy Physics 2016 (8) (2016) 122, `doi:10.1007/JHEP08(2016)122`.

[44] I. Esteban *et al.*, Updated fit to three neutrino mixing: exploring the accelerator-reactor complementarity, Journal of High Energy Physics 2017 (1) (2017) 87, `doi:10.1007/JHEP01(2017)087`.

[45] B. C. Allanach *et al.*, The Snowmass Points and Slopes: benchmarks for SUSY searches, The European Physical Journal C - Particles and Fields 25 (1) (2002) 113–123, `doi:10.1007/s10052-002-0949-3`.

[46] J. A. Casas, A. Ibarra, Oscillating neutrinos and $\mu \to$ e,γ, Nuclear Physics B 618 (1) (2001) 171–204, `doi:https://doi.org/10.1016/S0550-3213(01)00475-8`.

[47] M. L. Brooks *et al.*, New limit for the lepton-family-number nonconserving decay $\mu^+ \to e^+\gamma$, Physical Review Letters 83 (8) (1999) 1521–1524, `doi:10.1103/PhysRevLett.83.1521`.

[48] A. E. Pifer, T. Bowen, K. R. Kendall, A high stopping density μ^+ beam, Nuclear Instruments and Methods 135 (1) (1976) 39–46, `doi:https://doi.org/10.1016/0029-554X(76)90823-5`.

[49] A. Oya, Development of ultra-low material RPC detector for further sensitivity improvement of MEG II experiment (in Japanese), Master's thesis, The University of Tokyo (2020).

[50] S. Ritt, R. Dinapoli, U. Hartmann, Application of the DRS chip for fast waveform digitizing, Nuclear Instruments and Methods in Physics Research Section A: Accelerators, Spectrometers, Detectors and Associated Equipment 623 (1) (2010) 486–488, `doi:https://doi.org/10.1016/j.nima.2010.03.045`.

[51] R. Bertoni *et al.*, A laser diode based system for calibration of fast time-of-flight detectors, Journal of Instrumentation 11 (05) (2016) P05024–P05024, `doi:10.1088/1748-0221/11/05/p05024`.

[52] A. Ferrari, The KLOE drift chamber, Nuclear Instruments and Methods in Physics Research, Section A: Accelerators, Spectrometers, Detectors and Associated Equipment 494 (1-3) (2002) 163–172, `doi:10.1016/S0168-9002(02)01461-4`.

[53] California Fine Wire (CFW) company. available at `https://calfinewire.com/`(accessed on 2021-05-04) .

[54] A. M. Baldini *et al.*, Single-hit resolution measurement with MEG II drift chamber prototypes, Journal of Instrumentation 11 (2016) P07011—-P07011, `doi:10.1088/1748-0221/11/07/P07011`.

[55] G. Chiarello *et al.*, An automatic system for the wiring of Drift Chambers for modern high intensity and high precision

particle physics experiments, Journal of Instrumentation 15 (07) (2020) C07034—-C07034, doi:10.1088/1748-0221/15/07/c07034.

[56] M. Cascella, F. Grancagnolo, G. Tassielli, Cluster Counting/Timing Techniques for Drift Chambers, Nuclear Physics B - Proceedings Supplements 248-250 (2014) 127–130, doi:https://doi.org/10.1016/j.nuclphysbps.2014.02.025.

[57] E. Garutti, Y. Musienko, Radiation damage of SiPMs, Nuclear Instruments and Methods in Physics Research Section A: Accelerators, Spectrometers, Detectors and Associated Equipment 926 (2019) 69–84, doi:https://doi.org/10.1016/j.nima.2018.10.191.

[58] C. Xu *et al.*, Influence of X-ray irradiation on the properties of the Hamamatsu silicon photomultiplier S10362-11-050C, Nuclear Instruments and Methods in Physics Research Section A: Accelerators, Spectrometers, Detectors and Associated Equipment 762 (2014) 149–161, doi:https://doi.org/10.1016/j.nima.2014.05.112.

[59] C. Inguimbert *et al.*, "Effective NIEL" in Silicon: Calculation Using Molecular Dynamics Simulation Results, IEEE Transactions on Nuclear Science 57 (4) (2010) 1915–1923, doi:10.1109/TNS.2010.2049581.

[60] M. Simonetta *et al.*, Test and characterisation of SiPMs for the MEGII high resolution Timing Counter, Nuclear Instruments and Methods in Physics Research Section A: Accelerators, Spectrometers, Detectors and Associated Equipment 824 (2016) 145–147, doi:https://doi.org/10.1016/j.nima.2015.11.023.

[61] The homepage of the MIDAS information. available at https://midas.triumf.ca/MidasWiki/index.php/Main_Page(accessed on 2021-05-04) .

[62] P. W. Cattaneo *et al.*, The architecture of MEG simulation and analysis software, European Physical Journal Plus 126 (2011) 60, doi:10.1140/epjp/i2011-11060-6.

[63] S. Agostinelli *et al.*, Geant4—a simulation toolkit, Nuclear Instruments and Methods in Physics Research Section A: Accelerators, Spectrometers, Detectors and Associated Equipment 506 (3) (2003) 250–303, doi:https://doi.org/10.1016/S0168-9002(03)01368-8.

[64] J. Allison *et al.*, Recent developments in Geant4, Nuclear Instruments and Methods in Physics Research Section A: Accelerators, Spectrometers, Detectors and Associated Equipment 835 (2016) 186–225, doi:https://doi.org/10.1016/j.nima.2016.06.125.

[65] The homepage of the SPICE software. available at http://bwrcs.eecs.berkeley.edu/Classes/IcBook/SPICE/(accessed on 2021-05-04) .

[66] V. Blobel, C. Kleinwort, A New Method for the High-Precision Alignment of Track Detectors (2002), arXiv:hep-ex/0208021.

[67] Millepede software homepage. available at https://www.desy.de/~kleinwrt/MP2/doc_180/html/index.html(accessed on 2021-05-04) .

[68] M. Venturini *et al.*, Ageing tests for the MEG II drift chamber, Nuclear Instruments and Methods in Physics Research Section A: Accelerators, Spectrometers, Detectors and Associated Equipment 824 (2016) 592–594, doi:https://doi.org/10.1016/j.nima.2015.09.030.

[69] ROOT Reference Guide, MINUIT. available at https://root.cern.ch/doc/master/classTMinuit.html(accessed on 2021-03-18) .

[70] A. Fratangelo, Calibration of the MEGII drift chamber, Master's thesis, Sapienza University of Rome (2018).

[71] ALICE Offline Project homepage. available at https://alice-offline.web.cern.ch/(accessed on 2021-05-04) .

[72] R. Barlow, Extended maximum likelihood, Nuclear Instruments and Methods in Physics Research Section A: Accelerators, Spectrometers, Detectors and Associated Equipment 297 (3) (1990) 496–506, doi:10.1016/0168-

9002(90)91334-8.

[73] G. Cowan *et al.*, Asymptotic formulae for likelihood-based tests of new physics, The European Physical Journal C 71 (2) (2011) 1554, doi:10.1140/epjc/s10052-011-1554-0.

[74] HAMAMATSU PHOTONICS K.K., PLP-10 Laser diode head Series FEATURES. available at https://www.hamamatsu.com/resources/pdf/sys/SOCS0003E_PLP-10.pdf(accessed on 2021-03-08) .

[75] OZ OPTICS, QMMJ-31-IRVIS-50/125-1HYWT-2.5-SP. available at https://shop.ozoptics.com/multi-mode-patchcords(accessed on 2021-03-08) .

[76] OZ OPTICS, MMJ-33-IRVIS-50/125-3-10. available at https://shop.ozoptics.com/multi-mode-patchcords(accessed on 2021-03-08) .

[77] Arden PHOTONICS, ModCon Mode Controller - Telecom - Arden Photonics. available at https://www.ardenphotonics.com/products/modcon-mode-controller-telecom/(accessed on 2021-03-08) .

[78] OZ OPTICS, FUSED-12-IRVIS-50/125-50/50-3S3S3S-3-0.25. available at https://shop.ozoptics.com/mm-fiber-fixed-couplers-splitters(accessed on 2021-03-08) .

[79] Lightel Technologies Inc., MMC-18-A-EVEN-1-A-30CM-R-1. available at https://lightel.com/product/5/multimode-coupler(accessed on 2021-03-08) .

[80] THORLABS, DET02AFC. available at https://www.thorlabs.com/thorproduct.cfm?partnumber=DET02AFC/M#ad-image-0(accessed on 2021-03-08) .

[81] LEONI, fibre Optical Switch mol 1x12-50 µ m. available at https://www.leoni-fiber-optics.com/en/products-and-services/optical-components/optical-switches/(accessed on 2021-03-08) .

[82] H. Nishiguchi, An Innovative Positron Spectrometer to Search for the Lepton Flavour Violating Muon Decay with a Sensitivity of 10^{-13}, Ph.D. thesis, The University of Tokyo (2008).

[83] R. Frühwirth, A. Strandlie, Track fitting with ambiguities and noise: A study of elastic tracking and nonlinear filters, Computer Physics Communications 120 (2) (1999) 197–214, doi:https://doi.org/10.1016/S0010-4655(99)00231-3.